

# ABSTRACT

MENDLOW, MICAELA ROSE. Analysis and Validation of Three-Dimensional Models for Corneal Topography from Optical Coherence Tomography Point Cloud Data. (Under the direction of Mansoor Haider.)

Optical coherence tomography (OCT) presents a promising alternative to traditional corneal topography due to its high resolution and ability to image both the anterior and posterior surfaces of the cornea. Accurate maps of both corneal elevation and curvature are essential to the diagnosis of refractive disorders. Therefore, models constructed from OCT point cloud data must take both metrics into account. Modeling of the posterior corneal surface is further complicated by optical distortion in the imaging data caused by refraction as the light from the OCT scanner crosses the anterior surface boundary.

While there are currently several different techniques for modeling local features of the cornea, these approaches often involve some fundamental assumptions about the shape of the surface or surfaces being measured. Zernike polynomials—which form an orthonormal basis on the unit disc—are widely used in ophthalmology for classifying spherical aberrations of the eye. Polynomial expansion using Zernike basis functions has also become a popular choice for 3D modeling of corneal height data due to their ability to fit complex surface shapes such as one might encounter in a highly diseased cornea. Recently, it has been proposed that such models could also be used for the computation of local curvature. However, little research has been done to validate the use of Zernike elevation models for computing corneal curvature maps from OCT data, particularly in the context of a two-surface model. Furthermore, selection of the optimal Zernike order for modeling a particular surface remains a difficult question. Often the topic is not considered at all, with clinicians selecting a specific model order based on the standard practices. Most papers that do address the topic of Zernike model order selection focus only on the accuracy of the surface fit, leaving questions about whether the model is also the optimal choice for curvature computation.

We investigate and validate the use of finite Zernike polynomial expansions for 3D modeling of volumetric OCT point cloud data from corneal imaging. The suitability of each Zernike model order is evaluated according to the accuracy of not only the model fit but also the meridional (tangential) curvature maps and principal curvatures computed from those models. A similar analysis—in which we also describe and validate a 3D

refraction correction algorithm from the literature—is performed for the posterior surface. Our methods are applied to real OCT data from two imaging phantoms with known design specifications, as well as synthetic data generated from these design equations. In our analyses, we also consider the impact of quantization error inherent in imaging data in order to determine whether this results in a theoretical bound on the accuracy of the models.

Propagation of error within the two-surface model, particularly as it affects curvature, is analyzed using several statistical techniques. Confidence intervals for the Zernike coefficient estimates from regression analysis are compared to Bayesian density estimates obtained using the delayed rejection adaptive Metropolis (DRAM) algorithm. Uncertainty from these estimates is propagated through the model using Monte Carlo simulations to quantify its effect on surface fit and curvature calculations. We also consider several methods from global sensitivity analysis to evaluate the sensitivity of the principal curvature estimates to error in the Zernike coefficients.

© Copyright 2020 by Micaela Rose Mendlow

All Rights Reserved

Analysis and Validation of Three-Dimensional Models for Corneal Topography from  
Optical Coherence Tomography Point Cloud Data

by  
Micaela Rose Mendlow

A dissertation submitted to the Graduate Faculty of  
North Carolina State University  
in partial fulfillment of the  
requirements for the Degree of  
Doctor of Philosophy

Applied Mathematics

Raleigh, North Carolina

2020

APPROVED BY:

---

Ralph Smith

---

Hien Tran

---

Alen Alexandarian

---

Eric Buckland  
External Member

---

Mansoor Haider  
Chair of Advisory Committee

## BIOGRAPHY

Micaela Mendlow grew up in Brooklyn, New York. She has always loved math and science, and has explored every letter of the STEM acronym. In addition to academic research in organic chemistry, neurobiology, quantum physics, computer science, and applied mathematics, her career has also included a range of positions in both software development and STEM education.

Micaela attended Amherst College in Massachusetts for her undergraduate education, from which she graduated *magna cum laude* with a double major in Physics and Music. Nearly a decade later—after several career changes and a semester in the Smith College math post-baccalaureate program—Micaela enrolled in the doctoral program in applied mathematics at North Carolina State University, earning an M.S. in Applied Mathematics with a Computational Mathematics concentration along the way. Her outstanding academic performance has earned her numerous STEM fellowships as well as membership in two invitation-only scholastic honors societies: Sigma Xi and Phi Kappa Phi.

While in graduate school, Micaela was actively involved in serving her community, both as a member of the NC State University Student Conduct Board and as a volunteer counsellor at a local crisis center for survivors of domestic violence and sexual assault. During this time she also discovered passions for rock climbing and amateur speleology. Micaela's other hobbies include hiking, music composition, and music performance (she is skilled in both voice and piano, and has made several valiant attempts to learn classical guitar).

Micaela hails from a large extended family of intellectual overachievers and accomplished academics. Despite being a middle child, she will be the last of the three siblings in her immediate family to obtain a doctorate. Apropos of the fact that she will be completing this degree in the midst of a global pandemic, she hopes to find a way to apply her quantitative acumen to the field of public health.

## ACKNOWLEDGEMENTS

This thesis would never have been completed without the guidance of my advisor, Dr. Mansoor Haider, whose support and encouragement have upon numerous occasions rescued me from my own ambivalence about my own work. I am especially grateful to Dr. Haider for helping me stay on task and for always taking pains to ensure that my academic accomplishments did not come at the cost of my physical or mental wellbeing.

I would also like to express my deepest appreciation for the mentorship of Drs. Eric Buckland and Ralph Smith, as well as the input and patience of the rest of my committee—including Dr. H. Thomas Banks, who sadly passed away before this thesis was finalized. Further acknowledgements are owed to Ashavini Pavaskar and Dorothy Branco for their collaborative work on this project; my family and friends for all their emotional support; my very best friend (and husband) Dr. Jan Cannizzo for... well, everything; and my rescue dog Laika for reminding me to take breaks for the two most important things in life: walks and dinner.

The research presented in this thesis was funded in part by Leica Microsystems (formerly Bioptigen), the Amherst College Alumni Fellowship, and the U.S. Department of Education for Graduate Assistance in Areas of National Need (GAANN) fellowship.

# TABLE OF CONTENTS

<b>LIST OF TABLES . . . . .</b>	<b>vii</b>
<b>LIST OF FIGURES . . . . .</b>	<b>x</b>
<b>Chapter 1 Introduction . . . . .</b>	<b>1</b>
<b>Chapter 2 Data Collection &amp; Preprocessing . . . . .</b>	<b>5</b>
2.1 Terminology . . . . .	6
2.2 OCT Data Collection . . . . .	13
2.2.1 Image Acquisition . . . . .	13
2.2.2 Segmentation & Outlier Removal . . . . .	15
2.2.3 Conversion to 3D . . . . .	18
2.2.4 Scanner Calibration . . . . .	21
2.3 Imaging Phantoms . . . . .	22
2.3.1 Aspheric Lens . . . . .	23
2.3.2 Toric Lens . . . . .	24
2.3.3 Refractive Index . . . . .	26
2.4 Synthetic Data & Quantization Error . . . . .	27
2.4.1 Simulation of Surface Data . . . . .	28
2.4.2 Distribution of Quantization Error . . . . .	28
<b>Chapter 3 Single-Surface Lens Model . . . . .</b>	<b>32</b>
3.1 Zernike Polynomial Interpolation . . . . .	32
3.1.1 Background . . . . .	33
3.1.2 Zernike Expansion . . . . .	35
3.1.3 General Lens Model . . . . .	36
3.2 Synthetic Data for Single-Surface Model . . . . .	37
3.3 Coefficient Estimation & Surface Reconstruction . . . . .	39
3.4 Curvature Mapping . . . . .	42
3.5 Zernike Model Validation . . . . .	45
3.5.1 Model Order Selection . . . . .	47
3.5.2 Discrete Fit versus Numerical Integration . . . . .	48
3.5.3 Impact of Quantization Error . . . . .	52
3.5.4 Curvature . . . . .	55
3.6 Summary . . . . .	67
<b>Chapter 4 Optical Distortion Correction for Two-Surface Lens Model . . . . .</b>	<b>71</b>
4.1 Geometrical Optics . . . . .	71
4.1.1 Background . . . . .	71
4.1.2 Refraction at the Front Lens Surface . . . . .	73

4.1.3	Proof of General Boundary Conditions . . . . .	75
4.1.4	Path Length . . . . .	77
4.2	Refraction Correction . . . . .	79
4.2.1	Dewarping in 2D . . . . .	79
4.2.2	Dewarping in 3D . . . . .	83
4.3	Synthetic Data for Two-Surface Model . . . . .	87
4.4	Validation of Two-Surface Model . . . . .	90
4.4.1	Dewarping Step . . . . .	91
4.4.2	Front Surface Partial Derivatives . . . . .	95
4.4.3	Full Implementation . . . . .	98
4.5	Summary . . . . .	107
<b>Chapter 5</b>	<b>Application to Imaging Data . . . . .</b>	<b>110</b>
5.1	Full Lens Model . . . . .	110
5.1.1	Realignment . . . . .	110
5.1.2	Model Overview . . . . .	114
5.1.3	Quantities of Interest . . . . .	117
5.2	Results for OCT Data . . . . .	118
5.2.1	Anterior Surface Fit . . . . .	119
5.2.2	Anterior Surface Curvature . . . . .	122
5.2.3	Posterior Surface Fit After Dewarping . . . . .	125
5.2.4	Posterior Surface Curvature After Dewarping . . . . .	129
5.3	Summary . . . . .	133
<b>Chapter 6</b>	<b>Uncertainty Analysis . . . . .</b>	<b>137</b>
6.1	Mathematical Models . . . . .	138
6.1.1	Anterior Lens Model . . . . .	139
6.1.2	Posterior Lens Model . . . . .	140
6.1.3	Normalized Model . . . . .	142
6.2	Statistical Models . . . . .	144
6.3	Model Calibration . . . . .	146
6.3.1	Reduced Order Model . . . . .	146
6.3.2	Model Calibration . . . . .	155
6.4	Uncertainty Propagation . . . . .	172
6.5	Global Sensitivity Analysis . . . . .	175
<b>Chapter 7</b>	<b>Discussion . . . . .</b>	<b>189</b>
<b>References</b>	<b>. . . . .</b>	<b>198</b>
<b>Appendices</b>	<b>. . . . .</b>	<b>207</b>
Appendix A	Table of Zernike Polynomials . . . . .	208

Appendix B	Error Distribution for OCT Data & Synthetic Data for UQ . . .	214
Appendix C	Convergence of Sobol' Indices . . . . .	220

## LIST OF TABLES

Table 2.1	Technical specifications for the Envisu R4410 SDOCT Contact Lens Metrology System [50]. . . . .	13
Table 2.2	Design specifications and tolerances for the Edmund Optics TECHSPEC® Precision Aspheric Lens from [65]. . . . .	24
Table 2.3	Target specifications for the Universal Optics toric meniscus lens. (Tolerances are based on third party measurements of the specific lens artifact.) . . . . .	24
Table 2.4	Group refractive indices for saline solution and lens substrates at the sodium d-line ( $\lambda_{Na} = 589.3$ nm) and near the central wavelength of the Leica Microsystems OCT system ( $\lambda_{OCT} = 880$ nm). . . . .	26
Table 3.1	Table of normalized Zernike polynomials with their corresponding aberration names ordered according to Noll’s single indexing system $j$ [6, 64].	35
Table 3.2	MAE (in mm) of surface reconstruction when coefficients are obtained via numerical integration ( $\bar{e}^{(i)}$ ) versus OLS fit ( $\bar{e}$ ). . . . .	49
Table 3.3	MAE (in mm) of surface reconstruction without noise ( $\bar{e}$ ) and with quantization error ( $\bar{e}^*$ ). . . . .	53
Table 3.4	Mean signed quantization error ( $\bar{e}^*$ ) and smallest MAE in surface fit to quantized data ( $\bar{e}^*$ ), in millimeters. . . . .	53
Table 3.5	Actual finite difference step sizes ( $h = Ah'$ ) for curvature, in millimeters.	55
Table 3.6	MAE (in $\text{mm}^{-1}$ ) in meridional curvature without noise ( $\bar{e}_k$ ) and with quantization error ( $\bar{e}_k^*$ ). . . . .	57
Table 3.7	MAE (in mm) in the meridional radius of curvature without noise ( $\bar{e}_{roc}$ ) and with quantization error ( $\bar{e}_{roc}^*$ ). . . . .	61
Table 3.8	Principal radius of curvature estimates and absolute error (in mm) without noise ( $\hat{R}$ ) and with quantization error ( $\hat{R}^*$ ). . . . .	66
Table 3.9	Results (in mm) for the best Zernike orders for Surfaces 1, 3, and 4 using quantized data. (Bolded entries indicate optimal results.) . . . .	68
Table 4.1	MAE fit to the back surfaces (in mm) with no refraction effects versus MAE when dewarping is done using exact values for the front surface gradient. . . . .	94
Table 4.2	MAE in curvature (in $\text{mm}^{-1}$ ) for the back surfaces without refraction effects and using exact gradient values for dewarping. . . . .	94
Table 4.3	Principal radius of curvature estimates (in mm) for the back surface of the toric lens, with and without refraction effects. . . . .	97
Table 4.4	Best case error results for front surface derivatives and back surface radii of curvature after dewarping non-quantized toric lens data using $z^a \approx f_{Na}$ . . . . .	101

Table 4.5	Results (in mm) for the posterior toric lens for each back surface model order $N_p$ after dewarping using front surface model order $N_a$ (versus without refraction effects). . . . .	108
Table 5.1	Analysis zones from [5] for assessing accuracy of curvature estimates. .	118
Table 5.2	Error in elevation and curvature estimates from real lens data. . . . .	134
Table 6.1	Order of the Zernike expansion used to fit each lens surface ( $N$ ), as well as the total number of terms in the complete expansion ( $m$ ). . . . .	139
Table 6.2	The $\ell^2$ condition number of the Fisher information matrix $X_n^T X_n$ . . .	147
Table 6.3	OLS error variance estimates ( $\hat{\sigma}^2$ ) in square millimeters for all lens surfaces, using the full model (all Zernike coefficients) versus the reduced order model. . . . .	153
Table 6.4	Zernike polynomials included in reduced order models for each lens surface. . . . .	154
Table 6.5	Zernike coefficient estimates (in mm) and 95% confidence intervals using ordinary least squares (OLS) for full anterior aspheric lens model with all coefficients and reduced order lens model. . . . .	160
Table 6.6	Coefficient estimates and 95% confidence intervals for full and reduced posterior aspheric lens models. . . . .	160
Table 6.7	Coefficient estimates and 95% confidence intervals for full and reduced anterior toric lens models. . . . .	161
Table 6.8	Coefficient estimates and 95% confidence intervals for full and reduced posterior toric lens models. . . . .	161
Table 6.9	Error variance ( $\hat{\sigma}^2$ ) in square millimeters from OLS and DRAM. . . .	169
Table 6.10	Comparison of the mean and standard error (in mm) for Zernike coefficients of the anterior aspheric lens using OLS and DRAM. . . . .	170
Table 6.11	Comparison of the Zernike coefficients (in mm) of the anterior toric lens using OLS and DRAM. . . . .	170
Table 6.12	Comparison of the Zernike coefficients (in mm) of the posterior aspheric lens using OLS and DRAM. . . . .	171
Table 6.13	Comparison of the Zernike coefficients (in mm) of the posterior toric lens using OLS and DRAM. . . . .	171
Table 6.14	First order Sobol' indices ( $S_i$ ), total Sobol' indices ( $S_{T_i}$ ), and Morris measures ( $\mu_i^*$ , $\sigma_i$ ) for the front of the aspheric lens. . . . .	179
Table 6.15	Sobol' indices and Morris measures for the front of the toric lens. . . .	179
Table 6.16	Sobol' indices and Morris measures for the back surface of the toric lens.	180
Table 6.17	Sobol' indices and Morris measures of the front surface Zernike coefficients for the posterior quantities of interest of the toric lens. . . . .	181
Table 7.1	Analysis zones used in Table 7.2. . . . .	189

Table 7.2	RMS elevation error and mean curvature error ( $\pm$ one standard deviation), and compared to quantized synthetic data using same model orders. . . . .	190
Table 7.3	Principal radii of curvature and central thickness ( $t_C$ ) in millimeters, from synthetic data with quantization error (QE) and from real data. . . . .	193
Table A.1	The first 66 Zernike basis functions (ordered according to Noll's index $j$ ), corresponding to all polynomials up to and including radial order $N = 10$ . The polynomials have been normalized to preserve the orthogonality relation in (3.3). . . . .	208
Table B.1	Model error variance $\sigma^2$ computed from real data, in square millimeters. . . . .	214
Table B.2	Zernike order $N$ used to fit each lens surface. . . . .	218

# LIST OF FIGURES

Figure 2.1	The solid curve represents a cross section of the surface $z(\rho, \theta)$ confined to the meridional plane $\theta = \theta_k$ . The radius of curvature at $(\rho, z(\rho, \theta_k))$ is the radius of the osculating circle at that point, indicated by the dashed curve. . . . .	7
Figure 2.2	Meridional curvature maps in keratometric diopters (D) for the (a) front surface of the aspheric lens, (b) front surface of the toric lens, and (c) back surface of the toric lens. The dashed lines in (c) indicate the principal meridians. . . . .	10
Figure 2.3	Envisu metrology assembly with handheld R4410 OCT probe [51]. . .	12
Figure 2.4	Sample holder (left) and sample positioning stage (right) [51]. . . . .	12
Figure 2.5	A B-scan of the toric lens obtained using the Envisu R4410. . . . .	14
Figure 2.6	Illustration of the radial scan pattern (a) as multiple B-scans aligned in $\mathbb{R}^3$ at the CT axis, and (b) in the $xy$ -plane perpendicular to the CT axis (the highlighted points represent a single frame of data). . . . .	15
Figure 2.7	Good segmentation results for a frame of toric lens data. . . . .	17
Figure 2.8	Two frames of toric lens data with poor segmentation results. . . . .	17
Figure 2.9	Point cloud data from Figure 2.8a (left) and Figure 2.8b (right) superimposed over the original B-scans. . . . .	18
Figure 2.10	Illustration of $\mathfrak{X} = (\rho, \theta)$ on a sample grid with $\rho = 2\Delta_\rho$ and $\theta = 6\Delta_\theta$ . . . . .	20
Figure 2.11	Rendering of aspheric lens from the design equations. . . . .	23
Figure 2.12	Rendering of toric lens from the design equations. . . . .	25
Figure 2.13	Real point cloud data from OCT and synthetic point cloud data generated from the design equations for the aspheric lens. . . . .	29
Figure 2.14	Real point cloud data from OCT and synthetic point cloud data generated from the design equations for the toric lens. . . . .	29
Figure 2.15	Quantization error in the first frame of synthetic data for the (a) front of the aspheric lens, (b) front of the toric lens, (c) back of the aspheric lens after warping, and (d) back of the toric lens after warping. . . . .	30
Figure 2.16	Q-Q plots of the quantization error in the synthetic data versus the uniform distribution, for the (a) front of the aspheric lens, (b) front of the toric lens, (c) back of the aspheric lens after warping, and (d) back of the toric lens after warping. . . . .	31
Figure 3.1	Visual representation of Zernike polynomials from (3.1). . . . .	34
Figure 3.2	Surface reconstructions using an $N^{\text{th}}$ order Zernike fit to synthetic data without noise and with quantization error (QE) for (a) Surface 1, (b) Surface 2, (c) Surface 3, and (d) Surface 4. . . . .	40
Figure 3.3	Surface error for Zernike fits in Figure 3.2 for (a) Surface 1, (b) Surface 2, (c) Surface 3, and (d) Surface 4. . . . .	41

Figure 3.4	Meridional curvature maps for (a) Surface 1, (b) Surface 2, (c) Surface 3, and (d) Surface 4. . . . .	43
Figure 3.5	Error for curvature maps in Figure 3.4 for (a) Surface 1, (b) Surface 2, (c) Surface 3, and (d) Surface 4. . . . .	44
Figure 3.6	MAE in surface fit for (a) Surface 1, (b) Surface 2, (c) Surface 3, and (d) Surface 4, when coefficients are obtained using numerical integration versus OLS. . . . .	50
Figure 3.7	Local surface error from integration (left) and OLS (right) for (a) Surface 1, (b) Surface 2, and (c) Surface 3. . . . .	51
Figure 3.8	Local surface error for principal meridians of Surface 4 from integration (left) and OLS (right). . . . .	52
Figure 3.9	Local surface error for Zernike fit to quantized synthetic data for (a) Surface 1, (b) Surface 3, (c) Surface 4 at $0^\circ$ , and (d) Surface 4 at $90^\circ$ . . . . .	55
Figure 3.10	MAE in meridional curvature for (a) Surface 1, (b) Surface 2, (c) Surface 3, and (d) Surface 4. . . . .	56
Figure 3.11	Local error in surface fit (left) and curvature (right) when quantization error is present for (a) Surface 1 and (b) Surface 3. . . . .	58
Figure 3.12	Local error in surface fit (left) and curvature (right) for the principal meridians of Surface 4 when quantization error is present. . . . .	59
Figure 3.13	Local curvature error when quantization error is present in Surface 4 principal meridians for Zernike fits of order (a) $N = 10$ and (b) $N = 12$ . . . . .	59
Figure 3.14	Local error in surface fit (left) and curvature (right) without noise for (a) Surface 1, (b) Surface 3, (c) Surface 4 meridian at $0^\circ$ , and (d) Surface 4 meridian at $90^\circ$ . . . . .	60
Figure 3.15	MAE in surface fit (left) and radius of curvature (right) for (a) Surface 1, (b) Surface 3, and (c) Surface 4. . . . .	62
Figure 3.16	Radius of curvature for (a) Surface 1, (b) Surface 3, (c) Surface 4 at $0^\circ$ , and (d) Surface 4 at $90^\circ$ . . . . .	64
Figure 3.17	Absolute error in principal radius of curvature for (a) Surface 1, (b) Surface 3, (c) Surface 4 at $0^\circ$ ( $R_1$ ), and (d) Surface 4 at $90^\circ$ ( $R_2$ ). . . . .	65
Figure 3.18	Absolute errors in principal radii of curvature for Surface 4 (a) without noise and (b) with quantization error. . . . .	65
Figure 3.19	Absolute error in principal radius (or radii) of curvature from quantized synthetic data for (a) Surface 1, (b) Surface 3, and (c) Surface 4 relative to established ISO guidelines for ophthalmometer accuracy [35]. . . . .	69
Figure 4.1	A light ray $n_s \mathbf{u}_{in}$ incident to the interface $T$ of the saline and the front of the lens. The refracted ray $n_\ell \mathbf{u}_{ref}$ lies in the plane formed by $n_s \mathbf{u}_{in}$ and the surface normal vector $\mathbf{n}$ . The fact that $n_s < n_\ell$ means that $\theta_{in} < \theta_{ref}$ . . . . .	73
Figure 4.2	The 2D transition region $\Sigma$ lies in the plane formed by the incident ray $n_s \mathbf{u}_{in}$ and the normal vector $\mathbf{n}$ at the point of incidence. . . . .	74

Figure 4.3	The boundary of $\Sigma$ (shown in Figure 4.2) is the piecewise-smooth curve $\Gamma$ that runs counterclockwise around $ABB'A'$ . The unit vectors $\mathbf{t}_{in}$ and $\mathbf{t}_{ref}$ are respectively normal to sides $AB$ and $B'A'$ , while $\mathbf{b}$ is the out-of-plane unit vector perpendicular $\Sigma$ . . . . .	75
Figure 4.4	The OPL is the vertical distance between corresponding A-scans. . .	77
Figure 4.5	Illustration of optical path length (OPL) versus geometric path length ( $L$ ) for a given B-scan. By assumption, the front surface (green) and <i>apparent</i> back surface (solid blue) are in the same meridional plane as the B-scan, which is defined by the $z$ -axis and the incident light ray $\mathbf{u}_{in}$ . However, the normal vector $\mathbf{n}$ may be out-of-plane. The refracted ray $L\mathbf{u}_{ref}$ is contained in the plane of incidence formed by $\mathbf{u}_{in}$ and $\mathbf{n}$ .*	78
Figure 4.6	Geometry of the angle of incidence $\theta_{in}$ for a 2D surface. . . . .	80
Figure 4.7	Decomposition of refracted light ray $L\mathbf{u}_{ref}$ into $x$ - and $y$ -components.	81
Figure 4.8	Projection of the refracted light ray $\mathbf{u}_{ref}$ onto the $z$ -axis in $\mathbb{R}^3$ . In this case the normal vector $\mathbf{n}$ is <i>not</i> assumed to lie in the meridional plane. Therefore, $\mathbf{u}_{ref}$ lies in the plane of incidence (determined by $\mathbf{n}$ and $\mathbf{u}_{in}$ ), so both $\theta_{in}$ and $\theta_{ref}$ must also be measured in the plane of incidence. . . . .	85
Figure 4.9	Real point cloud data from OCT of the aspheric lens versus synthetic point cloud data generated from the design equations (4.19). . . . .	89
Figure 4.10	Real point cloud data from OCT of the toric lens versus synthetic point cloud data generated from the design equations (4.20). . . . .	89
Figure 4.11	Average error in the Zernike fit for the back of the aspheric lens (a) without warping and (b) after dewarping using front surface design equation. . . . .	92
Figure 4.12	Average error in the Zernike fit for the back of the toric lens (a) without warping and (b) after dewarping using front surface design equation.	92
Figure 4.13	Average error in curvature for the back of the aspheric lens (a) without warping and (b) after dewarping using front surface design equation.	93
Figure 4.14	Average error in curvature for the back of the toric lens (a) without warping and (b) after dewarping using front surface design equation.	93
Figure 4.15	Absolute error in the estimates of $R_{p_1}$ (top) and $R_{p_2}$ (bottom) for the toric lens (a) without warping and (b) after dewarping using front surface design equation. . . . .	96
Figure 4.16	Absolute error in posterior principal curvatures for both lenses from quantized data after dewarping using front surface design equation. .	96
Figure 4.17	MAE in front surface partial derivatives for the (a) aspheric lens and (b) toric lens. (Due to symmetry, the average error is the same for both partial derivatives.) . . . . .	98

Figure 4.18	Average error in posterior (a) surface fit and (b) curvature, and absolute error in (c) $\hat{R}_{p_1}$ and (d) $\hat{R}_{p_2}$ from non-quantized toric lens data after dewarping using front surface Zernike fit. Results with no warping/dewarping from Chapter 3 are included for comparison. . . . .	100
Figure 4.19	Average error in posterior (a) surface fit and (b) curvature from non-quantized aspheric lens data after dewarping using front surface Zernike fit. . . . .	102
Figure 4.20	Absolute error in $\hat{K}_p$ for the non-quantized aspheric lens data after dewarping using front surface Zernike fit. . . . .	102
Figure 4.21	Average surface error from quantized synthetic data for the back of the (a) aspheric lens and (b) toric lens after dewarping. Results are depicted using both the front surface design equations and Zernike fits to quantized data. . . . .	104
Figure 4.22	Average curvature error from quantized synthetic data for the back of the (a) aspheric lens and (b) toric lens after dewarping. . . . .	105
Figure 4.23	Absolute error after dewarping in (a) $\hat{K}_p^*$ for aspheric lens and (b) $\hat{K}_{p_1}^*$ and (c) $\hat{K}_{p_2}^*$ for the toric lens. . . . .	106
Figure 4.24	Absolute error in (a) $\hat{R}_{p_1}^*$ and (b) $\hat{R}_{p_2}^*$ for the toric lens after dewarping using Zernike fit to quantized front surface data. . . . .	109
Figure 5.1	(a) Slight misalignment of radial scanning pattern relative to lens vertex. (b) Radial grid re-centered at the lens vertex for calculating final results. . . . .	111
Figure 5.2	Meridians at (a) $0^\circ$ and (b) $90^\circ$ for the aspheric lens without realignment. . . . .	112
Figure 5.3	Meridians at (a) $0^\circ$ and (b) $90^\circ$ for the aspheric lens after realignment. . . . .	112
Figure 5.4	Meridians at (a) $0^\circ$ and (b) $90^\circ$ for the toric lens without realignment. . . . .	113
Figure 5.5	Meridians at (a) $0^\circ$ and (b) $90^\circ$ for the toric lens after realignment. . . . .	113
Figure 5.6	RMS surface error for the anterior aspheric lens from (a) synthetic data and (b) real lens data. . . . .	120
Figure 5.7	RMS surface error for the anterior toric lens from (a) synthetic data and (b) real lens data. . . . .	120
Figure 5.8	Mean surface error and $2\sigma$ interval for the anterior aspheric lens from (a) synthetic data and (b) real lens data. . . . .	121
Figure 5.9	Mean surface error and $2\sigma$ interval for the anterior toric lens from (a) synthetic data and (b) real lens data. . . . .	121
Figure 5.10	$\hat{K}_a$ for the aspheric lens from (a) synthetic data and (b) real data. . . . .	123
Figure 5.11	$\hat{K}_a$ for the toric lens from (a) synthetic data and (b) real data. . . . .	123
Figure 5.12	Mean curvature error and $2\sigma$ interval for the anterior aspheric lens using (a) synthetic data and (b) real lens data. . . . .	124

Figure 5.13	Mean curvature error and $2\sigma$ interval for the anterior toric lens using (a) quantized synthetic data, (b) non-quantized synthetic data, and (c) real lens data. (Note different $y$ -axis limits for synthetic and real data.) . . . . .	124
Figure 5.14	RMS surface error for the posterior aspheric lens after dewarping with anterior Zernike models $z^a$ , using (a) quantized synthetic data and (b) real lens data. . . . .	126
Figure 5.15	RMS surface error for the posterior toric lens after dewarping using (a) synthetic data and (b) real lens data. . . . .	126
Figure 5.16	Mean surface error and $2\sigma$ interval for the posterior aspheric lens after dewarping a) quantized synthetic data ( $z^a \approx f_6$ ), and b) real lens data ( $z^a \approx f_4$ ). . . . .	127
Figure 5.17	Mean surface error and $2\sigma$ interval for the posterior toric lens after dewarping a) quantized synthetic data ( $z^a \approx f_{10}$ ), b) real lens data after reorientating the data to align the principal axes with the design equation ( $z^a \approx f_8$ ), and c) real lens data without principal axis reorientation ( $z^a \approx f_8$ ). . . . .	128
Figure 5.18	Back principal curvature for aspheric lens after dewarping, using (a) quantized synthetic data and (b) real lens data. . . . .	130
Figure 5.19	Back principal curvatures ( $K_{p1} = 40.18$ D, $K_{p2} = 36.67$ D) for the toric lens after dewarping, using (a) synthetic data and (b) real lens data. . . . .	130
Figure 5.20	Mean curvature error and $2\sigma$ interval for the posterior aspheric lens after dewarping a) synthetic data ( $z^a \approx f_6$ ), and b) real lens data ( $z^a \approx f_4$ ). . . . .	131
Figure 5.21	Mean curvature error and $2\sigma$ interval for the posterior toric lens from a) quantized synthetic data dewarped using $z^a \approx f_{10}$ , b) quantized synthetic data without warping/dewarping, and real lens data dewarped using $z^a \approx f_8$ c) with axis reorientation and d) without axis reorientation. . . . .	132
Figure 5.22	Meridional curvature maps based on the design equations for the (a) anterior aspheric lens, (b) anterior toric lens, and (c) posterior toric lens. . . . .	135
Figure 5.23	Meridional curvature maps from OCT data for the (a) anterior aspheric lens, (b) anterior toric lens, and (c) posterior toric lens. . . . .	135
Figure 5.24	Local curvature error for the (a) anterior aspheric lens, (b) anterior toric lens, (c) posterior aspheric lens, and (d) posterior toric lens. . . . .	136
Figure 6.1	Renderings of the aspheric lens (left) and the toric lens (right) from the design equations in Section 2.3. . . . .	138
Figure 6.2	Zernike coefficients of the front surface of the aspheric lens, using numerical integration and linear least squares. . . . .	148

Figure 6.3	Singular values of $X_n^T X_n$ (left) and components of the right singular vectors corresponding to the singular values above the dashed line (right) for the anterior surface of the aspheric lens. . . . .	148
Figure 6.4	Zernike coefficients of the front surface of the toric lens. . . . .	149
Figure 6.5	Singular values (left) and right singular vectors (right) for the anterior surface of the toric lens. . . . .	149
Figure 6.6	Zernike coefficients of the back surface of the aspheric lens. . . . .	150
Figure 6.7	Singular values (left) and right singular vectors (right) for the posterior surface of the aspheric lens. . . . .	150
Figure 6.8	Zernike coefficients of the posterior surface of the toric lens. . . . .	151
Figure 6.9	Singular values (left) and right singular vectors (right) for the posterior surface of the toric lens. . . . .	151
Figure 6.10	Error variance ( $\hat{\sigma}^2$ ) according to the number of Zernike polynomials included in the reduced order model (ROM) for the posterior toric lens.	152
Figure 6.11	Significant Zernike polynomials for (a) the aspheric lens, (b) the front of the toric lens, and (c) the back of the toric lens. . . . .	154
Figure 6.12	Difference between the full Zernike fit and the reduced order model for (a) the anterior aspheric lens, (b) the anterior toric lens, (c) the posterior aspheric lens, and (d) the posterior toric lens. . . . .	155
Figure 6.13	Joint sample points for the significant Zernike coefficients of the front surface of the aspheric lens. . . . .	163
Figure 6.14	Sample paths for the front surface of the aspheric lens. . . . .	163
Figure 6.15	Parameter densities for the front surface of the aspheric lens. . . . .	163
Figure 6.16	Joint sample points for the significant Zernike coefficients of the front surface of the toric lens. . . . .	164
Figure 6.17	Sample paths for the front surface of the toric lens. . . . .	165
Figure 6.18	Parameter densities for the front surface of the toric lens. . . . .	165
Figure 6.19	Sample path (left) and density (right) for $c_1$ for the back surface of the aspheric lens. . . . .	166
Figure 6.20	Joint sample points for the significant Zernike coefficients of the back surface of the toric lens. . . . .	167
Figure 6.21	Sample paths for the back surface of the toric lens. . . . .	168
Figure 6.22	Parameter densities for the back surface of the toric lens. . . . .	168
Figure 6.23	Prediction intervals for central elevation of the (a) anterior aspheric lens, (b) anterior toric lens, (c) posterior aspheric lens, and posterior toric lens (d) at $0^\circ$ , and (e) at $90^\circ$ . (Credible intervals are also depicted but are too narrow to be visible.) . . . . .	173
Figure 6.24	Prediction and credible intervals for meridional curvature of the (a) anterior aspheric lens, (b) anterior toric lens, and posterior toric lens (c) at $0^\circ$ , and (d) at $90^\circ$ . . . . .	174

Figure 6.25	Centered parameter study for the anterior principal curvature ( $K_a$ ) of the aspheric lens. . . . .	183
Figure 6.26	Sobol' indices ( $S_i$ , $S_{T_i}$ ) and Morris measures ( $\mu_i$ , $\sigma_i$ ) for the anterior principal curvature of the aspheric lens. . . . .	183
Figure 6.27	Centered parameter study for the anterior principal curvature of the toric lens. . . . .	184
Figure 6.28	Sobol' indices and Morris measures for the anterior principal curvature of the toric lens. . . . .	184
Figure 6.29	Centered parameter study of the back surface Zernike coefficients for the posterior maximum curvature ( $K_{p_1}$ ) of the toric lens. . . . .	185
Figure 6.30	Sobol' indices and Morris measures of the back surface Zernike coefficients for the posterior maximum curvature of the toric lens. . . . .	185
Figure 6.31	Centered parameter study of the back surface Zernike coefficients for the difference in the posterior principal curvatures ( $K_{p_1} - K_{p_2}$ ) of the toric lens. . . . .	186
Figure 6.32	Sobol' indices and Morris measures of the back surface Zernike coefficients for the difference in the posterior principal curvatures of the toric lens. . . . .	186
Figure 6.33	Centered parameter study of the front surface Zernike coefficients for the posterior maximum curvature of the toric lens. . . . .	187
Figure 6.34	Sobol' indices and Morris measures of the front surface Zernike coefficients for the posterior maximum curvature of the toric lens. . . . .	187
Figure 6.35	Centered parameter study of the front surface Zernike coefficients for the difference in the posterior principal curvatures of the toric lens. . . . .	188
Figure 6.36	Sobol' indices and Morris measures of the front surface Zernike coefficients for the difference in the posterior principal curvatures of the toric lens. . . . .	188
Figure B.1	Residuals for the 1 <sup>st</sup> (left) and 60 <sup>th</sup> (right) frames of real data for the (a) front of the asphere, (b) front of the toric lens, (c) back of the asphere, and (d) back of the toric lens. . . . .	215
Figure B.2	Q-Q plots of real data residuals vs. $\mathcal{N}(0, \sigma^2)$ for the (a) front of the asphere, (b) front of the toric lens, (c) back of the asphere, and (d) back of the toric lens. . . . .	216
Figure B.3	Q-Q plots of synthetic data residuals vs. $\mathcal{N}(0, \sigma^2)$ for the (a) front of the asphere, (b) front of the toric lens, (c) back of the asphere, and (d) back of the toric lens. . . . .	216
Figure B.4	Residuals for the 1 <sup>st</sup> frame of synthetic data for the (a) front of the asphere, (b) front of the toric lens, (c) back of the asphere, and (d) back of the toric lens. . . . .	217
Figure B.5	Real axial elevation data and synthetic data with normally distributed noise for the front surface of the (a) aspheric lens and (b) toric lens. . . . .	219

Figure B.6	Real geometric path length (GPL) data and synthetic GPL data with normally distributed noise for the back surface of the (a) aspheric lens and (b) toric lens. . . . .	219
Figure C.1	Convergence of first order Sobol' indices ( $S_i$ ) for (a) the principal curvature of the anterior aspheric lens, (b) the principal curvature of the anterior toric lens, (c) the maximum principal curvature of the posterior toric lens with respect to the back surface coefficients, (d) the difference in principal curvatures of the posterior toric lens with respect to the back surface coefficients, (e) the maximum principal curvature of the posterior toric lens with respect to the front surface coefficients (after dewarping), and (f) the difference in principal curvatures of the posterior toric lens with respect to the front surface coefficients (after dewarping). . . . .	221
Figure C.2	Convergence of total Sobol' indices ( $S_{T_i}$ ) for (a) the principal curvature of the anterior aspheric lens, (b) the principal curvature of the anterior toric lens, (c) the maximum principal curvature of the posterior toric lens with respect to the back surface coefficients, (d) the difference in principal curvatures of the posterior toric lens with respect to the back surface coefficients, (e) the maximum principal curvature of the posterior toric lens with respect to the front surface coefficients (after dewarping), and (f) the difference in principal curvatures of the posterior toric lens with respect to the front surface coefficients (after dewarping). . . . .	222

# Chapter 1

## Introduction

Optical coherence tomography (OCT) is a non-invasive medical imaging modality that uses low-coherence interferometry to produce detailed images of biological tissues [31]. Spectral domain OCT (SDOCT) works by scanning a broadband beam of near-infrared light from a superluminescent diode through an interferometer consisting of a sample arm, which contains the object being imaged, and a reference arm. A spectrometer registers the spectral interference pattern produced when the reflected light from the two arms is recombined. This interference data, which is a function of wavelength, is then Fourier transformed to obtain a reflectivity profile of the entire depth scan. In this way, SDOCT permits simultaneous imaging of multiple tissue layers [17, 69].

Due to its relative ease of operation and micrometer-scale resolution, OCT has enjoyed widespread use in the field of ophthalmology [47, 48, 57]. While primarily used to diagnose and monitor ophthalmic diseases through qualitative analysis of ocular structures [70, 110], OCT imaging is also being investigated as a potential means for quantitative measurement of various biometrics including principal radius of curvature and local elevation, curvature, and thickness (*pachymetry*) maps of the cornea [55, 110]. As the cornea is responsible for most of the eye's refractive power, accurate corneal topography is essential to the detection and management of many eye conditions [23, 44, 56, 62, 69]. Volumetric OCT imaging of the cornea has been proposed for measuring refractive power before and after surgical procedures [48, 54, 55]. Other possible applications for this technology include research into the relationship between eye disorders and eye shape [57], prescriptive lens fitting [44, 56], and contact lens metrology [15].

Placido disc-based topographers—long considered the standard in corneal topography—

measure curvature by detecting the deviations in concentric rings of light projected onto the cornea [4, 23, 44]. These devices are only able to measure the anterior surface of the cornea and rely on assumptions about the internal features of the eye to estimate refractive power, assumptions that may be inaccurate for people who have certain eye diseases or who have had refractive surgery [48, 56, 67]. Corneal topography systems using slit-scanning or Scheimpflug photography are able to measure interior surfaces of the eye; however, in principle OCT has the potential for superior image resolution and depth [55, 69, 69, 110]. In fact, OCT has the potential to allow quantitative 3D modeling of the entire human eye, including the crystalline lens and retina [56, 69]. Recent studies have assessed the performance of corneal topography from OCT relative to the results of other widely used topography and keratometry systems. In particular, OCT has been compared to both Placido disc systems and Scheimpflug photography for mapping the topography of imaging phantoms and *in vivo* human corneas [48, 54, 55, 56, 69, 70, 99, 110]. OCT topography has also been validated against a dedicated mouse keratometer for use on *in vivo* mouse corneas and imaging phantoms [52]. Other studies have also investigated corneal biometry from OCT using imaging phantoms as well as human, porcine, and guinea pig subjects [18, 66, 67, 71, 72, 100].

One drawback to measuring surface height rather than measuring curvature directly is that differentiation amplifies errors in the surface fit [44]. However, the standard curvature maps in ophthalmology involve 2D curvatures [4, 23]. The use of elevation data allows us to compute the curvature along any direction of our choosing, which is especially important in cases of off-axis imaging or when the desired reference axis for the curvature map does not correspond to the one used for data collection [44, 60, 78, 85]. Another problem with using OCT for corneal topography is that the cornea by its very nature refracts light from the scanner, leading to unavoidable warping of the posterior surface data. Several algorithms for correcting this type of optical distortion in three dimensions have been proposed [52, 69, 110]. The 3D refraction correction algorithm presented in Chapter 4 is based on [110] and has been validated on imaging phantoms and various parts of the human eye [16, 17, 18, 29, 48, 54, 55, 56, 110].

In this thesis, we will investigate the mathematical implications of using segmentation data from volumetric OCT imaging to model both the anterior and posterior surfaces of two imaging phantoms with known design specifications<sup>i</sup>. However, whereas many of the

---

<sup>i</sup>See Section 2.3.

biometrics reported in the aforementioned studies have involved at least some general assumptions about the shape of the surface or surfaces being measured [48, 56, 67, 68, 69, 70], our methods are intended to be applicable to an optical body of arbitrary shape. For this purpose, 3D modeling of elevation data is performed using Zernike polynomials<sup>ii</sup>, which form an orthogonal basis on the unit disc and are widely used for modeling corneal elevation [34, 77, 84, 91]. In addition to their utility in wavefront aberrometry, Zernike polynomials have been used to fit OCT surface height data [52, 54, 55, 68, 70, 71, 72, 97, 99, 110], as well as to compute local curvature maps for human and mouse corneas [52, 55, 103]. Nevertheless, we are not aware of any rigorous efforts to validate the curvature maps generated from Zernike polynomial fitting of OCT elevation data. While some papers do consider different Zernike model orders for fitting phantom cornea data from other imaging modalities, we have not encountered any literature that examines the impact of model order selection on curvature mapping or within the context of a multi-surface model where refraction correction of the posterior surface depends on the anterior surface fit. There also appears to be minimal research addressing uncertainty propagation and sensitivity analysis associated with the Zernike elevation and curvature models.

This thesis is structured as follows: Chapter 2 presents the relevant scientific background and terminology, including the design specifications of the two imaging phantoms. In Chapter 3, we investigate and validate the use of finite Zernike polynomial expansions for 3D modeling of synthetic elevation data as well as curvature mapping. In Chapter 4, we describe a ray tracing algorithm for 3D refraction correction of the posterior lens surface, which we then validate using synthetic lens data. The implications for curvature mapping of refraction-corrected surfaces are also discussed. The methods discussed in Chapters 3–4 are then applied to real OCT data in Chapter 5. Finally, Chapter 6 investigates the quantification of uncertainty in both the anterior and posterior lens surface models. As we did not have direct access to the raw OCT data, issues pertaining to imaging and image processing—such as noise reduction, edge detection, parameter estimation involving OCT scan parameters, and quantification of error in point cloud data—will not be addressed. Image registration is discussed only insofar as it can be done using point cloud data.

The OCT data used in this thesis were obtained using an Envisu R4410 SDOCT Contact Lens Metrology System (Leica Microsystems, Inc., formerly Bioptigen, Inc.; Mor-

---

<sup>ii</sup>See Section 3.1.

risville, North Carolina), the specifications of which can be found in Section 2.2. Most of the analyses described in Chapters 3–6 were coded in MATLAB version R2019b (MathWorks; Natick, Massachusetts).

## Chapter 2

# Data Collection & Preprocessing

The analyses described in this thesis were conducted on two test phantoms: a plano-convex glass lens with an aspheric front surface (the “aspheric lens”), and a positive meniscus (convex-concave) acrylic lens with a spherical front surface and toric back surface (the “toric lens”). Although we eventually intend to apply these algorithms to human cornea data, there are a number of important reasons to first validate on such lenses. In particular, the front and back surfaces of both lenses have known design equations against which we can easily compare our results. Using lens data also allows us to assess algorithm performance without having to account for motion during data collection, as is likely to occur when live imaging a human eye [75].

Another benefit to using manufactured test surfaces is that the optical properties of most lenses are well-defined with respect to their geometrical structure. By contrast, the field of physiological optics has yet to reach a consensus regarding the optimal reference axis to use when evaluating anomalies in the human eye, and the impact of such anomalies on focal properties at the retina. The four refracting surfaces (the anterior and posterior of the cornea and the anterior and posterior of the crystalline lens) are generally neither coaxial nor rotationally symmetric [60, 62, 85, 101]. Even if we were to ignore minor asymmetries, the eye’s other key optical components—the pupil (the central aperture in the iris which dilates or contracts to control light exposure) and the foveola (the point on the retina where the resulting image is projected)—also tend to be displaced from any sort of geometrical axis and can vary significantly from person to person, thus introducing additional variables that can impact vision quality [60, 62, 101]. Not only does this lead to the characterization of numerous reference axes for the human eye, but the precise

definitions of these various axes in the literature are inconsistent and sometimes even contradictory [60, 85]. Despite widespread agreement on the benefits of a standardized axis, debate continues as to which of these axes is most appropriate for alignment during ophthalmological procedures [7, 60, 101]. As we will discuss in the next section, no such ambiguity exists for the lenses used in this thesis.

## 2.1 Terminology

While separate ANSI and ISO standards exist for contact lens metrology and corneal topography, and although contact lens metrology is also among Leica’s target applications for the OCT system, we will mainly focus on concepts that are essential for assessing the health of the cornea. Most of the following clinical terms are based on the definitions provided in ANSI Z80.23-2008 (corneal topography systems – standard terminology, requirements) [5], which is largely mirrored by ISO 19980:2012 (ophthalmic instruments – corneal topographers) [37]. For clarity, a few additional terms not included in the ANSI standard have been adapted from other sources, including ISO 10343:2014 (ophthalmic instruments – ophthalmometers) [35] and ISO 18369-1:2017 (contact lenses – vocabulary, classification system and recommendations for labelling specifications) [36].

**Definition 2.1.1 (Optical Axis).** Any line along which the path of a light ray exiting an optical system is coincident with its path upon entry [27]. For a single refracting surface with some degree of rotational symmetry, the optical axis coincides with the axis of symmetry. For two such surfaces placed in series, the optical axis would be the line connecting their centers of curvature.<sup>i</sup>

**Definition 2.1.2 (CT Axis).** The corneal topographer (CT) axis is a line parallel or coincident with the Envisu’s optical axis, which serves to define the  $z$ -axis during data collection [5].

**Definition 2.1.3 (Design Equation).** A function  $z(\rho, \theta)$  which, along with specified parameters, provides the intended shape of the given lens surface.

---

<sup>i</sup>It is commonly stipulated in the vision community that the human eye lacks a true optical axis because the centers of curvature of the refracting elements are generally not coaxial [60, 85]. There is still significant debate as to which of the eye’s axes best serves as a proxy for the optical axis when conducting the type of analysis discussed in this thesis [7, 60, 85, 101].

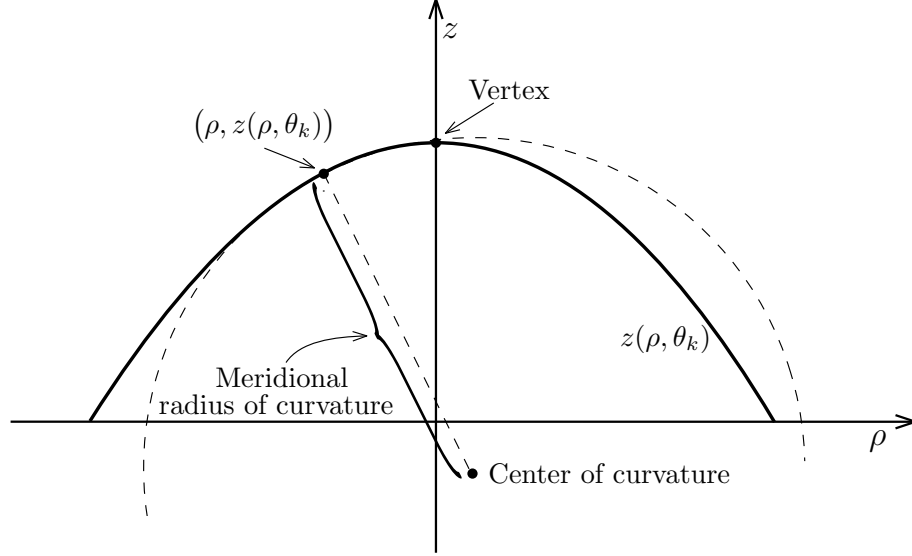


Figure 2.1: The solid curve represents a cross section of the surface  $z(\rho, \theta)$  confined to the meridional plane  $\theta = \theta_k$ . The radius of curvature at  $(\rho, z(\rho, \theta_k))$  is the radius of the osculating circle at that point, indicated by the dashed curve.

The design equations for each lens are defined so that the optical axes of the anterior and posterior (front and back) surfaces are coincident with one another as well as with the  $z$ -axis. By convention, the  $z$ -axis is oriented so that the positive direction points from the lens toward the OCT probe [6, 38].

**Definition 2.1.4 (Lens Vertex<sup>ii</sup>).** The point at which a lens’s optical axis crosses one of its surface boundaries [36]. Unless otherwise specified, we will use this term to describe the front vertex of the lens.

The sample alignment protocol in the probe’s user manual [51] aims to align the CT axis with the optical axis of the lens. However, as this protocol must be performed by hand, we cannot rule out the possibility of non-negligible human error. Therefore it is

---

<sup>ii</sup>This is one place in which we have chosen to depart from the terminology in the ANSI standard, which defines the term *corneal vertex* as the “point of tangency of a plane perpendicular to the CT axis with the corneal surface” [5]. In other words, if we let the CT axis determine the  $z$ -axis of the coordinate system, then the corneal vertex is the point at which the basis vector  $\mathbf{e}_z = \langle 0, 0, 1 \rangle$  is normal to anterior surface of the eye. However, the standard does not include specific guidelines on the alignment of the CT axis. Despite claims that it is a “morphologically stable” reference [7, 60], it would appear that the corneal vertex is not in fact an inherent property of the eye, but instead depends on the choice of reference axis used for CT alignment.

helpful to distinguish between the true vertex of the lens and the approximation of the vertex obtained using the sample alignment protocol. We will refer to the approximate vertex—that is, point at which the CT axis crosses the front surface of the lens—as the *scan vertex*.

**Definition 2.1.5 (Meridional Plane).** Any plane containing the specified reference axis [5]. A particular meridian is identified by its angular position  $0 \leq \theta < \pi$  in standard cylindrical coordinates (see Section 2.2.1).

**Definition 2.1.6 (Meridional Curvature<sup>iii</sup>).** A measure of local curvature of the surface  $z(\rho, \theta)$  within the meridional plane  $\theta = \theta_k$ . The meridional curvature of the resulting plane curve is given by the reciprocal of the radius of its osculating circle, which is itself a function of  $\rho$ . Figure 2.1 illustrates the meridian  $\theta = \theta_k$  of the surface  $z(\rho, \theta)$ , as well as the meridional radius of curvature at an arbitrary off-axis point  $(\rho, z(\rho, \theta_k))$ .

By convention, the curvature is considered positive whenever the surface is bending away from the imaging system (as it would for a healthy cornea). Therefore, to be consistent with the orientation of our design equation  $z(\rho, \theta)$ , we must write the signed meridional curvature  $k(\rho, \theta)$  as

$$k(\rho, \theta) = \frac{-z_{\rho\rho}(\rho, \theta)}{\left(1 + (z_{\rho}(\rho, \theta))^2\right)^{3/2}}, \quad (2.1)$$

where  $z_{\rho}$  and  $z_{\rho\rho}$  denote the first and second partial derivatives with respect to  $\rho$ . The reciprocal of (2.1) yields the corresponding *radius of curvature* [5].

The ANSI standard stipulates that curvature results should be reported in units of *keratometric diopters* (abbreviated “D”), which are inverse millimeters times the keratometric constant 337.5.<sup>iv</sup> The maps shown in Figure 2.2 illustrate this convention. Keratometric diopters were introduced in order to relate the curvature of the cornea to its refractive power; however, this relationship is only meaningful at the corneal vertex [44], and even then it is merely an approximation based on assumptions about other shape properties of the cornea (*e.g.*, curvature of the posterior surface and thickness).

---

<sup>iii</sup>Meridional curvature is also sometimes referred to as *tangential curvature*.

<sup>iv</sup>It is also not unusual to see the term “curvature” used in reference to radius of curvature measurements (in units of millimeters), particularly in older literature that predates the standard.

Since there is no practical purpose for using keratometric diopters in lieu of inverse millimeters, we will use the latter for the theoretical analyses in Chapters 3–4 and switch to the former only when discussing the real lens data in Chapters 5–6.

**Definition 2.1.7 (Principal Curvatures).** The principal curvatures are the maximum and minimum *normal curvatures*<sup>v</sup> ( $k_1(\mathfrak{X})$  and  $k_2(\mathfrak{X})$ , respectively) at the point  $\mathfrak{X}$ , where a normal curvature is simply the meridional curvature (2.1) within a plane referenced to the local surface normal vector [5]. Since we are primarily interested in the principal curvatures at the vertex, we refer to the maximum and minimum curvatures at  $\rho = 0$  as  $k_1$  and  $k_2$ , respectively; *i.e.*,

$$k_1 \equiv \max_{0 \leq \theta < \pi} k(0, \theta), \quad k_2 \equiv \min_{0 \leq \theta < \pi} k(0, \theta).$$

The maximum and minimum radii of curvature at the vertex will be denoted by  $R_1 = \frac{1}{k_2}$  and  $R_2 = \frac{1}{k_1}$ .

**Definition 2.1.8 (Principal Meridians).** The two meridional planes corresponding to the principal curvatures at the vertex (*i.e.*, the principal directions) [35].<sup>vi</sup>

Note that the vertex of an axisymmetric surface (one with continuous rotational symmetry about the  $z$ -axis) is an umbilical point—in other words, the surface is locally spherical, so there is only one principal radius of curvature  $R = R_1 = R_2$ . For such a surface,  $R$  is sometimes referred to as “the” radius of curvature of the lens, and every meridian is thus a principal meridian. The continuous rotational symmetry of the front surfaces of both lenses can be seen in Figures 2.2a–b, where the curvature at the vertex is

---

<sup>v</sup>There is a subtle distinction between the ANSI and ISO corneal topography standards when it comes to the definitions of principal curvature. While the ANSI definition (referenced above) agrees with the standard mathematical usage from differential geometry [5], the ISO standard omits the word “normal” and instead defines the principal curvature simply as the “maximum or minimum curvature at a point on the surface” [37]. One possible explanation for this omission might be that clinicians tend to be interested in the principal curvatures at the corneal vertex, where the surface normal vector is parallel to the CT axis by definition (see footnote ii). However, while many CT systems include an alignment procedure to ensure that the CT axis is itself perpendicular to the cornea at the point of incidence [44, 78], neither the ANSI nor ISO standard explicitly states such a requirement. Furthermore, this leaves some ambiguity regarding the definition of the principal curvatures for off-axis surface points like the corneal apex.

<sup>vi</sup>As discussed in footnote v, in practice the normality of the axis at the vertex is often assumed but not necessarily true. Thus, the principal meridians of a cornea may fail the perpendicularity consequence of Euclid’s curvature theorem [20], resulting in a condition labeled *irregular astigmatism*.

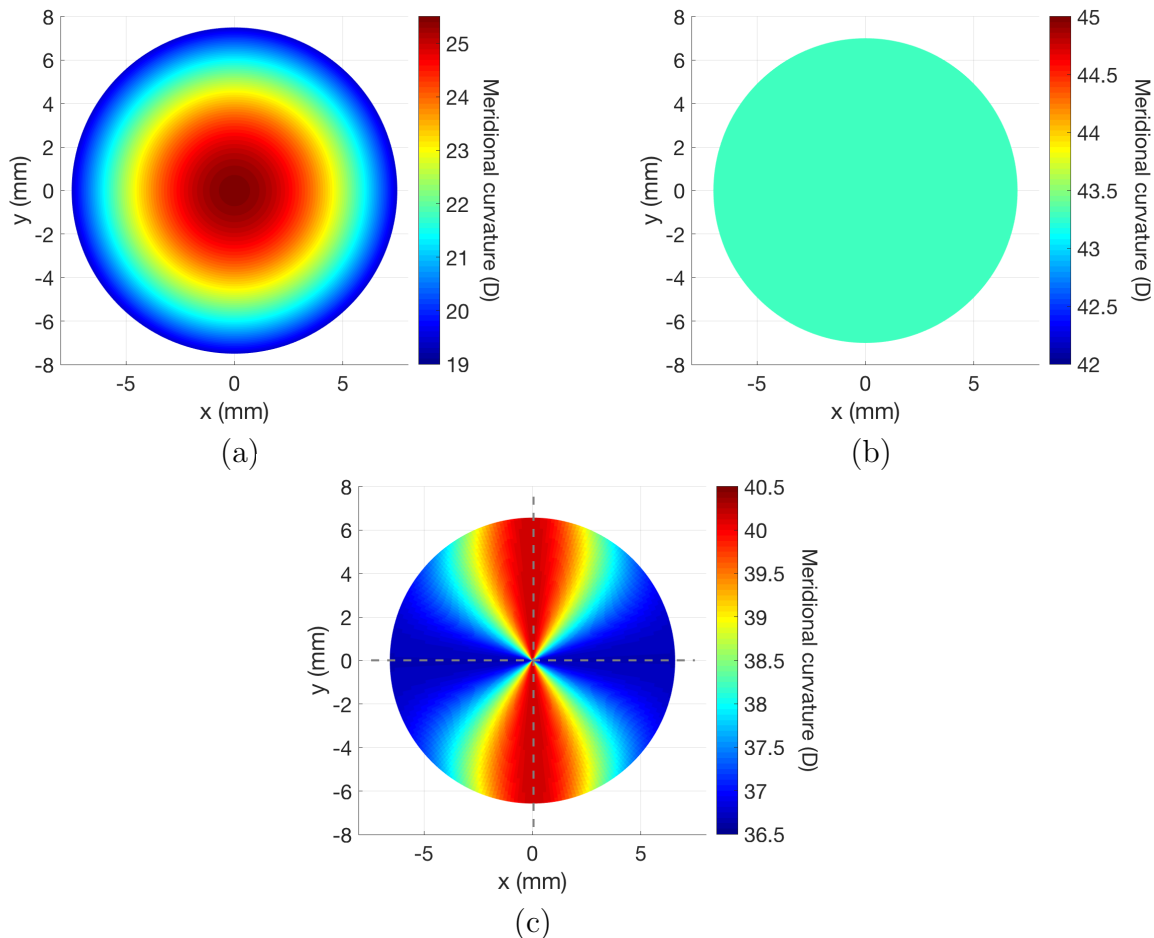


Figure 2.2: Meridional curvature maps in keratometric diopters (D) for the (a) front surface of the aspheric lens, (b) front surface of the toric lens, and (c) back surface of the toric lens. The dashed lines in (c) indicate the principal meridians.

clearly the same in every radial direction. On the other hand, the back surface of the toric lens (shown in Figure 2.2c) is not axisymmetric. The principal meridians are indicated by the dashed lines.

Most corneal topography systems generate a number of different metrics based on the surface data collected. Of these, there are two common measures of curvature that conform to the ANSI standard [5]: meridional curvature and *axial curvature*<sup>vii</sup> [44, 55]. Within a given meridian, the axial curvature  $k_a$  at each lateral coordinate  $\rho$  is defined as the

<sup>vii</sup>Axial curvature is also sometimes referred to as *sagittal curvature*.

integral from the reference axis to  $\rho$  of the meridional curvature  $k_m$ ,

$$k_a(\rho) = \frac{1}{\rho} \int_0^\rho k_m(x) dx.$$

Whereas the meridional curvature map provides a measure of “instantaneous” curvature, the axial curvature map is valued by clinicians because of its relationship to refractive power under ideal circumstances [11, Ch. 4]. To limit the sources of numerical error—such as that introduced by numerical integration—this thesis will only address the former metric.

The significance of either the meridional or axial curvature maps depends upon the accuracy of the reference axis. However, as we noted earlier, perfect alignment of the CT axis with the lens’ optical axis is difficult even under ideal conditions. We expect to see some variability in the position of the scan vertex across repeated measurements; therefore, there may be discrepancies among the local maps produced from independent scans unless an effort is made to identify the correct axis before calculating curvature. The use of synthetic OCT data based on known design equations allows us to perform some preliminary validation of the methods described in Chapters 3 and 4 without having to address possible misalignment of the CT axis with the sample’s optical axis. For a non-axisymmetric lens, using synthetic data also avoids the need to account for errors in the orientation of the principal meridians. Both of these issues will be discussed in Chapter 5.

The ANSI standard also includes several measures of local curvature that do not depend on the choice of reference axis. For example, according to the mathematical definition of the principal curvature, the minimum and maximum curvature at each point depends only on the local normal vector, which is unique (up to its sign). The mean curvature ( $H$ ) and Gaussian curvature ( $\kappa$ ) of a surface at a point  $\mathfrak{X} \in \mathbb{R}^2$  are, respectively, the arithmetic mean and the product of the local principal curvatures

$$H(\mathfrak{X}) = \frac{k_1(\mathfrak{X}) + k_2(\mathfrak{X})}{2}$$

$$\kappa(\mathfrak{X}) = k_1(\mathfrak{X})k_2(\mathfrak{X}).$$

However, while some of these maps could prove clinically useful, they have not yet been widely adopted in practice [44]. Therefore, they will not be covered in this thesis.



Figure 2.3: Envisu metrology assembly with handheld R4410 OCT probe [51].

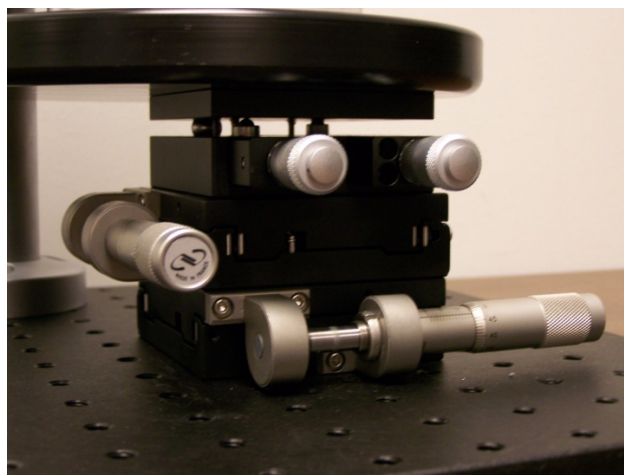
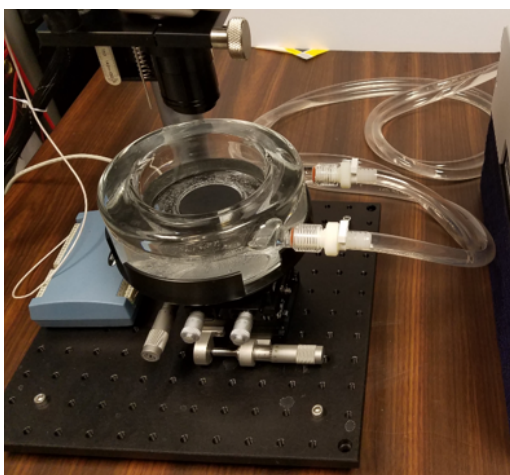


Figure 2.4: Sample holder (left) and sample positioning stage (right) [51].

Table 2.1: Technical specifications for the Envisu R4410 SDOCT Contact Lens Metrology System [50].

Parameter	Value
Central wavelength	883.9 nm
3 dB bandwidth	63.7 nm
Axial pixel resolution in saline	5.2 $\mu\text{m}$
Optical axial resolution in saline	7.5 $\mu\text{m}$
Maximum scan depth in saline	11 mm
Recommended use depth in saline	7 mm
Lateral Field of View (diameter)	20 mm
Lateral resolution	23 $\mu\text{m}$

## 2.2 OCT Data Collection

Each lens was imaged *ex vivo* in a saline medium using an Envisu R4410 SDOCT Contact Lens Metrology System (Leica Microsystems, Inc.; Morrisville, NC)<sup>viii</sup>—shown in Figure 2.3—at a central wavelength of 883.9 nm. Figure 2.4 depicts the sample positioning stage, which facilitates proper orientation and alignment of the lens prior to imaging. Table 2.1 contains additional technical specifications for the Envisu system.

### 2.2.1 Image Acquisition

The data collected by the Envisu consist of 2D cross-sectional images, or *B-scans*, in meridional planes referenced to and centered at the instrument (CT) axis, which is approximately aligned with the optical axis of the lens according to the sample alignment protocol in the user manual [51]. An example of a B-scan from the toric lens can be seen in Figure 2.5.

The individual depth measurements comprising a B-scan are referred to as *A-scans*. Each A-scan contains information for the full axial depth  $D$ , including both the front and back surfaces, in the form of a fixed number of vertical *samples*. Collectively, the number of A-scans and samples correspond, respectively, to the horizontal resolution and vertical resolution of the resulting image.

<sup>viii</sup>The Envisu R4410 is based on Leica’s Envisu S4410 series.

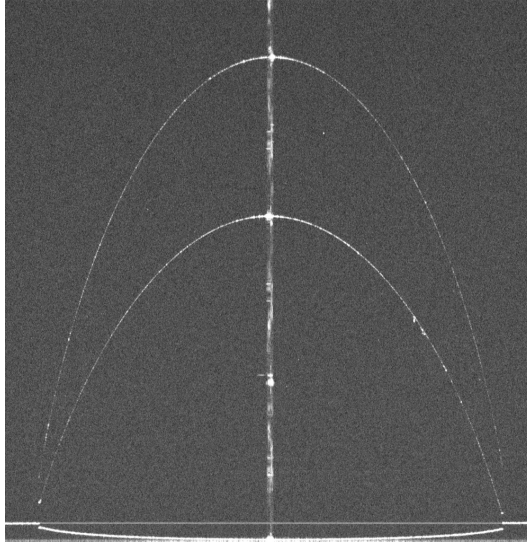


Figure 2.5: A B-scan of the toric lens obtained using the Envisu R4410.

*Volumetric imaging* is achieved using a *radial sampling pattern*, consisting of multiple B-scans acquired at regular angular intervals  $0 \leq \theta < \pi$  around the CT axis as shown in Figure 2.6a. The general structure of the sampling pattern in the  $xy$ -plane is illustrated in Figure 2.6b. Recall from Section 2.1 that the positive  $z$ -axis points from the lens toward the OCT probe along the CT axis, and that  $\theta$  is measured in the counterclockwise direction starting from the positive  $x$ -axis.<sup>ix</sup>

The radial sampling pattern has several key advantages over a raster (rectangular) pattern. With a radial scan, each independent frame of data is a cross-section through the scan vertex. If the number of A-scans is odd, then the central coordinate of each frame is the same—*i.e.*,  $(0, 0)$ . This redundancy is critical for three-dimensional image registration. Furthermore, radial scan data are not distributed evenly across the surface (as they would be in a raster scan), and are instead concentrated near the vertex, providing greater resolution for the region in which we desire the greatest computational accuracy due to its physiological relevance. Conversely, the main drawback to the radial pattern is that azimuthal density of the data points falls off near the periphery of the scan region, resulting in an increased fitting error near the edges.

---

<sup>ix</sup>For *in vivo* measurements on an upright human subject, the  $x$ -axis is taken to lie along the horizontal, with positive values pointing to the right [6, 38].

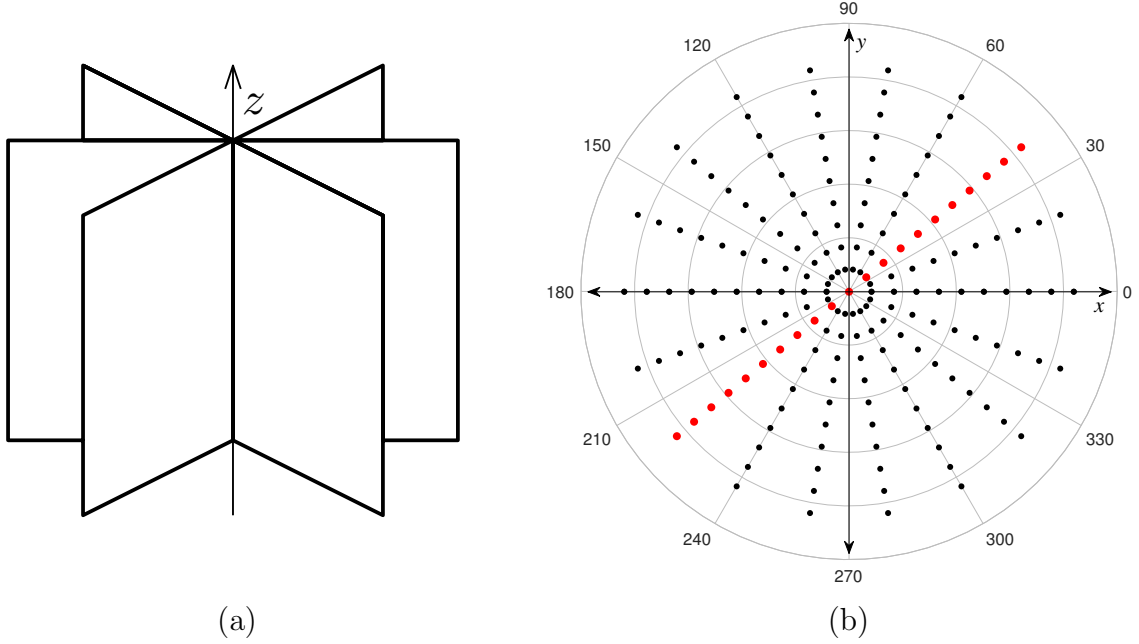


Figure 2.6: Illustration of the radial scan pattern (a) as multiple B-scans aligned in  $\mathbb{R}^3$  at the CT axis, and (b) in the  $xy$ -plane perpendicular to the CT axis (the highlighted points represent a single frame of data).

### 2.2.2 Segmentation & Outlier Removal

Each B-scan is interpreted, effectively, as an array of pixel indices whose intensities have been determined by the interference pattern formed via recombination of the light from the sample and reference arms of the OCT scanner. Before we conduct our own analysis, a *segmentation* process is performed to extract *point cloud data* reflecting the axial ( $z$ ) coordinates of the pixels comprising the anterior and posterior surfaces of the lens. We did not perform any of the image processing ourselves, and the precise segmentation and outlier removal protocols used on our lens data are considered proprietary by Leica Microsystems, so this step will be regarded as a black box for the purposes of this thesis. The following is a somewhat-simplified overview of the underlying concepts.

The main principle involved in segmentation of OCT data is *edge detection*, which describes a class of algorithms designed to identify the pixels comprising the surface boundaries by looking for rapid transitions in the brightness. The end result of this process is a list of all the A-scans in each B-scan along with the pixel location (using zero-indexing from the top of the frame) of each surface. We have adopted the convention

of reporting the pixel index as “−1” if segmentation fails to identify a boundary.

In addition to background white noise that is present in all OCT images, pixel intensities can vary for a number of reasons. More scattering occurs in the reflected light as the angle of incidence increases, so image contrast tends to suffer near the edges where the plane tangent to the lens is steeper. If, on the other hand, too much light is reflected (which can occur for a variety of reasons), the pixels in the vicinity of the surface boundary might be completely saturated, obscuring the exact location of the boundary. These areas of over- and under-exposure cause image artifacts that, in turn, give rise to outliers in the point cloud data. Furthermore, particularly strong Purkinje-like reflections [98] where the angle of incidence is close to zero can cause a narrow vertical band of oversaturated pixels throughout the entire B-scan. This effect—which appears in all of our lens data and is illustrated in Figure 2.5—is most likely to arise in the region immediately surrounding the scan vertex when the scan axis is coincident with the optical axis, due to the fact that the latter is normal to the surface at the point of incidence. Because of this oversaturation, every B-scan in both of our data sets contains a central gap of 20–100 A-scans (out of a total of 1001 A-scans) where the segmentation algorithm was unable to identify a surface. This is equivalent to 0.32–1.6 millimeters of missing data at the center of each 16 millimeter frame.

After segmentation, most of the remaining outliers are removed using a combination of kernel methods and the RANSAC (RANdom SAMple Consensus) algorithm described in [21]. However, due to the difficulties in developing a robust outlier removal process that can be automatically applied to a broad range of asymmetric surfaces, some outliers typically remain in the lens data after this step. Occasionally, segmentation may identify the wrong surface entirely, particularly in areas of very low contrast. Outlier removal is only intended to remove isolated points, so clusters of points forming a smooth curve will not be flagged, even if they cause a jump discontinuity in the surface. Except in these cases, there is no apparent spatial bias in the noise that remains in the point cloud data after outlier removal, and the variance of this remaining noise is typically quite small.

## A Note About Poor Segmentation Results

RANSAC can also underperform when a heavily-corrupted data set contains an insufficient ratio of inliers to outliers. While this was not an issue for the aspheric lens data, it did turn out to be a problem for at least a quarter of the toric lens B-scans. After

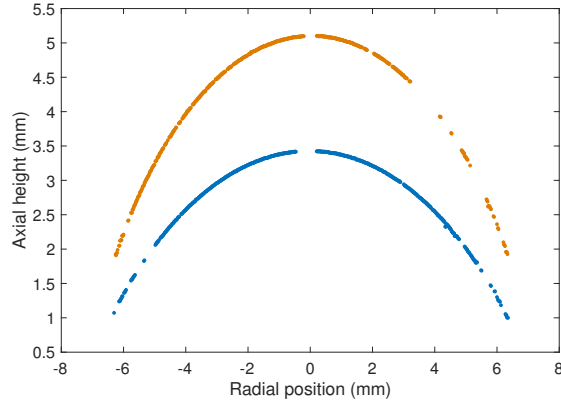


Figure 2.7: Good segmentation results for a frame of toric lens data.

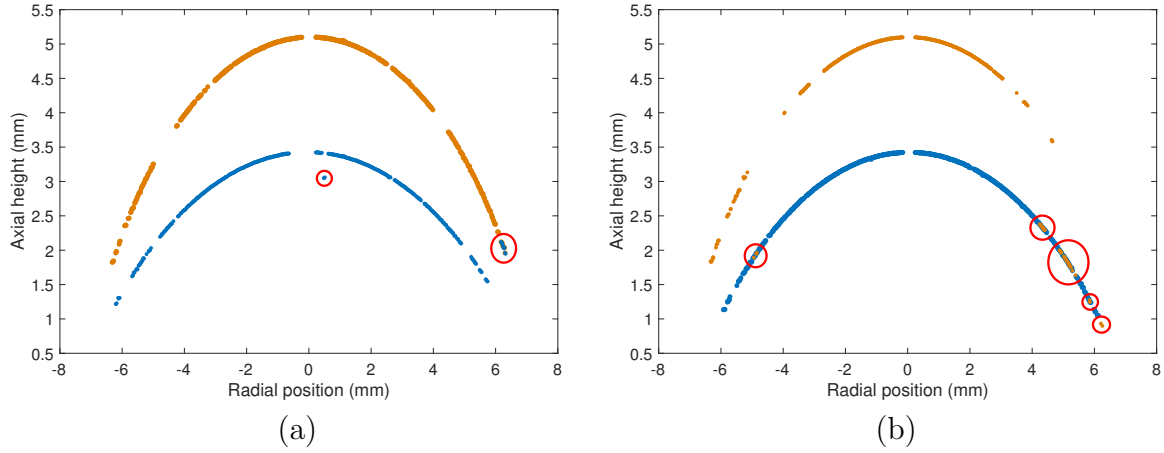


Figure 2.8: Two frames of toric lens data with poor segmentation results.

segmentation and outlier removal, the toric lens point cloud data *should* resemble Figure 2.7. However, visual inspection of the data revealed that 33 of the 120 frames still contained obvious outliers that had been overlooked by Leica's outlier removal algorithm. Two such frames are illustrated in Figure 2.8. For reference, the original B-scan images corresponding Figure 2.8 are shown in Figure 2.9.

In Figure 2.8a, we can see that edge detection has assigned a number of pixels clearly on the boundary of the front surface to both the front and back surfaces. Not only is the outlier removal algorithm unable to identify these points, but their presence also prevents

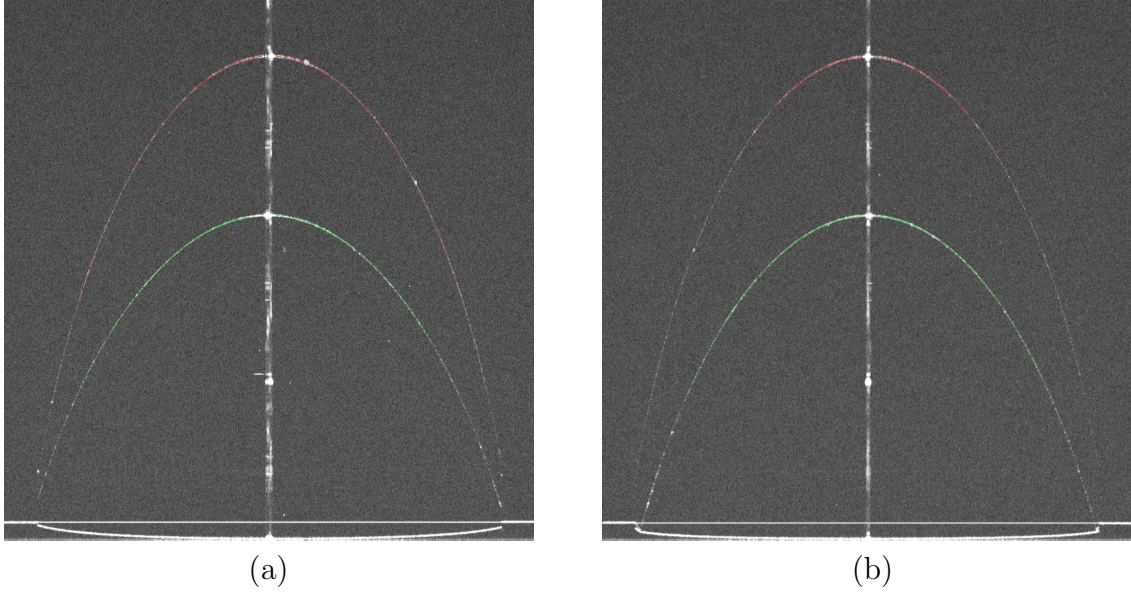


Figure 2.9: Point cloud data from Figure 2.8a (left) and Figure 2.8b (right) superimposed over the original B-scans.

the algorithm from detecting the handful of outliers near the center. Figure 2.8b depicts a more common issue with this data set, in which low contrast away from the center in the original image results in the duplicate assignment of numerous back surface pixels to both surfaces.

We were instructed by Leica’s senior engineer to exclude the 33 frames of bad segmentation data from our analysis in Chapters 5 and 6. Leica is working on improvements to their automatic segmentation algorithm in order to eliminate the need for this kind of manual intervention in the future.

### 2.2.3 Conversion to 3D

The point cloud data we receive for analysis is reported as a list of pixel indices for each B-scan describing the boundaries of the anterior and posterior lens surfaces, along with the corresponding lateral position of the measurement relative to the scan vertex. These data must next be converted to 3D spatial coordinates, after which a small vertical adjustment is applied to the entire data set to correct for local deviations introduced by the OCT scanner’s internal components.

Even in the ideal situation where segmentation performs perfectly, the point cloud data will still inherit uniform noise in the form of quantization error from the original OCT image data. While the height and width of each frame (the distance between the first and last measurement) is fixed prior to data collection, the pixel dimensions are determined only by the sampling density. When converting to spatial coordinates, we use the position corresponding to the center of each pixel. Error due to pixel quantization is discussed further in Section 2.4.1.

**Definition 2.2.1 (Sample Grid).** Given the radial sampling pattern, the location of each point  $\mathfrak{X}$  in the resulting grid shown in Figure 2.6 is most easily defined in terms of polar coordinates. If  $W$  is the width of each frame in millimeters and  $a$  is the number of A-scans per B-scan, then the distance between adjacent A-scans is  $\Delta_\rho = \frac{W}{a-1}$ . The radial coordinates corresponding to each A-scan (which we will refer to as the *radial sample grid*) can therefore be written as the set

$$\begin{aligned} R &= \left\{ \rho_j = -\frac{W}{2} + j \cdot \Delta_\rho, \ j = 0, \dots, a-1 \right\} \\ &= \left\{ -\frac{W}{2}, -\frac{W}{2} + \frac{W}{a-1}, -\frac{W}{2} + \frac{2W}{a-1}, \dots, \frac{W}{2} - \frac{W}{a-1}, \frac{W}{2} \right\}. \end{aligned} \quad (2.2)$$

Each meridional B-scan corresponds to an angular coordinate on the interval  $[0, \pi)$ . If  $b$  is the total number of B-scans, then the angular distance between consecutive B-scans is  $\Delta_\theta = \frac{\pi}{b}$ . Thus, the *meridional sample grid* is given by

$$\Theta = \left\{ \theta_k = k \cdot \Delta_\theta \mid k = 0, \dots, b-1 \right\} = \left\{ 0, \frac{\pi}{b}, \frac{2\pi}{b}, \dots, \frac{(b-1)\pi}{b} \right\}, \quad (2.3)$$

The *sample grid*  $S$  is the cartesian product of  $R$  and  $\Theta$ :

$$S = R \times \Theta = \{ \mathfrak{X} = (\rho, \theta) \mid \rho \in R, \ \theta \in \Theta \}. \quad (2.4)$$

**Example 2.2.1.** Figure 2.10 depicts  $\Delta_\rho$  and  $\Delta_\theta$  on a radial sample grid of dimension  $b \times a = 9 \times 7$ , along with the specific point  $\mathfrak{X} = (\rho, \theta) = (2\Delta_\rho, 6\Delta_\theta)$ . The sample grid referenced throughout the rest of this thesis will be considerably denser at  $b \times a = 100 \times 1001$ .

While it is convenient to define the sample grid according to the above construction,

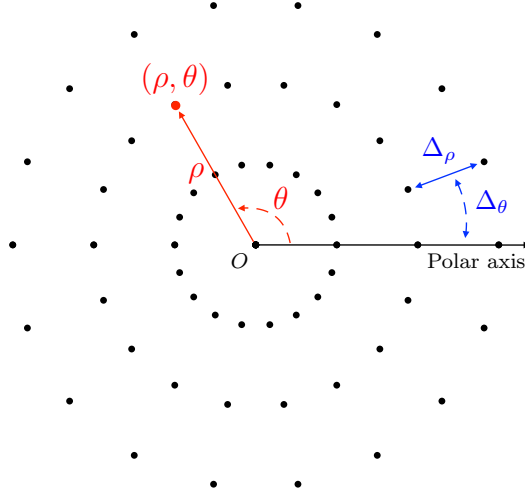


Figure 2.10: Illustration of  $\mathfrak{X} = (\rho, \theta)$  on a sample grid with  $\rho = 2\Delta_\rho$  and  $\theta = 6\Delta_\theta$ .

each value of  $\mathfrak{X} \in S$  should be thought of as merely a point in  $\mathbb{R}^2$  rather than an ordered pair in a particular coordinate system. We will find it useful to express these points in terms of different coordinate systems depending on the context.

To convert the point cloud data to units of distance, we must first note that, although the axial depth  $D$  is constant across all the A-scans, this measurement does **not** represent an actual geometric distance but rather the *optical path length (OPL)* of the light from the OCT scanner. The axial depth should be thought of as the OPL between the first and the last sample in each A-scan. For each surface, our data set will comprise all the OPL measurements  $w_i^a$  (for the anterior surface) and  $w_i^p$  (for the posterior surface) for each  $\mathfrak{X}_i \in S$ , given as the distance in millimeters from the top of the frame to the particular surface boundary.<sup>x</sup> Letting  $f$  represent the number of samples in each A-scan (*i.e.*, the vertical resolution of the B-scans), the path length between adjacent samples can be expressed as  $\Delta_z = \frac{D}{f-1}$ . The back surface observations  $w_i^p$  are thus obtained by multiplying  $\Delta_z$  by the vertical pixel index of the corresponding point in the point cloud

---

<sup>x</sup>Illustrations of lens data and surface reconstructions throughout this thesis show the front surface oriented above the back surface—that is, if  $w^a$  and  $w^p$  correspond respectively to surface observations for the front and back surface at the grid point  $\mathfrak{X}$ , then  $w^a > w^p$ . However, this relationship would technically be reversed if the  $z$ -axis represented the distance from the OCT probe as implied. For the sake of simplicity, we have chosen to invert the data in order to depict the surfaces in their original spatial configuration within the sample holder, as shown in Figure 2.4.

data. Note that due to segmentation failures and outlier removal, we are not guaranteed an observation for every point on the sample grid.

The geometric path length  $L$  can be computed by dividing the optical path length by the refractive index  $n$  of the medium through which the light is traveling, meaning that we must account for the different media at some point (as well as the angle of incidence at the surface boundaries). The light exiting the sample arm of the Envisu R4410 is sufficiently close to telecentric (*i.e.*, parallel to the  $z$ -axis) that we can convert the observations for the anterior surface to actual  $z$ -coordinate values simply by dividing the observations by the refractive index  $n_s$  of the saline medium.<sup>xi</sup> However, the presence of multiple media within an A-scan means that refraction occurs at the boundary of the lens. After accounting for that refraction, we will see that light passing through the front surface at the point  $(\mathfrak{X}, w^a)$  only *appears* to intersect the back surface at the point  $(\mathfrak{X}, w^p)$ . The true coordinates of a particular data point on the posterior surface are determined by the shape of the lens—specifically the normal vector at the point of incidence on the front surface. The topic of 3D refraction correction will be addressed in depth in Chapter 4.

When it is not necessary to distinguish between the front and back surface data, we will drop the superscript and use  $w$  interchangeably for both surfaces.

## 2.2.4 Scanner Calibration

Due to variations in spatial group velocity across the OCT scanner’s internal optical components, there will be small distortions in scanning field flatness of the imaging system.<sup>xii</sup> This optical path length error can be modeled as a function  $E_z$  of the lateral position  $\mathfrak{X} = (x, y) \in S$  using a sixth order binomial expansion

$$E_z(\mathfrak{X}) = E_z(x, y) = \sum_{n=0}^6 c_n x^{6-n} y^n,$$

where the coefficients  $c_n$  have been obtained by the manufacturer through factory calibration using a precision optical flat [51, 82]. The corrected location  $(\mathfrak{X}_i, w_i)$  of the particular

---

<sup>xi</sup>Since the anterior surface data points are only off by a scalar constant  $n_s$ , we will generally assume that the rescaling to compute geometric path length has already been done when referring to the front surface data points  $w_i^a$ .

<sup>xii</sup>Previous papers have discussed the need to account for fan distortion due to the lack of incident ray telecentricity in the OCT probe [69, 70, 76, 105]. However, the Envisu system is sufficiently telecentric that fan distortion is effectively negligible compared to the optical path length error [82].

raw data point  $(\mathfrak{x}_i, w'_i)$  after accounting for scanning field flatness is subsequently given by

$$(\mathfrak{x}_i, w_i) = (\mathfrak{x}_i, w'_i - E_z(\mathfrak{x}_i)).$$

Note that this correction is applied to all of the data, including the posterior surface, prior to any adjustments for optical distortion within the lens sample itself. Any images of B-scans or point cloud data shown throughout this thesis (*e.g.*, Figure 2.5) have already taken this correction into account, and we will not be modeling this effect in our synthetic data.

## 2.3 Imaging Phantoms

The data analyzed in this thesis were collected from two imaging phantoms (*i.e.*, test surfaces) with known design equations: a) an *aspheric lens*, consisting of an axisymmetric front surface and a flat back surface; and b) a *toric lens* with a spherical front surface, whose back surface matches the shape of a cap taken from a spindle torus. Both lenses were submerged in saline and imaged using identical scan dimensions. To minimize the effects of background imaging noise, each frame was scanned eight times in immediate succession and then averaged using the Envisu’s registration and averaging tool.

Each of the  $b = 120$  B-scans comprising the two data sets contain  $a = 1001$  A-scans. The frame width is  $W = 16$  mm, while the axial depth of each frame is  $D = 15.298$  mm containing 2048 samples. Therefore the sample spacings are  $\Delta_\rho = \frac{W}{a-1} = \frac{16}{1001-1} = 0.016$  mm (16  $\mu\text{m}$ ),  $\Delta_\theta = \frac{\pi}{b} = \frac{\pi}{120}$  radians (1.5°), and  $\Delta_z = \frac{D}{f-1} = \frac{15.298}{2048-1} \approx 0.0075$  mm (7.5  $\mu\text{m}$ ). To eliminate concerns about optical effects for the top surface, we can rescale the axial depth using the refractive index of the imaging medium (see Table 2.4). The new axial depth and vertical resolution are thus  $D' = D/n_s \approx 11.428$  mm and  $\Delta'_z \approx 0.0056$  mm (5.6  $\mu\text{m}$ ). Note that this overcorrects the OPL between first and second surfaces, so we will have to multiply those values by  $n_s$  before dewarping them.

Intensity data for each pixel (*i.e.*, signal strength) is initially stored as a 16-bit unsigned integer, and subsequently converted to an 8-bit unsigned integer prior to segmentation. The surface boundaries for the lenses vary from one to three pixels in thickness, with the boundary being thickest at the center. When there are multiple pixels comprising the boundary, the edge detection algorithm essentially chooses the brightest pixel out of that subset (in the case of three pixels, this generally ends up being the one in the

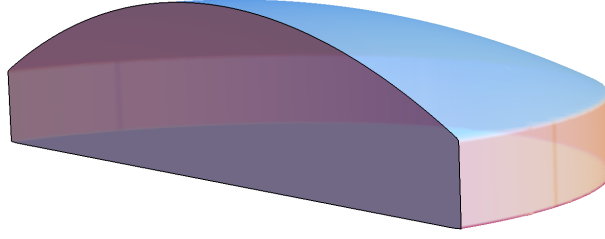


Figure 2.11: Rendering of aspheric lens from the design equations.

middle).

### 2.3.1 Aspheric Lens

The aspheric lens we used is a commercially produced uncoated glass lens with 15 mm diameter from the Edmund Optics TECHSPEC<sup>®</sup> Precision line (EO stock #47-728), made from L-BAL35. The front surface is axisymmetric and designed according to the (inverted) asphere equation

$$z(\rho, \theta) = - \left( \frac{\rho^2}{R_a \left( 1 + \sqrt{1 - (1 + \kappa) \frac{\rho^2}{R_a^2}} \right)} + a_4 \rho^4 + a_6 \rho^6 + a_8 \rho^8 + a_{10} \rho^{10} \right), \quad (2.5)$$

where  $R_a = 13.255$  mm is the radius of curvature at the vertex,  $\kappa = -2.3641$  is the conic constant, and  $a_4$ ,  $a_6$ ,  $a_8$ ,  $a_{10}$  are the 4<sup>th</sup>, 6<sup>th</sup>, 8<sup>th</sup>, and 10<sup>th</sup> order aspheric coefficients specified in Table 2.2. Tolerances were not provided for these values, but the surface accuracy given by the manufacturer is  $0.75 \mu\text{m}$ , as measured by the root mean square of the residual.

The back surface of the aspheric lens is a flat plane ( $1/R_p = 0 \text{ mm}^{-1}$ ), positioned such that the center thickness is  $t_C = 4.0$  mm with a tolerance of  $\pm 0.1$  mm. Figure 2.11 depicts a graphical rendering of the aspheric lens from the design parameters, which are summarized in Table 2.2. Additional information about aspheric lenses can be found at on the Edmund Optics website [19].

Table 2.2: Design specifications and tolerances for the Edmund Optics TECHSPEC® Precision Aspheric Lens from [65].

Parameter name	Variable	Value
Total diameter	$\varnothing_T$	15.0 +0.0/−0.1 mm
Center thickness	$t_C$	4.0 ± 0.1 mm
Conic constant	$\kappa$	−2.3641
Front radius of curvature	$R_a$	13.255 mm
Back radius of curvature	$R_p$	$\infty$
Higher order terms	$a_4$	$9.5567 \times 10^{-5} \text{ mm}^{-4}$
	$a_6$	$-2.6095 \times 10^{-7} \text{ mm}^{-6}$
	$a_8$	$1.1246 \times 10^{-9} \text{ mm}^{-8}$
	$a_{10}$	$-2.9990 \times 10^{-12} \text{ mm}^{-10}$
Asphere figure error (RMS)	—	0.75 $\mu\text{m}$

Table 2.3: Target specifications for the Universal Optics toric meniscus lens. (Tolerances are based on third party measurements of the specific lens artifact.)

Parameter name	Variable	Value
Total diameter (outer)	$\varnothing_{T_a}$	14.0 mm
Total diameter (inner)	$\varnothing_{T_p}$	13.1446 mm
Center thickness	$t_C$	1.500 ± 0.002 mm
Front radius of curvature	$R_a$	7.80 ± 0.01 mm
Back radius of curvature (max)	$R_{p_1}$	9.20 ± 0.01 mm
Back radius of curvature (min)	$R_{p_2}$	8.40 ± 0.01 mm

### 2.3.2 Toric Lens

The other phantom we used is a rigid gas permeable poly(methyl methacrylate) (PMMA) lens with a spherical front surface and a toric back surface, which was manufactured by Universal Optics. The toric lens is a positive meniscus lens, meaning that it is a convex-concave lens configured such that the focal length is positive.

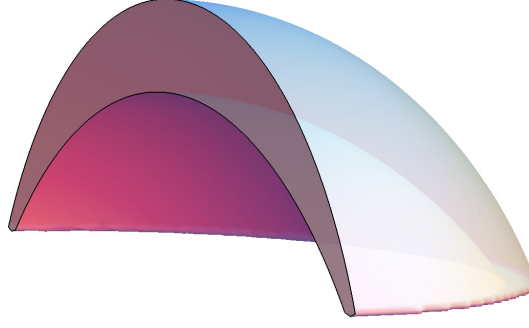


Figure 2.12: Rendering of toric lens from the design equations.

Since the front surface is spherical, its shape is simply given by

$$z(x, y) = \sqrt{R_a^2 - x^2 - y^2}, \quad (2.6a)$$

where  $R_a = 7.8$  mm. The back surface is shaped like a “cap” from a spindle torus with minor and major radii  $R_{p_2} = 8.4$  mm and  $R_{p_1} - R_{p_2} = 0.8$  mm, respectively. The design equation for this surface can therefore be derived from the general formula for a torus and written as

$$z(x, y) = \sqrt{\left(R_{p_1} - R_{p_2} + \sqrt{R_{p_2}^2 - y^2}\right)^2 - x^2}. \quad (2.6b)$$

Unlike the three other lens surfaces we will consider, the back surface of the toric lens is not axisymmetric, although it does possess 2<sup>nd</sup> order discrete rotational symmetry. Hence, it is the only surface to possess two unique principal radii of curvature:  $R_{p_1} = 9.2$  mm and  $R_{p_2} = 8.4$  mm. The front and back surfaces are positioned such that the center thickness is  $t_C = 1.5$  mm.

A summary of the design parameters for the toric lens is given in Table 2.3. Figure 2.12 illustrates an ideal lens based on these parameters. Validation was performed on behalf of Universal Optics by an unspecified third party. The radii of curvature were determined using a Zygo VeriFire<sup>TM</sup> Asphere (VFA) interferometer to be  $R_a = 7.814$  mm,  $R_{p_1} = 9.212$  mm, and  $R_{p_2} = 8.392$  mm. The center thickness was measured at  $t_C = 1.498$  mm using a Lumetrics OptiGauge system.

Table 2.4: Group refractive indices for saline solution and lens substrates at the sodium d-line ( $\lambda_{Na} = 589.3$  nm) and near the central wavelength of the Leica Microsystems OCT system ( $\lambda_{OCT} = 880$  nm).

Material	$n_g(\lambda_{Na})$	$n_g(\lambda_{OCT})$
Saline solution	1.33520	$n_s = 1.33865$
Aspheric lens (L-BAL35)	1.58905	$n_\ell = 1.59653$
Toric lens (PMMA)	1.49110	$n_\ell = 1.49449$

### 2.3.3 Refractive Index

Throughout this thesis, we use the notation  $n_s$  and  $n_\ell$  to refer to the refractive index of the saline and the lens, respectively. Specifically, these values represent the group refractive index of the relevant material at the imaging wavelength. By fitting published refractive index data from [14, 74] to the Conrady dispersion model

$$n_p(\lambda) = n_0 + \frac{A}{\lambda} + \frac{B}{\lambda^{3.5}},$$

the absolute phase refractive index for each lens medium can be written as a function of vacuum wavelength [13].<sup>xiii</sup> The group refractive index is then given by

$$n_g(\lambda) = n_p(\lambda) - \lambda \cdot n'_p(\lambda),$$

which follows from the relationship between phase velocity and group velocity [11, Ch. 1]. Table 2.4 shows the group refractive indices for the saline solution and the two lenses at 880 nm (roughly the central wavelength of the Envisu), as well as 589.3 nm (the sodium d-line).<sup>xiv</sup>

---

<sup>xiii</sup>The saline solution in which the lenses were suspended during imaging is a proprietary contact lens packaging solution whose refractive index was provided to us by the manufacturer.

<sup>xiv</sup>We did not compute the refractive indices ourselves. Both calculations were carried out by Leica.

## 2.4 Synthetic Data & Quantization Error

In this chapter, we have discussed a number of potential sources of measurement error in point cloud data obtained from OCT. These can be divided into two main categories: data acquisition error and image segmentation error. Sources of data acquisition error include misalignment of the CT axis and the lens’ optical axis, warping caused by refraction at surface boundaries within the sample, spatial variations due to the internal optical components of the OCT probe, digital compression and quantization of signal strength (*e.g.*, pixel intensity), and pixel quantization of the image plane. Segmentation error can be caused by fluctuations in pixel intensity due to background noise, areas of over- and under-saturation due to reflections and scattering, and variations in surface boundary thickness. Some of the error introduced at this stage is mitigated by outlier removal; however, the success of the outlier removal algorithm can vary widely depending on the quality of the data and the shape of the surface, and at best only results in further loss of data.

Registration of the B-scans to a common reference point is unnecessary, since we are imaging a stationary lens and may safely assume that the position of the lens remains fixed with respect to the scan vertex throughout the entire data collection process. In the case of off-axis imaging, identification of the lens vertex does not affect the surface reconstruction. Re-alignment (addressed in Chapter 5) is only necessary for the final meridional curvature calculations and algorithm validation against the design specifications. Dewarping of the back lens surface due to refraction at the front surface boundary is handled during the fitting process, and will be the subject of Chapter 4. (Refraction effects are neglected in Chapter 3, as they do not affect results for the front surface itself.) Errors due to the internal mechanics of the probe are corrected in pre-processing using the model and specifications provided to us by the manufacturer, as discussed in Section 2.2.4.

As we lack detailed insight into the specifics of the segmentation algorithm, the “noise” discussed throughout this thesis will refer to any error remaining in the point cloud data after segmentation and outlier removal. The exact nature of the noise due to segmentation error can vary from data set to data set, so it is difficult to build a single noise model for this application. Furthermore, the variance of the noise in good segmentation results is generally quite small. Given that pixel quantization is both unavoidable and straightforward to model, quantization error is the only type of noise we have chosen to account for in the synthetic data for Chapters 3–4.

The combined error in the OCT data due to both measurement *and* 3D model selection is addressed in Appendix B. The impact of this error will be discussed in Chapter 6.

### 2.4.1 Simulation of Surface Data

In order to evaluate the performance of 3D surface fitting and refraction correction algorithms in the absence of instrument mis-calibration, off-axis imaging (*i.e.*, the center of the scan pattern does not align with the lens' axis of symmetry), or segmentation failures, Chapters 3 and 4 will deal only with synthetic data based on the specified design parameters and the refractive indices given in Tables 2.4. The synthetic data sets were constructed by sampling the design equations (2.5–2.6) at all the points  $\mathfrak{X}_i$  in the sample grid  $S$  that fall within the specified diameters from Tables 2.2–2.3 (*i.e.*,  $\varnothing_T$  for both surfaces of the aspheric lens, and  $\varnothing_{T_a}$  and  $\varnothing_{T_p}$  for the anterior and posterior surfaces of the toric lens, respectively). To validate the dewarping algorithm described in Section 4.2.2, optical distortion can be added to the back surface following the protocol developed in Section 4.3.

To simulate quantization, the axial coordinate is rounded to the closest “pixel” position. Thus, the quantized synthetic data point  $(\mathfrak{X}_i, w_i^*)$  is given by

$$w_i^* = \Delta'_z \cdot \text{round}(w_i / \Delta'_z),$$

where  $w_i$  is the non-quantized data point (after warping, if applicable) and  $\Delta'_z = 5.6 \times 10^{-3}$  mm is the vertical distance between the samples after correcting the OPL for the first surface (as described in Section 2.3). Figures 2.13–2.14 show examples of corresponding frames of synthetic and real data for both lenses<sup>xv</sup>. For convenience, the design equations have been vertically translated so that the maximum  $z$ -value of the front surface is roughly the same as for the real data. This translation does not impact our results.

### 2.4.2 Distribution of Quantization Error

Since the adjusted vertical pixel spacing is  $\Delta'_z = 5.6 \times 10^{-3}$  mm, pixel quantization introduces a measurement error of up to  $\pm 2.8 \times 10^{-3}$  mm in any individual data point

---

<sup>xv</sup>Correspondence between frames of the synthetic data and OCT data for the toric lens (in Figure 2.14) was determined by identifying the correct principal directions for the real OCT lens data as discussed in Section 5.2.3.

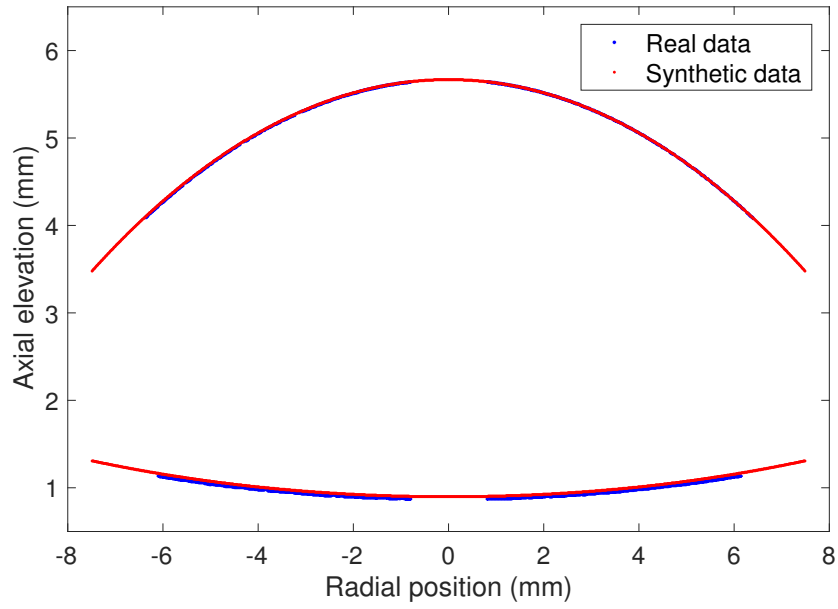


Figure 2.13: Real point cloud data from OCT and synthetic point cloud data generated from the design equations for the aspheric lens.

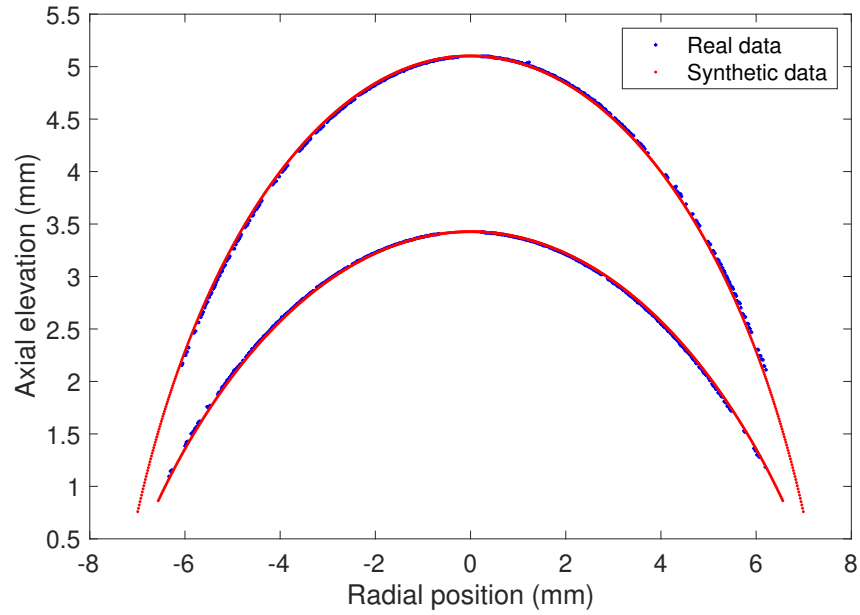


Figure 2.14: Real point cloud data from OCT and synthetic point cloud data generated from the design equations for the toric lens.

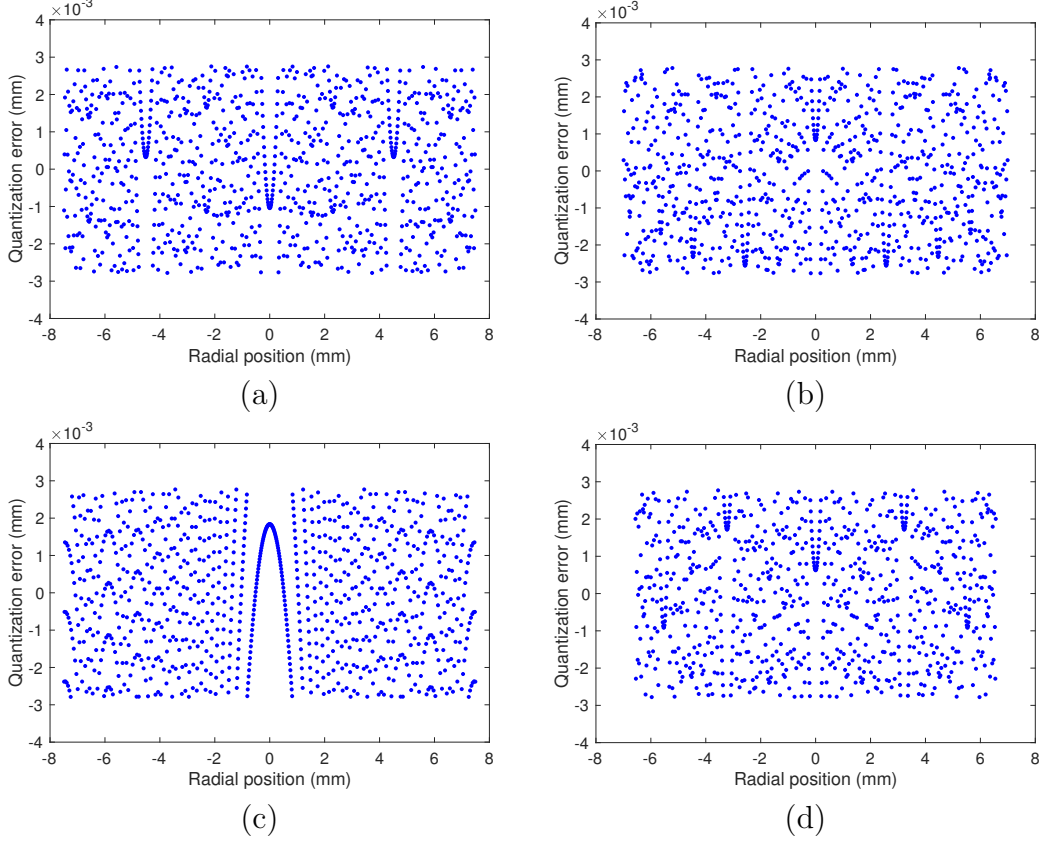


Figure 2.15: Quantization error in the first frame of synthetic data for the (a) front of the aspheric lens, (b) front of the toric lens, (c) back of the aspheric lens after warping, and (d) back of the toric lens after warping.

$w_i$ . We will designate the *signed error* due to quantization by

$$\epsilon_i^* = w_i^* - w_i.$$

Figure 2.15 illustrates the signed quantization error in the first frame of synthetic data for all four lens surfaces when we account for warping of the posterior surface due to refraction. It is important to note that the error introduced by quantization of the synthetic data is *not* independent and identically distributed (iid).

Assuming the true<sup>xvi</sup> position  $w_i$  of the surface boundary is equally likely to fall anywhere within the interval  $(w_i^* - \frac{1}{2}\Delta'_z, w_i^* + \frac{1}{2}\Delta'_z)$ , the quantization error should also

---

<sup>xvi</sup>Or the apparent position, if warping has occurred.

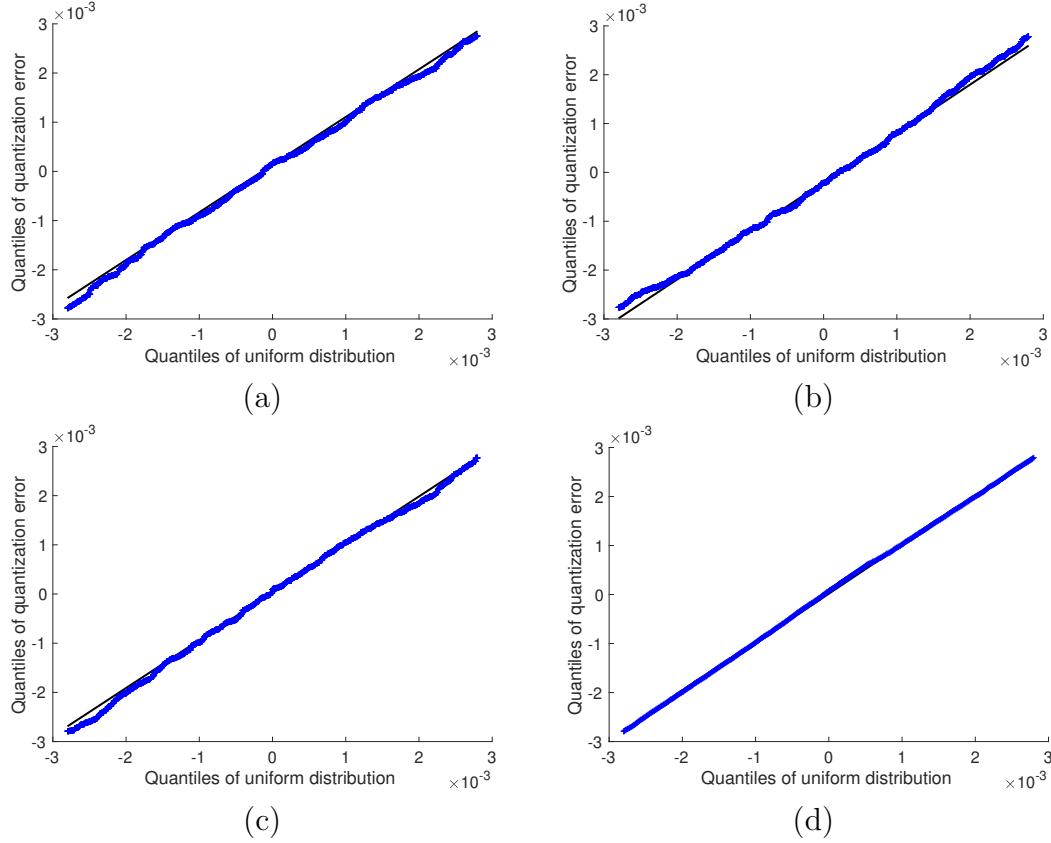


Figure 2.16: Q-Q plots of the quantization error in the synthetic data versus the uniform distribution, for the (a) front of the aspheric lens, (b) front of the toric lens, (c) back of the aspheric lens after warping, and (d) back of the toric lens after warping.

follow the uniform distribution  $\epsilon_i^* \sim \mathcal{U}\left(-\frac{1}{2}\Delta'_z, \frac{1}{2}\Delta'_z\right)$ .<sup>xvii</sup> The quantile-quantile (Q-Q) plots in Figure 2.16 demonstrate that this is indeed the case for the synthetic data for all four surfaces (recall that  $\frac{1}{2}\Delta'_z = 2.8 \times 10^{-3}$  mm).

<sup>xvii</sup>For the back surface of the aspheric lens (*i.e.*, the flat plane), this assumption is only valid if we account for warping due to refraction. In the unwarped case, the true position of the surface—and therefore also the distribution of the quantization error—is constant rather than uniform.

# Chapter 3

## Single-Surface Lens Model

### 3.1 Zernike Polynomial Interpolation

Originally proposed by physicist Frits Zernike in 1934 [108], the Zernike circle polynomials are a complete set of polynomials that are orthogonal on the unit disk and represent optimally balanced aberrations with minimum variance from a unit sphere [24, 53]. Due to their unique properties, Zernike polynomials are extremely popular within the fields of optics and optical engineering for modeling wavefront error [11, 24, 63, 101]. They are also considered the standard method for describing corneal aberrations, as detailed in the ANSI American National Standard for Ophthalmics for Reporting Optical Aberration in Eyes (ANSI Z80.28-2017) [6].

*Optical Shop Testing* by Daniel Malacara [53] is widely viewed as the definitive reference manual on the background and application of Zernike polynomials. The mathematical properties of Zernike polynomials are explored in greater depth in Max Born and Emil Wolf's classic textbook *Principles of Optics* [11], as well as Gregory Gbur's *Mathematical Methods for Optical Physics and Engineering* [24]. In addition to the ANSI standard mentioned above, we will also be borrowing conventions and notation from Malacara, Born and Wolf, and Gbur.

### 3.1.1 Background

The normalized Zernike polynomial of *radial index*  $n$  and *meridional index*  $m$  is given by

$$Z_n^m(\rho, \theta) = \begin{cases} \mathcal{N}_n^m R_n^{|m|}(\rho) \cos m\theta, & m \geq 0 \\ -\mathcal{N}_n^m R_n^{|m|}(\rho) \sin m\theta, & m < 0 \end{cases}, \quad (3.1)$$

where  $n$  is a non-negative integer,  $m$  is an integer such that  $-n \leq m \leq n$  and  $m \equiv n \pmod{2}$ , and  $\mathcal{N}_n^m$  is a normalization constant. The radial polynomials  $R_n^m$  are a special case of Jacobi polynomials and can be written in closed form as

$$R_n^m(\rho) = \sum_{k=0}^{\frac{n-m}{2}} \frac{(-1)^k (n-k)!}{k! \left(\frac{n+m}{2} - k\right)! \left(\frac{n-m}{2} - k\right)!} \rho^{n-2k}. \quad (3.2)$$

The radial index  $n$  also determines the *order* of the Zernike polynomial [6]. The polynomials are illustrated in Figure 3.1.

There are different conventions for normalizing the Zernike polynomials. In keeping with the ANSI standard, we have chosen  $\mathcal{N}_n^m = \sqrt{\frac{2(n+1)}{1+\delta_{m0}}}$  (where  $\delta_{ij}$  denotes the Kronecker delta) so that the orthogonality relation for the sequence can be written as

$$\langle Z_n^m, Z_{n'}^{m'} \rangle := \frac{1}{\pi} \int_0^{2\pi} \int_0^1 Z_n^m(\rho, \theta) Z_{n'}^{m'}(\rho, \theta) \rho d\rho d\theta = \delta_{mm'} \delta_{nn'}. \quad (3.3)$$

As Jacobi polynomials, the radial polynomials are orthogonal for fixed  $m$  under the inner product

$$\langle R_n^m, R_{n'}^m \rangle := 2(n+1) \int_0^1 R_n^m(\rho) R_{n'}^m(\rho) \rho d\rho = \delta_{nn'},$$

whereas orthogonality for the angular part is readily illustrated by the properties

$$\begin{aligned} \frac{1}{\pi} \int_0^{2\pi} \cos m\theta \cos m'\theta d\theta &= (1 + \delta_{m0}) \delta_{mm'}, & (m, m' \geq 0) \\ \frac{1}{\pi} \int_0^{2\pi} \sin m\theta \sin m'\theta d\theta &= \delta_{mm'}, & (m, m' < 0) \\ \frac{1}{\pi} \int_0^{2\pi} \sin m\theta \cos m'\theta d\theta &= 0. \end{aligned}$$

The first few Zernike polynomials are listed in Table 3.1, along with the corresponding

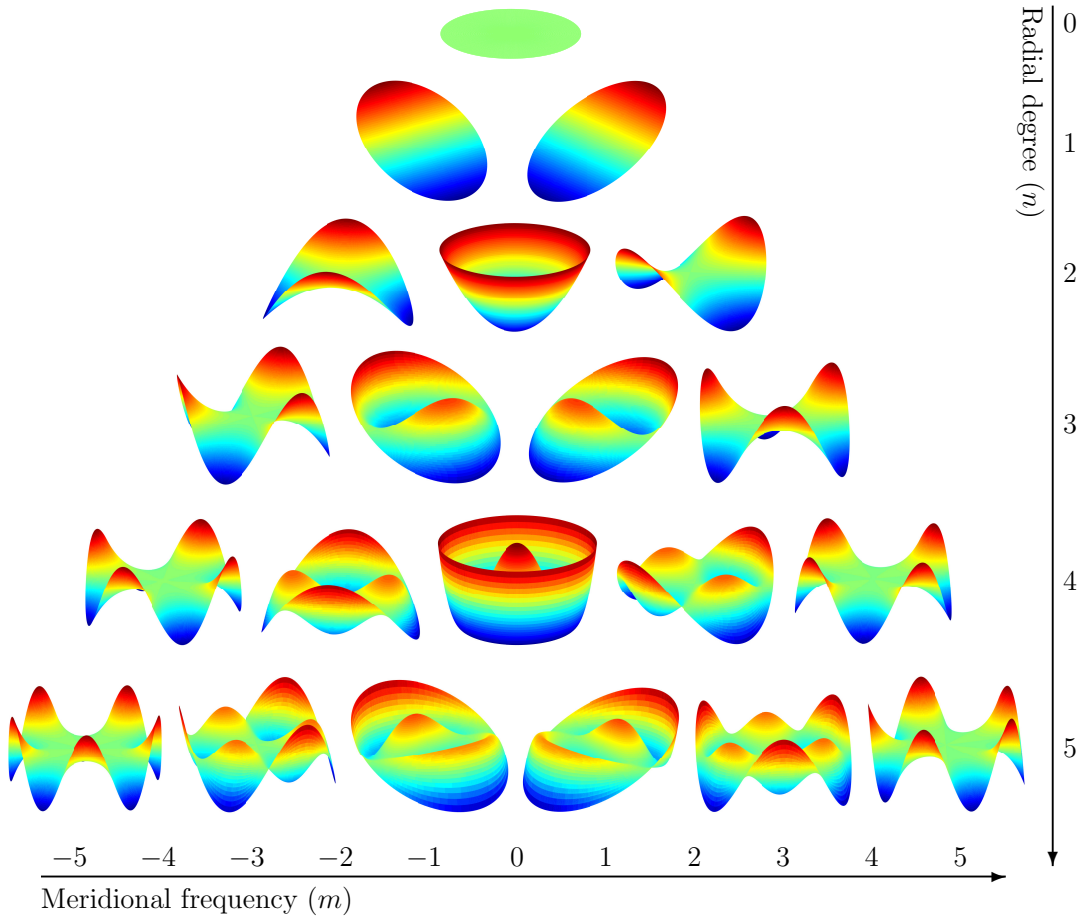


Figure 3.1: Visual representation of Zernike polynomials from (3.1).

name of the aberration described. The table also illustrates the relationship between the dual-index ordering system  $(n, m)$  and a single-indexing system  $(j)$  proposed by Robert Noll in [64], which assigns even indices to the polynomials with a symmetric  $\cos(m\theta)$  part, and odd indices to the antisymmetric  $\sin(m\theta)$  polynomials.<sup>i</sup> In this thesis, we will refer to the individual Zernike polynomials using Noll's indices, although other single-indexing systems do exist (*e.g.*, see [6]). A longer list of Zernike polynomials can be found in Appendix A.

---

<sup>i</sup>Functions with azimuthal index  $m = 0$  may have an even or an odd index under Noll's ordering scheme.

Table 3.1: Table of normalized Zernike polynomials with their corresponding aberration names ordered according to Noll's single indexing system  $j$  [6, 64].

j	n	m	$Z_j(\rho, \theta)$	Aberration Name
1	0	0	1	Piston
2	1	1	$2\rho \cos \theta$	Horizontal tilt
3	1	-1	$2\rho \sin \theta$	Vertical tilt
4	2	0	$\sqrt{3}(2\rho^2 - 1)$	Defocus
5	2	-2	$\sqrt{6}\rho^2 \sin 2\theta$	Astigmatism (oblique)
6	2	2	$\sqrt{6}\rho^2 \cos 2\theta$	Astigmatism
7	3	-1	$\sqrt{8}(3\rho^3 - 2\rho) \sin \theta$	Vertical coma
8	3	1	$\sqrt{8}(3\rho^3 - 2\rho) \cos \theta$	Horizontal coma
9	3	-3	$\sqrt{8}\rho^3 \sin 3\theta$	Vertical trefoil
10	3	3	$\sqrt{8}\rho^3 \cos 3\theta$	Oblique trefoil
11	4	0	$\sqrt{5}(6\rho^4 - 6\rho^2 + 1)$	Spherical
12	4	2	$\sqrt{10}(4\rho^4 - 3\rho^2) \cos 2\theta$	Secondary astigmatism
13	4	-2	$\sqrt{10}(4\rho^4 - 3\rho^2) \sin 2\theta$	Secondary astigmatism (oblique)
14	4	4	$\sqrt{10}\rho^4 \cos 4\theta$	Quatrefoil
15	4	-4	$\sqrt{10}\rho^4 \sin 4\theta$	Quatrefoil (oblique)

### 3.1.2 Zernike Expansion

A function  $z = f(\rho, \theta)$  that is continuous for all  $|\rho| \leq A$ —and whose norm according to the inner product in (3.3) is finite—can be expressed within the disk of radius  $A$  as a linear combination of Zernike polynomials. Using Noll's single indexing system for notational simplicity, the generalized Fourier series of  $f$  in terms of the Zernike polynomials is given by

$$f(A\rho, \theta) = \sum_{j=1}^{\infty} c_j Z_j(\rho, \theta), \quad (3.4)$$

where  $\rho \in [0, 1]$  and  $\theta \in [0, 2\pi]$ . The coefficients  $c_j$  are given explicitly by

$$c_j = \langle f, Z_j \rangle = \frac{1}{\pi} \int_0^{2\pi} \int_0^1 f(A\rho, \theta) Z_j(\rho, \theta) \rho d\rho d\theta. \quad (3.5)$$

The  $N^{\text{th}}$  order truncation of (3.4) includes all polynomials of radial index less than or equal to  $N$  (for a total of  $\frac{1}{2}(N+1)(N+2)$ ), and is given by

$$f_N(A\rho, \theta) = \sum_{j=1}^p c_j Z_j(\rho, \theta), \quad p = \frac{1}{2}(N+1)(N+2). \quad (3.6)$$

Since  $f_N$  converges to  $f$  as  $N \rightarrow \infty$ , we will often find it convenient to drop the subscript notation for the truncation. Even in this case,  $f$  should always be understood to imply a finite Zernike expansion, whereas the exact surface described by the design equation will be denoted by  $z$ .

### 3.1.3 General Lens Model

In terms of the  $N^{\text{th}}$  order Zernike expansion in (3.6), our goal is to fit the lens surface data  $(\mathfrak{X}_i, w_i)$  using the model

$$w_i = f(\mathfrak{X}_i, c) = \sum_{j=1}^p c_j Z_j(\mathfrak{X}_i'), \quad (3.7)$$

where  $w_i$  is the observed value of the surface height at the lateral coordinate  $\mathfrak{X}_i$  based on the point cloud data, and  $c = [c_1, \dots, c_p]^T$  are the Zernike coefficients. The grid points  $\mathfrak{X}_1, \dots, \mathfrak{X}_s$  comprise the subset  $S_A$  of the full sample grid  $S$  (defined in Section 2.2.3) that falls within the disk of a specified radius  $A$ . That is,

$$S_A = \{\mathfrak{X} = (\rho, \theta) \in S \mid |\rho| \leq A\}.$$

The corresponding values  $\mathfrak{X}'_1, \dots, \mathfrak{X}'_s$  are normalized by a factor of  $A$  to comply with the Zernikes' unit circle domain:

$$S'_A = \{\mathfrak{X}' = (\rho/A, \theta) \mid (\rho, \theta) \in S_A\}.$$

Note that the Zernikes also require  $\rho \geq 0$ . Thus, points  $(\rho, \theta)$  in  $S_A$  (or  $S'_A$ ) where  $\rho < 0$  will be mapped to  $(-\rho, \theta + \pi)$ .

Due to the linearity of the Zernike expansion, (3.7) can be written more compactly in matrix form as

$$w = Xc, \quad (3.8)$$

where  $w = [w_1, \dots, w_s]^T$  is the point cloud data and  $X$  is the design matrix consisting of the Zernike polynomials evaluated on  $S'_A$ :

$$X = \begin{bmatrix} Z_1(\mathfrak{X}'_1) & Z_2(\mathfrak{X}'_1) & \cdots & Z_p(\mathfrak{X}'_1) \\ \vdots & \vdots & & \vdots \\ Z_1(\mathfrak{X}'_s) & Z_2(\mathfrak{X}'_s) & \cdots & Z_p(\mathfrak{X}'_s) \end{bmatrix}. \quad (3.9)$$

## 3.2 Synthetic Data for Single-Surface Model

In this chapter, we are primarily concerned with ensuring that the Zernike polynomial model (3.7) is an appropriate representation of the four lens surfaces (front and back of the aspheric and toric lenses) described in Section 2.3. To validate the model, we will use synthetic data constructed by sampling the design equation  $z(\mathfrak{X})$  for each surface at the points  $\mathfrak{X}_i \in S_A$ , where  $A$  is derived from the relevant diameter listed in Tables 2.2–2.3. Warping of the back surfaces due to refraction is neglected here (this will be addressed separately in Chapter 4). Thus, the non-quantized synthetic data points  $(\mathfrak{X}_i, w_i)$  are given by

$$w_i = z(\mathfrak{X}_i),$$

while the quantized points  $(\mathfrak{X}_i, w_i^*)$  mimic an adjusted vertical pixel spacing of  $\Delta'_z = 5.6 \times 10^{-3}$  mm according to the formula

$$w_i^* = \Delta'_z \cdot \text{round}(w_i / \Delta'_z),$$

as described in Section 2.4.1.

### Surface 1 (Asphere)

Surface 1 corresponds to the design equation for the front surface of the aspheric lens:

$$z(\rho, \theta) = \frac{-\rho^2}{R_a \left( 1 + \sqrt{1 - (1 + \kappa) \frac{\rho^2}{R_a^2}} \right)} - a_4 \rho^4 - a_6 \rho^6 - a_8 \rho^8 - a_{10} \rho^{10}, \quad |\rho| \leq A, \quad (3.10)$$

where  $A = 7.5$  mm (half of the 15 mm lens diameter) and the principal radius of curvature is  $R_a = 13.225$  mm. The remaining parameters  $\kappa$ ,  $a_4$ ,  $a_6$ ,  $a_8$ , and  $a_{10}$  can be found in Table 2.2. The number of points on the sample grid that fall within the radius  $A$  is  $s = 112440$ .

### Surface 2 (Plane)

Surface 2 corresponds to the back of the aspheric lens, which is the flat plane

$$z(\rho, \theta) = 0, \quad |\rho| \leq A. \quad (3.11)$$

The domain is again restricted to the disk with radius  $A = 7.5$  mm. As with Surface 1, the number of sample points is  $s = 112440$ .

### Surface 3 (Sphere)

Surface 3 corresponds to the design equation for the front of the toric lens, which follows the outer surface of a sphere of radius  $R_a = 7.8$  mm:

$$z(x, y) = \sqrt{R_a^2 - x^2 - y^2}, \quad \sqrt{x^2 + y^2} \leq A. \quad (3.12)$$

Restricting the domain to the disk of radius  $A = 7$  mm means there are  $s = 105000$  sample points for this surface.

### Surface 4 (Torus)

Surface 4 corresponds to the design equation for the back of the toric lens. This is the cap from the spindle torus, given by

$$z(x, y) = \sqrt{\left(R_{p_1} - R_{p_2} + \sqrt{R_1^2 - y^2}\right)^2 - x^2}, \quad \sqrt{x^2 + y^2} \leq A, \quad (3.13)$$

where  $R_{p_1} = 9.2$  mm is the maximum radius of curvature and  $R_{p_2} = 8.4$  mm is the minimum principal radius of curvature. The radius of the disk specifying the domain is  $A = 6.5723$  mm. There are  $s = 98520$  sample points contained within this domain.

Note that some amount of vertical translation is required in order to align the surfaces with the dewarped lens data for the sake of presentation. This adjustment is not reflected in the design equations (3.10–3.13) presented here, but it should not impact the results discussed in Section 3.5.

### 3.3 Coefficient Estimation & Surface Reconstruction

To estimate the Zernike coefficients  $c$  in (3.7) and (3.8), we want to find the values  $\hat{c}$  that minimize the model residual in the least squares sense. In other words, we must solve

$$\hat{c} = \arg \min_c \|w - Xc\|^2. \quad (3.14)$$

This is achieved using Moore-Penrose pseudoinverse of  $X^+$ , which is frequently defined in terms of the normal equations:

$$\hat{c} = X^+w = (X^T X)^{-1} X^T w.$$

The value  $\hat{c}$  is also referred to as the ordinary least squares (OLS) solution to (3.14) [58, Ch. 5].

Although the Zernike polynomials are orthogonal over the continuous domain enclosed by the unit disk, neither orthogonality nor completeness is guaranteed for an arbitrary set of discrete data points [53]. Even with oversampling, the hexapolar sampling pattern comprising  $S_A$  contains redundancy at the vertex when the number of A-scans is odd. This is critical to image registration but could cause  $X^T X$  to be ill-conditioned if the number of samples  $s$  is too small. We can mitigate this effect somewhat by ensuring that  $s \gg p$  [104]. The highest order Zernike expansion we will consider is  $N = 20$  (which has  $p = 231$  basis functions), whereas  $s$  ranges from 98,520 to 112,440 for the synthetic data discussed in this chapter. As for the actual lens data discussed in Chapters 5 and 6, after accounting for segmentation failures, cropping, and omission of frames with poor segmentation results, we are left with  $s > 30,000$  in even the worst case.

The maximum condition number for any of the design matrices used in this chapter is only  $\kappa(X^T X) \approx 22$ , so theoretically we could obtain  $\hat{c}$  using the normal equations in (3.14). However, the uneven distribution of valid data points in the real OCT data can cause the condition number of  $X^T X$  to be quite large even when  $s \gg p$ . Therefore, we will rely on a numerically stable method of obtaining  $X^+$  that does not involve forming the product  $X^T X$ . The results presented in this thesis are obtained using the MATLAB backslash command (“\”, or `mldivide.m`), which generally solves dense overdetermined systems using a QR decomposition with partial pivoting.

Figure 3.2 depicts surface reconstructions based on the  $N^{\text{th}}$  order Zernike interpolating

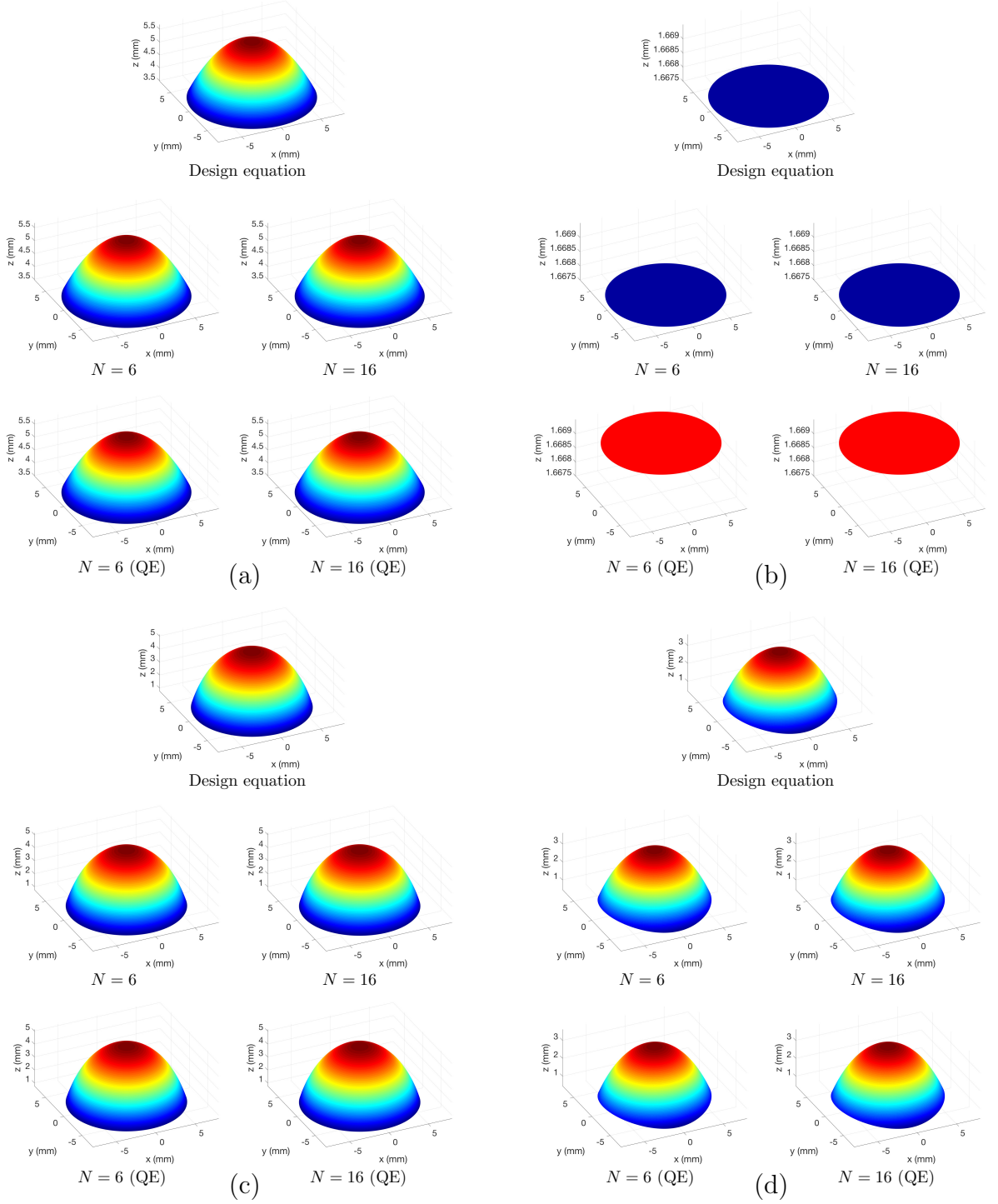


Figure 3.2: Surface reconstructions using an  $N^{\text{th}}$  order Zernike fit to synthetic data without noise and with quantization error (QE) for (a) Surface 1, (b) Surface 2, (c) Surface 3, and (d) Surface 4.

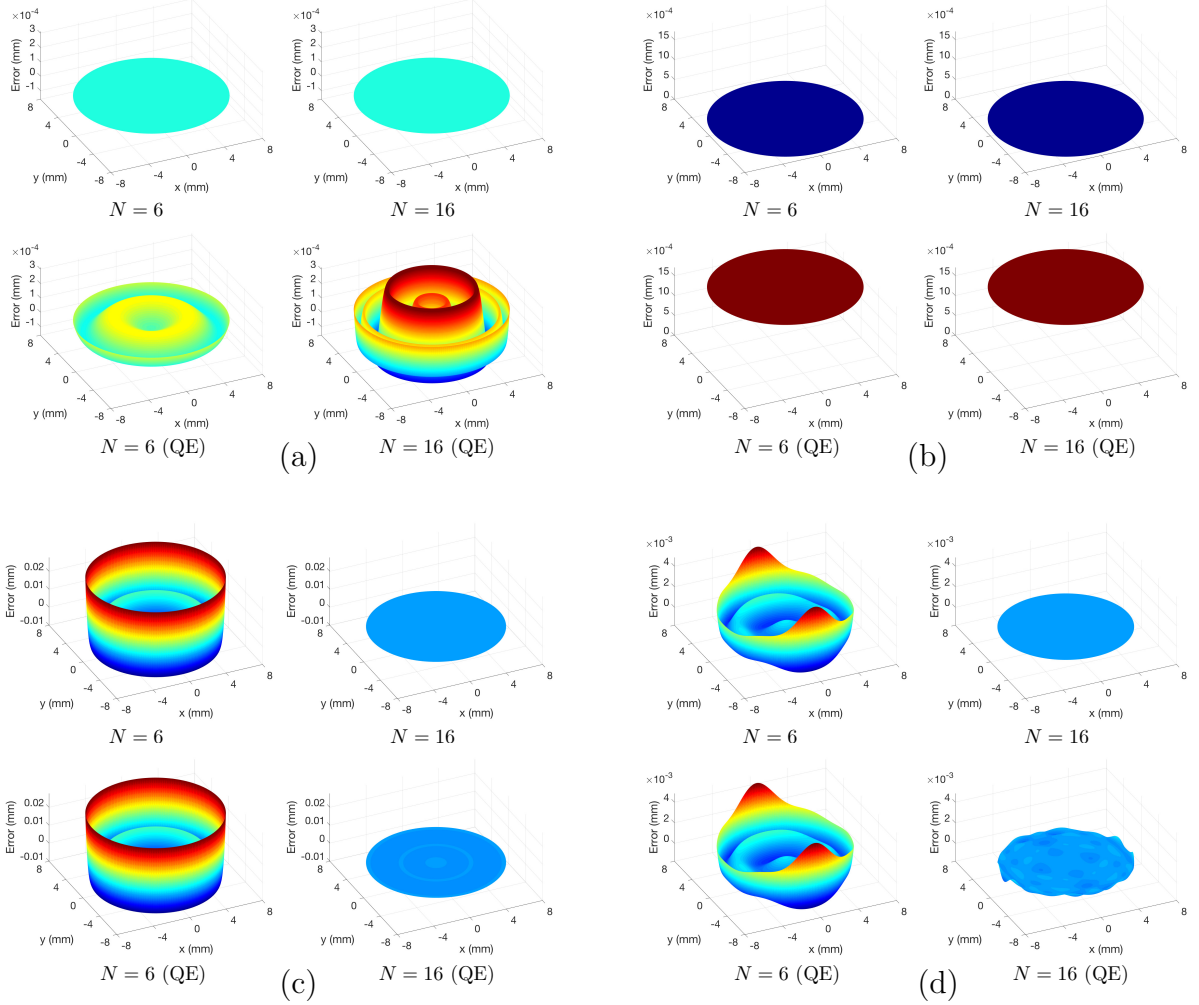


Figure 3.3: Surface error for Zernike fits in Figure 3.2 for (a) Surface 1, (b) Surface 2, (c) Surface 3, and (d) Surface 4.

polynomial  $f_N(\mathbf{x}, c)$ , for orders  $N = 6$  ( $p = 28$  polynomials) and  $N = 16$  ( $p = 153$  polynomials) to the synthetic data described in Section 3.2, alongside the exact surface from the design equation. Fits are provided for both synthetic data without noise and synthetic data with added quantization error (indicated by “QE”). Maps of the error between each Zernike model and the design equation are shown in Figure 3.3.

It is apparent that most of the time the additional terms in the Zernike expansion improve the accuracy of the fit for both the non-quantized and quantized data sets. The exception is Surface 1 (the aspheric surface, shown in Figure 3.3a) when quantization

error is present. In this case, the 16<sup>th</sup> order expansion clearly results in oscillations that do not occur when  $N = 6$ . Overfitting of this nature becomes an even greater concern in real OCT data, which is likely to have significantly more noise due to measurement and segmentation error.

### 3.4 Curvature Mapping

Once we have identified the optimal Zernike fit for our surface data, our objective is to use this model to generate accurate maps of local curvature. We are especially interested in determining the principal radii of curvature of the surface.

In Section 2.1, we defined the meridional curvature relative to the meridians through the  $z$ -axis as the partial derivative of a surface function  $z(\rho, \theta)$  with respect to  $\rho$ . In terms of the Zernike expansion  $z \approx f(\rho, \theta)$ , this becomes

$$k(\rho, \theta) \approx \frac{\left(-f_{\rho\rho}(\rho, \theta)\right)}{\left(1 + \left(f_{\rho}(\rho, \theta)\right)^2\right)^{3/2}}. \quad (3.15)$$

The principal radii of curvature  $R_1$  and  $R_2$  are the extrema of the reciprocal of (3.15) evaluated at the vertex  $\rho = 0$ :

$$R_1 \approx \max_{\theta \in [0, \pi)} \frac{\left(1 + \left(f_{\rho}(0, \theta)\right)^2\right)^{3/2}}{\left(-f_{\rho\rho}(0, \theta)\right)}, \quad R_2 \approx \min_{\theta \in [0, \pi)} \frac{\left(1 + \left(f_{\rho}(0, \theta)\right)^2\right)^{3/2}}{\left(-f_{\rho\rho}(0, \theta)\right)}. \quad (3.16)$$

If  $R_1 = R_2$ , this implies that  $f$  has continuous rotational symmetry, and we denote the principal radius of curvature simply by  $R$ .<sup>ii</sup>

The easiest way to obtain the partial derivatives in (3.15) is via a finite difference method. Using centered finite differences with step size  $h$  for both the first and second

---

<sup>ii</sup>Note that we can restrict  $\theta$  to the interval  $[0, \pi)$  because the continuity of the first and second derivatives ensures that  $k(0, \theta) = k(0, \theta + \pi)$ .

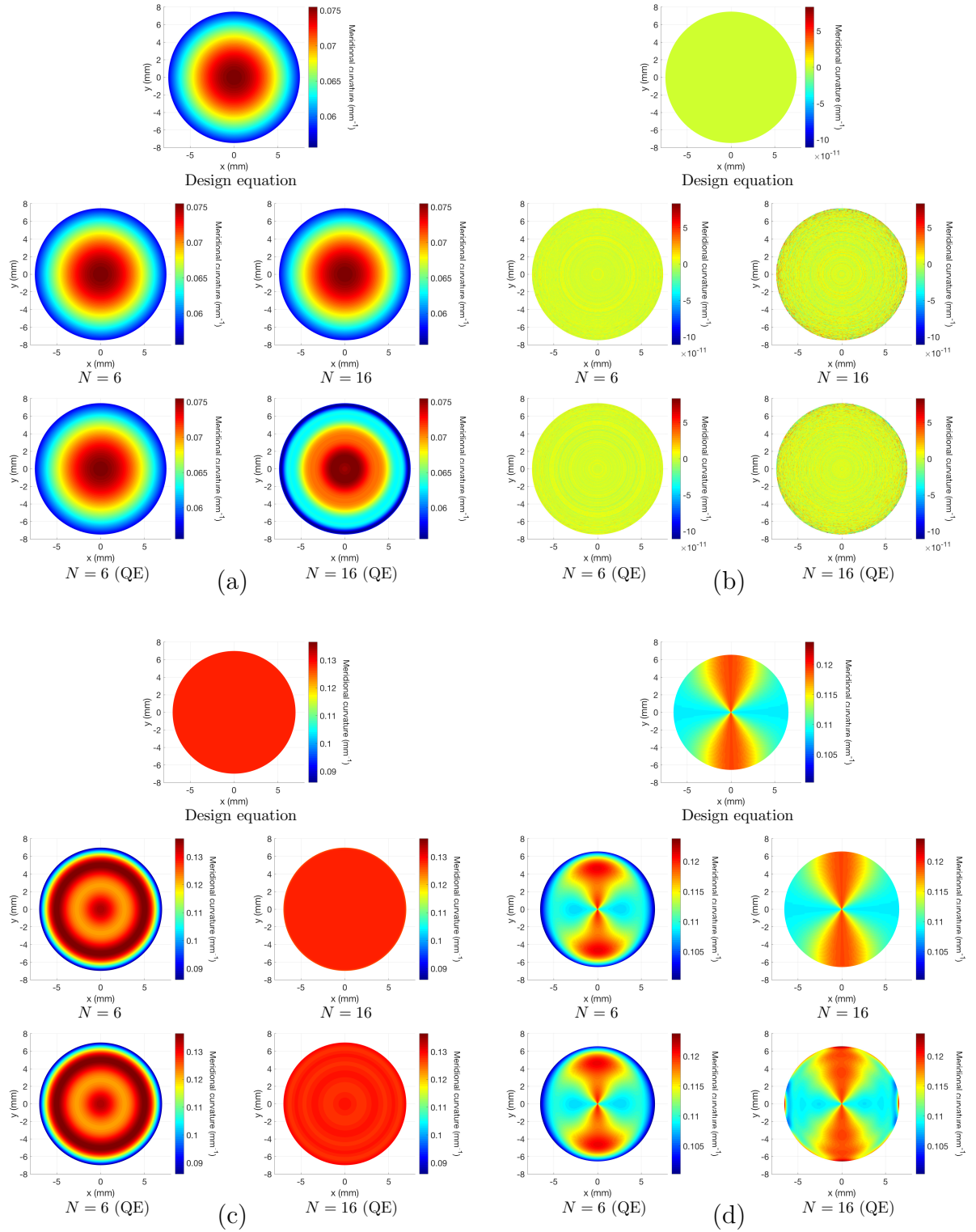


Figure 3.4: Meridional curvature maps for (a) Surface 1, (b) Surface 2, (c) Surface 3, and (d) Surface 4.

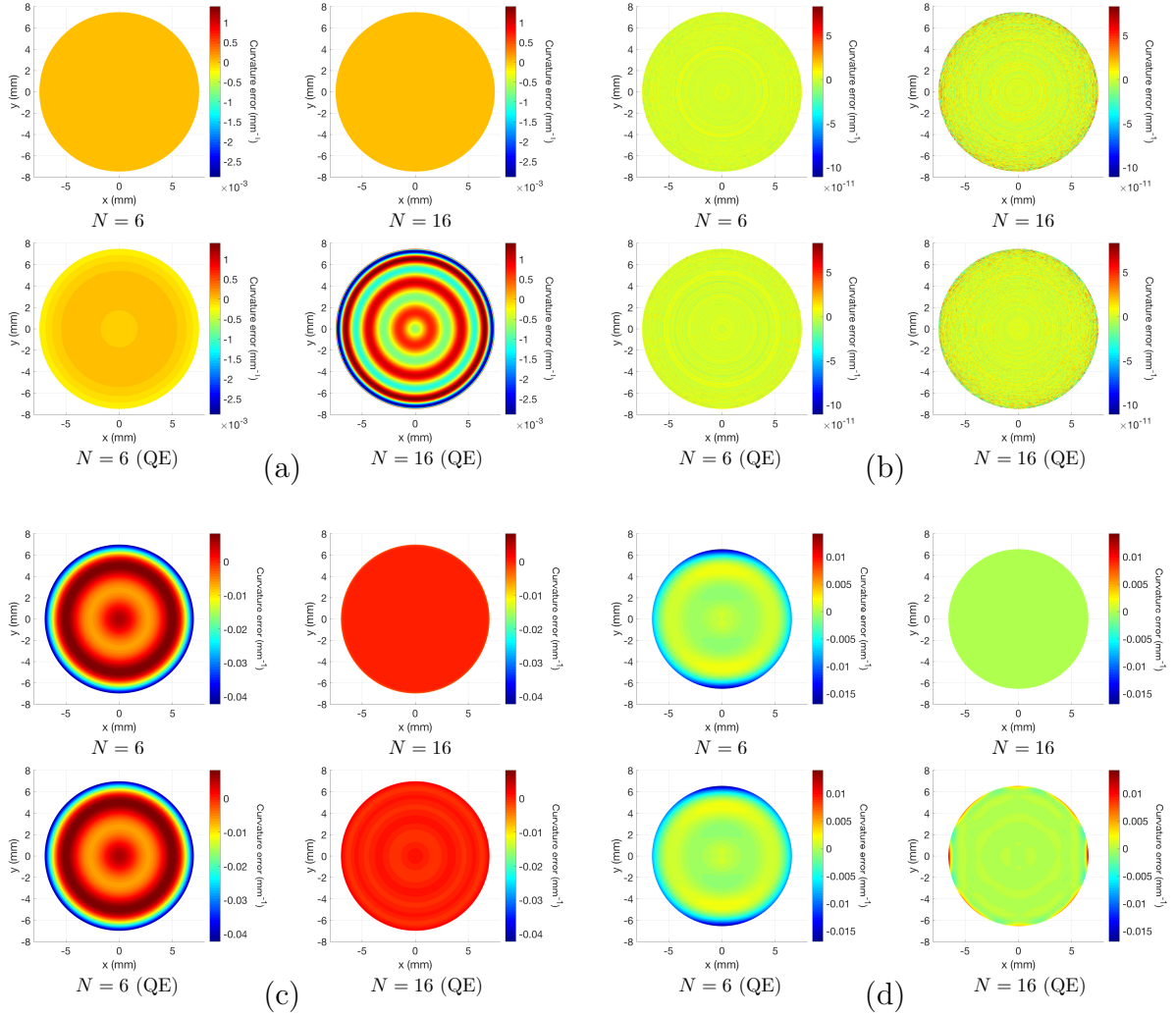


Figure 3.5: Error for curvature maps in Figure 3.4 for (a) Surface 1, (b) Surface 2, (c) Surface 3, and (d) Surface 4.

derivative, the estimated meridional curvature  $\hat{k}$  can be expressed in discretized form as

$$\hat{k}(\rho, \theta) = - \frac{\left( \frac{f(\rho+h, \theta) - 2f(\rho, \theta) + f(\rho-h, \theta)}{h^2} \right)}{\left( 1 + \left( \frac{f(\rho+h, \theta) - f(\rho-h, \theta)}{2h} \right)^2 \right)^{3/2}}. \quad (3.17)$$

For convenience—and to parallel the surface model validation—we will be validating (3.17) at the points  $(\rho, \theta) \in S_A$  for which  $|\rho| < A$ . (As long as the step size  $h$  is no

greater than the distance between the data points  $\Delta_\rho$ , the exclusion of points where  $|\rho| = A$  ensures that the central difference method does not require evaluating  $f$  outside its domain.) However, we should note that if  $f$  is in fact a suitable model for our data, (3.17) should be valid for any arbitrary point  $(\rho, \theta)$  such that  $|\rho| \leq A - h$ .

Evaluating the reciprocal of (3.17) at all the points in  $S_A$  where  $\rho = 0$  yields a discretized solution for the meridional radius of curvature at the vertex as a function of the meridian  $\theta_k$ :

$$\hat{R}(\theta_k) \equiv \frac{1}{\hat{k}(0, \theta_k)} = - \frac{\left(1 + \left(\frac{f(h, \theta_k) - f(h, \theta_k + \pi)}{2h}\right)^2\right)^{3/2}}{\left(\frac{f(h, \theta_k) - 2f(0, \theta_k) + f(h, \theta_k + \pi)}{h^2}\right)}. \quad (3.18a)$$

The estimated principal curvatures are then given by

$$\hat{R}_1 = \max_{\theta_k \in \Theta} \hat{R}(\theta_k), \quad \hat{R}_2 = \min_{\theta_k \in \Theta} \hat{R}(\theta_k), \quad (3.18b)$$

where  $\Theta$  is the meridional sample grid defined in Section 2.2.3. Note that the reparameterization  $(-h, \theta_k) \rightarrow (h, \theta_k + \pi)$  in (3.18a) ensures a nonnegative radial input.

Figure 3.4 illustrates examples of the meridional curvature maps for all four surfaces from solving (2.1) analytically for each design equation, and when using the discretized formulation shown in (3.17) with a step size of  $h = A \times 10^{-3}$  (where  $A$  is the radius of the Zernike fitting region) for the 6<sup>th</sup> and 16<sup>th</sup> order Zernike models in Figure 3.2. As before, results are shown for synthetic data without noise and with added quantization error. Plots of the local error  $\hat{k}(\mathfrak{x}_i) - k(\mathfrak{x}_i)$  corresponding to each estimate in Figure 3.4 are shown in Figure 3.5. (The true curvature  $k(\mathfrak{x})$  is obtained analytically from (2.1) and the design equations in Section 3.2.)

### 3.5 Zernike Model Validation

To assess the suitability of the Zernike model (3.7) for the four surfaces described in Section 3.2, we will consider both synthetic data with no added noise ( $\epsilon_i^* = 0$ ) and synthetic data that accounts for pixel quantization. Using the non-quantized data, we will first demonstrate that the surface fits generated from the linear least squares solution (3.14)

over the discrete data points are at least as reliable as the fits obtained from numerical integration of (3.5) using the design equations (3.10-3.13). We will then assess the limitations of the model when quantization error is present. Finally, we will look at how the modeling error for both non-quantized and quantized synthetic data affects the accuracy of the meridional curvature and principal radii of curvature calculations. Because the quantization error is neither Gaussian nor iid (as illustrated in Section 2.4.2), methods of estimating confidence intervals and sampling densities for the Zernike coefficients do not apply. Parameter estimation, model calibration, and error propagation will be addressed further in Chapter 6 in the context of Gaussian noise.

We will use the mean absolute error (MAE) as a measure of average error, in both the surface reconstruction and the meridional curvature. For the surface fit, this is just the arithmetic average of the absolute difference between the Zernike model and the design equation evaluated on the original sample grid:

$$\bar{e} = \frac{1}{s} \sum_{i=1}^s \left| f(\mathfrak{x}_i, c) - z(\mathfrak{x}_i) \right|. \quad (3.19)$$

The centered difference curvature  $\hat{k}(\mathfrak{x})$  given in (3.17) is not defined at the two end points for each of the  $b$  meridians, so we determined the MAE in the meridional curvature using the remaining  $s - 2b$  sample points:

$$\bar{e}_k = \frac{1}{s - 2b} \sum_{i=1}^{s-2b} \left| \hat{k}(\mathfrak{x}_i) - k(\mathfrak{x}_i) \right|, \quad (3.20)$$

where  $k(\mathfrak{x}_i)$  is once again the analytic curvature at  $\mathfrak{x}_i$  based on the design equation. We selected the MAE over the root mean square error (RMSE) or sum of squares error (SSE) because the MAE represents an actual tangible value of the average distance between the data points and the model. While the RMSE provides some useful information regarding the variance of the error, its interpretation is more abstract and it cannot easily be converted to other units of measurement. Furthermore, we compared the MAE to both the RMSE and the absolute maximum error for all of the synthetic data analyses presented here, and found that all three metrics led to the same interpretation of the results.

To avoid confusion, we will reserve the notation  $\bar{e}$  exclusively for the results of the linear least squares fit to synthetic data without added noise. We will use  $\bar{e}^{(i)}$  to dis-

tinguish the MAE of the surface fit when the coefficients are obtained by solving (3.5) using numerical integration, and  $\bar{e}^*$  to indicate the MAE for the least squares fit to quantized synthetic data. When this fit to the quantized data is used to calculate  $\hat{k}(\mathfrak{X})$ , the subsequent error will be denoted  $\bar{e}_k^*$ .

### 3.5.1 Model Order Selection

Clearly, the optimal model order to avoid under- or overfitting will depend on the nature of the surface we want to model. The established precedent for vision research seems to be limited to only the first 15 Zernike functions listed in Table 3.1 ( $N = 4$ ); however, this is likely just a holdover from attempting to model wavefronts using a Taylor series expansion, and not actually a referendum on best practices [34]. Moreover, while they may lack clinical significance, the additional terms become essential in the case where rotational symmetry is lost due to off-axis data collection [107].

Of the previous work we investigated that made similar use of Zernike polynomials for modeling optical surfaces, the vast majority considered model orders ranging from  $N = 4$  to  $N = 14$ . Zhao et al.—whose research laid the groundwork for the problems investigated in this thesis—specify an 8<sup>th</sup> order fit as part of their protocol for error correction and clinical parameter extraction from SDOCT detailed in [39] and [110], and the subsequent results on corneal curvature and refractive power from SDOCT presented by McNabb et al. in [55] are based on a 5<sup>th</sup> order Zernike fit. Zernike polynomials have also been used for surface reconstruction from videokeratography. Smolek and Klyce tested Zernike models up to order  $N = 14$  on a wide variety of eye conditions and determined that this was sufficient for all but the most severe corneal diseases [91]. In [88], Sicam et al. outline an approach involving 5<sup>th</sup>–10<sup>th</sup> order fits for various lens phantoms and cornea data, while Turuwhenua’s proposed improvements to this method in [102] employ 10<sup>th</sup>–14<sup>th</sup> order fits for the phantom data. Based on all these results, we decided that a maximum model order of  $N = 20$  ( $p = 231$  polynomials) would be more than adequate for our purposes.<sup>iii</sup>

In attempting to determine a protocol for automatic model order selection based on corneal height data, Iskander et al. found that the classical information theoretic methods (*i.e.*, the Akaike information criterion and corrected Akaike information criterion, the

---

<sup>iii</sup>This was also the maximum order for which we were able to calculate the Zernike coefficients using numerical integration before the computations became prohibitively expensive.

minimum description length, and the Hannan-Quinn criterion) yielded unreliable results [34]. This is due to the nature of most optical surfaces and the construction of the Zernike polynomials: even for a highly abnormal cornea, the magnitude of the Zernike coefficients decreases rapidly as the polynomial order increases. In a subsequent paper [1], Alkhaldi et al. expanded their work to investigate additional information theoretic approaches as well as resampling methods, and found that most methods either fail to impose a strong enough penalty on the higher order terms or are computationally demanding. As an alternative, they illustrated that model order selection can be accomplished through the use of the efficient detection criterion proposed in [109]. However, the success of this approach is predicated on the selection of an appropriate penalty function, which is a non-trivial task. Most recently, Muma and Zoubir proposed a robust version of the corrected Akaike information criterion based on  $\tau$  estimation [61], although this approach does not appear to have been rigorously validated.

Owing to the complicated nature of this problem, the model order selection will not be addressed in this thesis.

### 3.5.2 Discrete Fit versus Numerical Integration

Calculating the coefficients directly from (3.5) involves elliptic integrals that must be solved numerically. We used MATLAB's `integral2.m` function, which employs an adaptive quadrature method to evaluate the double integral. The discrete Zernike points comprising the design matrix  $X$  were computed in MATLAB using the `zernfun.m` function, written by MathWorks engineer Paul Fricker [22]. We then obtained the least squares estimate for the coefficients using the MATLAB backslash command.

Figure 3.6 provides a visual rendering of the MAE in the reconstruction of each surface when the Zernike coefficients are computed using numerical integration ( $\bar{e}^{(i)}$ ) as well as the discrete linear least squares fit without noise ( $\bar{e}$ ). The exact values for  $\bar{e}^{(i)}$  and  $\bar{e}$  are listed in Table 3.2. In most cases, the two methods arrive at nearly identical results. There are however some notable discrepancies, particularly in the higher model orders for Surfaces 1 and 2. These discrepancies are due to the limitations of adaptive quadrature in the presence of very high frequency oscillations like the ones that start to show up as the Zernike order increases. The reason this appears to cause problems only for Surfaces 1 and 2 is because the relative contributions from these noisy terms happen to be disproportionately greater than for Surfaces 3 and 4. By contrast, the error in

Table 3.2: MAE (in mm) of surface reconstruction when coefficients are obtained via numerical integration ( $\bar{e}^{(i)}$ ) versus OLS fit ( $\bar{e}$ ).

$N$	Surface 1		Surface 2		Surface 3		Surface 4	
	$\bar{e}^{(i)}$	$\bar{e}$	$\bar{e}^{(i)}$	$\bar{e}$	$\bar{e}^{(i)}$	$\bar{e}$	$\bar{e}^{(i)}$	$\bar{e}$
0	$6.7 \times 10^{-1}$	$5.6 \times 10^{-1}$	$2.2 \times 10^{-16}$	$8.7 \times 10^{-15}$	1.2	1.0	$8.7 \times 10^{-1}$	$7.2 \times 10^{-1}$
1	$6.7 \times 10^{-1}$	$5.6 \times 10^{-1}$	$2.2 \times 10^{-16}$	$8.7 \times 10^{-15}$	1.2	1.0	$8.7 \times 10^{-1}$	$7.2 \times 10^{-1}$
2	$6.0 \times 10^{-3}$	$4.9 \times 10^{-3}$	$5.4 \times 10^{-16}$	$4.9 \times 10^{-14}$	$1.2 \times 10^{-1}$	$9.1 \times 10^{-2}$	$4.5 \times 10^{-2}$	$3.5 \times 10^{-2}$
3	$6.0 \times 10^{-3}$	$4.9 \times 10^{-3}$	$6.2 \times 10^{-16}$	$5.6 \times 10^{-15}$	$1.2 \times 10^{-1}$	$9.1 \times 10^{-2}$	$4.5 \times 10^{-2}$	$3.5 \times 10^{-2}$
4	$5.6 \times 10^{-5}$	$4.6 \times 10^{-5}$	$2.6 \times 10^{-14}$	$4.5 \times 10^{-14}$	$2.2 \times 10^{-2}$	$1.7 \times 10^{-2}$	$4.5 \times 10^{-3}$	$3.5 \times 10^{-3}$
5	$5.6 \times 10^{-5}$	$4.6 \times 10^{-5}$	$2.6 \times 10^{-14}$	$3.2 \times 10^{-14}$	$2.2 \times 10^{-2}$	$1.7 \times 10^{-2}$	$4.5 \times 10^{-3}$	$3.5 \times 10^{-3}$
6	$3.7 \times 10^{-7}$	$3.6 \times 10^{-7}$	$2.6 \times 10^{-14}$	$4.2 \times 10^{-14}$	$5.3 \times 10^{-3}$	$4.0 \times 10^{-3}$	$5.8 \times 10^{-4}$	$4.4 \times 10^{-4}$
7	$3.7 \times 10^{-7}$	$3.6 \times 10^{-7}$	$2.6 \times 10^{-14}$	$4.0 \times 10^{-14}$	$5.3 \times 10^{-3}$	$4.0 \times 10^{-3}$	$5.8 \times 10^{-4}$	$4.4 \times 10^{-4}$
8	$2.5 \times 10^{-7}$	$2.3 \times 10^{-7}$	$2.5 \times 10^{-14}$	$2.8 \times 10^{-14}$	$1.4 \times 10^{-3}$	$1.1 \times 10^{-3}$	$8.4 \times 10^{-5}$	$6.3 \times 10^{-5}$
9	$2.5 \times 10^{-7}$	$2.3 \times 10^{-7}$	$2.5 \times 10^{-14}$	$2.8 \times 10^{-14}$	$1.4 \times 10^{-3}$	$1.1 \times 10^{-3}$	$8.4 \times 10^{-5}$	$6.3 \times 10^{-5}$
10	$1.7 \times 10^{-7}$	$1.3 \times 10^{-7}$	$2.4 \times 10^{-14}$	$1.2 \times 10^{-14}$	$4.1 \times 10^{-4}$	$3.1 \times 10^{-4}$	$1.3 \times 10^{-5}$	$9.8 \times 10^{-6}$
11	$1.7 \times 10^{-7}$	$1.3 \times 10^{-7}$	$2.4 \times 10^{-14}$	$1.8 \times 10^{-14}$	$4.1 \times 10^{-4}$	$3.1 \times 10^{-4}$	$1.3 \times 10^{-5}$	$9.8 \times 10^{-6}$
12	$1.2 \times 10^{-8}$	$9.4 \times 10^{-9}$	$6.8 \times 10^{-14}$	$1.3 \times 10^{-14}$	$1.3 \times 10^{-4}$	$9.4 \times 10^{-5}$	$2.2 \times 10^{-6}$	$1.6 \times 10^{-6}$
13	$1.2 \times 10^{-8}$	$9.4 \times 10^{-9}$	$6.8 \times 10^{-14}$	$1.2 \times 10^{-14}$	$1.3 \times 10^{-4}$	$9.4 \times 10^{-5}$	$2.2 \times 10^{-6}$	$1.6 \times 10^{-6}$
14	$8.7 \times 10^{-10}$	$6.9 \times 10^{-10}$	$4.8 \times 10^{-13}$	$1.9 \times 10^{-14}$	$4.0 \times 10^{-5}$	$2.9 \times 10^{-5}$	$3.8 \times 10^{-7}$	$2.8 \times 10^{-7}$
15	$8.7 \times 10^{-10}$	$6.9 \times 10^{-10}$	$4.8 \times 10^{-13}$	$2.3 \times 10^{-14}$	$4.0 \times 10^{-5}$	$2.9 \times 10^{-5}$	$3.8 \times 10^{-7}$	$2.8 \times 10^{-7}$
16	$6.8 \times 10^{-11}$	$5.2 \times 10^{-11}$	$4.8 \times 10^{-13}$	$2.3 \times 10^{-14}$	$1.3 \times 10^{-5}$	$9.4 \times 10^{-6}$	$6.9 \times 10^{-8}$	$5.0 \times 10^{-8}$
17	$6.8 \times 10^{-11}$	$5.2 \times 10^{-11}$	$5.8 \times 10^{-13}$	$1.9 \times 10^{-14}$	$1.3 \times 10^{-5}$	$9.4 \times 10^{-6}$	$6.9 \times 10^{-8}$	$5.0 \times 10^{-8}$
18	$2.2 \times 10^{-11}$	$4.0 \times 10^{-12}$	$8.2 \times 10^{-12}$	$9.6 \times 10^{-15}$	$4.2 \times 10^{-6}$	$3.1 \times 10^{-6}$	$1.3 \times 10^{-8}$	$9.1 \times 10^{-9}$
19	$2.2 \times 10^{-11}$	$4.0 \times 10^{-12}$	$8.3 \times 10^{-12}$	$9.8 \times 10^{-15}$	$4.2 \times 10^{-6}$	$3.1 \times 10^{-6}$	$1.3 \times 10^{-8}$	$9.1 \times 10^{-9}$
20	$7.3 \times 10^{-11}$	$3.1 \times 10^{-13}$	$2.9 \times 10^{-11}$	$4.3 \times 10^{-15}$	$1.4 \times 10^{-6}$	$1.0 \times 10^{-6}$	$2.5 \times 10^{-9}$	$1.7 \times 10^{-9}$

the least squares coefficients remains close to machine epsilon regardless of model order. (Thanks to the built-in optimization in MATLAB's backslash operation, this is true even for the ill-conditioned problems discussed in Chapter 5.)

A few general patterns arise that are independent of the method used to obtain the Zernike coefficients. In particular, because all four surfaces have some degree of rotational symmetry around the  $z$ -axis, the MAE is nearly identical for each pair of consecutive model orders ( $N = 0$  and 1,  $N = 2$  and 3, etc.) Surfaces 1, 2, and 3 are axisymmetric, so they only have non-zero contributions from Zernike functions with meridional degree  $m = 0$ , which do not occur with odd radial indices. Note that the apparent fluctuations in the MAE for Surface 2 are from numerical error near machine precision. While Surface 4 is not axisymmetric, its 2<sup>nd</sup> order discrete symmetry means that it also will not include contributions from Zernike functions with odd radial degree.

Convergence rates among the three non-trivial surfaces also tend to be similar for both numerical integration and linear least squares. While it may initially seem surprising that Surface 3 is the slowest to converge despite being a simple sphere, this trend makes more

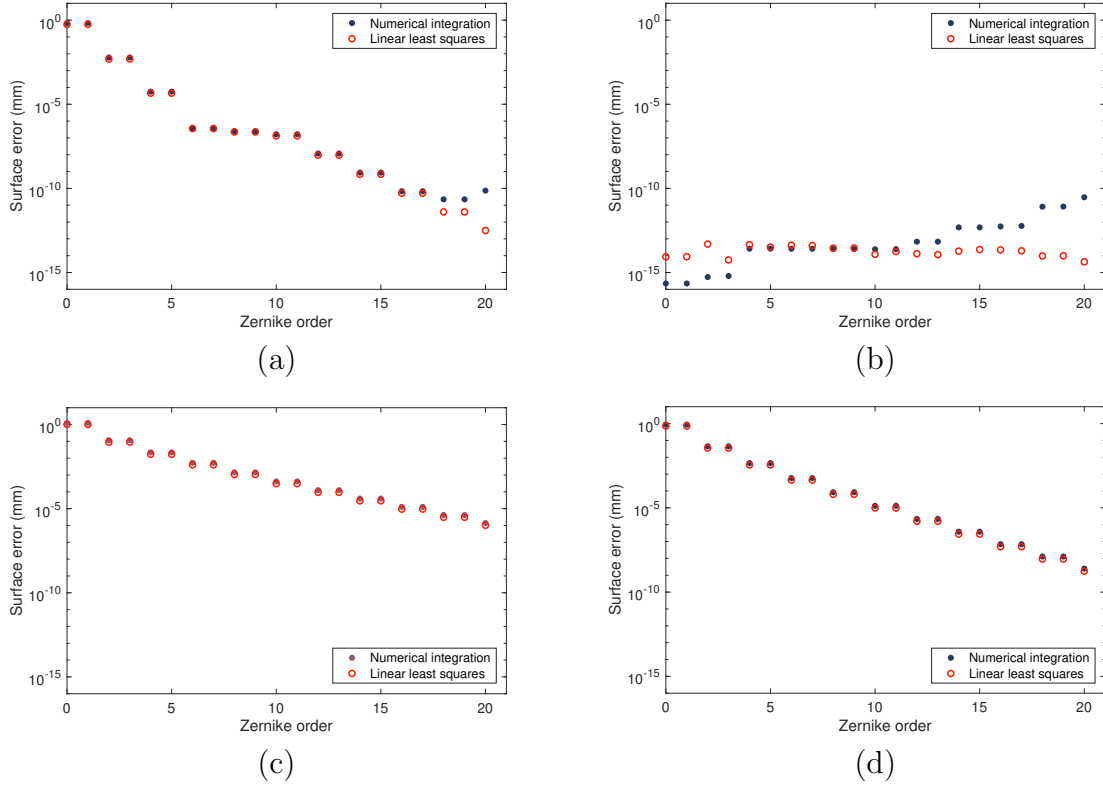


Figure 3.6: MAE in surface fit for (a) Surface 1, (b) Surface 2, (c) Surface 3, and (d) Surface 4, when coefficients are obtained using numerical integration versus OLS.

sense once we recall that the Zernike polynomials represent *aberrations* from a sphere, and not a sphere itself. In fact, the Zernike polynomials are frequently used for modeling the difference between the measured surface elevations and a reference sphere in order to better visualize comparatively small aberrations [84]. This issue will be discussed further in Chapter 7.

One drawback to using an average measure of the error across the entire surface is that two model orders with similar average errors might look very different at a local level. Figure 3.7 shows the local surface error for both numerical methods over an entire cross-sectional meridian for each of the axisymmetric surfaces (Surfaces 1–3), while Figure 3.8 shows the surface error across both of Surface 4’s principal meridians. In some cases, the error is considerably higher near the edges of the meridian. While this effect arises for both methods of computing the Zernike expansion, the least squares estimate tends

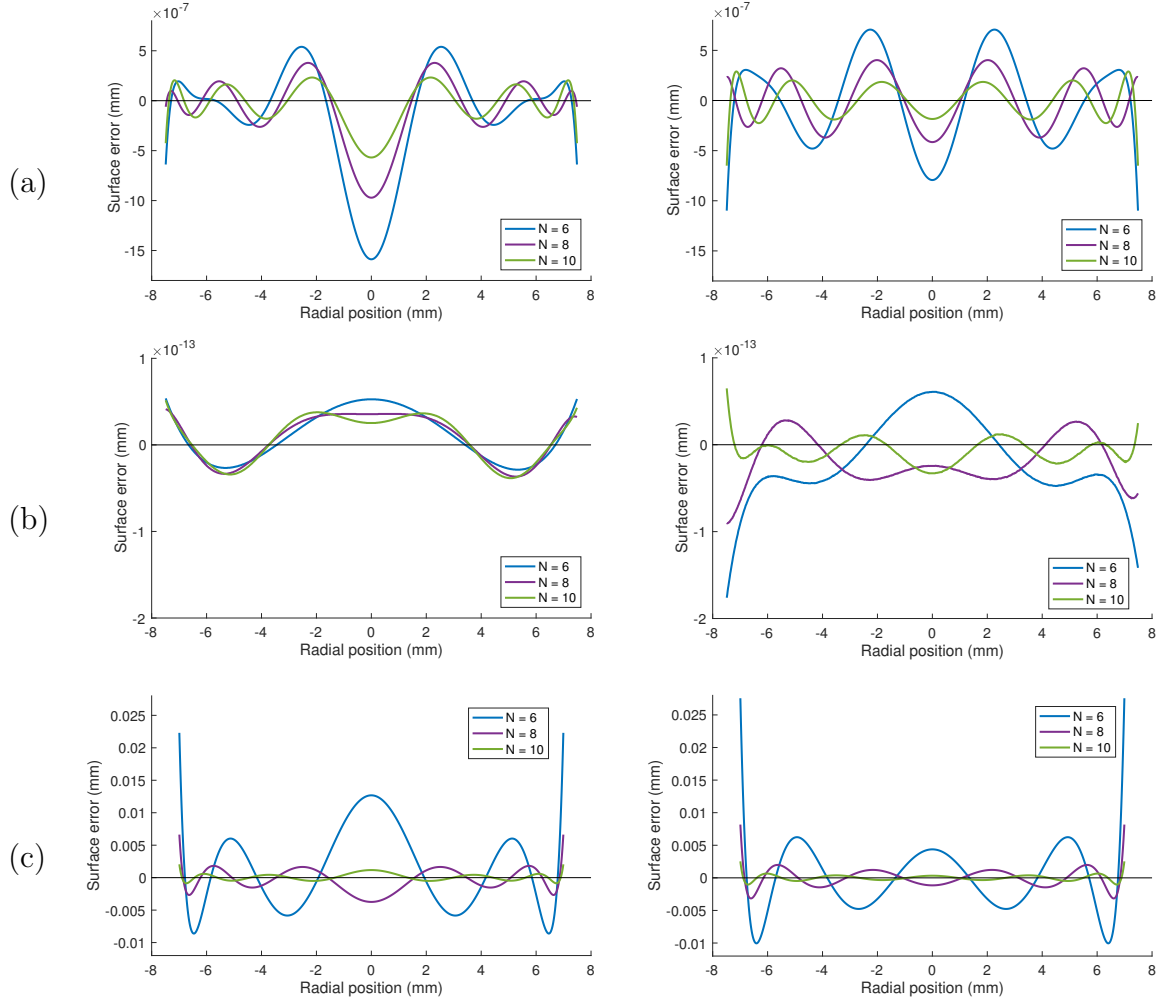
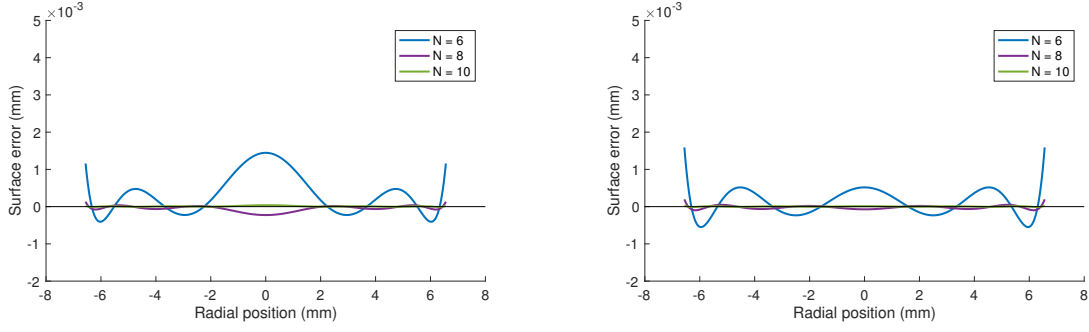


Figure 3.7: Local surface error from integration (left) and OLS (right) for (a) Surface 1, (b) Surface 2, and (c) Surface 3.

to provide a better fit near the center, where the interpolation points are most densely concentrated. In the worst cases, such as the order  $N = 6$  fits shown in Figures 3.7 and 3.8, this improvement near the center comes at the cost of an amplified error near the edges of the disk. However, given the decreased SNR in the OCT image data near the periphery, we already expect that some sacrifice may be necessary in this region.

Meridian at  $0^\circ$



Meridian at  $90^\circ$

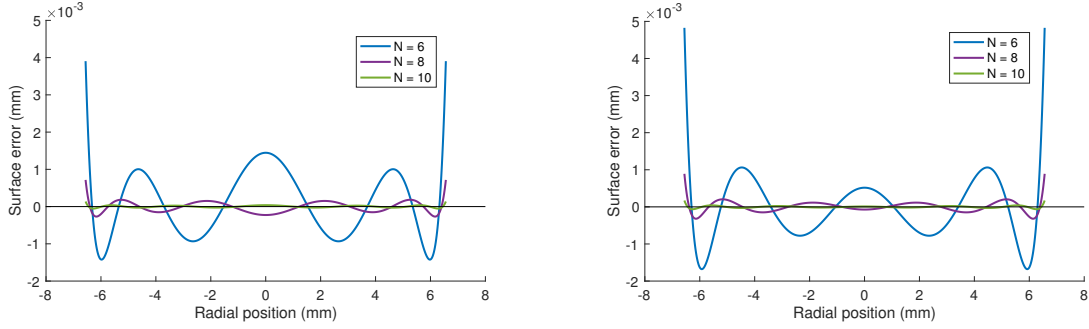


Figure 3.8: Local surface error for principal meridians of Surface 4 from integration (left) and OLS (right).

### 3.5.3 Impact of Quantization Error

While much of the noise in our OCT data could be eliminated by improving the segmentation algorithms, the error due to quantization is unavoidable. It is interesting to observe the model performance on our chosen surfaces in the idealized case of minimal measurement error. The MAE in surface fit for synthetic data with added quantization error ( $\bar{e}^*$ ) is shown in Table 3.3, alongside the results we obtained in Section 3.5.2 for the linear least squares fit to synthetic data without noise ( $\bar{e}$ ). Corresponding plots for Surfaces 1, 3 and 4 can be found in Figure 3.15.

It is immediately apparent that the addition of quantization error sets a bound on the accuracy of the fit, on the order of  $10^{-3}$  mm to  $10^{-5}$  mm depending on the surface. Quantization ends up having the greatest impact on Surface 2 (the flat plane), where it merely shifts the plane up by a constant  $1.7 \times 10^{-3}$  mm. For Surfaces 1, 3, and 4, we showed in Section 2.4.2 that the noise introduced by quantization is  $\epsilon_i^* \sim \mathcal{U}(-\frac{1}{2}\Delta'_z, \frac{1}{2}\Delta'_z)$ ,

Table 3.3: MAE (in mm) of surface reconstruction without noise ( $\bar{e}$ ) and with quantization error ( $\bar{e}^*$ ).

	Surface 1		Surface 2		Surface 3		Surface 4	
$N$	$\bar{e}$	$\bar{e}^*$	$\bar{e}$	$\bar{e}^*$	$\bar{e}$	$\bar{e}^*$	$\bar{e}$	$\bar{e}^*$
0	$5.6 \times 10^{-1}$	$5.6 \times 10^{-1}$	$8.7 \times 10^{-15}$	$1.7 \times 10^{-3}$	1.0	1.0	$7.2 \times 10^{-1}$	$7.2 \times 10^{-1}$
1	$5.6 \times 10^{-1}$	$5.6 \times 10^{-1}$	$8.7 \times 10^{-15}$	$1.7 \times 10^{-3}$	1.0	1.0	$7.2 \times 10^{-1}$	$7.2 \times 10^{-1}$
2	$4.9 \times 10^{-3}$	$4.9 \times 10^{-3}$	$4.9 \times 10^{-14}$	$1.7 \times 10^{-3}$	$9.1 \times 10^{-2}$	$9.1 \times 10^{-2}$	$3.5 \times 10^{-2}$	$3.5 \times 10^{-2}$
3	$4.9 \times 10^{-3}$	$4.9 \times 10^{-3}$	$5.6 \times 10^{-15}$	$1.7 \times 10^{-3}$	$9.1 \times 10^{-2}$	$9.1 \times 10^{-2}$	$3.5 \times 10^{-2}$	$3.5 \times 10^{-3}$
4	$4.6 \times 10^{-5}$	$6.6 \times 10^{-5}$	$4.5 \times 10^{-14}$	$1.7 \times 10^{-3}$	$1.7 \times 10^{-2}$	$1.7 \times 10^{-2}$	$3.5 \times 10^{-3}$	$3.5 \times 10^{-3}$
5	$4.6 \times 10^{-5}$	$6.6 \times 10^{-5}$	$3.2 \times 10^{-14}$	$1.7 \times 10^{-3}$	$1.7 \times 10^{-2}$	$1.7 \times 10^{-2}$	$3.5 \times 10^{-3}$	$3.5 \times 10^{-2}$
6	$3.6 \times 10^{-7}$	$5.8 \times 10^{-5}$	$4.2 \times 10^{-14}$	$1.7 \times 10^{-3}$	$4.0 \times 10^{-3}$	$4.0 \times 10^{-3}$	$4.4 \times 10^{-4}$	$4.4 \times 10^{-4}$
7	$3.6 \times 10^{-7}$	$5.8 \times 10^{-5}$	$4.0 \times 10^{-14}$	$1.7 \times 10^{-3}$	$4.0 \times 10^{-3}$	$4.0 \times 10^{-3}$	$4.4 \times 10^{-4}$	$4.4 \times 10^{-4}$
8	$2.3 \times 10^{-7}$	$5.9 \times 10^{-5}$	$2.8 \times 10^{-14}$	$1.7 \times 10^{-3}$	$1.1 \times 10^{-3}$	$1.1 \times 10^{-3}$	$6.3 \times 10^{-5}$	$6.7 \times 10^{-5}$
9	$2.3 \times 10^{-7}$	$5.9 \times 10^{-5}$	$2.8 \times 10^{-14}$	$1.7 \times 10^{-3}$	$1.1 \times 10^{-3}$	$1.1 \times 10^{-3}$	$6.3 \times 10^{-5}$	$6.7 \times 10^{-5}$
10	$1.3 \times 10^{-7}$	$6.5 \times 10^{-5}$	$1.2 \times 10^{-14}$	$1.7 \times 10^{-3}$	$3.1 \times 10^{-4}$	$3.6 \times 10^{-4}$	$9.8 \times 10^{-6}$	$3.1 \times 10^{-5}$
11	$1.3 \times 10^{-7}$	$6.5 \times 10^{-5}$	$1.8 \times 10^{-14}$	$1.7 \times 10^{-3}$	$3.1 \times 10^{-4}$	$3.6 \times 10^{-4}$	$9.8 \times 10^{-6}$	$3.1 \times 10^{-5}$
12	$9.4 \times 10^{-9}$	$6.5 \times 10^{-5}$	$1.3 \times 10^{-14}$	$1.7 \times 10^{-3}$	$9.4 \times 10^{-5}$	$2.1 \times 10^{-4}$	$1.6 \times 10^{-6}$	$3.4 \times 10^{-5}$
13	$9.4 \times 10^{-9}$	$6.5 \times 10^{-5}$	$1.2 \times 10^{-14}$	$1.7 \times 10^{-3}$	$9.4 \times 10^{-5}$	$2.1 \times 10^{-4}$	$1.6 \times 10^{-6}$	$3.4 \times 10^{-5}$
14	$6.9 \times 10^{-10}$	$1.1 \times 10^{-4}$	$1.9 \times 10^{-14}$	$1.7 \times 10^{-3}$	$2.9 \times 10^{-5}$	$2.2 \times 10^{-4}$	$2.8 \times 10^{-7}$	$3.6 \times 10^{-5}$
15	$6.9 \times 10^{-10}$	$1.1 \times 10^{-4}$	$2.3 \times 10^{-14}$	$1.7 \times 10^{-3}$	$2.9 \times 10^{-5}$	$2.2 \times 10^{-4}$	$2.8 \times 10^{-7}$	$3.6 \times 10^{-5}$
16	$5.2 \times 10^{-11}$	$1.2 \times 10^{-4}$	$2.3 \times 10^{-14}$	$1.7 \times 10^{-3}$	$9.4 \times 10^{-6}$	$2.2 \times 10^{-4}$	$5.0 \times 10^{-8}$	$4.1 \times 10^{-5}$
17	$5.2 \times 10^{-11}$	$1.2 \times 10^{-4}$	$1.9 \times 10^{-14}$	$1.7 \times 10^{-3}$	$9.4 \times 10^{-6}$	$2.2 \times 10^{-4}$	$5.0 \times 10^{-8}$	$4.1 \times 10^{-5}$
18	$4.0 \times 10^{-12}$	$1.2 \times 10^{-4}$	$9.6 \times 10^{-15}$	$1.7 \times 10^{-3}$	$3.1 \times 10^{-6}$	$2.4 \times 10^{-4}$	$9.1 \times 10^{-9}$	$4.4 \times 10^{-5}$
19	$4.0 \times 10^{-12}$	$1.2 \times 10^{-4}$	$9.8 \times 10^{-15}$	$1.7 \times 10^{-3}$	$3.1 \times 10^{-6}$	$2.4 \times 10^{-4}$	$9.1 \times 10^{-9}$	$4.4 \times 10^{-5}$
20	$3.1 \times 10^{-13}$	$1.2 \times 10^{-4}$	$4.3 \times 10^{-15}$	$1.7 \times 10^{-3}$	$1.0 \times 10^{-6}$	$2.4 \times 10^{-4}$	$1.7 \times 10^{-9}$	$4.6 \times 10^{-5}$

with  $\Delta'_z = 5.6 \times 10^{-3}$  mm. Because this noise is uniform, it is not surprising that the mean absolute value of the quantization error  $\frac{1}{s} \sum_{i=1}^s |\epsilon_i^*|$  is approximately  $1.4 \times 10^{-3}$  mm for all three surfaces. However, Table 3.4 illustrates that lower bound on the accuracy of the fit for each surface is actually on the same order as the mean *signed* quantization error  $\bar{\epsilon}^* = \frac{1}{s} \sum_{i=1}^s \epsilon_i^*$ .

Figure 3.9 shows the local cross-sectional error in the surface fit for different Zernike fits for the remaining three surfaces when quantization error is included. For comparison, we selected three Zernike orders for each surface that result in a low MAE. All the error

Table 3.4: Mean signed quantization error ( $\bar{\epsilon}^*$ ) and smallest MAE in surface fit to quantized data ( $\bar{e}^*$ ), in millimeters.

	Surface 1	Surface 2	Surface 3	Surface 4
$\bar{\epsilon}^*$	$5.7 \times 10^{-5}$	$1.7 \times 10^{-3}$	$-1.5 \times 10^{-4}$	$-1.2 \times 10^{-5}$
$\bar{e}^*$	$5.8 \times 10^{-5}$	$1.7 \times 10^{-3}$	$2.1 \times 10^{-4}$	$3.1 \times 10^{-5}$

plots are shown on the same  $y$ -axis to accentuate the issues mentioned in Section 3.5.2 that arise for the different surfaces. Figure 3.9a reveals some key differences between the 4<sup>th</sup> and 10<sup>th</sup> order fits to Surface 1 that are obscured by their nearly identical  $\bar{e}^*$  values from Table 3.3 ( $6.6 \times 10^{-5}$  mm and  $6.5 \times 10^{-5}$  mm, respectively). In particular, the error at the center is almost zero for  $N = 4$ , but not for  $N = 10$ . The error for the 6<sup>th</sup> order fit is also slightly worse near the center than it is for the 4<sup>th</sup> order fit; however, the infinity norm is smaller for the 6<sup>th</sup> order, leading to an average error of just  $\bar{e}^* = 5.8 \times 10^{-5}$  mm. Recall from Section 2.3 that the manufacturer specification for the accuracy of the aspheric lens surface is  $0.75 \mu\text{m}$ , in terms of the RMSE. The RMSE in microns for the quantized synthetic data from Surface 1 is *at worst*  $6.5 \times 10^{-4} \mu\text{m}$  for any of the Zernike orders we considered, and for  $4 \leq N \leq 20$  the RMSE ranges from  $6.9 \times 10^{-8} \mu\text{m}$  to  $1.6 \times 10^{-7} \mu\text{m}$ . Therefore, we can be assured that quantization error alone will not prevent us from obtaining a comparable degree of accuracy in our surface reconstruction.

Similarly, the local error for Surface 3, depicted in Figure 3.9b, is much larger at the edges and smaller at the center for  $N = 12$  than for  $N = 14$ , despite respective  $\bar{e}^*$  values of  $2.1 \times 10^{-4}$  mm and  $2.2 \times 10^{-4}$  mm. The 18<sup>th</sup> order fit appears to be slightly worse going by the average error ( $\bar{e}^* = 2.4 \times 10^{-4}$  mm), yet in spite of the noticeable increase in the oscillations of the local error, the error is nevertheless smaller near the center for the 18<sup>th</sup> order fit than for the 14<sup>th</sup> order fit. These seemingly minor differences are likely to be amplified as they propagate through the curvature calculations.

Figures 3.9c–d illustrate another concern that arises for surfaces like Surface 4 that lack continuous rotational symmetry about the  $z$ -axis—*i.e.*, any time the CT axis is not perfectly aligned with the lens’ optical axis during data collection (generally the case even under optimal conditions). Specifically, the Zernike order that provides the closest fit for one principal meridian may not be the best choice for the other principal meridian. This behavior was also true for the non-quantized data (shown in Figure 3.8). Since one of our primary goals is to minimize the error in the principal radii of curvature, discrepancies between the principal meridians will necessarily be a significant factor in determining the optimal Zernike order for any non-axisymmetric surface.

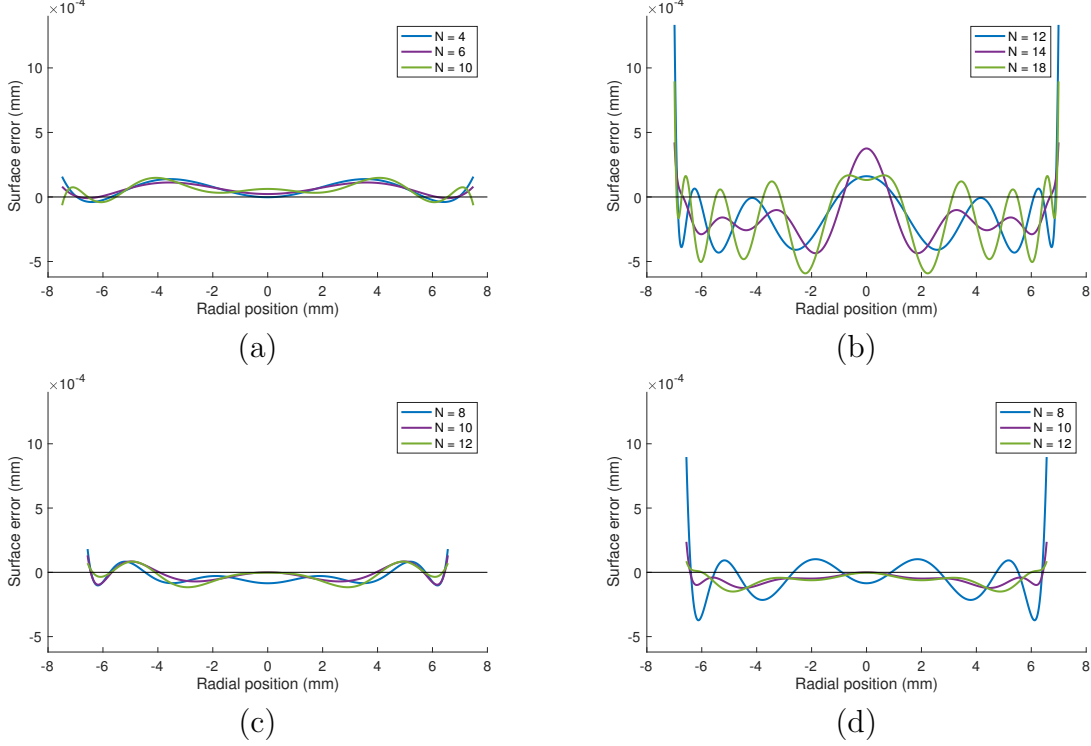


Figure 3.9: Local surface error for Zernike fit to quantized synthetic data for (a) Surface 1, (b) Surface 3, (c) Surface 4 at  $0^\circ$ , and (d) Surface 4 at  $90^\circ$ .

### 3.5.4 Curvature

In this section, we will consider the impact of Zernike order on the local meridional curvature and the principal radius (or radii) of curvature, defined respectively in (3.17) and (3.18). We initially performed all the calculations using scaled finite difference step sizes of  $h' = h/A = 10^{-2}$ ,  $10^{-3}$ ,  $10^{-4}$ ,  $10^{-5}$ , and  $10^{-6}$ . However, we found that the magnitude of  $h'$  had a relatively minor impact on our quantities of interest. For all four surfaces, the principal radii of curvature and the MAE in the meridional curvature

Table 3.5: Actual finite difference step sizes ( $h = Ah'$ ) for curvature, in millimeters.

	Surface 1	Surface 2	Surface 3	Surface 4
$h$	0.0075	0.0075	0.0070	0.0066

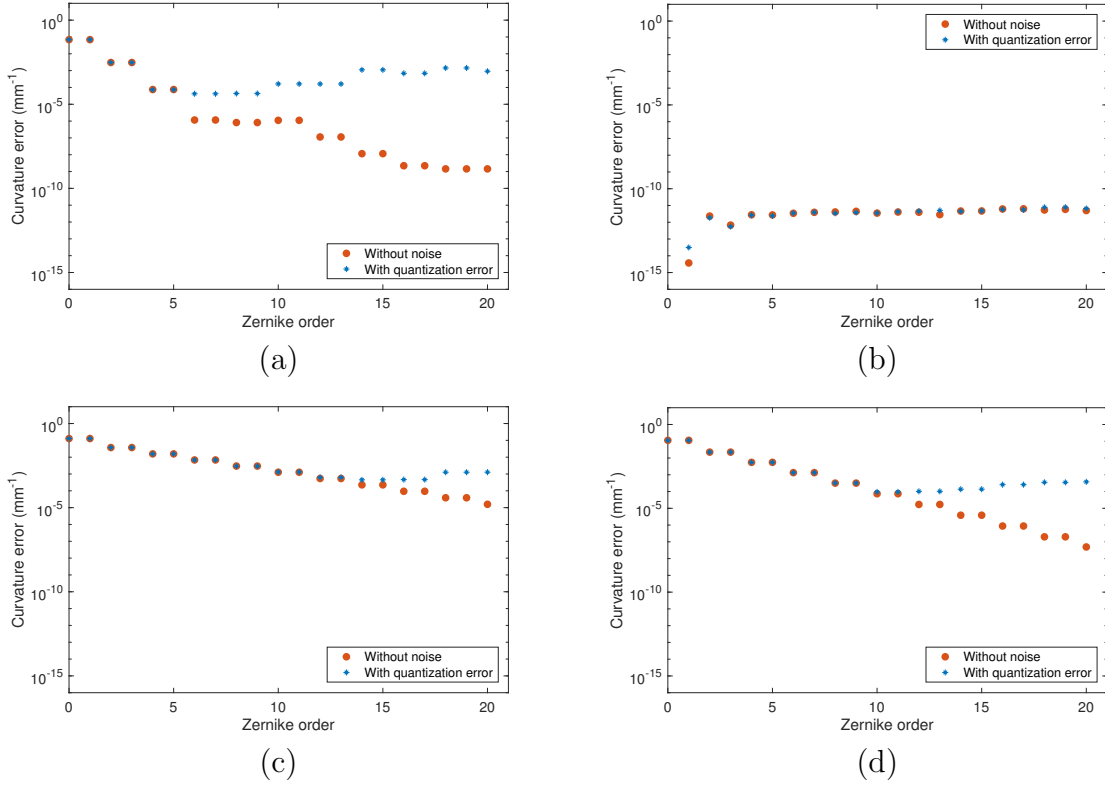


Figure 3.10: MAE in meridional curvature for (a) Surface 1, (b) Surface 2, (c) Surface 3, and (d) Surface 4.

(defined in (3.20)) for any given model order were nearly identical using  $h' = 10^{-3}$ ,  $10^{-4}$ , and  $10^{-5}$ , and while the results were slightly less consistent for  $10^{-2}$  and  $10^{-6}$ , these effects were dwarfed by the variations due to model order. Thus, we chose to limit our analysis to a single step size for each surface. The results presented here are based on a scaled step size of  $h' = 10^{-3}$ , which ensures that the actual finite difference step size  $h = A \times 10^{-3}$  (shown in Table 3.5) remains an order of magnitude smaller than the distance  $\Delta_\rho = 0.016$  mm between the data points.

### Meridional Curvature

The MAE in the meridional curvature for the different model orders is depicted graphically in Figure 3.10, for both non-quantized ( $\bar{e}_k$ ) and quantized data ( $\bar{e}_k^*$ ). The exact values can be found in Table 3.6. Local curvature error plots based on quantized syn-

Table 3.6: MAE (in  $\text{mm}^{-1}$ ) in meridional curvature without noise ( $\bar{e}_k$ ) and with quantization error ( $\bar{e}_k^*$ ).

	Surface 1		Surface 2		Surface 3		Surface 4	
$N$	$\bar{e}_k$	$\bar{e}_k^*$	$\bar{e}_k$	$\bar{e}_k^*$	$\bar{e}_k$	$\bar{e}_k^*$	$\bar{e}_k$	$\bar{e}_k^*$
0	$6.9 \times 10^{-2}$	$6.9 \times 10^{-2}$	0.0	0.0	$1.3 \times 10^{-1}$	$1.3 \times 10^{-1}$	$1.1 \times 10^{-1}$	$1.1 \times 10^{-1}$
1	$6.9 \times 10^{-2}$	$6.9 \times 10^{-2}$	$3.7 \times 10^{-15}$	$3.1 \times 10^{-14}$	$1.3 \times 10^{-1}$	$1.3 \times 10^{-1}$	$1.1 \times 10^{-1}$	$1.1 \times 10^{-1}$
2	$3.0 \times 10^{-3}$	$3.0 \times 10^{-3}$	$2.3 \times 10^{-12}$	$1.9 \times 10^{-12}$	$3.7 \times 10^{-2}$	$3.7 \times 10^{-2}$	$2.2 \times 10^{-2}$	$2.2 \times 10^{-2}$
3	$3.0 \times 10^{-3}$	$3.0 \times 10^{-3}$	$6.8 \times 10^{-13}$	$5.5 \times 10^{-13}$	$3.7 \times 10^{-2}$	$3.7 \times 10^{-2}$	$2.2 \times 10^{-2}$	$2.2 \times 10^{-2}$
4	$7.5 \times 10^{-5}$	$7.3 \times 10^{-5}$	$2.8 \times 10^{-12}$	$2.6 \times 10^{-12}$	$1.6 \times 10^{-2}$	$1.6 \times 10^{-2}$	$5.5 \times 10^{-3}$	$5.5 \times 10^{-3}$
5	$7.5 \times 10^{-5}$	$7.3 \times 10^{-5}$	$2.7 \times 10^{-12}$	$2.4 \times 10^{-12}$	$1.6 \times 10^{-2}$	$1.6 \times 10^{-2}$	$5.5 \times 10^{-3}$	$5.5 \times 10^{-3}$
6	$1.2 \times 10^{-6}$	$4.2 \times 10^{-5}$	$3.4 \times 10^{-12}$	$3.5 \times 10^{-12}$	$6.8 \times 10^{-3}$	$6.8 \times 10^{-3}$	$1.3 \times 10^{-3}$	$1.3 \times 10^{-3}$
7	$1.2 \times 10^{-6}$	$4.2 \times 10^{-5}$	$3.9 \times 10^{-12}$	$3.9 \times 10^{-12}$	$6.8 \times 10^{-3}$	$6.8 \times 10^{-3}$	$1.3 \times 10^{-3}$	$1.3 \times 10^{-3}$
8	$8.2 \times 10^{-7}$	$4.3 \times 10^{-5}$	$4.1 \times 10^{-12}$	$3.4 \times 10^{-12}$	$3.0 \times 10^{-3}$	$2.9 \times 10^{-3}$	$3.2 \times 10^{-4}$	$3.2 \times 10^{-4}$
9	$8.2 \times 10^{-7}$	$4.3 \times 10^{-5}$	$4.5 \times 10^{-12}$	$3.8 \times 10^{-12}$	$3.0 \times 10^{-3}$	$2.9 \times 10^{-3}$	$3.2 \times 10^{-4}$	$3.2 \times 10^{-4}$
10	$1.1 \times 10^{-6}$	$1.6 \times 10^{-4}$	$3.5 \times 10^{-12}$	$3.6 \times 10^{-12}$	$1.3 \times 10^{-3}$	$1.3 \times 10^{-3}$	$7.4 \times 10^{-5}$	$9.5 \times 10^{-5}$
11	$1.1 \times 10^{-6}$	$1.6 \times 10^{-4}$	$4.1 \times 10^{-12}$	$4.3 \times 10^{-12}$	$1.3 \times 10^{-3}$	$1.3 \times 10^{-3}$	$7.4 \times 10^{-5}$	$9.5 \times 10^{-5}$
12	$1.1 \times 10^{-7}$	$1.6 \times 10^{-4}$	$4.0 \times 10^{-12}$	$4.6 \times 10^{-12}$	$5.4 \times 10^{-4}$	$6.3 \times 10^{-4}$	$1.7 \times 10^{-5}$	$1.0 \times 10^{-4}$
13	$1.1 \times 10^{-7}$	$1.6 \times 10^{-4}$	$2.9 \times 10^{-12}$	$5.1 \times 10^{-12}$	$5.4 \times 10^{-4}$	$6.3 \times 10^{-4}$	$1.7 \times 10^{-5}$	$1.0 \times 10^{-4}$
14	$1.2 \times 10^{-8}$	$1.1 \times 10^{-3}$	$4.7 \times 10^{-12}$	$4.5 \times 10^{-12}$	$2.3 \times 10^{-4}$	$4.5 \times 10^{-4}$	$3.9 \times 10^{-6}$	$1.4 \times 10^{-4}$
15	$1.2 \times 10^{-8}$	$1.1 \times 10^{-3}$	$4.7 \times 10^{-12}$	$4.7 \times 10^{-12}$	$2.3 \times 10^{-4}$	$4.5 \times 10^{-4}$	$3.9 \times 10^{-6}$	$1.4 \times 10^{-4}$
16	$2.2 \times 10^{-9}$	$6.9 \times 10^{-4}$	$6.2 \times 10^{-12}$	$5.9 \times 10^{-12}$	$9.4 \times 10^{-5}$	$4.6 \times 10^{-4}$	$8.8 \times 10^{-7}$	$2.6 \times 10^{-4}$
17	$2.2 \times 10^{-9}$	$6.9 \times 10^{-4}$	$6.3 \times 10^{-12}$	$5.6 \times 10^{-12}$	$9.4 \times 10^{-5}$	$4.6 \times 10^{-4}$	$8.8 \times 10^{-7}$	$2.6 \times 10^{-4}$
18	$1.4 \times 10^{-9}$	$1.4 \times 10^{-3}$	$5.4 \times 10^{-12}$	$7.8 \times 10^{-12}$	$3.9 \times 10^{-5}$	$1.3 \times 10^{-3}$	$2.0 \times 10^{-7}$	$3.5 \times 10^{-4}$
19	$1.4 \times 10^{-9}$	$1.4 \times 10^{-3}$	$5.9 \times 10^{-12}$	$7.9 \times 10^{-12}$	$3.9 \times 10^{-5}$	$1.3 \times 10^{-3}$	$2.0 \times 10^{-7}$	$3.5 \times 10^{-4}$
20	$1.4 \times 10^{-9}$	$9.1 \times 10^{-4}$	$5.0 \times 10^{-12}$	$6.6 \times 10^{-12}$	$1.6 \times 10^{-5}$	$1.3 \times 10^{-3}$	$4.9 \times 10^{-8}$	$3.8 \times 10^{-4}$

thetic data for Surfaces 1, 3, and 4 are shown in Figures 3.11–3.12, juxtaposed with the corresponding local surface error from Figure 3.9. (Calculation of the derivatives for Surface 2 involves a lot of arithmetic near machine precision, so the local curvature error for that surface is not terribly informative.) This discussion will be focused mainly on the results for the quantized data; however, a similar presentation of the local curvature errors for the non-quantized data and the local surface errors from Figures 3.7–3.8 can be seen in Figure 3.14.

Note that both  $\bar{e}_k$  and  $\bar{e}_k^*$  for Surface 2 (the flat plane) are zero for  $N = 0$  in Table 3.6. This is due to the fact that the one Zernike basis function for this model order,  $Z_1$ , is itself a flat disk with constant curvature  $0 \text{ mm}^{-1}$ . Furthermore, because the only source of noise in the quantized synthetic data for this surface was a uniform vertical shift, it is also not surprising that the average error for the curvature calculation—which relies only on derivatives of the Zernike functions—is similar for both quantized and non-quantized data. This is why it is possible to have a average curvature error of less than  $10^{-11} \text{ mm}^{-1}$ , despite the fact that the average surface error is  $\sim 10^{-3} \text{ mm}$ .

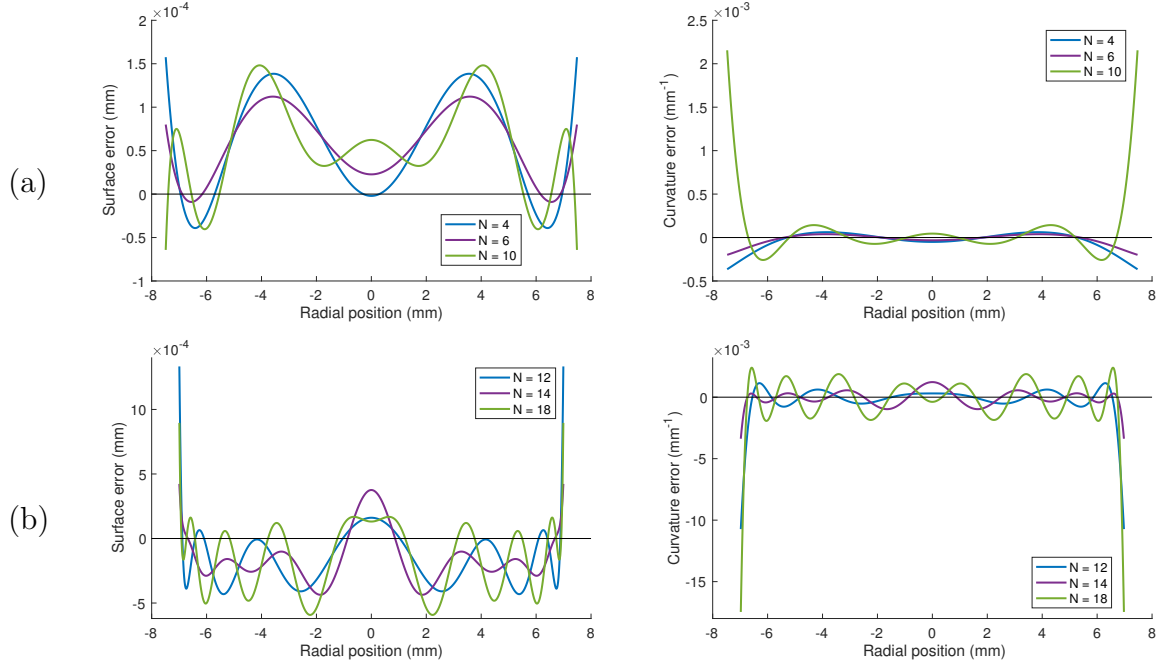
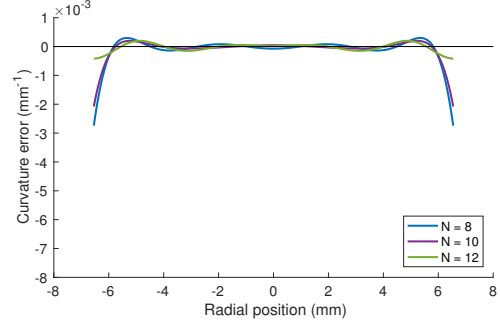
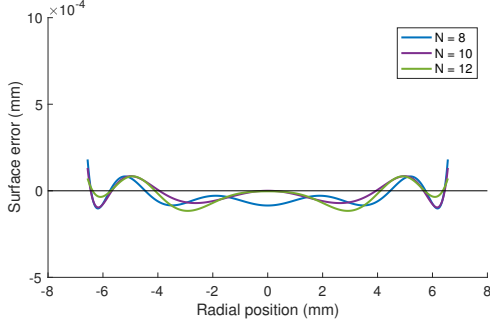


Figure 3.11: Local error in surface fit (left) and curvature (right) when quantization error is present for (a) Surface 1 and (b) Surface 3.

In Section 3.5.3, we noted that the 4<sup>th</sup> and 10<sup>th</sup> order fits for Surface 1 had almost the same average surface error (in fact, the average error for  $N = 4$  was slightly greater at  $\bar{e}^* = 6.6 \times 10^{-5}$  mm, versus  $\bar{e}^* = 6.5 \times 10^{-5}$  mm for  $N = 10$ ). However, at  $\bar{e}_k^* = 1.6 \times 10^{-4}$  mm<sup>-1</sup>, the average curvature error for the 10<sup>th</sup> order fit is more than double that of the 4<sup>th</sup> order fit, which yields  $\bar{e}_k^* = 7.3 \times 10^{-5}$  mm<sup>-1</sup>. The cause of this is apparent in Figure 3.11a: the small oscillations we observed in the 10<sup>th</sup> order fit become magnified by the curvature calculation, and eventually cause the error to blow up near the edges.

If we compare the exact values for the surface and curvature errors for Surface 3, we can see that while  $\bar{e}^*$  is minimized when  $N = 12$ , both the 14<sup>th</sup> or 16<sup>th</sup> order fits result in smaller values for  $\bar{e}_k^*$ . However, when we look more closely at the local curvature error cross section shown in Figure 3.11b, it becomes clear that the larger  $\bar{e}_k^*$  value for  $N = 12$  is due to an overwhelming contribution towards the edges. In fact, the error near the center remains very small for the 12<sup>th</sup> order fit, whereas the error in the 14<sup>th</sup> order fit is actually quite large at the center—larger even than for  $N = 18$ , which fits rather poorly everywhere.

Meridian at  $0^\circ$



Meridian at  $90^\circ$

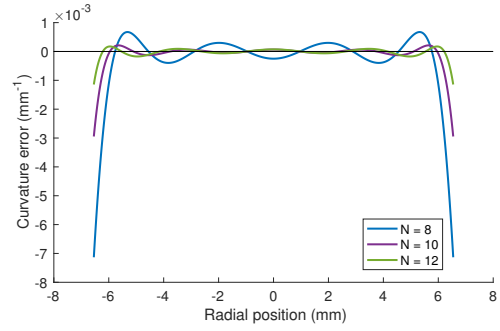
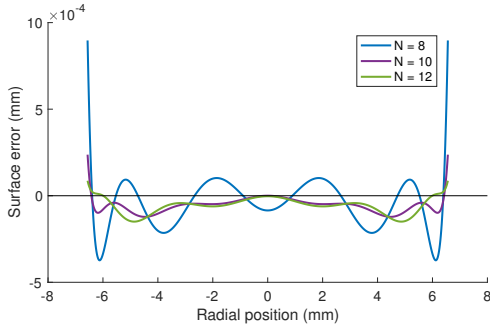
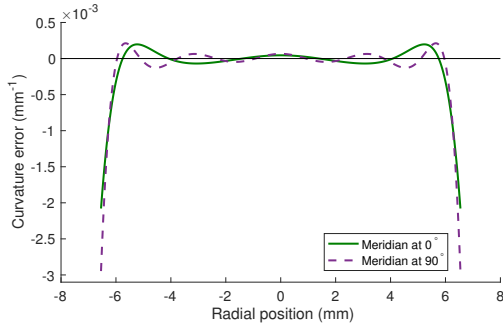
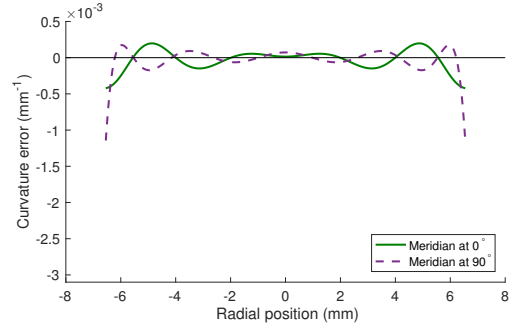


Figure 3.12: Local error in surface fit (left) and curvature (right) for the principal meridians of Surface 4 when quantization error is present.



(a)



(b)

Figure 3.13: Local curvature error when quantization error is present in Surface 4 principal meridians for Zernike fits of order (a)  $N = 10$  and (b)  $N = 12$ .

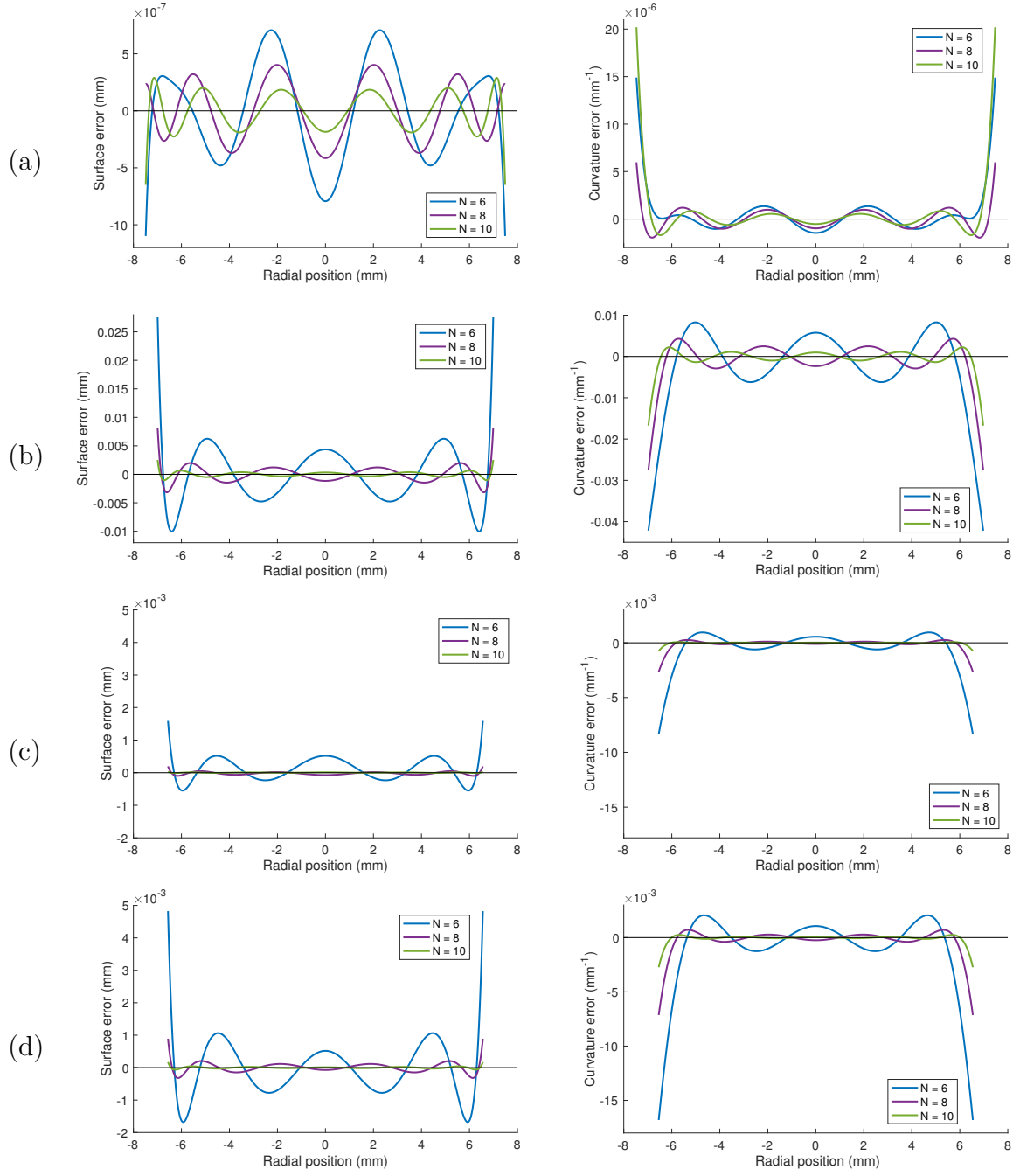


Figure 3.14: Local error in surface fit (left) and curvature (right) without noise for (a) Surface 1, (b) Surface 3, (c) Surface 4 meridian at  $0^\circ$ , and (d) Surface 4 meridian at  $90^\circ$ .

Table 3.7: MAE (in mm) in the meridional radius of curvature without noise ( $\bar{e}_{\text{roc}}$ ) and with quantization error ( $\bar{e}_{\text{roc}}^*$ ).

	Surface 1		Surface 3		Surface 4	
$N$	$\bar{e}_{\text{roc}}$	$\bar{e}_{\text{roc}}^*$	$\bar{e}_{\text{roc}}$	$\bar{e}_{\text{roc}}^*$	$\bar{e}_{\text{roc}}$	$\bar{e}_{\text{roc}}^*$
2	$7.8 \times 10^{-1}$	$7.8 \times 10^{-1}$	3.8	3.8	2.5	2.5
3	$7.8 \times 10^{-1}$	$7.8 \times 10^{-1}$	3.8	3.8	2.5	2.5
4	$1.9 \times 10^{-2}$	$1.8 \times 10^{-2}$	1.2	1.2	$4.8 \times 10^{-1}$	$4.8 \times 10^{-1}$
5	$1.9 \times 10^{-2}$	$1.8 \times 10^{-2}$	1.2	1.2	$4.8 \times 10^{-1}$	$4.8 \times 10^{-1}$
6	$2.8 \times 10^{-4}$	$1.0 \times 10^{-2}$	$4.7 \times 10^{-1}$	$4.7 \times 10^{-1}$	$1.1 \times 10^{-1}$	$1.1 \times 10^{-1}$
7	$2.8 \times 10^{-4}$	$1.0 \times 10^{-2}$	$4.7 \times 10^{-1}$	$4.7 \times 10^{-1}$	$1.1 \times 10^{-1}$	$1.1 \times 10^{-1}$
8	$1.9 \times 10^{-4}$	$1.1 \times 10^{-2}$	$1.9 \times 10^{-1}$	$1.9 \times 10^{-1}$	$2.5 \times 10^{-2}$	$2.5 \times 10^{-2}$
9	$1.9 \times 10^{-4}$	$1.1 \times 10^{-2}$	$1.9 \times 10^{-1}$	$1.9 \times 10^{-1}$	$2.5 \times 10^{-2}$	$2.5 \times 10^{-2}$
10	$2.9 \times 10^{-4}$	$4.2 \times 10^{-2}$	$8.0 \times 10^{-2}$	$8.3 \times 10^{-2}$	$5.7 \times 10^{-3}$	$7.4 \times 10^{-3}$
11	$2.9 \times 10^{-4}$	$4.2 \times 10^{-2}$	$8.0 \times 10^{-2}$	$8.3 \times 10^{-2}$	$5.7 \times 10^{-3}$	$7.4 \times 10^{-3}$
12	$3.0 \times 10^{-5}$	$4.1 \times 10^{-2}$	$3.3 \times 10^{-2}$	$3.9 \times 10^{-2}$	$1.3 \times 10^{-3}$	$8.0 \times 10^{-3}$
13	$3.0 \times 10^{-5}$	$4.1 \times 10^{-2}$	$3.3 \times 10^{-2}$	$3.9 \times 10^{-2}$	$1.3 \times 10^{-3}$	$8.0 \times 10^{-3}$
14	$3.1 \times 10^{-6}$	$3.8 \times 10^{-1}$	$1.4 \times 10^{-2}$	$2.7 \times 10^{-2}$	$2.9 \times 10^{-4}$	$1.1 \times 10^{-2}$
15	$3.1 \times 10^{-6}$	$3.8 \times 10^{-1}$	$1.4 \times 10^{-2}$	$2.7 \times 10^{-2}$	$2.9 \times 10^{-4}$	$1.1 \times 10^{-2}$
16	$5.1 \times 10^{-7}$	$1.6 \times 10^{-1}$	$5.7 \times 10^{-3}$	$2.8 \times 10^{-2}$	$6.6 \times 10^{-5}$	$2.0 \times 10^{-2}$
17	$5.1 \times 10^{-7}$	$1.6 \times 10^{-1}$	$5.7 \times 10^{-3}$	$2.8 \times 10^{-2}$	$6.6 \times 10^{-5}$	$2.0 \times 10^{-2}$
18	$2.8 \times 10^{-7}$	$3.3 \times 10^{-1}$	$2.4 \times 10^{-3}$	$7.9 \times 10^{-2}$	$1.5 \times 10^{-5}$	$2.7 \times 10^{-2}$
19	$2.8 \times 10^{-7}$	$3.3 \times 10^{-1}$	$2.4 \times 10^{-3}$	$7.9 \times 10^{-2}$	$1.5 \times 10^{-5}$	$2.7 \times 10^{-2}$
20	$2.8 \times 10^{-7}$	$2.1 \times 10^{-1}$	$9.6 \times 10^{-4}$	$8.0 \times 10^{-2}$	$3.7 \times 10^{-6}$	$2.9 \times 10^{-2}$

For Surface 4, both  $\bar{e}^*$  and  $\bar{e}_k^*$  are at a minimum when  $N = 10$ , with  $N = 12$  doing only slightly worse. The main issue here is that looking only at  $\bar{e}_k^*$  for a particular order obscures the differences between the local curvature errors in the two principal meridians. This is most apparent for the 8<sup>th</sup> order fit shown in Figure 3.12, where the curvature error for the meridian at 90° is consistently more than twice the amplitude of the error in the meridian at 0°. Figure 3.13 illustrates direct comparisons of the error along the principal meridians for the 10<sup>th</sup> and 12<sup>th</sup> order fits. Although the differences between the two meridians are not quite as dramatic for either of these Zernike orders as they were for  $N = 8$ , the meridian at 90° continues to fare worse in both cases. However, aside from right at the edges (and perhaps directly in the center), it appears that the meridian at 0° suffers more than the meridian at 90° when we add the additional terms for the 12th order fit.

## Meridional Radius of Curvature

Note that while the height of the surface is measured in millimeters, the meridional curvature is given in inverse millimeters. To make direct comparisons between the fitting

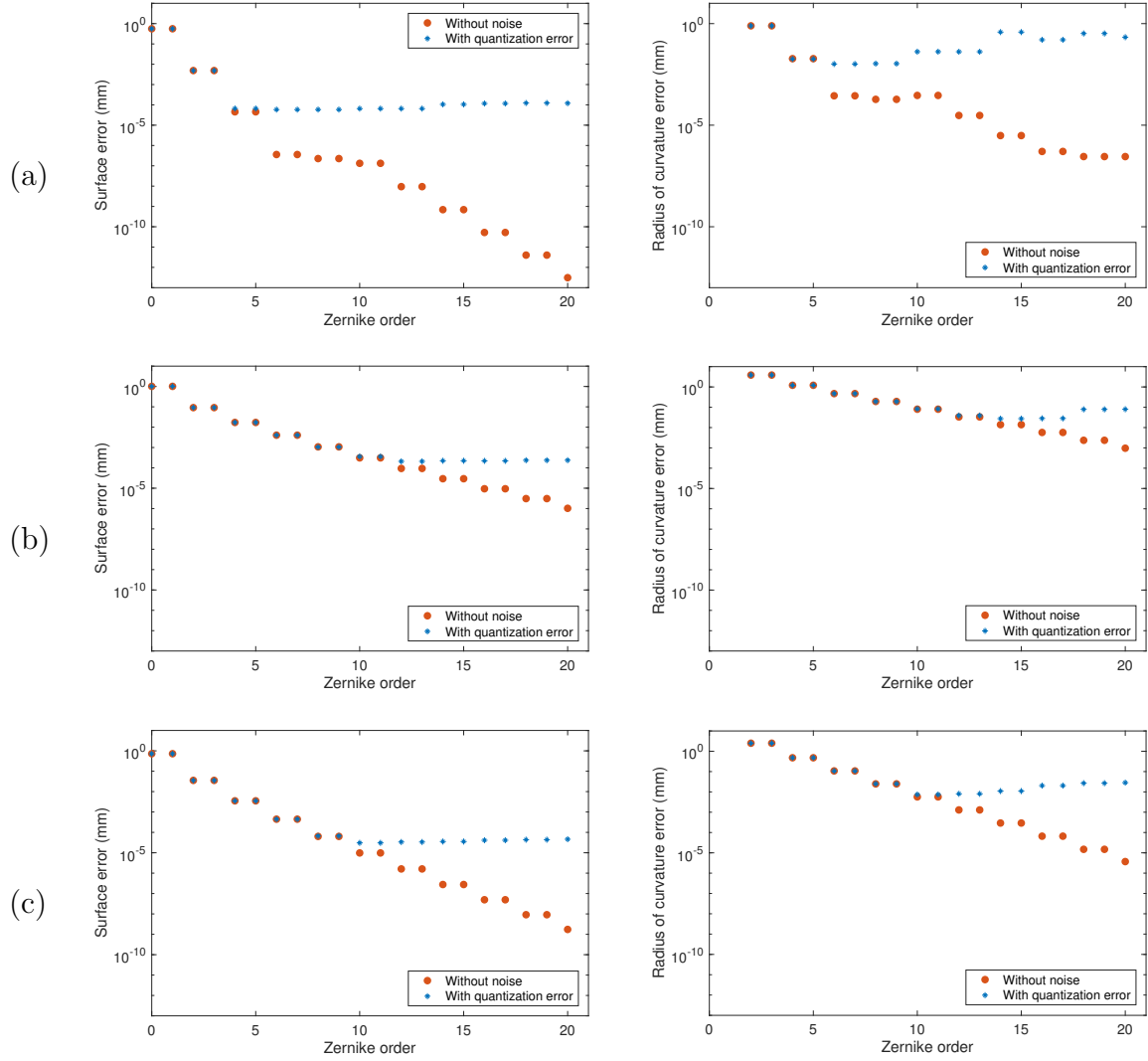


Figure 3.15: MAE in surface fit (left) and radius of curvature (right) for (a) Surface 1, (b) Surface 3, and (c) Surface 4.

error and the error in the corresponding curvature calculation it is more instructive to consider the *radius* of curvature, which is the reciprocal of the curvature and therefore shares the same units as the surface fit. We will define the mean absolute error in the meridional radius of curvature in the same manner as (3.20), only this time using the

reciprocal of the true and calculated values at each point:

$$\bar{e}_{\text{roc}} = \frac{1}{s-2b} \sum_{i=1}^{s-2b} \left| \frac{1}{\hat{k}(\mathfrak{x}_i)} - \frac{1}{k(\mathfrak{x}_i)} \right|. \quad (3.21)$$

As before, we will use  $\bar{e}_{\text{roc}}$  and  $\bar{e}_{\text{roc}}^*$  to respectively indicate the error in the non-quantized and quantized data.

Table 3.7 shows  $\bar{e}_{\text{roc}}$  and  $\bar{e}_{\text{roc}}^*$  using Zernike models of order  $N = 2, 3, \dots, 20$  for Surfaces 1, 3 and 4. The first three Zernike functions shown in Figure 3.1 and Table 3.1 ( $Z_1 = 1$ ,  $Z_2 = 2\rho \sin \theta$ , and  $Z_3 = 2\rho \cos \theta$ ) all clearly have zero curvature, as their second derivatives with respect to  $\rho$  are all zero. As a result, any polynomial expansion of radial order 0 or 1 will have an infinite radius of curvature everywhere, which renders futile any error estimates for models of order  $N = 0$  or  $N = 1$ . For similar reasons, Surface 2 has been entirely omitted from this discussion as its true radius of curvature is infinite.

Figure 3.15 depicts the results from Table 3.7 alongside the corresponding surface errors from Table 3.3. Note that both  $\bar{e}_{\text{roc}}$  and  $\bar{e}_{\text{roc}}^*$  display the same general convergence patterns as  $\bar{e}_k$  and  $\bar{e}_k^*$  from Figure 3.10, just in terms of different units, so our previous remarks about Zernike order for each surface are still applicable.

As we would expect, the radius of curvature converges much more slowly than surface fit, for both the non-quantized and quantized synthetic data. For the latter, the average error in the radius of curvature is at best two to three orders of magnitude greater for each surface than the smallest surface error we observed in Section 3.5.3. Even using non-quantized data, the accuracy of  $\bar{e}_{\text{roc}}$  appears to be limited to  $\sim 10^{-7}$  mm. All of these error values are invariant to the choice of finite difference step size.

## Principal Radius of Curvature

While we do want to be able to calculate curvature everywhere, the principal curvatures at the vertex (discussed in Section 3.4) carry special significance when dealing with optical components. These values are typically reported in terms of their corresponding radii of curvature  $R_1$  and  $R_2$ , which were defined in (3.16). Recall that an axisymmetric surface—such as Surfaces 1, 2, or 3—will satisfy  $R \equiv R_1 = R_2$ . For Surface 4 (the toric cap),  $R_1$  and  $R_2$  correspond to the principal radii of curvature at  $0^\circ$  and  $90^\circ$ , respectively.

Figure 3.16 shows estimates of the principal radii of curvature for Surfaces 1, 3, and 4 obtained using (3.18), while the absolute error between each estimate  $\hat{R}$  and the true

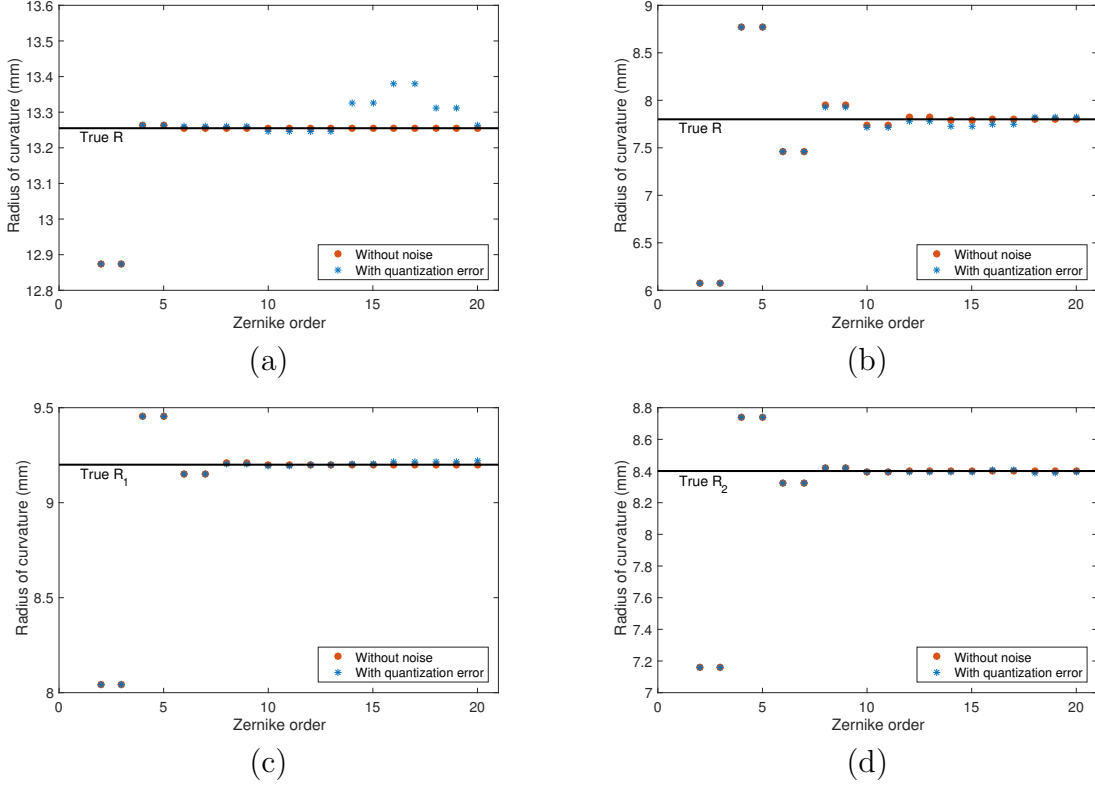


Figure 3.16: Radius of curvature for (a) Surface 1, (b) Surface 3, (c) Surface 4 at  $0^\circ$ , and (d) Surface 4 at  $90^\circ$ .

radius of curvature  $R$  is shown in Figure 3.17. The principal curvature error for Surface 2 was trivial for all Zernike orders, for both non-quantized and quantized data, so it will again be omitted from this discussion. Actual numerical values are listed in Table 3.8, with  $\hat{R}$  denoting the estimate obtained from the synthetic data without noise and  $\hat{R}^*$  specifying the estimate from quantized data.

As with the surface and curvature errors, the error in  $\hat{R}^*$  for Surface 1 is smallest for the 6th and 8th order Zernike fits. However, while  $\bar{e}^*$  and  $\bar{e}_{\text{roc}}^*$  were both a little bit lower for the 6th order fit, it turns out that the 8th order fit produces a slightly better estimate for the principal radius of curvature with  $|\hat{R}^* - R| = 5.4 \times 10^{-3}$  mm for  $N = 8$  compared to  $|\hat{R}^* - R| = 5.6 \times 10^{-3}$  mm for  $N = 6$ . This difference may seem minor; however, recall that the true value of  $R$  is specified to three digits of precision.

As hypothesized, the absolute error in  $\hat{R}^*$  for Surface 3 is minimized for the 12th order

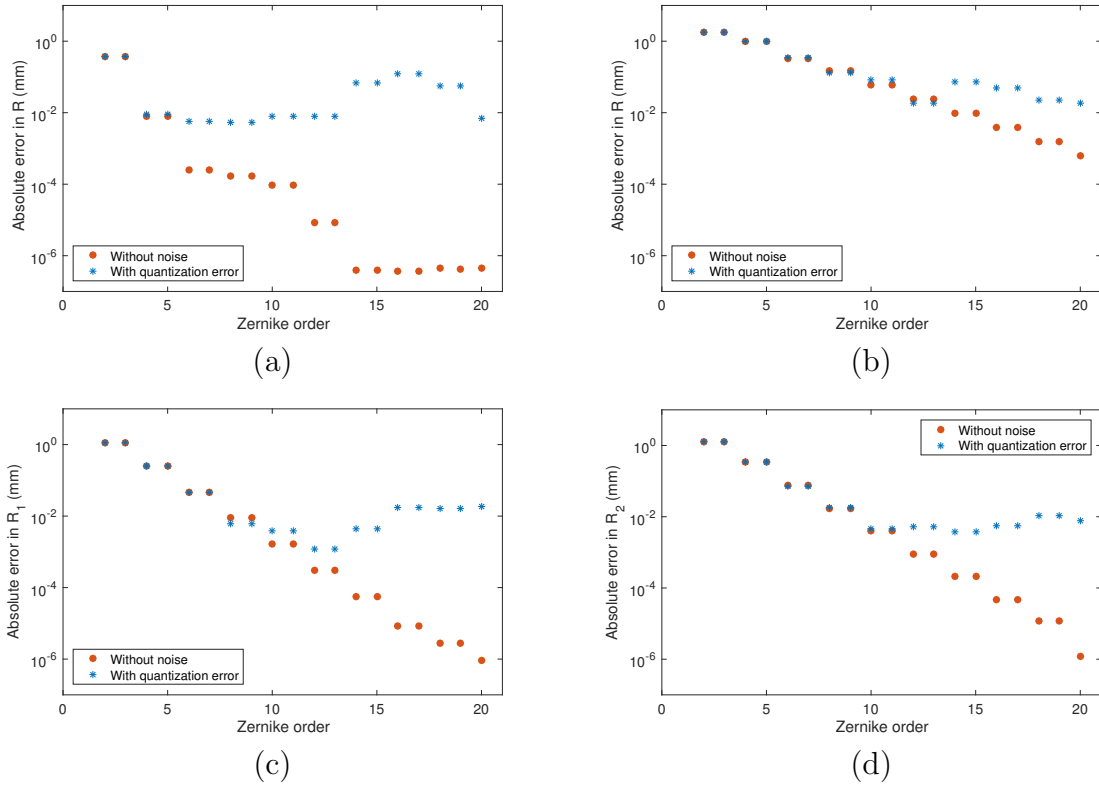


Figure 3.17: Absolute error in principal radius of curvature for (a) Surface 1, (b) Surface 3, (c) Surface 4 at  $0^\circ$  ( $R_1$ ), and (d) Surface 4 at  $90^\circ$  ( $R_2$ ).

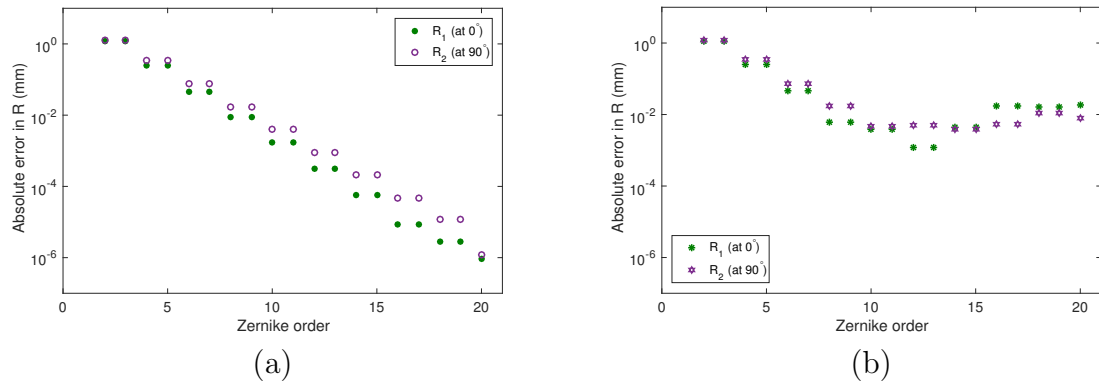


Figure 3.18: Absolute errors in principal radii of curvature for Surface 4 (a) without noise and (b) with quantization error.

Table 3.8: Principal radius of curvature estimates and absolute error (in mm) without noise ( $\hat{R}$ ) and with quantization error ( $\hat{R}^*$ ).

Surface 1 ( $R = 13.255$ mm)					Surface 3 ( $R = 7.8$ mm)				
$N$	$\hat{R}$	$ \hat{R}-R $	$\hat{R}^*$	$ \hat{R}^*-R $	$N$	$\hat{R}$	$ \hat{R}-R $	$\hat{R}^*$	$ \hat{R}^*-R $
2	12.874	$3.8 \times 10^{-1}$	12.874	$3.8 \times 10^{-1}$	2	6.078	1.7	6.078	1.7
3	12.874	$3.8 \times 10^{-1}$	12.874	$3.8 \times 10^{-1}$	3	6.078	1.7	6.078	1.7
4	13.263	$8.1 \times 10^{-3}$	13.264	$8.9 \times 10^{-3}$	4	8.769	$9.7 \times 10^{-1}$	8.766	$9.7 \times 10^{-1}$
5	13.263	$8.1 \times 10^{-3}$	13.264	$8.9 \times 10^{-3}$	5	8.769	$9.7 \times 10^{-1}$	8.766	$9.7 \times 10^{-1}$
6	13.255	$2.6 \times 10^{-4}$	13.261	$5.6 \times 10^{-3}$	6	7.465	$3.4 \times 10^{-1}$	7.461	$3.4 \times 10^{-1}$
7	13.255	$2.6 \times 10^{-4}$	13.261	$5.6 \times 10^{-3}$	7	7.465	$3.4 \times 10^{-1}$	7.461	$3.4 \times 10^{-1}$
8	13.255	$1.7 \times 10^{-4}$	13.260	$5.4 \times 10^{-3}$	8	7.946	$1.5 \times 10^{-1}$	7.932	$1.3 \times 10^{-1}$
9	13.255	$1.7 \times 10^{-4}$	13.260	$5.4 \times 10^{-3}$	9	7.946	$1.5 \times 10^{-1}$	7.932	$1.3 \times 10^{-1}$
10	13.255	$9.2 \times 10^{-5}$	13.247	$7.9 \times 10^{-3}$	10	7.742	$5.8 \times 10^{-2}$	7.718	$8.2 \times 10^{-2}$
11	13.255	$9.2 \times 10^{-5}$	13.247	$7.9 \times 10^{-3}$	11	7.742	$5.8 \times 10^{-2}$	7.718	$8.2 \times 10^{-2}$
12	13.255	$8.4 \times 10^{-6}$	13.247	$8.0 \times 10^{-3}$	12	7.824	$2.4 \times 10^{-2}$	7.781	$1.9 \times 10^{-2}$
13	13.255	$8.4 \times 10^{-6}$	13.247	$8.0 \times 10^{-3}$	13	7.824	$2.4 \times 10^{-2}$	7.781	$1.9 \times 10^{-2}$
14	13.255	$4.0 \times 10^{-7}$	13.324	$6.9 \times 10^{-2}$	14	7.790	$9.7 \times 10^{-3}$	7.726	$7.4 \times 10^{-2}$
15	13.255	$3.9 \times 10^{-7}$	13.324	$6.9 \times 10^{-2}$	15	7.790	$9.7 \times 10^{-3}$	7.726	$7.4 \times 10^{-2}$
16	13.255	$3.6 \times 10^{-7}$	13.380	$1.3 \times 10^{-1}$	16	7.804	$3.9 \times 10^{-3}$	7.749	$5.1 \times 10^{-2}$
17	13.255	$3.7 \times 10^{-7}$	13.380	$1.3 \times 10^{-1}$	17	7.804	$3.9 \times 10^{-3}$	7.749	$5.1 \times 10^{-2}$
18	13.255	$4.3 \times 10^{-7}$	13.312	$5.7 \times 10^{-2}$	18	7.798	$1.6 \times 10^{-3}$	7.823	$2.3 \times 10^{-2}$
19	13.255	$4.1 \times 10^{-7}$	13.312	$5.7 \times 10^{-2}$	19	7.798	$1.6 \times 10^{-3}$	7.823	$2.3 \times 10^{-2}$
20	13.255	$4.4 \times 10^{-7}$	13.262	$7.2 \times 10^{-3}$	20	7.801	$6.3 \times 10^{-4}$	7.819	$1.9 \times 10^{-2}$

Surface 4 ( $R_1 = 9.2$ mm)					Surface 4 ( $R_2 = 8.4$ mm)				
$N$	$\hat{R}_1$	$ \hat{R}_1-R_1 $	$\hat{R}_1^*$	$ \hat{R}_1^*-R_1 $	$N$	$\hat{R}_2$	$ \hat{R}_2-R_2 $	$\hat{R}_2^*$	$ \hat{R}_2^*-R_2 $
2	8.044	1.2	8.045	1.2	2	7.161	1.2	7.160	1.2
3	8.044	1.2	8.045	1.2	3	7.161	1.2	7.160	1.2
4	9.453	$2.5 \times 10^{-1}$	9.453	$2.5 \times 10^{-1}$	4	8.739	$3.4 \times 10^{-1}$	8.739	$3.4 \times 10^{-1}$
5	9.453	$2.5 \times 10^{-1}$	9.453	$2.5 \times 10^{-1}$	5	8.739	$3.4 \times 10^{-1}$	8.739	$3.4 \times 10^{-1}$
6	9.153	$4.7 \times 10^{-2}$	9.153	$4.7 \times 10^{-2}$	6	8.326	$7.4 \times 10^{-2}$	8.326	$7.4 \times 10^{-2}$
7	9.153	$4.7 \times 10^{-2}$	9.153	$4.7 \times 10^{-2}$	7	8.326	$7.4 \times 10^{-2}$	8.326	$7.4 \times 10^{-2}$
8	9.209	$8.9 \times 10^{-3}$	9.206	$6.3 \times 10^{-3}$	8	8.417	$1.7 \times 10^{-2}$	8.418	$1.8 \times 10^{-2}$
9	9.209	$8.9 \times 10^{-3}$	9.206	$6.3 \times 10^{-3}$	9	8.417	$1.7 \times 10^{-2}$	8.418	$1.8 \times 10^{-2}$
10	9.198	$1.7 \times 10^{-3}$	9.196	$3.8 \times 10^{-3}$	10	8.396	$4.0 \times 10^{-3}$	8.395	$4.6 \times 10^{-3}$
11	9.198	$1.7 \times 10^{-3}$	9.196	$3.8 \times 10^{-3}$	11	8.396	$4.0 \times 10^{-3}$	8.395	$4.6 \times 10^{-3}$
12	9.200	$3.1 \times 10^{-4}$	9.199	$1.2 \times 10^{-3}$	12	8.401	$9.1 \times 10^{-4}$	8.395	$5.1 \times 10^{-3}$
13	9.200	$3.1 \times 10^{-4}$	9.199	$1.2 \times 10^{-3}$	13	8.401	$9.1 \times 10^{-4}$	8.395	$5.1 \times 10^{-3}$
14	9.200	$5.7 \times 10^{-5}$	9.204	$4.4 \times 10^{-3}$	14	8.400	$2.1 \times 10^{-4}$	8.396	$3.8 \times 10^{-3}$
15	9.200	$5.7 \times 10^{-5}$	9.204	$4.4 \times 10^{-3}$	15	8.400	$2.1 \times 10^{-4}$	8.396	$3.8 \times 10^{-3}$
16	9.200	$8.7 \times 10^{-6}$	9.217	$1.7 \times 10^{-2}$	16	8.400	$4.6 \times 10^{-5}$	8.405	$5.4 \times 10^{-3}$
17	9.200	$8.7 \times 10^{-6}$	9.217	$1.7 \times 10^{-2}$	17	8.400	$4.6 \times 10^{-5}$	8.405	$5.4 \times 10^{-3}$
18	9.200	$2.9 \times 10^{-6}$	9.217	$1.7 \times 10^{-2}$	18	8.400	$1.2 \times 10^{-5}$	8.389	$1.1 \times 10^{-2}$
19	9.200	$2.9 \times 10^{-6}$	9.217	$1.7 \times 10^{-2}$	19	8.400	$1.2 \times 10^{-5}$	8.389	$1.1 \times 10^{-2}$
20	9.200	$9.0 \times 10^{-7}$	9.218	$1.8 \times 10^{-2}$	20	8.400	$1.2 \times 10^{-6}$	8.392	$7.7 \times 10^{-3}$

fit, despite a higher value of  $\bar{e}_{\text{roc}}^*$  for that order than the 14<sup>th</sup> and 16<sup>th</sup> order fits (all three of which have very similar surface errors). In fact,  $|\hat{R}^* - R|$  is four times as large for  $N = 14$  as it is for  $N = 12$ . The absolute error in the principal radius of curvature then decreases steadily until it once again reaches the same value at  $N = 20$  that it had for  $N = 12$ ; however,  $\bar{e}_{\text{roc}}^*$  for the 20th order fit is double that of the 12<sup>th</sup> order fit. Even though we initially identified the 14<sup>th</sup> and 16<sup>th</sup> order fits as possible candidates for the quantized Surface 3 data given their low  $\bar{e}^*$  and  $\bar{e}_{\text{roc}}^*$  values, we see that the principal radius of curvature for these models is disproportionately impacted by overfitting—at  $N = 14$ , the error in  $\hat{R}^*$  suddenly jumps up to nearly three times the value of average radius of curvature error, and  $|\hat{R}^* - R|$  remains nearly double  $\bar{e}_{\text{roc}}^*$  for  $N = 16$ .

The error estimates for both of Surface 4's principal radii of curvature from non-quantized and quantized data are shown together on the same plot in Figure 3.18. With or without quantization error, the estimates for  $R_1$  converge faster than the estimates for  $R_2$ —at least initially. However,  $\hat{R}_1^*$  achieves a clear optimum at  $N = 12$ , after which the error begins to increase again dramatically, while the error in  $\hat{R}_2^*$  more or less levels off starting at  $N = 10$ . This suggests that the estimate for  $R_1$  is likely to be more sensitive to the model order than the estimate for  $R_2$ .

In almost every case, the principal radius of curvature converges faster than average radius of curvature across the entire surface, which is the result we aimed to achieve by using the hexapolar sampling pattern. However, the principal radius of curvature estimates for the non-quantized Surface 1 data stop converging once the absolute error reaches  $10^{-7}$  mm at  $N = 14$ , which happens to be the same accuracy threshold we noted for the average radius of curvature error. In fact, the only other radius of curvature measurement to even attain a minimum error of  $10^{-7}$  mm is the estimate for  $R_1$  from the 20<sup>th</sup> order Zernike fit to the non-quantized Surface 4 data. Coupled with the fact that  $|\hat{R} - R|$  for Surface 1 is no longer the same for pairs of even and odd Zernike orders after  $N = 14$ , this implies that  $10^{-7}$  mm may well be a lower bound on the accuracy of our radius of curvature algorithm.

## 3.6 Summary

In Section 3.5.2, we confirmed that the error in the Zernike approximation of each surface is very similar regardless of whether we calculate the coefficients of the Zernike expansion

Table 3.9: Results (in mm) for the best Zernike orders for Surfaces 1, 3, and 4 using quantized data. (Bolded entries indicate optimal results.)

<b>Surface 1</b> (Aspheric lens, front)				
	$N = 4$	$N = 6$	$N = 8$	
$\bar{e}^*$	$6.6 \times 10^{-5}$	<b><math>5.8 \times 10^{-5}</math></b>	$5.9 \times 10^{-5}$	
$\bar{e}_{\text{roc}}^*$	$1.8 \times 10^{-2}$	<b><math>1.0 \times 10^{-2}</math></b>	$1.1 \times 10^{-2}$	
$ \hat{R}^* - R $	$8.9 \times 10^{-3}$	$5.6 \times 10^{-3}$	<b><math>5.4 \times 10^{-3}</math></b>	

<b>Surface 3</b> (Toric lens, front)				
	$N = 10$	$N = 12$	$N = 14$	$N = 16$
$\bar{e}^*$	$3.6 \times 10^{-4}$	<b><math>2.1 \times 10^{-4}</math></b>	$2.2 \times 10^{-4}$	$2.2 \times 10^{-4}$
$\bar{e}_{\text{roc}}^*$	$8.3 \times 10^{-2}$	$3.9 \times 10^{-2}$	<b><math>2.7 \times 10^{-2}</math></b>	$2.8 \times 10^{-2}$
$ \hat{R}^* - R $	$8.2 \times 10^{-2}$	<b><math>1.9 \times 10^{-2}</math></b>	$7.4 \times 10^{-2}$	$5.1 \times 10^{-2}$

<b>Surface 4</b> (Toric lens, back)				
	$N = 8$	$N = 10$	$N = 12$	$N = 14$
$\bar{e}^*$	$6.7 \times 10^{-5}$	<b><math>3.1 \times 10^{-5}</math></b>	$3.4 \times 10^{-5}$	$3.6 \times 10^{-5}$
$\bar{e}_{\text{roc}}^*$	$2.5 \times 10^{-2}$	<b><math>7.4 \times 10^{-3}</math></b>	$8.0 \times 10^{-3}$	$1.1 \times 10^{-2}$
$ \hat{R}_1^* - R_1 $	$6.3 \times 10^{-3}$	$3.8 \times 10^{-3}$	<b><math>1.2 \times 10^{-3}</math></b>	$4.4 \times 10^{-3}$
$ \hat{R}_2^* - R_2 $	$1.8 \times 10^{-2}$	$4.6 \times 10^{-3}$	$5.1 \times 10^{-3}$	<b><math>3.8 \times 10^{-3}</math></b>

by numerically integrating the design equations or perform a discrete Zernike transform on the non-quantized synthetic data. With respect to the order of the Zernike expansion, two of the three non-planar surfaces (spherical Surface 3 and toric Surface 4) displayed linear convergence, whereas Surface 1 (asphere) converged a bit more slowly. These same general patterns of linear and sublinear convergence also applied to the curvature in Section 3.5.4.

We also observed that the choice of Zernike order appears to have a much more pronounced impact on the accuracy of the curvature than on the accuracy of the surface reconstruction, particularly for the quantized data. Table 3.9 provides a summary of the Zernike orders that yielded the best results for Surfaces 1, 3, and 4<sup>iv</sup> for each of

<sup>iv</sup>Surface 2 (the flat back surface of the aspheric lens) requires only one Zernike polynomial, so the fit will predictably get worse as more polynomials are included in the fit.

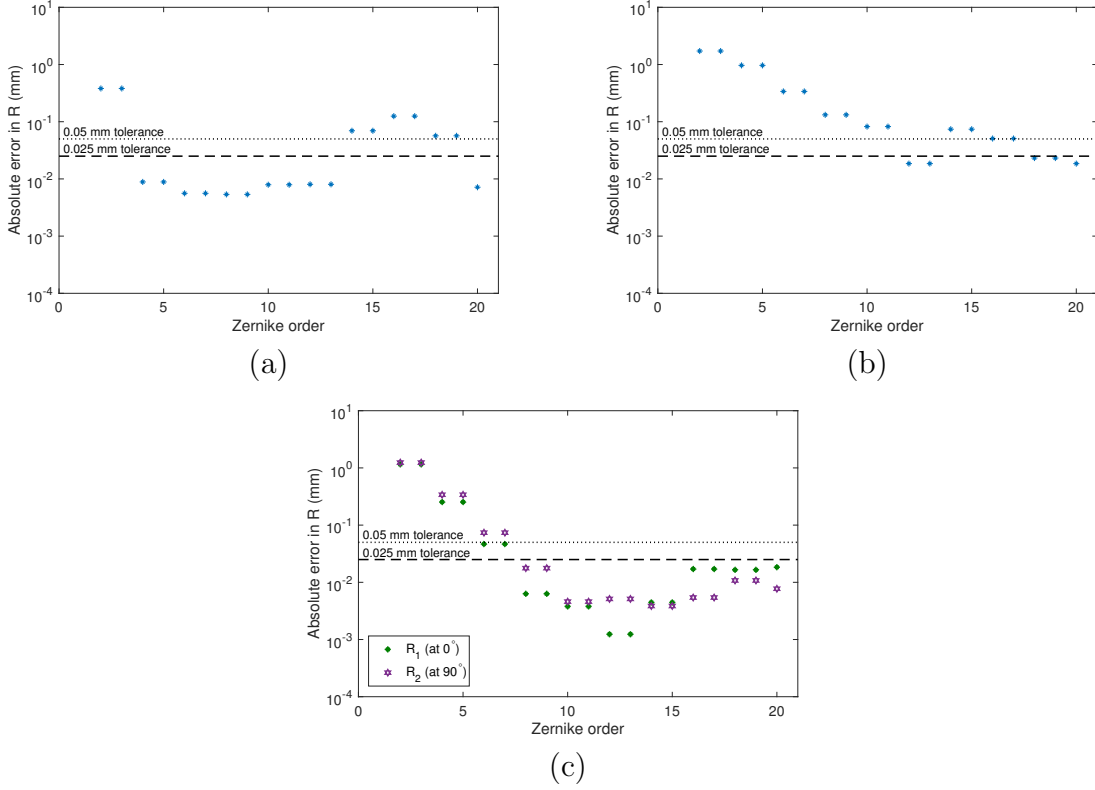


Figure 3.19: Absolute error in principal radius (or radii) of curvature from quantized synthetic data for (a) Surface 1, (b) Surface 3, and (c) Surface 4 relative to established ISO guidelines for ophthalmometer accuracy [35].

the three quantities of interest we considered: mean absolute error in surface fit ( $\bar{e}^*$ ), mean absolute error in radius of curvature ( $\bar{e}_{\text{roc}}^*$ ), and absolute error in principal radius of curvature ( $|\hat{R}^* - R|$ ).<sup>v</sup> For Surface 1, both the 6<sup>th</sup> and 8<sup>th</sup> order fits produced comparable results for all three quantities of interest. However, for Surfaces 3 and 4 the best model order depends on whether we care more about minimizing the overall error in meridional curvature or just the error in the principal curvature—in fact, the best Zernike order is not even the same for both principal curvatures of the toric back surface (Surface 4). This suggests that the problem of model order selection may have different solutions depending on which quantity of interest we want to prioritize—an issue we will revisit in

<sup>v</sup>Note that we have also included  $N = 4$  for Surface 1 and  $N = 10$  for Surface 3. Although other model orders performed better for these two surfaces using quantized data, these are the orders we chose for the analysis in Chapter 6, which uses Gaussian error in the synthetic data.

subsequent chapters.

Another notable conclusion of the results summarized in Table 3.9 is the relationship between the accuracy of our methods and the shape of the surface we are trying to measure. Due to its spheroidal shape, Surface 3 is consistently an order of magnitude worse than Surfaces 1 and 4. The ISO standards for ophthalmometers (ISO 10343:2014) specify two acceptable thresholds on the accuracy of an ophthalmometer (a device specifically intended for measuring the principal radius of curvature of a lens): such a device is considered a “Type A” ophthalmometer if twice of the standard deviation falls within 0.025 mm of the true value, or a “Type B” ophthalmometer if the result is within 0.05 mm [35]. Figure 3.19 demonstrates some possible problems with using the Zernike polynomial interpolation to achieve these goals. Even using idealized synthetic data with no additional noise beyond quantization error, we are only just able to meet either of these tolerances for Surface 3.

So far, we have discussed the implications of modeling each lens surface given ideal data without optical distortion. However, in a real lens, the back surface will require a different model from the front surface. In fact, we will see that the back surface model actually depends on the front surface model, as the precise nature of the refraction at the front surface boundary is determined by the shape of that boundary. In the following chapter, we will address the issue of how to incorporate this optical distortion due to refraction into a multi-surface lens model. We will also consider the implications of our choice of front surface model for refraction correction of the back surface and revisit the topic of which back surface model performs best in this context.

## Chapter 4

# Optical Distortion Correction for Two-Surface Lens Model

Although OCT allows for very high resolution imaging, one problem with using light waves for lens metrology is that lenses by design are meant to refract light. As the light from the sample arm crosses the anterior lens boundary, the change in refractive index of the medium through which the light is traveling causes it to bend; however, the imaging equipment assumes that it continues on its original trajectory. The consequence is that OCT images of all but the very first surface will appear warped.

Several methods have been proposed for correcting this effect in two dimensions based on either Snell's law or Fermat's principle of least time [73, 105]. However, these algorithms assume that refraction occurs within the same meridional plane as the B-scan. In the following sections, we will show why this assumption is incorrect, derive an algorithm for three-dimensional refraction correction, and validate this algorithm using synthetic data. We will also look at the local curvature estimates obtained using the methods of Chapter 3 on the dewarped posterior surface data.

## 4.1 Geometrical Optics

### 4.1.1 Background

The visible light spectrum consists of electromagnetic waves with wavelengths on the order of  $\lambda = 10^{-7}$  m. For many practical applications these wavelengths are at least

several orders of magnitude smaller than the scale of the other components involved—for example, the radius of curvature measurements in ophthalmology are typically no smaller than  $10^{-4}$  m. In the limiting case as  $\lambda$  approaches zero, Maxwell’s equations of electromagnetics give rise to the field of geometrical optics, in which light wave propagation is reformulated in terms of energy transport along curves called *light rays*. This approximation greatly simplifies the task of computing the trajectory of the light from the OCT scanner, thereby allowing us to account for any refraction effects that occur within the lens.

Given a monochromatic, homogeneous plane wave with negligible wavelength relative to other characteristic length scales, Maxwell’s equations can be reduced to a non-linear partial differential equation known as the eikonal equation:

$$\left(\frac{\partial \mathcal{S}}{\partial x}\right)^2 + \left(\frac{\partial \mathcal{S}}{\partial y}\right)^2 + \left(\frac{\partial \mathcal{S}}{\partial z}\right)^2 = n^2(x, y, z), \quad (4.1)$$

where the refractive index  $0 \leq n \leq \infty$  is a property of the medium through which the wave is traveling at the specified point. (A complete derivation of the eikonal equation from Maxwell’s equations can be found in Born and Wolf’s *Principles of Optics* [11, Ch. 3].) The solutions  $\mathcal{S}(x, y, z)$  (sometimes called the *optical paths*) to the eikonal equation are real scalar-valued functions such that the gradient  $\nabla \mathcal{S}$  indicates the wave’s direction of propagation.

According to *Principles of Optics*, *light rays* are the “orthogonal trajectories to the geometrical wavefronts  $\mathcal{S} = \text{constant}$ .” Since we know the gradient of  $\mathcal{S}$  must be orthogonal to these geometrical wavefronts, taking the square root of (4.1) allows us to write the equation for the light ray as

$$n\mathbf{u} = \nabla \mathcal{S}, \quad (4.2)$$

where

$$\mathbf{u} = \frac{\nabla \mathcal{S}}{\|\nabla \mathcal{S}\|}$$

is a unit vector in the direction of propagation of the light. Furthermore, Fermat’s principle of least time ensures that the light ray vector  $n\mathbf{u}$  always points in the same direction within a single isotropic medium (*i.e.*, local variations in the refractive index  $n$  are negligible).

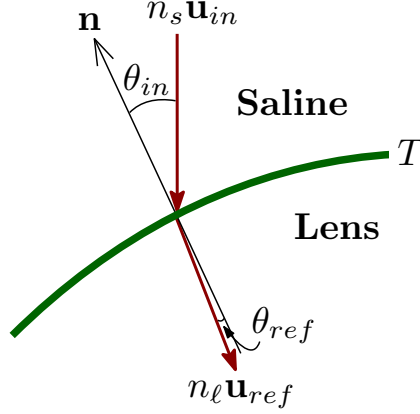


Figure 4.1: A light ray  $n_s \mathbf{u}_{in}$  incident to the interface  $T$  of the saline and the front of the lens. The refracted ray  $n_\ell \mathbf{u}_{ref}$  lies in the plane formed by  $n_s \mathbf{u}_{in}$  and the surface normal vector  $\mathbf{n}$ . The fact that  $n_s < n_\ell$  means that  $\theta_{in} < \theta_{ref}$ .

#### 4.1.2 Refraction at the Front Lens Surface

Recall that in Section 2.3 the refractive index of the saline was given by  $n_s = 1.338653$ , while the refractive indices of the two lenses were slightly greater at  $n_\ell = 1.49449$  (for the toric lens) or  $n_\ell = 1.59653$  (for the aspheric lens). If we assume that each medium is isotropic, we can represent the light ray vectors within the saline and the lens respectively by  $n_s \mathbf{u}_{in}$  (the *incident ray*) and  $n_\ell \mathbf{u}_{ref}$  (the *refracted ray*). We will show that several properties apply to a light ray traveling between the saline and the lens.

**Property 4.1.1.** *The refracted ray lies in the plane formed by the incident ray and the vector normal to the front surface of the lens at the point of incidence.*

**Property 4.1.2.** *Given that the lens has a higher refractive index than the saline, the angle of refraction will be smaller than the angle of incidence.*

Properties 4.1.1 and 4.1.2 are illustrated in Figure 4.1. The interface between the saline and the front of the lens, designated by  $T$ , represents a jump discontinuity in the refractive index. We indicate the outward-pointing unit vector normal to  $T$  at the point of incidence by  $\mathbf{n}$  (not to be confused with the refractive index  $n$ ). The plane formed by the incident ray  $n_s \mathbf{u}_{in}$  and the normal vector  $\mathbf{n}$  is called the *plane of incidence*. The *angle of incidence* ( $\theta_{in}$ ) and the *angle of refraction* ( $\theta_{ref}$ ) are defined as the respective angles between the incident and refracted rays and the normal vector. Note that  $\theta_{in}$  and  $\theta_{ref}$  are

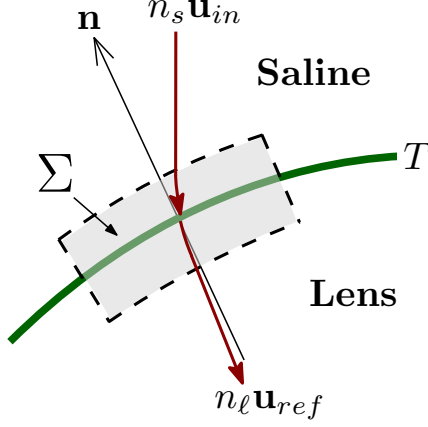


Figure 4.2: The 2D transition region  $\Sigma$  lies in the plane formed by the incident ray  $n_s \mathbf{u}_{in}$  and the normal vector  $\mathbf{n}$  at the point of incidence.

either both measured in the clockwise direction or both measured in the counterclockwise direction.

The precise amount by which the light ray is deflected at the saline-lens interface can be determined using Snell's law of refraction.

**Theorem 4.1.1 (Snell's Law).** *For any light ray crossing the boundary  $T$  between the saline and the lens, following relationship holds:*

$$n_s \sin(\theta_{in}) = n_\ell \sin(\theta_{ref}). \quad (4.3)$$

In 2D imaging, it is assumed that the plane of incidence at every point coincides with the plane of the image (*i.e.*, the B-scan). If this were true, these three properties would be sufficient to determine the impact of refraction for each A-scan so that we can dewarp the image accordingly. However, in practice there is no reason to assume that the normal vector at any particular point will lie within the B-scan. Even for an axisymmetric surface, off-axis imaging will result in precisely this problem. In the next section, we will develop a more general law of refraction, proving Properties 4.1.1 and 4.1.2 and Snell's law in the process.

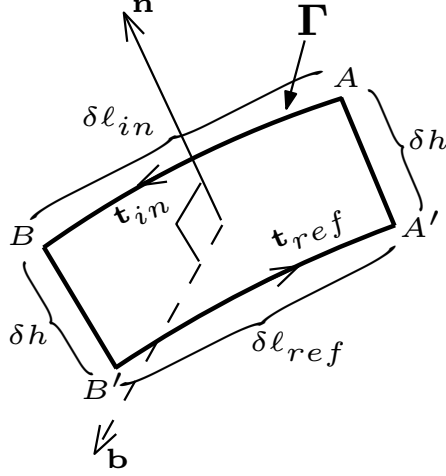


Figure 4.3: The boundary of  $\Sigma$  (shown in Figure 4.2) is the piecewise-smooth curve  $\Gamma$  that runs counterclockwise around  $ABB'A'$ . The unit vectors  $\mathbf{t}_{in}$  and  $\mathbf{t}_{ref}$  are respectively normal to sides  $AB$  and  $B'A'$ , while  $\mathbf{b}$  is the out-of-plane unit vector perpendicular  $\Sigma$ .

### 4.1.3 Proof of General Boundary Conditions

To understand the behavior of a light ray when the interface  $T$  between the two media consists of an arbitrary smooth surface in  $\mathbb{R}^3$ , we will derive a more general set of boundary conditions using an analogous approach to finding the boundary conditions for an electric field at a surface discontinuity [11, 95].

Instead of the discontinuous interface  $T$ , we imagine a smooth “transition layer” in which the refractive index changes continuously as we cross from one medium into the other. Let  $\Sigma$  be a plane element of this transition layer that contains both the incident ray vector  $n_s \mathbf{u}_{in}$  and the outward-pointing unit vector  $\mathbf{n}$  normal to  $T$  at the point of incidence. The transition region  $\Sigma$  is illustrated in Figure 4.2. As previously mentioned, we will prove that the refracted ray  $n_\ell \mathbf{u}_{ref}$  shown in Figure 4.2 must in fact lie in the same plane as the rest of the image.

The boundary of  $\Sigma$  is the piecewise smooth curve  $\Gamma$  shown in Figure 4.3, running counterclockwise around the “rectangle”  $ABB'A'$ . The upper and lower “sides” of  $\Gamma$  have length  $|AB| = \delta\ell_{in}$  and  $|B'A'| = \delta\ell_{ref}$ , and are parallel to and equidistant from the surface  $T$ . They are joined by two perpendicular components of length  $|A'A| = |B'B| = \delta h$ .

If  $\mathbf{b}$  is the unit vector perpendicular to the plane containing  $\Sigma$  (also shown in Fig-

ure 4.3), it follows from Stokes' theorem that

$$\oint_{\Gamma} n\mathbf{u} \cdot d\mathbf{\Gamma} = \iint_{\Sigma} (\nabla \times n\mathbf{u}) \cdot \mathbf{b} d\Sigma. \quad (4.4)$$

The surface integral must be identically zero given (4.2) and properties of vector calculus, which hold that

$$\nabla \times n\mathbf{u} = \nabla \times \nabla S = 0.$$

Therefore, (4.4) simplifies to

$$\oint_{\Gamma} n\mathbf{u} \cdot d\mathbf{\Gamma} = 0. \quad (4.5)$$

The line integral can be written out in terms of the contributions from each piece of the curve  $\Gamma$  as

$$\oint_{\Gamma} n\mathbf{u} \cdot d\mathbf{\Gamma} = n_s \mathbf{u}_{in} \cdot \delta\ell_{in} \mathbf{t}_{in} + n_{\ell} \mathbf{u}_{ref} \cdot \delta\ell_{ref} \mathbf{t}_{ref} + \text{contributions from the end pieces},$$

where  $\mathbf{t}_{in}$  and  $\mathbf{t}_{ref}$  are the unit vectors tangent to their respective sides in the direction of integration (Figure 4.3). Since this is a dot product, the contribution from the two perpendicular end pieces approaches zero as  $\delta h \rightarrow 0$ . Furthermore, in this limiting case the lengths of the two parallel sides approach a common value  $\delta\ell_{in} \rightarrow \delta\ell_{ref} \equiv \delta\ell$ , and the two unit tangent vectors are simply given by  $\mathbf{t}_{in} = \mathbf{b} \times \mathbf{n}$  and  $\mathbf{t}_{ref} = -\mathbf{b} \times \mathbf{n}$ . Thus, evaluating (4.5) around the entire curve yields

$$\begin{aligned} \oint_{\Gamma} n\mathbf{u} \cdot d\mathbf{\Gamma} &= n_s \mathbf{u}_{in} \cdot \delta\ell (\mathbf{b} \times \mathbf{n}) + n_{\ell} \mathbf{u}_{ref} \cdot \delta\ell (-\mathbf{b} \times \mathbf{n}) \\ &= \delta\ell (n_s \mathbf{u}_{in} - n_{\ell} \mathbf{u}_{ref}) \cdot (\mathbf{b} \times \mathbf{n}) \\ &= \delta\ell \mathbf{b} \cdot \left( (n_{\ell} \mathbf{u}_{ref} - n_s \mathbf{u}_{in}) \times \mathbf{n} \right) = 0, \end{aligned}$$

from which it follows that

$$(n_s \mathbf{u}_{in} - n_{\ell} \mathbf{u}_{ref}) \times \mathbf{n} = 0. \quad (4.6)$$

Properties 4.1.1 and 4.1.2 from Section 4.1.2 and Snell's law all follow from (4.6). We can immediately see that in order for (4.6) to hold, the incident ray  $n_s \mathbf{u}_{in}$ , the refracted ray  $n_{\ell} \mathbf{u}_{ref}$ , and the normal vector  $\mathbf{n}$  must all lie in the same plane. If we let  $\theta_{in}$  and  $\theta_{ref}$  respectively represent the angles between the normal vector and the incident and

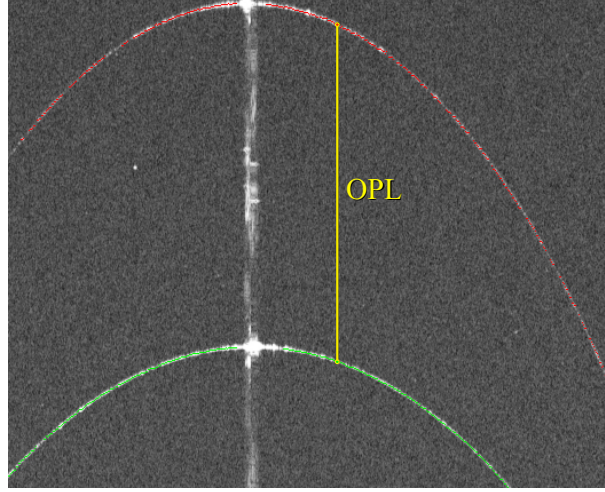


Figure 4.4: The OPL is the vertical distance between corresponding A-scans.

refracted rays and recall that  $\mathbf{u}_{in}$  and  $\mathbf{u}_{ref}$  are unit vectors, then we can simplify (4.6) to get

$$\begin{aligned} n_s \mathbf{u}_{in} \times \mathbf{n} &= n_\ell \mathbf{u}_{ref} \times \mathbf{n} \\ n_s \|\mathbf{u}_{in}\| \|\mathbf{n}\| \sin(\theta_{in}) &= n_\ell \|\mathbf{u}_{ref}\| \|\mathbf{n}\| \sin(\theta_{ref}) \\ n_s \sin(\theta_{in}) &= n_\ell \sin(\theta_{ref}). \end{aligned}$$

This is precisely the formula for Snell's law, given in (4.3).

Furthermore, (4.6) also implies that the tangential component of the ray vector is the same on both sides of the saline-lens interface. Since the lens has a higher refractive index than the saline ( $n_s < n_\ell$ ), this means that the component of the refracted ray that is parallel to  $\mathbf{n}$  must be larger than the corresponding component of the incident ray. Therefore, the light ray bends toward the normal vector as it crosses the boundary. For a convex surface like the front of the aspheric and toric lenses, the net effect is that the refracted light always bends in the direction of the optical axis.

#### 4.1.4 Path Length

The *optical path length* (OPL) is the apparent distance between consecutive surfaces along a given ray vector. As illustrated in Figure 4.4, this is simply the vertical distance

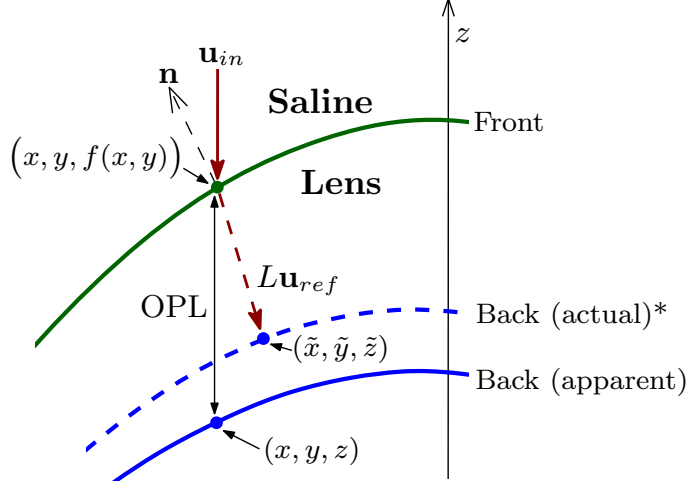


Figure 4.5: Illustration of optical path length (OPL) versus geometric path length ( $L$ ) for a given B-scan. By assumption, the front surface (green) and *apparent* back surface (solid blue) are in the same meridional plane as the B-scan, which is defined by the  $z$ -axis and the incident light ray  $\mathbf{u}_{in}$ . However, the normal vector  $\mathbf{n}$  may be out-of-plane. The refracted ray  $L\mathbf{u}_{ref}$  is contained in the plane of incidence formed by  $\mathbf{u}_{in}$  and  $\mathbf{n}$ .\*

---

\*Note that the normal vector at an arbitrary second point on the front surface in the B-scan need not lie within the particular plane of incidence illustrated in this example. Therefore, the other dewarped back surface points (represented by the dashed middle curve) may not be contained in the same plane as the vectors  $\mathbf{n}$  and  $\mathbf{u}_{ref}$ .

between corresponding surfaces within the same A-scan—*i.e.*, the same horizontal pixel position in the OCT image.

In terms of the original point cloud data, the OPL between every pair of points  $(\mathfrak{X}, w^a)$  and  $(\mathfrak{X}, w^p)$  is the difference

$$\text{OPL} = w^a - w^p.^i$$

The actual distance traveled by the refracted light ray before it intersects the back surface (the *geometric path length*) can be recovered by dividing the OPL by the medium's refractive index:

$$L = \text{OPL}/n_\ell.$$

---

<sup>i</sup>Recall from Section 2.3 that we actually divided *all* the point cloud data by  $n_s$  in order to correct the path length for the front surface points, thereby over-correcting the back surface points. Thus, when calculating the optical path length from the raw data it will also be necessary for us to multiply by  $n_s$  to account for this over-correction.

As discussed in Section 2.2.2, sometimes there is a valid back surface segmentation result  $w^p$  at  $\mathfrak{X}$ , but no corresponding front surface point  $(\mathfrak{X}, w^a)$ . For this reason, it is more robust to calculate the path length using the Zernike interpolated point  $f(\mathfrak{X})$  on the front surface rather than the data point  $w^a$ .

If we express the lateral coordinate  $\mathfrak{X}$  using Cartesian coordinates, the geometric path length can also be conceived in terms of the Euclidean distance

$$L = \sqrt{\left(\tilde{x} - x\right)^2 + \left(\tilde{y} - y\right)^2 + \left(\tilde{z} - f(x, y)\right)^2},$$

where  $(\tilde{x}, \tilde{y}, \tilde{z})$  is the (unknown) corrected point of intersection with the back surface of a light ray crossing the front surface at  $(x, y, f(x, y))$ . We can express the vector connecting these two points as

$$L\mathbf{u}_{ref} = \left\langle \tilde{x} - x, \tilde{y} - y, \tilde{z} - f(x, y) \right\rangle. \quad (4.7)$$

(For the 2D algorithm in Section 4.2.1, we use the 2D analog for  $L$  and  $\mathbf{u}_{ref}$ .)

The relationship between the optical path length and the geometric path length is illustrated in Figure 4.5, which depicts the front surface and apparent back surface as they would appear according to one 2D frame of point cloud data. While the incident ray  $\mathbf{u}_{in}$  is assumed to be parallel to the CT axis, the surface normal vector  $\mathbf{n}$ —and therefore the corrected back surface point  $(\tilde{x}, \tilde{y}, \tilde{z})$ —may not lie within the meridional plane of the B-scan.

## 4.2 Refraction Correction

### 4.2.1 Dewarping in 2D

Before we develop the 3D algorithm (detailed in Section 4.2.2), we will first consider the case where refraction correction is performed in 2D using meridional planes determined by the original sampling pattern (*i.e.*, the B-scans).

Without loss of generality, we can choose to model the front surface of the lens by

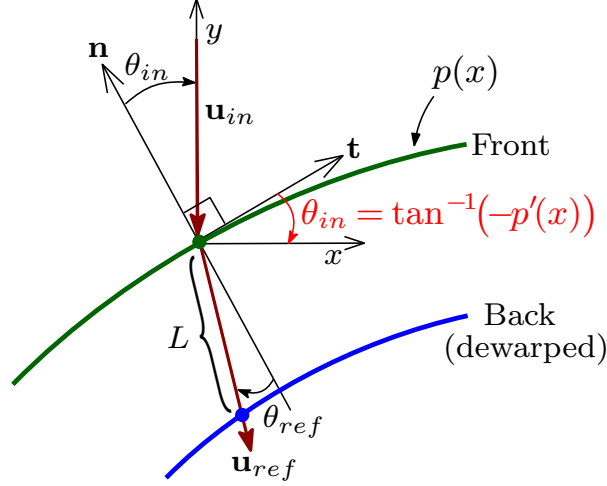


Figure 4.6: Geometry of the angle of incidence  $\theta_{in}$  for a 2D surface.

fitting the point cloud data for each frame to the  $N^{\text{th}}$ -degree polynomial

$$p(x) = \sum_{k=0}^N c_k x^k. \text{ii}$$

For a telecentric<sup>iii</sup> incident light ray  $\mathbf{u}_{in} = -\mathbf{e}_y = \langle 0, -1 \rangle$ , the angle of incidence  $\theta_{in}$  is congruent with the angle between the  $x$ -axis and the tangent vector at the point of incidence

$$\mathbf{t} = \langle 1, p'(x) \rangle.$$

(This follows from some straightforward geometry, illustrated in Figure 4.6.) Thus,  $\theta_{in}$  is related to the derivative at  $x$  according to

$$\tan(\theta_{in}) = -p'(x), \quad -\frac{\pi}{2} \leq \theta_{in} \leq \frac{\pi}{2}. \quad (4.8)$$

We use  $-p'(x)$  rather than  $p'(x)$  in order to preserve the convention that angles measured in the counter-clockwise direction starting from the normal vector are positive, whereas angles measured in the clockwise direction are negative. This means that  $\theta_{in}$  will have

<sup>ii</sup>There are numerous other equally suitable models. However, this is the method currently used by Leica Microsystems (with  $N = 20$ ).

<sup>iii</sup>In  $\mathbb{R}^2$ , we let the CT axis define the  $y$ -axis of the system rather than the  $z$ -axis.

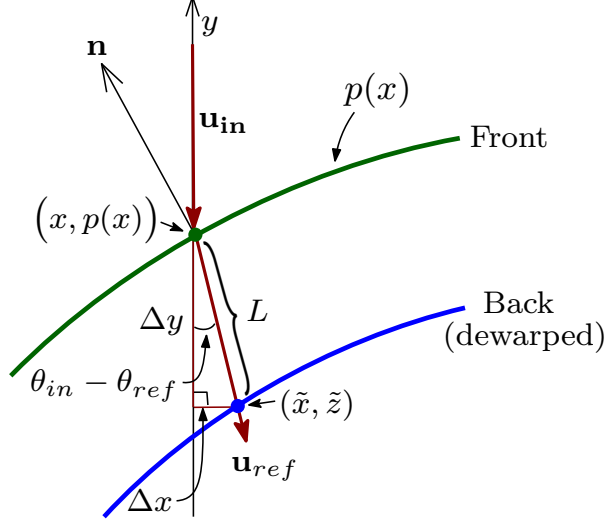


Figure 4.7: Decomposition of refracted light ray  $L\mathbf{u}_{ref}$  into  $x$ - and  $y$ -components.

the opposite sign from  $p'(x)$ .

The angle of refraction can be determined by substituting (4.8) into (4.3), yielding

$$\sin(\theta_{ref}) = \frac{n_s}{n_\ell} \sin(\theta_{in}) = -\frac{n_s}{n_\ell} \frac{p'(x)}{\sqrt{1 + p'(x)^2}}, \quad -\frac{\pi}{2} \leq \theta_{ref} \leq \frac{\pi}{2}. \quad (4.9)$$

Since  $n_s < n_\ell$ , we can see from (4.8–4.9) that

$$|\sin(\theta_{ref})| < |\sin(\theta_{in})| \leq 1,$$

and that  $\theta_{ref}$  must have the same sign as  $\theta_{in}$ . This implies that

$$|\theta_{ref}| < |\theta_{in}| \leq \frac{\pi}{2}, \quad \text{where } 0 \leq (\theta_{ref})(\theta_{in}). \quad (4.10)$$

As explained in Section 4.1.4, the refracted light ray  $\mathbf{u}_{ref}$  travels a distance  $L = \frac{\text{OPL}}{n_\ell}$  before crossing the lower surface, where the OPL is determined directly from the original point cloud data. Projections of  $L\mathbf{u}_{ref}$  onto the  $y$ - and  $x$ -axis (illustrated in Figure 4.7)

are respectively given by

$$\Delta y = L \cos(\theta_{in} - \theta_{ref}) \quad (4.11a)$$

$$\Delta x = L \sin(\theta_{in} - \theta_{ref}). \quad (4.11b)$$

Note that when the normal vector is parallel to the  $z$ -axis (*e.g.*, at the vertex of the lens), the slope of the tangent to the front surface is  $p'(x) = 0$ , so  $\theta_{in} = \theta_{ref} = 0$ . In this situation, (4.11) yields  $\Delta y = L$  and  $\Delta x = 0$ —that is, the  $y$ -coordinate is simply given by  $p(x) - \Delta y = p(x) - L$  and the  $x$ -coordinate does not require a correction at all. In fact, (4.10) implies that

$$|\theta_{in} - \theta_{ref}| < \frac{\pi}{2},$$

so  $0 < \cos(\theta_{in} - \theta_{ref}) \leq 1$  everywhere and  $\Delta y$  will therefore always be positive. Since we know that the back surface is always located below the front surface, it is safe to assume that the refraction-corrected  $y$ -coordinate is always given by  $p(x) - \Delta y$ .

In Section 4.1.3 we noted that in this particular application—*e.g.*, a lens with a convex front surface and a refractive index greater than that of the medium in which it is suspended—the refracted light ray will always bend in the direction of the optical axis. Specifically, when  $p'(x)$  is positive (as in the case depicted in Figure 4.7), the true  $x$ -coordinate will actually be larger than the apparent value, while the opposite will be true when  $p'(x)$  is negative. Based on our observations earlier in this section, we can conclude that

$$\begin{aligned} p'(x) > 0 &\iff \theta_{in} - \theta_{ref} \in \left(-\frac{\pi}{2}, 0\right) &\iff \sin(\theta_{in} - \theta_{ref}) \in (-1, 0) &\iff \Delta x < 0, \\ p'(x) < 0 &\iff \theta_{in} - \theta_{ref} \in \left(0, \frac{\pi}{2}\right) &\iff \sin(\theta_{in} - \theta_{ref}) \in (0, 1) &\iff \Delta x > 0. \end{aligned}$$

In other words,  $\Delta x$  will be positive when the derivative is negative, and negative when the derivative is positive. Therefore, the refraction-corrected coordinates  $(\tilde{x}, \tilde{z})$  of the back surface are given by

$$\begin{aligned} \tilde{z} &= p(x) - L \cos(\theta_{in} - \theta_{ref}) \\ \tilde{x} &= x - L \sin(\theta_{in} - \theta_{ref}). \end{aligned}$$

We can also rewrite the cosine and sine in terms of  $p'(x)$  and simplify the result using

trigonometric properties to get

$$\begin{aligned}\cos(\theta_{in} - \theta_{ref}) &= \frac{1}{1 + p'(x)^2} \left( \sqrt{1 + \left(1 - \frac{n_s^2}{n_\ell^2}\right) p'(x)^2} + \left(\frac{n_s}{n_\ell}\right) p'(x)^2 \right) \\ \sin(\theta_{in} - \theta_{ref}) &= -\frac{p'(x)}{1 + p'(x)^2} \left( \sqrt{1 + \left(1 - \frac{n_s^2}{n_\ell^2}\right) p'(x)^2} - \frac{n_s}{n_\ell} \right).\end{aligned}$$

Once again, we use the fact that  $n_s < n_\ell$  to deduce that a)  $\cos(\theta_{in} - \theta_{ref})$  will be strictly positive for all values of  $p'(x)$ , and b)  $\text{sgn}(\sin(\theta_{in} - \theta_{ref})) = -\text{sgn}(p'(x))$ .

In summary, the 2D dewarping algorithm asserts that the refraction-corrected coordinates  $(\tilde{x}, \tilde{z})$  of the back lens surface for each A-scan can be computed explicitly in terms of known quantities

$$\tilde{x} = x + L \frac{p'(x) \left( \sqrt{1 + \left(1 - \frac{n_s^2}{n_\ell^2}\right) p'(x)^2} - \frac{n_s}{n_\ell} \right)}{1 + p'(x)^2} \quad (4.12a)$$

$$\tilde{z} = p(x) - L \frac{\sqrt{1 + \left(1 - \frac{n_s^2}{n_\ell^2}\right) p'(x)^2} + \left(\frac{n_s}{n_\ell}\right) p'(x)^2}{1 + p'(x)^2}, \quad (4.12b)$$

where  $L = \frac{\text{OPL}}{n_\ell}$  is the geometric path length in the direction of the refracted light ray between the point of incidence  $(x, p(x))$  and the lower surface (described in Section 4.1.4).

### 4.2.2 Dewarping in 3D

The main problem with the 2D refraction correction algorithm in Section 4.2.1 is that it relies on the assumption that the normal vector  $\mathbf{n}$  lies in the meridional plane. However, this is only true for surfaces that are symmetric with respect to reflection across an arbitrary plane through the  $z$ -axis (*i.e.*, a surface that does not require odd Zernike polynomials to fit). Even when imaging a surface that does meet this condition, it can be virtually impossible to ensure that the CT-axis and optical axis are perfectly aligned, and small manufacturing defects may cause non-trivial local deviations in the surface gradient. Thus, we want a general algorithm that will account for refraction in three dimensions. We have chosen to use the forward ray tracing method proposed by Zhao et

al. in [110].

To motivate the 3D algorithm, it is more straightforward to return to the vector notation from Section 4.1. If  $z = f(x, y)$  is the Zernike representation of the top surface, then the upward-pointing unit normal at some incident point  $(x, y, z) = (x, y, f(x, y))$  is given by

$$\mathbf{n} = \frac{\nabla(z - f(x, y))}{|\nabla(z - f(x, y))|} = \frac{\langle -f_x, -f_y, 1 \rangle}{\sqrt{f_x^2 + f_y^2 + 1}}, \quad (4.13)$$

where  $f_x \equiv f_x(x, y)$  and  $f_y \equiv f_y(x, y)$  denote the  $x$  and  $y$  partial derivatives of  $f(x, y)$ , evaluated at the point of incidence. Recall that the incident light ray is taken to be antiparallel to the  $z$ -axis, so the corresponding unit vector is given by

$$\mathbf{u}_{in} = -\mathbf{e}_z = \langle 0, 0, -1 \rangle. \quad (4.14)$$

The corrected  $z$ -coordinate for the 3D case can be determined in the same manner as the  $y$ -coordinate in the 2D case (where the incident light ray pointed in the negative  $y$ -direction). Using a similar argument to the one in Section 4.2.1, the true vertical coordinate for the back surface is given by

$$\tilde{z} = f(x, y) - \Delta z, \quad (4.15a)$$

where  $\Delta z$  is the projection of  $L\mathbf{u}_{ref}$  along the vertical axis

$$\Delta z = L \cos(\theta_{in} - \theta_{ref}). \quad (4.15b)$$

The 3D case is illustrated in Figure 4.8 (recall that the plane of the image may not correspond to any of the original B-scans).

To find the angle of incidence, we use the definition of the angle between the two unit vectors in (4.13–4.14):

$$\cos(\theta_{in}) = \mathbf{n} \cdot -\mathbf{u}_{in} = \mathbf{n} \cdot \mathbf{e}_z = \frac{1}{\sqrt{f_x^2 + f_y^2 + 1}}.$$

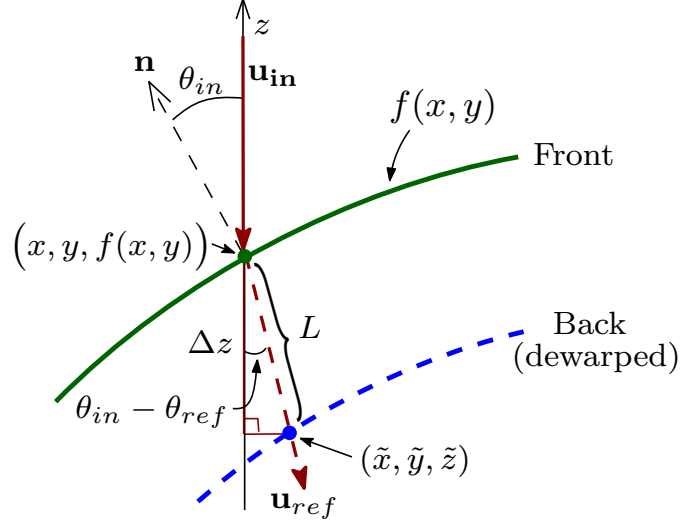


Figure 4.8: Projection of the refracted light ray  $\mathbf{u}_{ref}$  onto the  $z$ -axis in  $\mathbb{R}^3$ . In this case the normal vector  $\mathbf{n}$  is *not* assumed to lie in the meridional plane. Therefore,  $\mathbf{u}_{ref}$  lies in the plane of incidence (determined by  $\mathbf{n}$  and  $\mathbf{u}_{in}$ ), so both  $\theta_{in}$  and  $\theta_{ref}$  must also be measured in the plane of incidence.

The angle of refraction is once again given by Snell's law

$$\sin(\theta_{ref}) = \frac{n_s}{n_\ell} \sin(\theta_{in}) = \frac{n_s}{n_\ell} \sqrt{\frac{f_x^2 + f_y^2}{f_x^2 + f_y^2 + 1}}.$$

We can now rewrite  $\cos(\theta_{in} - \theta_{ref})$  explicitly in terms of known quantities using the same trigonometric properties we employed in Section 4.2.1. The cosine of the difference becomes

$$\cos(\theta_{in} - \theta_{ref}) = \frac{\sqrt{1 + \left(1 - \frac{n_s^2}{n_\ell^2}\right)(f_x^2 + f_y^2)} + \frac{n_s}{n_\ell}(f_x^2 + f_y^2)}{1 + f_x^2 + f_y^2}, \quad (4.15c)$$

which we can once again see will be strictly positive for  $n_s > n_\ell$ .

To find the corrected values  $\tilde{x}$  and  $\tilde{y}$ , we refer back to (4.6). The normal and incident vectors  $\mathbf{n}$  and  $\mathbf{u}_{in}$  are given by (4.13–4.14), while the unit vector for the refracted ray,

$$\mathbf{u}_{ref} = \frac{1}{L} \langle \tilde{x} - x, \tilde{y} - y, \tilde{z} - f(x, y) \rangle, \quad (4.16)$$

can be obtained from (4.16). Substituting these into (4.6) yields

$$\left(n_s \langle 0, 0, -1 \rangle - \frac{n_\ell}{L} \langle \tilde{x} - x, \tilde{y} - y, \tilde{z} - f(x, y) \rangle\right) \times \frac{\langle -f_x, -f_y, 1 \rangle}{\sqrt{f_x^2 + f_y^2 + 1}} = 0.$$

The first two components of the cross product provide equations for the corrected  $x$ - and  $y$ -coordinates (the third simply yields an identity):

$$\begin{aligned}\tilde{x} &= x + f_x \left( f(x, y) - \tilde{z} - \frac{n_s}{n_\ell} L \right) \\ \tilde{y} &= y + f_y \left( f(x, y) - \tilde{z} - \frac{n_s}{n_\ell} L \right).\end{aligned}$$

This can be written explicitly in terms of known quantities by substituting  $\Delta z = f(x, y) - \tilde{z}$  and using (4.15) to simplify the result. The corrected coordinates  $(\tilde{x}, \tilde{y}, \tilde{z})$  for the back surface are thus given by the system

$$\tilde{x} = x + L \frac{f_x \left( \sqrt{1 + \left(1 - \frac{n_s^2}{n_\ell^2}\right) (f_x^2 + f_y^2)} - \frac{n_s}{n_\ell} \right)}{1 + f_x^2 + f_y^2} \quad (4.17a)$$

$$\tilde{y} = y + L \frac{f_y \left( \sqrt{1 + \left(1 - \frac{n_s^2}{n_\ell^2}\right) (f_x^2 + f_y^2)} - \frac{n_s}{n_\ell} \right)}{1 + f_x^2 + f_y^2} \quad (4.17b)$$

$$\tilde{z} = f(x, y) - L \frac{\sqrt{1 + \left(1 - \frac{n_s^2}{n_\ell^2}\right) (f_x^2 + f_y^2)} + \frac{n_s}{n_\ell} (f_x^2 + f_y^2)}{1 + f_x^2 + f_y^2}, \quad (4.17c)$$

where  $L$  is once again the geometric path length between the two surfaces corresponding to the point of incidence  $(x, y, f(x, y))$ .

Furthermore, substituting the results of (4.17) into (4.16) also allows us to directly calculate the components of the refracted ray vector

$$\mathbf{u}_{ref} = \begin{pmatrix} u_x \\ u_y \\ u_z \end{pmatrix} = \frac{\sqrt{1 + \left(1 - \frac{n_s^2}{n_\ell^2}\right) (f_x^2 + f_y^2)}}{1 + f_x^2 + f_y^2} \begin{pmatrix} f_x \\ f_y \\ -1 \end{pmatrix} - \frac{\frac{n_s}{n_\ell}}{1 + f_x^2 + f_y^2} \begin{pmatrix} f_x \\ f_y \\ f_x^2 + f_y^2 \end{pmatrix}. \quad (4.18)$$

This result will be useful in the next section.

### 4.3 Synthetic Data for Two-Surface Model

To model refraction in our synthetic data, we modified the protocol described in Section 3.2 by adding refraction effects to the back surface. In this chapter, the design equations for the front and back surfaces— $z^a(x, y)$  and  $z^p(x, y)$ , respectively—have been translated vertically to produce a center thickness of  $t_c$ , with an additional vertical translation  $\delta h$  that ensures  $z^a, z^p > 0$  everywhere and aligns the synthetic data with the real data for the sake of visual comparison.

Once again, parameter values for the lenses can be found in Tables 2.2–2.3. The values of the refractive indices  $n_s$  and  $n_\ell$  are specified in Table 2.4.

#### Aspheric Lens

Design equations for the front and back surfaces of the aspheric lens correspond to those of Surfaces 1 and 2 in Section 3.2. For simplicity, we have rewritten the original equations in terms of Cartesian coordinates:

$$z^a(x, y) = \delta h - \frac{\frac{x^2+y^2}{R_a}}{1 + \sqrt{1 - (1 + \kappa) \left( \frac{x^2+y^2}{R_a^2} \right)}} - a_4 (x^2 + y^2)^2 - a_6 (x^2 + y^2)^3 - a_8 (x^2 + y^2)^4 - a_{10} (x^2 + y^2)^5, \quad (4.19a)$$

$$z^p(x, y) = \delta h - t_c, \quad (4.19b)$$

where  $\sqrt{x^2 + y^2} \leq A = 7.5$  mm for both surfaces. The vertical translation constant used for the aspheric lens data was  $\delta h \approx 5.1$  mm.

#### Toric Lens

The front and back surfaces of the toric lens correspond to Surfaces 3 and 4 in Section 3.2:

$$z^a(x, y) = \delta h - R_a + \sqrt{R_a^2 - x^2 - y^2}, \quad \sqrt{x^2 + y^2} \leq A = 7 \text{ mm}, \quad (4.20a)$$

$$z^p(x, y) = \delta h - R_{p1} - t_c + \sqrt{\left( R_{p1} - R_{p2} + \sqrt{R_{p1}^2 - y^2} \right)^2 - x^2}, \quad \sqrt{x^2 + y^2} \leq A \approx 6.57 \text{ mm}. \quad (4.20b)$$

For the toric lens data, we used  $\delta h \approx 5.7$  mm as the vertical translation constant.

Synthetic data for the front surface is obtained in the same manner as before, by sampling the design equation at all the points  $(x, y) \in S_A \subset S$ . Thus, the front surface data points

are simply the values  $(x, y, w^a)$  where

$$w^a = z^a(x, y). \quad (4.21a)$$

To construct synthetic data for the back surface we must first determine the distance  $L$  between the two surfaces along each refracted light ray. The warped synthetic data point  $(x, y, w^p)$  is then obtained by subtracting the OPL from the  $z$ -coordinate of the front surface

$$w^p = w^a - \text{OPL} = w^a - n_\ell L. \text{iv} \quad (4.21b)$$

Quantization error is a measurement error, so we simulate this effect last (in the manner described in Section 2.4.1).<sup>v</sup>

Note that (4.17) is the parametric equation for a line through the point  $(x, y, w^a)$ , with direction determined by  $\mathbf{u}_{ref} = \langle u_x, u_y, u_z \rangle$ . We also know from (4.18) that the components of  $\mathbf{u}_{ref}$  can be determined explicitly in terms of the refractive indices and the design equation for the front surface. If  $(\tilde{x}, \tilde{y}, z^p(\tilde{x}, \tilde{y}))$  indicates the refracted ray's true point of intersection with the back surface, then (4.17–4.18) yield the system

$$\tilde{x} = x + Lu_x \quad (4.22a)$$

$$\tilde{y} = y + Lu_y \quad (4.22b)$$

$$z^p(\tilde{x}, \tilde{y}) = w^a - Lu_z, \quad (4.22c)$$

where

$$\begin{pmatrix} u_x \\ u_y \\ u_z \end{pmatrix} = \frac{\sqrt{1 + \left(1 - \frac{n_s^2}{n_\ell^2}\right) \left((z^a)_x^2 + (z^a)_y^2\right)}}{1 + (z^a)_x^2 + (z^a)_y^2} \begin{pmatrix} (z^a)_x \\ (z^a)_y \\ -1 \end{pmatrix} - \frac{\frac{n_s}{n_\ell}}{1 + (z^a)_x^2 + (z^a)_y^2} \begin{pmatrix} (z^a)_x \\ (z^a)_y \\ (z^a)_x^2 + (z^a)_y^2 \end{pmatrix}. \quad (4.23)$$

As before,  $(z^a)_x$  and  $(z^a)_y$  denote the partial derivatives of the front surface evaluated at the point of incidence. If we substitute (4.22a–4.22b) into (4.22c), we see that the

---

<sup>iv</sup>In our data, the vertical alignment of the front surface is already scaled to account for the OPL within saline, so we actually want to overcorrect the OPL for the back surface by a factor of  $\frac{1}{n_s}$  for our synthetic data in order to be consistent. The point cloud data shown in Figures 4.9–4.10 were obtained using  $\text{OPL} = \frac{n_\ell}{n_s} L$ .

<sup>v</sup>Since we are overcorrecting the OPL for the back surface, we use the adjusted pixel spacing  $\frac{\Delta_z}{n_s} = \Delta'_z = 5.6 \times 10^{-3}$  mm.

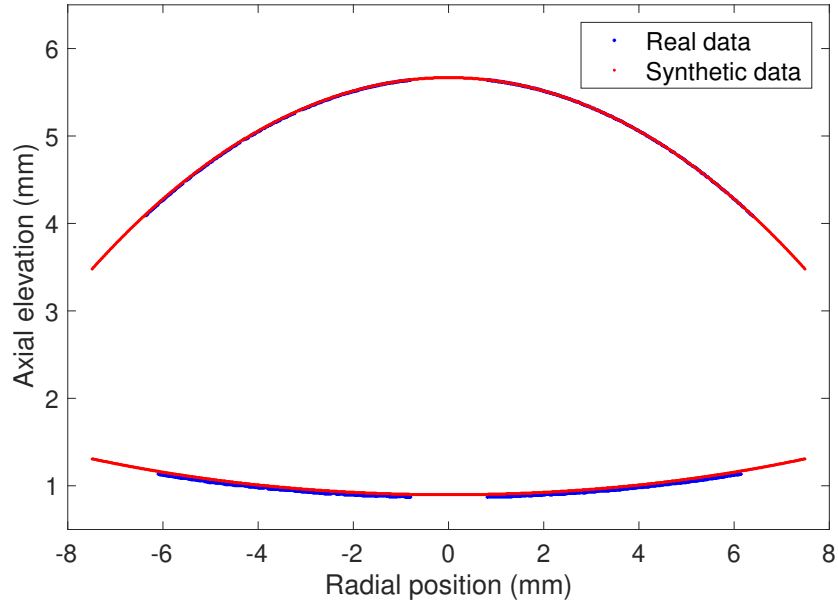


Figure 4.9: Real point cloud data from OCT of the aspheric lens versus synthetic point cloud data generated from the design equations (4.19).

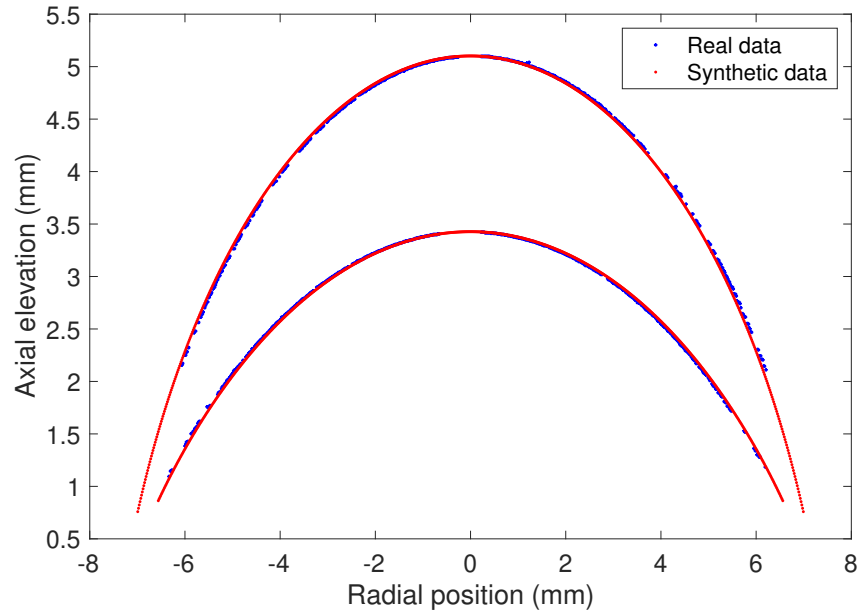


Figure 4.10: Real point cloud data from OCT of the toric lens versus synthetic point cloud data generated from the design equations (4.20).

geometric path length is the smallest value of  $L > 0$  that satisfies

$$z^p(x + Lu_x, y + Lu_y) = w^a + Lu_z, \quad (4.24)$$

where  $(x, y, w^a)$  is the point of incidence on the front surface,  $z^p(x, y)$  is the design equation of the back surface, and  $u_x, u_y, u_z$  are given by (4.23).

When the back surface is a flat plane such that  $z^p = C$  (as is the case for the aspheric lens), the path length is independent of  $\tilde{x}$  and  $\tilde{y}$  and we can calculate  $L$  directly:

$$L = \frac{w^a - C}{u_z}. \quad (4.25)$$

Figure 4.9 shows synthetic point cloud data for the aspheric lens using (4.19), (4.21), and (4.25). For comparison, the figure also includes real point cloud data from an OCT image of the aspheric lens before dewarping.

Solving (4.24) for an arbitrary lower surface (*e.g.*, the back of the toric lens) will generally involve a nonlinear system of equations. In this case, we can reformulate the problem so that  $L$  is the smallest positive root of the function

$$F(L) = w^a + Lu_z - z^p(x + Lu_x, y + Lu_y) = 0. \quad (4.26)$$

This problem can now be solved using an iterative root-finding algorithm with an intelligent initial guess, such as  $L_0 = w^a - z^p(x, y)$ . The synthetic data for the toric lens shown in Figure 4.10 was constructed in MATLAB using the vectorized Newton-Armijo solver `nsold.m`, written by C.T. Kelley [43]. Given the shape of the lens and the assumed angle of incidence, every A-scan is guaranteed to intersect the back surface somewhere, so we did not have to consider cases where (4.26) might not have a solution.

## 4.4 Validation of Two-Surface Model

When we explored the accuracy of Zernike polynomial fitting for the flat plane and toric cap in Chapter 3 (Surfaces 2 and 4), we assumed we had access to data for these two surfaces that was uncorrupted by refraction effects. In this section, we will take another look at the quantities of interest we considered in Section 3.5, only now we will consider both the front and back surfaces in our lens model. The 3D fitting protocol for the full

two-surface model can be summarized as follows:

1. Find geometric path length corresponding to all points on the back surface (see Section 4.1.4).
2. Fit front surface data to the Zernike model  $f^a(x, y) = f_{N_a}(r, \theta)$  (where  $N_a$  is the Zernike order) using the method described in Chapter 3.
3. Use centered finite differences to calculate partial derivatives

$$\begin{aligned} f_x^a(x, y) &\approx \frac{f^a(x+h, y) - f^a(x-h, y)}{2h} \\ f_y^a(x, y) &\approx \frac{f^a(x, y+h) - f^a(x, y-h)}{2h} \end{aligned} \quad (4.27)$$

at every grid point  $(x, y) = (\rho \cos \theta, \rho \sin \theta)$ .

4. Find corrected coordinates for all back surface points via the 3D dewarping algorithm (4.17).
5. Perform a separate Zernike fit  $f^p(x, y) = f_{N_p}(r, \theta)$  to dewarped back surface points  $(\tilde{x}, \tilde{y}, \tilde{z})$ .<sup>vi</sup>

The Zernike models for both surfaces are then used to calculate the meridional curvature and principal curvatures using the same methods described in Chapter 3.

The lens data we constructed in Section 4.3 provides a synthetic data set we can use for validation before testing this protocol on real OCT data in Chapter 5. We have already validated Step 2 for the front lens surfaces (Surfaces 1 and 3) in Section 3.5, so this chapter will look specifically at how the protocol affects the surface fit and curvature results for the back lens surface.

#### 4.4.1 Dewarping Step

To control for the modeling and discretization errors introduced in Steps 2 and 3, we will first consider the results when Steps 1, 4, and 5 are performed using analytic values for the front surface. That is, the path length will be given by

$$L = z^a(x, y) - w^p,$$

---

<sup>vi</sup>Since the Zernike fit is only defined on the unit disk, it is necessary to use only the points that fall within the appropriate radius  $A$  (*i.e.*,  $\sqrt{\tilde{x}^2 + \tilde{y}^2} \leq A$ ).

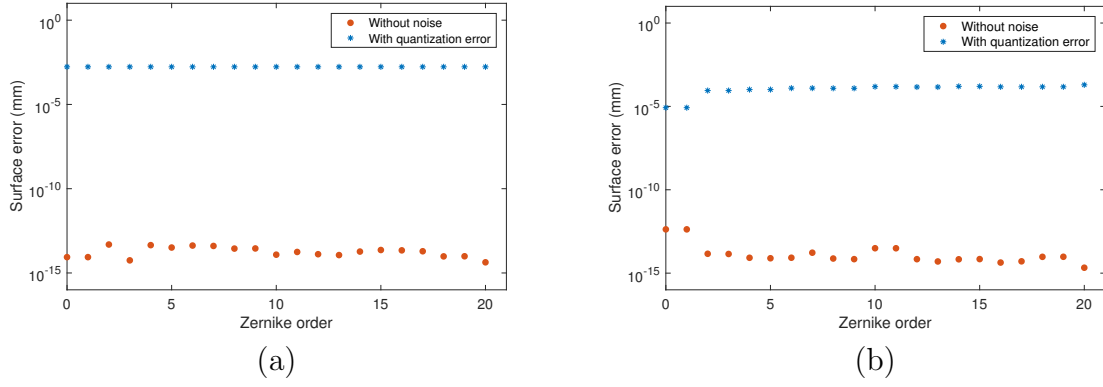


Figure 4.11: Average error in the Zernike fit for the back of the aspheric lens (a) without warping and (b) after dewarping using front surface design equation.

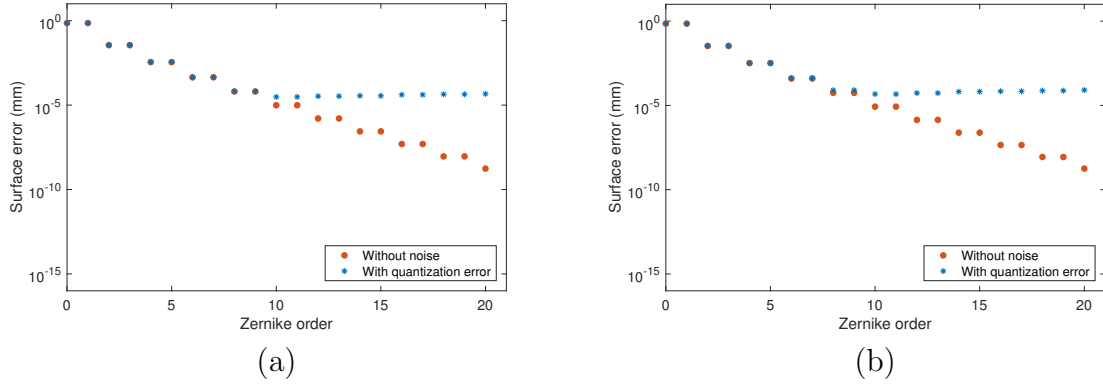


Figure 4.12: Average error in the Zernike fit for the back of the toric lens (a) without warping and (b) after dewarping using front surface design equation.

and the partial derivatives used in (4.17) are calculated by differentiating (4.19a) and (4.20a) directly. In this case, the mean absolute value of the error introduced into the path length for the quantized back surface data—given by  $\frac{1}{s} \sum_{i=1}^s |L_i - L_i^*|$ —is approximately  $1.16 \times 10^{-3}$  mm for the aspheric lens and  $1.25 \times 10^{-3}$  mm for the toric lens. (Recall from Chapter 3 that the mean absolute value of the quantization error in the synthetic data for Surfaces 2 and 4 were  $\frac{1}{s} \sum_{i=1}^s |z_i - z_i^*| \approx 1.7 \times 10^{-3}$  mm and  $\approx 1.4 \times 10^{-3}$  mm, respectively.) Figures 4.11–4.14 show the mean absolute error in surface fit ( $\bar{e}$ ,  $\bar{e}^*$ ) and curvature ( $\bar{e}_k$ ,  $\bar{e}_k^*$ ) for Zernike fits of different orders to the back surfaces of both lenses, after dewarping has been performed in this manner. For comparison, these results are

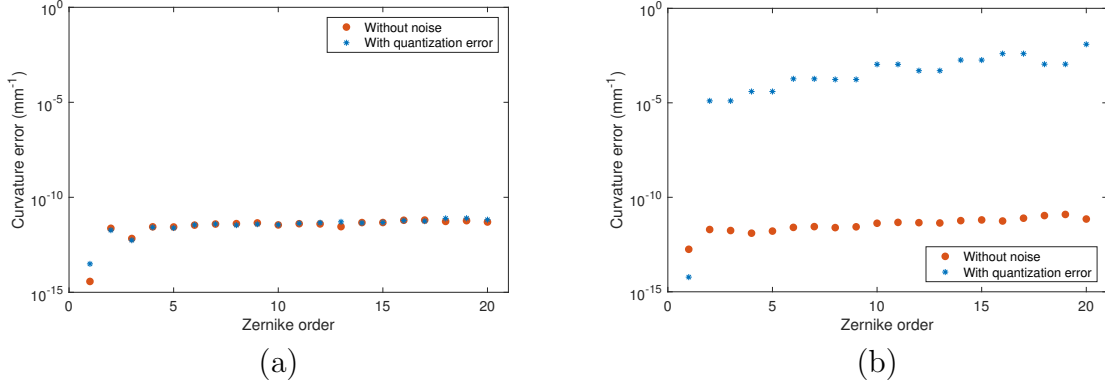


Figure 4.13: Average error in curvature for the back of the aspheric lens (a) without warping and (b) after dewarping using front surface design equation.

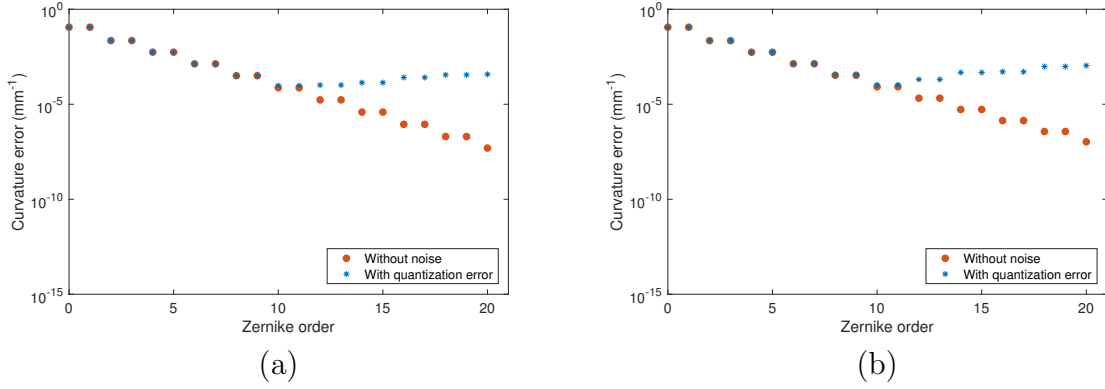


Figure 4.14: Average error in curvature for the back of the toric lens (a) without warping and (b) after dewarping using front surface design equation.

shown alongside the corresponding results from Chapter 3 in which the synthetic data did not include any refraction effects. Both sets of results are also summarized in Tables 4.1–4.2.

It is clear from this analysis that the dewarping step itself does not contribute additional surface error for either the quantized or non-quantized synthetic data. In fact, the surface error for the quantized aspheric lens data is even slightly mitigated by placing it in the context of the two surface model. On the other hand, while the average curvature error is largely unaffected by dewarping for both non-quantized data sets—as well as the quantized toric lens data—the curvature error in the quantized aspheric lens is greatly

Table 4.1: MAE fit to the back surfaces (in mm) with no refraction effects versus MAE when dewarping is done using exact values for the front surface gradient.

Aspheric Lens					Toric Lens				
$N_p$	$\bar{e}$		$\bar{e}^*$		$N_p$	$\bar{e}$		$\bar{e}^*$	
	No warping	Dewarped	No warping	Dewarped		No warping	Dewarped	No warping	Dewarped
0	$8.7 \times 10^{-15}$	$4.2 \times 10^{-14}$	$1.7 \times 10^{-3}$	$8.4 \times 10^{-6}$	0	$7.2 \times 10^{-1}$	$7.1 \times 10^{-1}$	$7.2 \times 10^{-1}$	$7.1 \times 10^{-1}$
1	$8.7 \times 10^{-15}$	$4.2 \times 10^{-14}$	$1.7 \times 10^{-3}$	$8.4 \times 10^{-6}$	1	$7.2 \times 10^{-1}$	$7.1 \times 10^{-1}$	$7.2 \times 10^{-1}$	$7.1 \times 10^{-1}$
2	$4.9 \times 10^{-14}$	$1.5 \times 10^{-14}$	$1.7 \times 10^{-3}$	$8.9 \times 10^{-5}$	2	$3.5 \times 10^{-2}$	$3.4 \times 10^{-2}$	$3.5 \times 10^{-2}$	$3.4 \times 10^{-2}$
3	$5.6 \times 10^{-15}$	$1.4 \times 10^{-14}$	$1.7 \times 10^{-3}$	$8.9 \times 10^{-5}$	3	$3.5 \times 10^{-2}$	$3.4 \times 10^{-2}$	$3.5 \times 10^{-2}$	$3.4 \times 10^{-2}$
4	$4.5 \times 10^{-14}$	$8.3 \times 10^{-15}$	$1.7 \times 10^{-3}$	$1.0 \times 10^{-4}$	4	$3.5 \times 10^{-3}$	$3.3 \times 10^{-3}$	$3.5 \times 10^{-3}$	$3.3 \times 10^{-3}$
5	$3.2 \times 10^{-14}$	$7.8 \times 10^{-15}$	$1.7 \times 10^{-3}$	$1.0 \times 10^{-4}$	5	$3.5 \times 10^{-3}$	$3.3 \times 10^{-3}$	$3.5 \times 10^{-3}$	$3.3 \times 10^{-3}$
6	$4.2 \times 10^{-14}$	$8.4 \times 10^{-15}$	$1.7 \times 10^{-3}$	$1.2 \times 10^{-4}$	6	$4.4 \times 10^{-4}$	$4.0 \times 10^{-4}$	$4.4 \times 10^{-4}$	$4.0 \times 10^{-4}$
7	$4.0 \times 10^{-14}$	$1.7 \times 10^{-14}$	$1.7 \times 10^{-3}$	$1.2 \times 10^{-4}$	7	$4.4 \times 10^{-4}$	$4.0 \times 10^{-4}$	$4.4 \times 10^{-4}$	$4.0 \times 10^{-4}$
8	$2.8 \times 10^{-14}$	$7.5 \times 10^{-15}$	$1.7 \times 10^{-3}$	$1.2 \times 10^{-4}$	8	$6.3 \times 10^{-5}$	$5.5 \times 10^{-5}$	$6.7 \times 10^{-5}$	$8.1 \times 10^{-5}$
9	$2.8 \times 10^{-14}$	$6.9 \times 10^{-15}$	$1.7 \times 10^{-3}$	$1.2 \times 10^{-4}$	9	$6.3 \times 10^{-5}$	$5.5 \times 10^{-5}$	$6.7 \times 10^{-5}$	$8.1 \times 10^{-5}$
10	$1.2 \times 10^{-14}$	$3.1 \times 10^{-14}$	$1.7 \times 10^{-3}$	$1.5 \times 10^{-4}$	10	$9.8 \times 10^{-6}$	$8.5 \times 10^{-6}$	$3.1 \times 10^{-5}$	$4.7 \times 10^{-5}$
11	$1.8 \times 10^{-14}$	$3.1 \times 10^{-14}$	$1.7 \times 10^{-3}$	$1.5 \times 10^{-4}$	11	$9.8 \times 10^{-6}$	$8.5 \times 10^{-6}$	$3.1 \times 10^{-5}$	$4.7 \times 10^{-5}$
12	$1.3 \times 10^{-14}$	$6.9 \times 10^{-15}$	$1.7 \times 10^{-3}$	$1.5 \times 10^{-4}$	12	$1.6 \times 10^{-6}$	$1.4 \times 10^{-6}$	$3.4 \times 10^{-5}$	$5.4 \times 10^{-5}$
13	$1.2 \times 10^{-14}$	$5.0 \times 10^{-15}$	$1.7 \times 10^{-3}$	$1.5 \times 10^{-4}$	13	$1.6 \times 10^{-6}$	$1.4 \times 10^{-6}$	$3.4 \times 10^{-5}$	$5.4 \times 10^{-5}$
14	$1.9 \times 10^{-14}$	$6.8 \times 10^{-15}$	$1.7 \times 10^{-3}$	$1.6 \times 10^{-4}$	14	$2.8 \times 10^{-7}$	$2.4 \times 10^{-7}$	$3.6 \times 10^{-5}$	$6.5 \times 10^{-5}$
15	$2.3 \times 10^{-14}$	$7.0 \times 10^{-15}$	$1.7 \times 10^{-3}$	$1.6 \times 10^{-4}$	15	$2.8 \times 10^{-7}$	$2.4 \times 10^{-7}$	$3.6 \times 10^{-5}$	$6.5 \times 10^{-5}$
16	$2.3 \times 10^{-14}$	$4.3 \times 10^{-15}$	$1.7 \times 10^{-3}$	$1.5 \times 10^{-4}$	16	$5.0 \times 10^{-8}$	$4.5 \times 10^{-8}$	$4.1 \times 10^{-5}$	$6.9 \times 10^{-5}$
17	$1.9 \times 10^{-14}$	$5.1 \times 10^{-15}$	$1.7 \times 10^{-3}$	$1.5 \times 10^{-4}$	17	$5.0 \times 10^{-8}$	$4.5 \times 10^{-8}$	$4.1 \times 10^{-5}$	$6.9 \times 10^{-5}$
18	$9.6 \times 10^{-15}$	$9.5 \times 10^{-15}$	$1.7 \times 10^{-3}$	$1.5 \times 10^{-4}$	18	$9.1 \times 10^{-9}$	$8.7 \times 10^{-9}$	$4.4 \times 10^{-5}$	$7.5 \times 10^{-5}$
19	$9.8 \times 10^{-15}$	$9.6 \times 10^{-15}$	$1.7 \times 10^{-3}$	$1.5 \times 10^{-4}$	19	$9.1 \times 10^{-9}$	$8.7 \times 10^{-9}$	$4.4 \times 10^{-5}$	$7.5 \times 10^{-5}$
20	$4.3 \times 10^{-15}$	$2.1 \times 10^{-15}$	$1.7 \times 10^{-3}$	$2.0 \times 10^{-4}$	20	$1.7 \times 10^{-9}$	$1.8 \times 10^{-9}$	$4.6 \times 10^{-5}$	$8.2 \times 10^{-5}$

Table 4.2: MAE in curvature (in  $\text{mm}^{-1}$ ) for the back surfaces without refraction effects and using exact gradient values for dewarping.

Aspheric Lens					Toric Lens				
$N_p$	$\bar{e}_k$		$\bar{e}_k^*$		$N_p$	$\bar{e}_k$		$\bar{e}_k^*$	
	No warping	Dewarped	No warping	Dewarped		No warping	Dewarped	No warping	Dewarped
0	0.0	0.0	0.0	0.0	0	$1.1 \times 10^{-1}$	$1.1 \times 10^{-1}$	$1.1 \times 10^{-1}$	$1.1 \times 10^{-1}$
1	$3.7 \times 10^{-15}$	$1.8 \times 10^{-13}$	$3.1 \times 10^{-14}$	$6.0 \times 10^{-15}$	1	$1.1 \times 10^{-1}$	$1.1 \times 10^{-1}$	$1.1 \times 10^{-1}$	$1.1 \times 10^{-1}$
2	$2.3 \times 10^{-12}$	$2.0 \times 10^{-12}$	$1.9 \times 10^{-12}$	$1.3 \times 10^{-5}$	2	$2.2 \times 10^{-2}$	$2.2 \times 10^{-2}$	$2.2 \times 10^{-2}$	$2.2 \times 10^{-2}$
3	$6.8 \times 10^{-13}$	$1.7 \times 10^{-12}$	$5.5 \times 10^{-13}$	$1.3 \times 10^{-5}$	3	$2.2 \times 10^{-2}$	$2.2 \times 10^{-2}$	$2.2 \times 10^{-2}$	$2.2 \times 10^{-2}$
4	$2.8 \times 10^{-12}$	$1.3 \times 10^{-12}$	$2.6 \times 10^{-12}$	$4.0 \times 10^{-5}$	4	$5.5 \times 10^{-3}$	$5.5 \times 10^{-3}$	$5.5 \times 10^{-3}$	$5.5 \times 10^{-3}$
5	$2.7 \times 10^{-12}$	$1.6 \times 10^{-12}$	$2.4 \times 10^{-12}$	$4.0 \times 10^{-5}$	5	$5.5 \times 10^{-3}$	$5.5 \times 10^{-3}$	$5.5 \times 10^{-3}$	$5.5 \times 10^{-3}$
6	$3.4 \times 10^{-12}$	$2.6 \times 10^{-12}$	$3.5 \times 10^{-12}$	$1.9 \times 10^{-4}$	6	$1.3 \times 10^{-3}$	$1.4 \times 10^{-3}$	$1.3 \times 10^{-3}$	$1.4 \times 10^{-3}$
7	$3.9 \times 10^{-12}$	$2.8 \times 10^{-12}$	$3.9 \times 10^{-12}$	$1.9 \times 10^{-4}$	7	$1.3 \times 10^{-3}$	$1.4 \times 10^{-3}$	$1.3 \times 10^{-3}$	$1.4 \times 10^{-3}$
8	$4.1 \times 10^{-12}$	$2.5 \times 10^{-12}$	$3.4 \times 10^{-12}$	$1.7 \times 10^{-4}$	8	$3.2 \times 10^{-4}$	$3.3 \times 10^{-4}$	$3.2 \times 10^{-4}$	$3.5 \times 10^{-4}$
9	$4.5 \times 10^{-12}$	$2.7 \times 10^{-12}$	$3.8 \times 10^{-12}$	$1.7 \times 10^{-4}$	9	$3.2 \times 10^{-4}$	$3.3 \times 10^{-4}$	$3.2 \times 10^{-4}$	$3.5 \times 10^{-4}$
10	$3.5 \times 10^{-12}$	$4.2 \times 10^{-12}$	$3.6 \times 10^{-12}$	$1.1 \times 10^{-3}$	10	$7.4 \times 10^{-5}$	$8.3 \times 10^{-5}$	$9.5 \times 10^{-5}$	$1.0 \times 10^{-4}$
11	$4.1 \times 10^{-12}$	$4.7 \times 10^{-12}$	$4.3 \times 10^{-12}$	$1.1 \times 10^{-3}$	11	$7.4 \times 10^{-5}$	$8.3 \times 10^{-5}$	$9.5 \times 10^{-5}$	$1.0 \times 10^{-4}$
12	$4.0 \times 10^{-12}$	$4.5 \times 10^{-12}$	$4.6 \times 10^{-12}$	$5.0 \times 10^{-4}$	12	$1.7 \times 10^{-5}$	$2.1 \times 10^{-5}$	$1.0 \times 10^{-4}$	$2.0 \times 10^{-4}$
13	$2.9 \times 10^{-12}$	$4.4 \times 10^{-12}$	$5.1 \times 10^{-12}$	$5.0 \times 10^{-4}$	13	$1.7 \times 10^{-5}$	$2.1 \times 10^{-5}$	$1.0 \times 10^{-4}$	$2.0 \times 10^{-4}$
14	$4.7 \times 10^{-12}$	$5.8 \times 10^{-12}$	$4.5 \times 10^{-12}$	$1.8 \times 10^{-3}$	14	$3.9 \times 10^{-6}$	$5.3 \times 10^{-6}$	$1.4 \times 10^{-4}$	$4.7 \times 10^{-4}$
15	$4.7 \times 10^{-12}$	$6.3 \times 10^{-12}$	$4.7 \times 10^{-12}$	$1.8 \times 10^{-3}$	15	$3.9 \times 10^{-6}$	$5.3 \times 10^{-6}$	$1.4 \times 10^{-4}$	$4.7 \times 10^{-4}$
16	$6.2 \times 10^{-12}$	$5.6 \times 10^{-12}$	$5.9 \times 10^{-12}$	$4.0 \times 10^{-3}$	16	$8.8 \times 10^{-7}$	$1.4 \times 10^{-6}$	$2.6 \times 10^{-4}$	$5.1 \times 10^{-4}$
17	$6.3 \times 10^{-12}$	$7.8 \times 10^{-12}$	$5.6 \times 10^{-12}$	$4.0 \times 10^{-3}$	17	$8.8 \times 10^{-7}$	$1.4 \times 10^{-6}$	$2.6 \times 10^{-4}$	$5.1 \times 10^{-4}$
18	$5.4 \times 10^{-12}$	$1.1 \times 10^{-11}$	$7.8 \times 10^{-12}$	$1.1 \times 10^{-3}$	18	$2.0 \times 10^{-7}$	$3.7 \times 10^{-7}$	$3.5 \times 10^{-4}$	$9.7 \times 10^{-4}$
19	$5.9 \times 10^{-12}$	$1.2 \times 10^{-11}$	$7.9 \times 10^{-12}$	$1.1 \times 10^{-3}$	19	$2.0 \times 10^{-7}$	$3.7 \times 10^{-7}$	$3.5 \times 10^{-4}$	$9.7 \times 10^{-4}$
20	$5.0 \times 10^{-12}$	$7.1 \times 10^{-12}$	$6.6 \times 10^{-12}$	$1.3 \times 10^{-2}$	20	$4.9 \times 10^{-8}$	$1.1 \times 10^{-7}$	$3.8 \times 10^{-4}$	$1.1 \times 10^{-3}$

increased for  $N_p > 1$ . However, it is also important to note that this new curvature error is roughly on the same order as the curvature error in the quantized toric lens data. Therefore, while it appears that dewarping may have a non-trivial impact on the results of the curvature calculation, there is no reason to believe that the net model error will be worse for any particular surface shape.

Comparisons of the absolute error (with and without warping) in the estimates for  $R_{p_1}$  and  $R_{p_2}$  for the toric lens are shown in Figure 4.15, with Table 4.3 providing a full summary of the principal radius of curvature. Once again, the results for both non-quantized and quantized data are very similar to the results from Chapter 3. However, note that the errors in  $\hat{R}_{p_1}^*$  and  $\hat{R}_{p_2}^*$  for the 14th order Zernike fit are no longer below the 0.025 mm tolerance for Type A ophthalmometers mentioned in Section 3.6. This suggests that the propagation of error through the dewarping step will be an influential factor in determining the appropriate Zernike order for the back surface curvature calculation.

Since the back surface of the aspheric lens is flat, the true radius of curvature everywhere is infinite, so measures of the error in its principal radius of curvature are meaningless. As with the unwarped synthetic data in Chapter 3, when there is no pixel quantization in the data, the error in the principal curvature ( $K_p = 0 \text{ mm}^{-1}$ ) after dewarping is zero regardless of which Zernike order we use. While this was also true in Chapter 3 for the quantized synthetic data, it is no longer the case after dewarping (with the obvious exceptions of  $N_p \in \{0, 1\}$ ). In other words, the dewarping algorithm does not *create* error at the vertex for the flat surface, but it does permit the amplification of existing noise. Figure 4.16 depicts the absolute error in the principal curvature  $\hat{K}_p^*$  for the aspheric lens, alongside the error in  $\hat{K}_{p_1}^*$  and  $\hat{K}_{p_2}^*$  for the toric lens after dewarping ( $K_{p_1} = \frac{1}{R_{p_2}} \approx 0.1190 \text{ mm}^{-1}$  and  $K_{p_2} = \frac{1}{R_{p_1}} \approx 0.1086 \text{ mm}^{-1}$ , respectively). Once again, this figure illustrates that even in the worst case the curvature error in the aspheric lens is on roughly the same order as the error in the toric lens.

#### 4.4.2 Front Surface Partial Derivatives

Clearly the discretization error from using the finite difference method (4.27) to calculate the front surface partial derivatives will affect the accuracy of the refraction-corrected coordinates for the back surface. We can quantify the error in the partial derivatives  $f_x^a(x, y)$  and  $f_y^a(x, y)$  in a similar manner to the curvature error (3.20) in Section 3.5.4. If  $s$  is the number of sample points and  $b$  is the number of B-scans, then the mean absolute

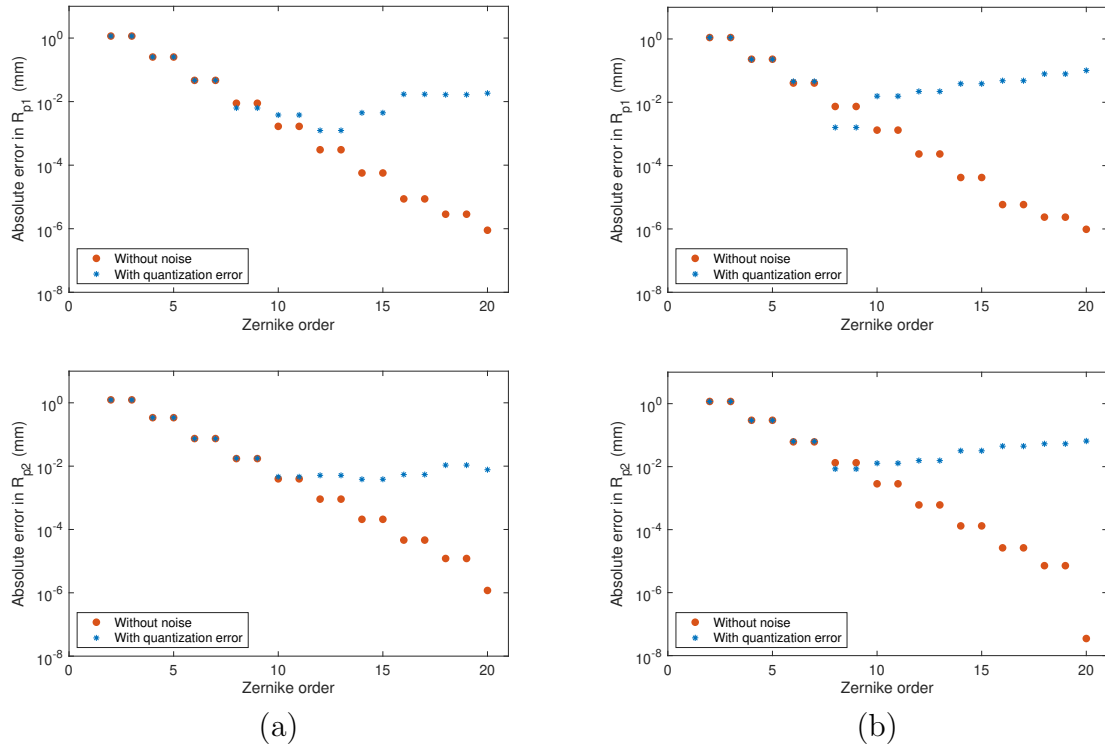


Figure 4.15: Absolute error in the estimates of  $R_{p1}$  (top) and  $R_{p2}$  (bottom) for the toric lens (a) without warping and (b) after dewarping using front surface design equation.

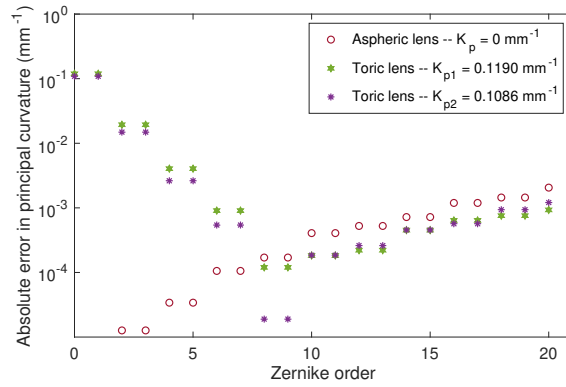


Figure 4.16: Absolute error in posterior principal curvatures for both lenses from quantized data after dewarping using front surface design equation.

Table 4.3: Principal radius of curvature estimates (in mm) for the back surface of the toric lens, with and without refraction effects.

No warping ( $R_{p_1} = 9.2$ mm)					Dewarped ( $R_{p_1} = 9.2$ mm)				
$N_p$	$\hat{R}_{p_1}$	$ \hat{R}_{p_1} - R_{p_1} $	$\hat{R}_{p_1}^*$	$ \hat{R}_{p_1}^* - R_{p_1} $	$N_p$	$\hat{R}_{p_1}$	$ \hat{R}_{p_1} - R_{p_1} $	$\hat{R}_{p_1}^*$	$ \hat{R}_{p_1}^* - R_{p_1} $
2	8.044	1.2	8.045	1.2	2	8.093	1.1	8.092	1.1
3	8.044	1.2	8.045	1.2	3	8.093	1.1	8.092	1.1
4	9.453	$2.5 \times 10^{-1}$	9.453	$2.5 \times 10^{-1}$	4	9.429	$2.3 \times 10^{-1}$	9.428	$2.3 \times 10^{-1}$
5	9.453	$2.5 \times 10^{-1}$	9.453	$2.5 \times 10^{-1}$	5	9.429	$2.3 \times 10^{-1}$	9.428	$2.3 \times 10^{-1}$
6	9.153	$4.7 \times 10^{-2}$	9.153	$4.7 \times 10^{-2}$	6	9.160	$4.0 \times 10^{-2}$	9.154	$4.6 \times 10^{-2}$
7	9.153	$4.7 \times 10^{-2}$	9.153	$4.7 \times 10^{-2}$	7	9.160	$4.0 \times 10^{-2}$	9.154	$4.6 \times 10^{-2}$
8	9.209	$8.9 \times 10^{-3}$	9.206	$6.3 \times 10^{-3}$	8	9.207	$7.4 \times 10^{-3}$	9.198	$1.6 \times 10^{-3}$
9	9.209	$8.9 \times 10^{-3}$	9.206	$6.3 \times 10^{-3}$	9	9.207	$7.4 \times 10^{-3}$	9.198	$1.6 \times 10^{-3}$
10	9.198	$1.7 \times 10^{-3}$	9.196	$3.8 \times 10^{-3}$	10	9.199	$1.3 \times 10^{-3}$	9.184	$1.6 \times 10^{-2}$
11	9.198	$1.7 \times 10^{-3}$	9.196	$3.8 \times 10^{-3}$	11	9.199	$1.3 \times 10^{-3}$	9.184	$1.6 \times 10^{-2}$
12	9.200	$3.1 \times 10^{-4}$	9.199	$1.2 \times 10^{-3}$	12	9.200	$2.3 \times 10^{-4}$	9.178	$2.2 \times 10^{-2}$
13	9.200	$3.1 \times 10^{-4}$	9.199	$1.2 \times 10^{-3}$	13	9.200	$2.3 \times 10^{-4}$	9.178	$2.2 \times 10^{-2}$
14	9.200	$5.7 \times 10^{-5}$	9.204	$4.4 \times 10^{-3}$	14	9.200	$4.2 \times 10^{-5}$	9.162	$3.8 \times 10^{-2}$
15	9.200	$5.7 \times 10^{-5}$	9.204	$4.4 \times 10^{-3}$	15	9.200	$4.2 \times 10^{-5}$	9.162	$3.8 \times 10^{-2}$
16	9.200	$8.7 \times 10^{-6}$	9.217	$1.7 \times 10^{-2}$	16	9.200	$5.9 \times 10^{-6}$	9.152	$4.8 \times 10^{-2}$
17	9.200	$8.7 \times 10^{-6}$	9.217	$1.7 \times 10^{-2}$	17	9.200	$5.9 \times 10^{-6}$	9.152	$4.8 \times 10^{-2}$
18	9.200	$2.9 \times 10^{-6}$	9.217	$1.7 \times 10^{-2}$	18	9.200	$2.4 \times 10^{-6}$	9.121	$7.9 \times 10^{-2}$
19	9.200	$2.9 \times 10^{-6}$	9.217	$1.7 \times 10^{-2}$	19	9.200	$2.4 \times 10^{-6}$	9.121	$7.9 \times 10^{-2}$
20	9.200	$9.0 \times 10^{-7}$	9.218	$1.8 \times 10^{-2}$	20	9.200	$9.7 \times 10^{-7}$	9.099	$1.0 \times 10^{-1}$

No warping ( $R_{p_2} = 8.4$ mm)					Dewarped ( $R_{p_2} = 8.4$ mm)				
$N_p$	$\hat{R}_{p_2}$	$ \hat{R}_{p_2} - R_{p_2} $	$\hat{R}_{p_2}^*$	$ \hat{R}_{p_2}^* - R_{p_2} $	$N_p$	$\hat{R}_{p_2}$	$ \hat{R}_{p_2} - R_{p_2} $	$\hat{R}_{p_2}^*$	$ \hat{R}_{p_2}^* - R_{p_2} $
2	7.161	1.2	7.160	1.2	2	7.226	1.2	7.225	1.2
3	7.161	1.2	7.160	1.2	3	7.226	1.2	7.225	1.2
4	8.739	$3.4 \times 10^{-1}$	8.739	$3.4 \times 10^{-1}$	4	8.697	$3.0 \times 10^{-1}$	8.695	$3.0 \times 10^{-1}$
5	8.739	$3.4 \times 10^{-1}$	8.739	$3.4 \times 10^{-1}$	5	8.697	$3.0 \times 10^{-1}$	8.695	$3.0 \times 10^{-1}$
6	8.326	$7.4 \times 10^{-2}$	8.326	$7.4 \times 10^{-2}$	6	8.339	$6.1 \times 10^{-2}$	8.337	$6.3 \times 10^{-2}$
7	8.326	$7.4 \times 10^{-2}$	8.326	$7.4 \times 10^{-2}$	7	8.339	$6.1 \times 10^{-2}$	8.337	$6.3 \times 10^{-2}$
8	8.417	$1.7 \times 10^{-2}$	8.418	$1.8 \times 10^{-2}$	8	8.413	$1.3 \times 10^{-2}$	8.409	$8.5 \times 10^{-3}$
9	8.417	$1.7 \times 10^{-2}$	8.418	$1.8 \times 10^{-2}$	9	8.413	$1.3 \times 10^{-2}$	8.409	$8.5 \times 10^{-3}$
10	8.396	$4.0 \times 10^{-3}$	8.395	$4.6 \times 10^{-3}$	10	8.397	$2.9 \times 10^{-3}$	8.387	$1.3 \times 10^{-2}$
11	8.396	$4.0 \times 10^{-3}$	8.395	$4.6 \times 10^{-3}$	11	8.397	$2.9 \times 10^{-3}$	8.387	$1.3 \times 10^{-2}$
12	8.401	$9.1 \times 10^{-4}$	8.395	$5.1 \times 10^{-3}$	12	8.401	$6.1 \times 10^{-4}$	8.384	$1.6 \times 10^{-2}$
13	8.401	$9.1 \times 10^{-4}$	8.395	$5.1 \times 10^{-3}$	13	8.401	$6.1 \times 10^{-4}$	8.384	$1.6 \times 10^{-2}$
14	8.400	$2.1 \times 10^{-4}$	8.396	$3.8 \times 10^{-3}$	14	8.400	$1.3 \times 10^{-4}$	8.368	$3.2 \times 10^{-2}$
15	8.400	$2.1 \times 10^{-4}$	8.396	$3.8 \times 10^{-3}$	15	8.400	$1.3 \times 10^{-4}$	8.368	$3.2 \times 10^{-2}$
16	8.400	$4.6 \times 10^{-5}$	8.405	$5.4 \times 10^{-3}$	16	8.300	$2.6 \times 10^{-5}$	8.355	$4.5 \times 10^{-2}$
17	8.400	$4.6 \times 10^{-5}$	8.405	$5.4 \times 10^{-3}$	17	8.400	$2.6 \times 10^{-5}$	8.355	$4.5 \times 10^{-2}$
18	8.400	$1.2 \times 10^{-5}$	8.389	$1.1 \times 10^{-2}$	18	8.300	$7.2 \times 10^{-6}$	8.347	$5.3 \times 10^{-2}$
19	8.400	$1.2 \times 10^{-5}$	8.389	$1.1 \times 10^{-2}$	19	8.400	$7.2 \times 10^{-6}$	8.347	$5.3 \times 10^{-2}$
20	8.400	$1.2 \times 10^{-6}$	8.392	$7.7 \times 10^{-3}$	20	8.400	$3.5 \times 10^{-8}$	8.335	$6.5 \times 10^{-2}$

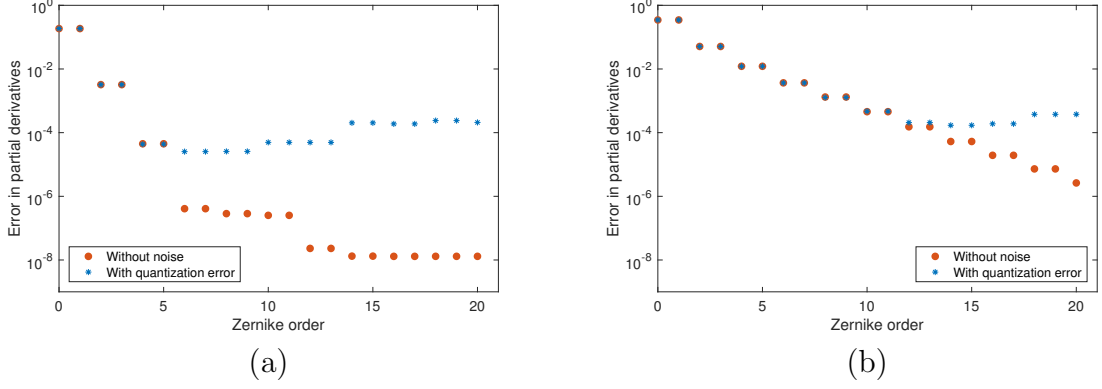


Figure 4.17: MAE in front surface partial derivatives for the (a) aspheric lens and (b) toric lens. (Due to symmetry, the average error is the same for both partial derivatives.)

error in the  $x$  and  $y$  partial derivatives for the front surface are given by

$$\bar{e}_x = \frac{1}{s-2b} \sum_i^s \left| f_x^a(\mathfrak{X}_i) - \frac{\partial z^a(\mathfrak{X}_i)}{\partial x} \right|, \quad \bar{e}_y = \frac{1}{s-2b} \sum_i^s \left| f_y^a(\mathfrak{X}_i, c) - \frac{\partial z^a(\mathfrak{X}_i)}{\partial y} \right|, \quad (4.28)$$

where  $\mathfrak{X} = (x, y)$  and  $\frac{\partial z^a(\mathfrak{X}_i)}{\partial x}$  and  $\frac{\partial z^a(\mathfrak{X}_i)}{\partial y}$  are the analytic derivatives of the design equations (4.19a) and (4.20a).

Note that the symmetry of both front surfaces means that  $\bar{e}_x = \bar{e}_y$ , so we do not need to look at both errors separately to see how the Zernike order affects the estimate of the partial derivatives. Figure 4.17 shows the error from (4.28) when the finite differences are calculated using a scaled step size of  $h = 10^{-3}$ . (As with the curvature, the partial derivatives are not particularly sensitive to the step size.) It is interesting to see that the error in partial derivatives follows a very similar trend to the curvature error we found in Section 3.5.4 (Figure 4.17), likely due to the similar discretization methods used to obtain the related values.

### 4.4.3 Full Implementation

In Section 4.4.1, we saw that when exact values for the front surface and front surface derivatives are used in the dewarping algorithm, the results for the non-quantized data after dewarping are very similar to the ones we obtained when we were not considering warping at all. This implies that the algorithm we used to add the refraction effects to

the synthetic data is not itself a major source of computational error.

If instead of the exact values for the front surface we use the Zernike approximation  $z^a(\mathfrak{X}) \approx f_{N_a}(\mathfrak{X})$ , it is therefore reasonable to infer that any differences between the dewarped results and those of the unwarped surfaces in Chapter 3 are primarily due to errors introduced during the dewarping step. In particular, the finite difference derivatives contain discretization error (which is explored in Section 4.4.2), and any modeling error from the front surface will also propagate to the back surface due to the use of the interpolated  $z$ -coordinate in the dewarping algorithm. Measurement error in the point cloud data for either surface will be included in the OPL calculation; however, this is only a concern for the quantized synthetic data. For the non-quantized data, the OPL will be exactly the same as it was in Section 4.4.1.

Rather than running every possible combination of Zernike orders for the front and back surface fits, we selected a subset of six orders to try for the front surface:  $N_a \in \{6, 8, 10, 12, 14, 16\}$ . The front surfaces of both lenses are axisymmetric, so the odd-ordered polynomials are unnecessary. Recall that the design matrix (3.9) for an  $N^{\text{th}}$  order Zernike polynomial model fit to  $s$  sample points consists of each of the  $p = \frac{1}{2}(N+1)(N+2)$  Zernike polynomials evaluated at all  $s$  locations  $(\rho, \theta)$  on the original sample grid. Perhaps the most expensive part of constructing the design matrix is finding the powers of  $\rho$  in the radial polynomials (3.2), which involves a cost of  $O(s^N)$ . Given this exponential increase in computational load, running the algorithms described in this thesis on a typical 64-bit desktop processor (the kind likely to be found in a clinical setting) starts to become impractical around  $N = 18$  for data sets containing  $s \sim 10^5$  points. Since overfitting is much more likely to pose a problem in real clinical applications where noisy data are inevitable—and considering that similar research discussed in Section 3.5.1 did not exceed  $N = 14$ —we decided that it was not necessary to include front surface Zernike models for which  $N_a > 16$ .

## Non-quantized Data

Figures 4.18–4.20 depict the various quantities of interest pertaining to surface fit and curvature for the back surface of each lens when dewarping is performed using non-quantized synthetic data for both surfaces. Results are included for front surface Zernike models  $z^a \approx f_{N_a}$ , where  $N_a \in \{8, 10, 12, 14, 16\}$ . For comparison, the plots also depict the results we obtained in Chapter 3 when refraction effects were not included in the

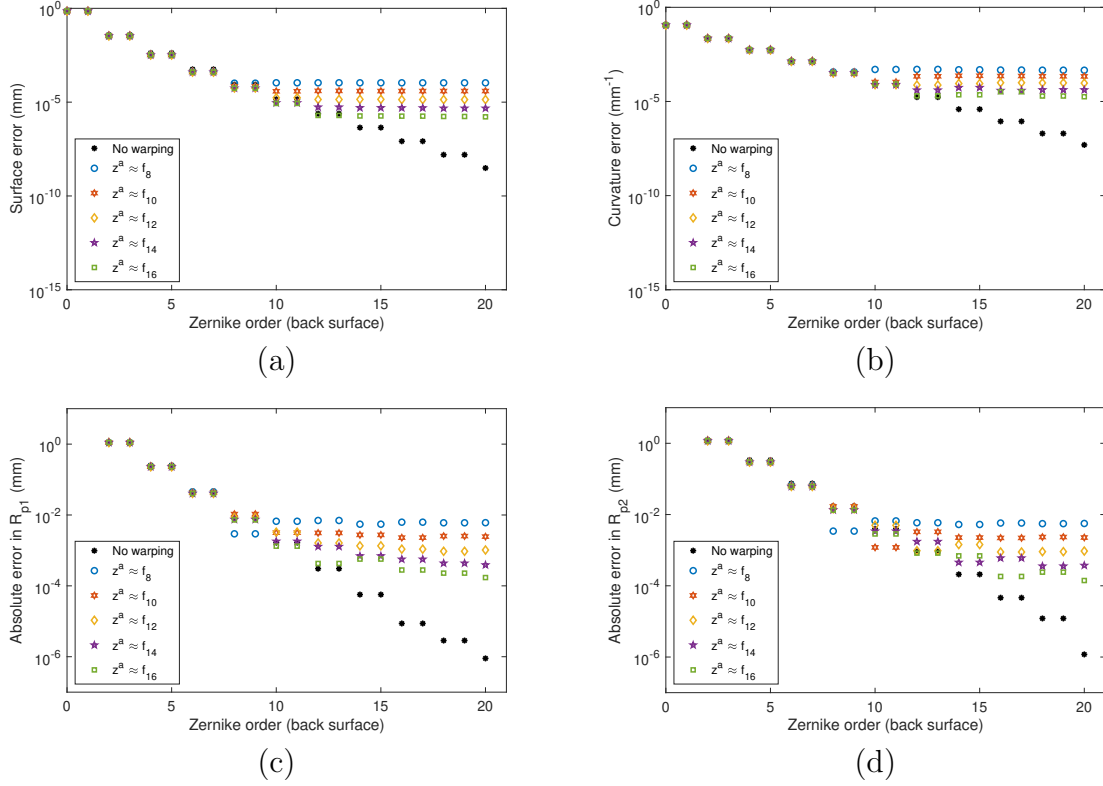


Figure 4.18: Average error in posterior (a) surface fit and (b) curvature, and absolute error in (c)  $\hat{R}_{p1}$  and (d)  $\hat{R}_{p2}$  from non-quantized toric lens data after dewarping using front surface Zernike fit. Results with no warping/dewarping from Chapter 3 are included for comparison.

synthetic data. Note that the absence of noise in the synthetic data means that the OPL used in the calculations contains no simulated measurement error.

For the first few Zernike orders, the dewarped results for the toric lens (Figure 4.18) are comparable to those of the unwarped data. However, this trend breaks around  $z^p \approx f_8$ . Despite the lack of noise in the synthetic data, we can see that the choice of Zernike order for the front surface ultimately determines the accuracy of the surface fit and curvature measurements for the back surface, no matter how many Zernike polynomials we include in the back surface fit. Table 4.4 shows the relationship between the error in the partial derivatives for each of the five front surface Zernike models and the corresponding best case accuracy of the back surface measurements after dewarping. Recall that elevation and radius of curvature are both measured in units of millimeters, while the partial

Table 4.4: Best case error results for front surface derivatives and back surface radii of curvature after dewarping non-quantized toric lens data using  $z^a \approx f_{N_a}$ .

Front Surface			Back Surface		
$N_a$	$\bar{e}_x/\bar{e}_y$	$\bar{e}$	$\bar{e}_{\text{roc}}$	$ \hat{R}_{p_1} - R_{p_1} $	$ \hat{R}_{p_2} - R_{p_2} $
8	$1.3 \times 10^{-3}$	$\sim 10^{-4}$ mm	$\sim 10^{-4}$ mm	$\sim 10^{-3}$ mm	$\sim 10^{-3}$ mm
10	$4.6 \times 10^{-4}$	$\sim 10^{-5}$ mm	$\sim 10^{-4}$ mm	$\sim 10^{-3}$ mm	$\sim 10^{-3}$ mm
12	$1.5 \times 10^{-4}$	$\sim 10^{-5}$ mm	$\sim 10^{-4}$ mm	$\sim 10^{-3}$ mm	$\sim 10^{-3}$ mm
14	$5.3 \times 10^{-5}$	$\sim 10^{-6}$ mm	$\sim 10^{-5}$ mm	$\sim 10^{-4}$ mm	$\sim 10^{-4}$ mm
16	$1.9 \times 10^{-5}$	$\sim 10^{-6}$ mm	$\sim 10^{-5}$ mm	$\sim 10^{-4}$ mm	$\sim 10^{-4}$ mm

derivative error ( $\bar{e}_x = \bar{e}_y$ ) is dimensionless. Given the results of Chapter 3, it should not be surprising that the elevation is as much as two orders of magnitude better than the radius of curvature measurements in some cases.

What *is* somewhat surprising is how the choice of front surface Zernike order affects the principal curvatures for certain back surface Zernike orders. On average, the back surface measurements become more accurate as the Zernike order for the front surface model is increased. However, as we can see in Figures 4.18a–b, when we use an 8<sup>th</sup> order Zernike model to fit the back surface, suddenly it is the 8<sup>th</sup> order model for the *front* surface that produces the best estimates for both principal radii of curvature—outperforming even the case without refraction effects. This result is an anomaly for the maximum principal radius of curvature ( $R_{p_1}$ ); however, for  $R_{p_2}$  there does appear to be a trend of matched front and back Zernike orders producing the best results.

Figure 4.19 illustrates the average surface and curvature errors for the back surface of the asphere after dewarping, as well as the non-warped results for the flat surface from Chapter 3. Although the surface error (Figure 4.19a) for the dewarped results is consistently several orders of magnitude higher than the error without warping, the maximum error for the dewarped case is still quite small at just  $\bar{e} \sim 10^{-8}$  mm (recall that the *minimum* surface error for the toric lens was  $\bar{e} \sim 10^{-6}$  mm). Furthermore, neither the Zernike order of the front surface fit nor that of the back surface seem to have a notable impact on the surface error, which is only  $\sim 10^{-10}$  mm even in the best case.

This stands in contrast to the average curvature error in Figure 4.19b, which is quite sensitive to the Zernike order of both the front and back surfaces. Since  $Z_1(\rho, \theta)$  is just

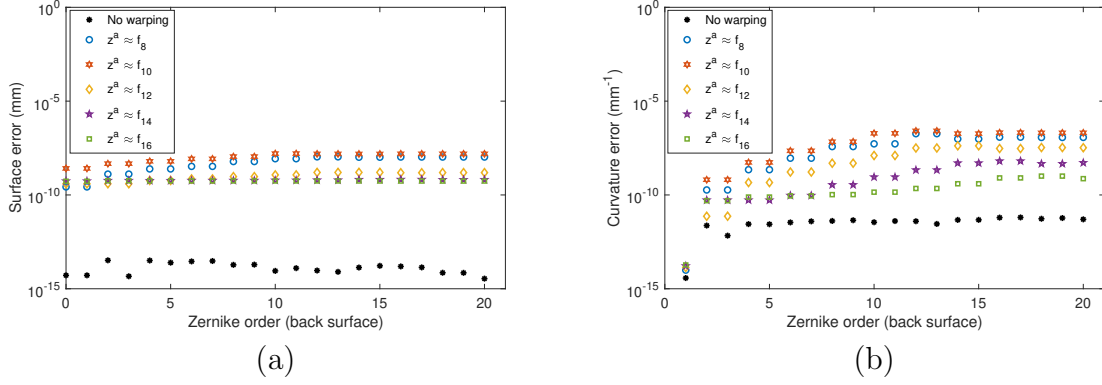


Figure 4.19: Average error in posterior (a) surface fit and (b) curvature from non-quantized aspheric lens data after dewarping using front surface Zernike fit.

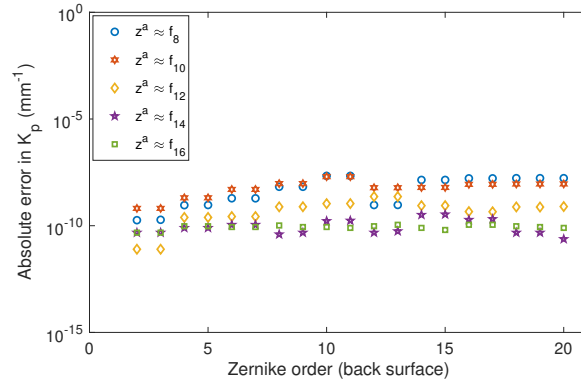


Figure 4.20: Absolute error in  $\hat{K}_p$  for the non-quantized aspheric lens data after dewarping using front surface Zernike fit.

a flat disc (Table 3.1), the average curvature error for  $z^p \approx f_0$  is exactly zero regardless of how dewarping is performed. The curvature error is also very small (at most  $\sim 10^{-14} \text{ mm}^{-1}$ ) for  $z^p \approx f_1$  due to the fact that the two additional basis polynomials included when  $N_p = 1$  merely represent tilt. Furthermore, while this is slightly larger than the average error we obtained without warping ( $\bar{e}_k \sim 10^{-15} \text{ mm}^{-1}$ ), it is an entire order of magnitude smaller than what we got in Section 4.4.1 using the exact front surface values in the dewarping algorithm.

Unlike with the toric lens, when we dewarp the back of the aspheric lens using the Zernike approximation for  $z^a$ , there is in fact a *positive* correlation between the Zernike

order of the back surface fit and the back surface curvature error. In fact, this also was not true for either the non-warped asphere results or when dewarping was performed using the exact values for the front surface—in both of those cases, the average curvature error was  $\bar{e}_k \sim 10^{-12} \text{ mm}^{-1}$  for all the back surface fits of order  $N_p \geq 2$ . This is likely due to the propagation of modeling and discretization error through the dewarping calculation. The error in the finite difference derivatives—which ranged from  $\bar{e}_x \sim 10^{-8}$  for  $N_a \in \{12, 14, 16\}$  to  $\bar{e}_x \sim 10^{-7}$  when  $N_a \in \{8, 10\}$ —almost appears to set an upper bound on the error in the average curvature for the back surface. For comparison, the *smallest* we are able to make the average curvature error for the toric lens is  $\bar{e}_k \sim 10^{-5} \text{ mm}^{-1}$ .

For the non-quantized data, the absolute error in the back surface principal curvature estimate for the aspheric lens was  $|\hat{K}_p - K_p| \equiv 0 \text{ mm}^{-1}$  regardless of the Zernike order selected for the back surface, for both the non-warped case in Chapter 3 and after dewarping using analytic values for  $z^a$  and its partial derivatives. As we can see in Figure 4.20, dewarping error clearly has a strong impact on the principal curvature results. While there does not appear to be an obvious trend in the accuracy of the principal curvature estimates with respect to either the front or back Zernike order, once again the *maximum* principal curvature error for the aspheric lens is just  $\sim 10^{-8} \text{ mm}^{-1}$ , while the *minimum* error for either principal curvature of the toric lens is  $\sim 10^{-5} \text{ mm}^{-1}$ .

## Quantized Data

In Section 3.6, we proposed that when using quantized synthetic data, the best Zernike orders for fitting the front surfaces of the aspheric and toric lenses seemed likely to fall respectively in the sets  $N_a \in \{6, 8, 10, 12\}$  and  $N_a \in \{10, 12, 14, 16\}$ . The average partial derivative errors in Section 4.4.2 provide further evidence to suggest that these models will introduce the least additional error to the back surface during dewarping when both surfaces contain quantization error. These results are illustrated in Figures 4.21–4.23, with one small adjustment: the toric lens demonstrated nearly identical outcomes for  $z^a \approx f_{14}$  and  $z^a \approx f_{16}$ , so the latter order has been replaced by  $N_a = 8$ . For comparison, these plots also include the corresponding error calculations from Section 4.4.1, where we used quantized data for the back surface only and analytic values for the front surface.

When both surfaces contain quantization error, the MAE in the path length  $L^*$  becomes roughly  $1.55 \times 10^{-3} \text{ mm}$  for the aspheric lens and  $1.65 \times 10^{-3} \text{ mm}$  for the toric lens—a very modest increase from what we had in Section 4.4.1 (where the path length

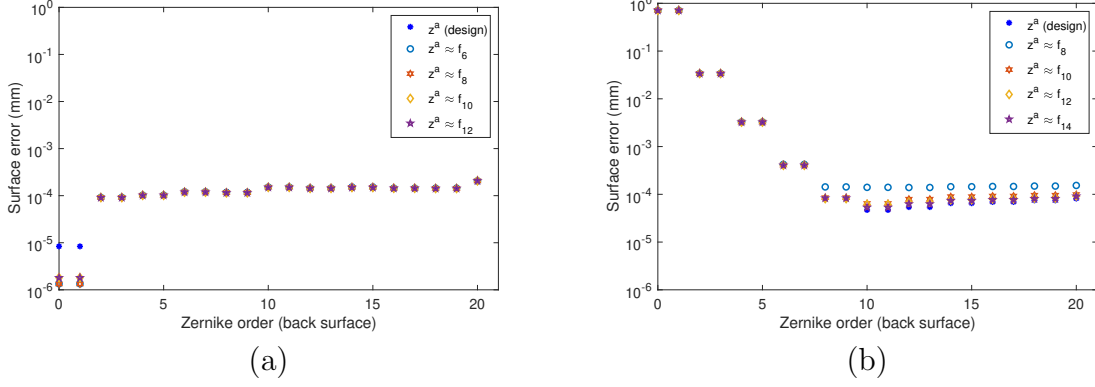


Figure 4.21: Average surface error from quantized synthetic data for the back of the (a) aspheric lens and (b) toric lens after dewarping. Results are depicted using both the front surface design equations and Zernike fits to quantized data.

was determined using analytic values for  $z^a$ ). The surface error for the front surface of the aspheric lens is  $\sim 10^{-5}$  mm for all four of the selected Zernike models, and the error in the partial derivatives (which is dimensionless) is also  $\sim 10^{-5}$  for all four models. For the toric lens, the front surface error is  $\sim 10^{-3}$  mm for  $z^a \approx f_8$ , and  $\sim 10^{-4}$  mm for the remaining three models. Similarly, the partial derivative error is  $\sim 10^{-3}$  for  $N_a = 8$  and  $\sim 10^{-4}$  for  $N_a \in \{10, 12, 14\}$ . Given that the errors due to Zernike fitting are at least an order of magnitude smaller than the error in the data itself (except in the case of  $z^a \approx f_8$  for the toric lens), it is reasonable to expect that using these Zernike models in place of the analytic function for the front surface in the dewarping algorithm should not dramatically alter the surface fit or curvature results for the back surface.

For reasons already discussed, it is no surprise that the back surface models  $z^p \approx f_0$  and  $z^p \approx f_1$  would produce the best results across the board for the aspheric lens. What *is* somewhat surprising is that the surface errors (Figure 4.21a) for these two models are actually an entire order of magnitude smaller when using the Zernike fit to quantized data for the front surface versus the exact values for the function and its partial derivatives. For the remaining back surface models ( $N_p \geq 2$ ), the surface error is virtually identical for all five front surface models (the four Zernike fits and the analytic function  $z^a$ ), following a gradually increasing trend but remaining on the order of  $10^{-4}$  mm throughout. This positive correlation between the error and the back surface Zernike order is much more pronounced for the two curvature computations (Figures 4.22a and 4.23a), although

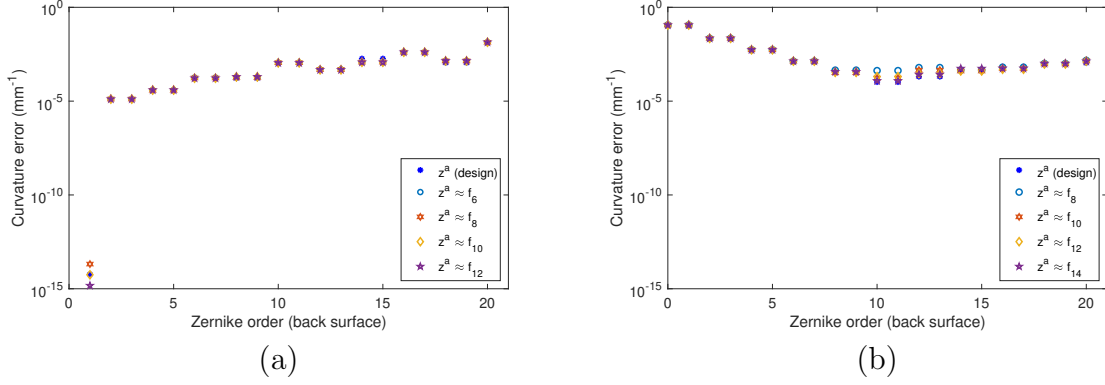


Figure 4.22: Average curvature error from quantized synthetic data for the back of the (a) aspheric lens and (b) toric lens after dewarping.

once again there are no obvious differences between the five front surface models. This indicates that while overfitting poses a potentially significant problem in the accurate calculation of the back surface curvature for the aspheric lens, error propagation from the front surface may not ultimately be as great a cause for concern. It is also worth noting that the error in the principal curvature estimate is consistent with the scale of the error in the two principal curvatures for the toric lens, shown in Figures 4.23b–c.

Not including  $z^a \approx f_8$ , the four remaining models for the front surface of the toric lens (including the analytic one) produce very similar average surface fit and curvature results for the back surface. For these four front surface models, the surface MAE (Figure 4.21b) converges to  $\sim 10^{-5}$  mm for back surface fits of order  $N_p \geq 8$ . The curvature MAE (Figure 4.22b) also drops to its minimum value of  $\sim 10^{-4}$  mm $^{-1}$  when  $z^p \approx f_8$ , and while it does increase slightly for the higher order fits, it maintains the same order of magnitude for all the back surface models up to  $N_p < 20$ . The average curvature error for  $z^a \approx f_8$  is comparable, although the error in the fit for this front surface model only converges to  $\sim 10^{-4}$  mm. For back surface Zernike fits of order  $6 \leq N_p < 20$ , the absolute error in both principal curvatures is never worse than  $\sim 10^{-4}$  mm $^{-1}$  for any of the front surface models, including  $z^a \approx f_8$ . Furthermore, we can see from Figures 4.23b–c that regardless of which front surface model we use, the principal curvature estimates will likely be most accurate using a Zernike fit to the back surface of order  $N_p \in \{8, 10, 12\}$  (we ignore the odd orders due to the surface’s rotational symmetry).

The obvious standout for the back surface is  $z^p \approx f_8$ , which results in the lowest error

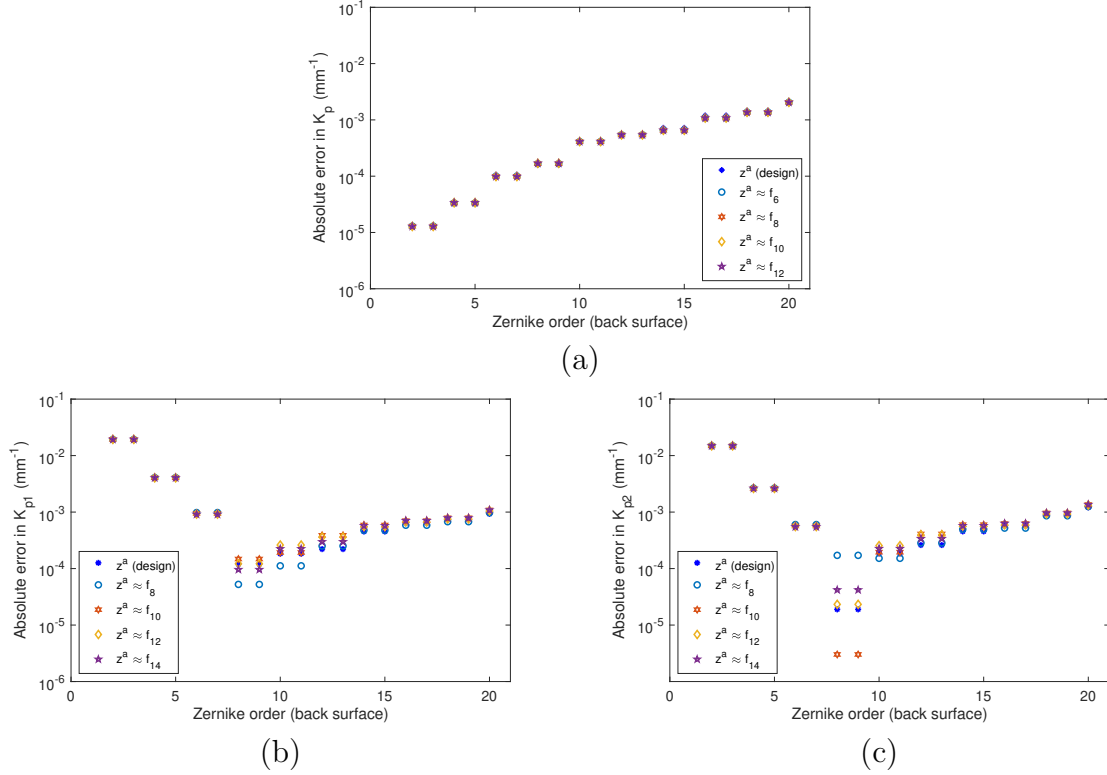


Figure 4.23: Absolute error after dewarping in (a)  $\hat{K}_p^*$  for aspheric lens and (b)  $\hat{K}_{p1}^*$  and (c)  $\hat{K}_{p2}^*$  for the toric lens.

in both principal curvatures for nearly every front surface model. We can also see that for the right Zernike fit to the back surface, the principal curvature does in fact end up being quite sensitive to the dewarping algorithm. Somewhat surprisingly, it is the 8<sup>th</sup> order fit to the front surface that produces the most accurate estimate of  $\hat{K}_{p1}^*$ , performing better in this aspect than even the analytic function  $z^a$  itself. However, while  $z^a \approx f_8$  does at least as well for both principal curvatures as the other front surface models everywhere else, it also yields the *worst* approximation of  $\hat{K}_{p2}^*$  when  $z^p \approx f_8$ . Instead it is  $z^a \approx f_{10}$  that produces by far the best estimate for the minimum curvature, despite its otherwise modest performance. This underscores the difficulty in trying to simultaneously identify suitable models for both the front and back lens surfaces in this application.

## 4.5 Summary

We have presented a model for the second of two surfaces being imaged via OCT (Sections 4.1–4.2.1), as well as a technique for adding refractive error to the design equations in order to construct synthetic lens data (Section 4.3). We validated the dewarping step by showing in Section 4.4.1 that, in most cases, using the exact front surface gradient computed from the design equations on this new synthetic data produces elevation and curvature results very similar to those obtained when no refraction effects are considered.

For the toric lens, the error introduced by using a front surface Zernike model and finite difference derivatives (Section 4.4.2) effectively created a lower bound on the error for most of the back surface quantities of interest, even for the non-quantized synthetic data. This bound also did not seem to be affected by the choice of finite difference step size, which implies that it is mainly the Zernike fit and not the numerical derivative that is responsible for this additional error. In other words, the error from the front surface model propagates through to the back surface, giving rise to yet another consideration when determining the best Zernike order for modeling the front surface. This effect was also somewhat noticeable (although to a much lesser extent) for the mean posterior curvature of the aspheric lens, but did not seem to be a major concern for the surface fit or principal curvature. This is likely due to the superior accuracy of the numerical derivatives from the front surface Zernike model.

When considering the quantized synthetic data in Section 4.4.3, we observed that the choice of front surface Zernike order  $N_a$  did not make a notable difference on the back surface quantities of interest for the aspheric lens. Since the posterior aspheric lens is flat, the error naturally increases as the back surface order  $N_p$  increases and begins modeling noise in the data. The error in the surface fit jumps from  $\sim 10^{-6}$  mm for  $N_p \in \{0, 1\}$  to  $\sim 10^{-4}$  mm for  $N_p \geq 2$ , whereas the error in the curvature goes from effectively zero to around  $10^{-5}$  mm<sup>-1</sup> for  $N_p = 2$  and continues to increase steadily to about  $10^{-3}$  mm<sup>-1</sup> for  $N_p = 20$ .

Table 4.5 shows the elevation and radius of curvature errors for each combination of the four front surface models and three best back surface models for the toric lens. The table also includes the corresponding error for each posterior Zernike model from Chapter 3, where we did not consider refraction effects at all. As was the case for no refraction,  $N_p = 10$  still provides the best results for mean elevation and mean radius of curvature, regardless of the front surface model used—*i.e.*, all three front surface models

Table 4.5: Results (in mm) for the posterior toric lens for each back surface model order  $N_p$  after dewarping using front surface model order  $N_a$  (versus without refraction effects).

		$N = 8$	$N = 10$	$N = 12$
$\bar{e}^*$	No warping	$6.7 \times 10^{-5}$	<b><math>3.1 \times 10^{-5}</math></b>	$3.4 \times 10^{-5}$
	$N_a = 8$	$1.4 \times 10^{-4}$	$1.4 \times 10^{-4}$	$1.4 \times 10^{-4}$
	$N_a = 10$	$8.5 \times 10^{-5}$	$6.4 \times 10^{-5}$	$7.9 \times 10^{-5}$
	$N_a = 12$	$8.1 \times 10^{-5}$	$6.1 \times 10^{-5}$	$6.9 \times 10^{-5}$
	$N_a = 14$	$8.3 \times 10^{-5}$	<b><math>5.3 \times 10^{-5}</math></b>	$6.3 \times 10^{-5}$
$\bar{e}_{\text{roc}}^*$	No warping	$2.5 \times 10^{-2}$	<b><math>7.4 \times 10^{-3}</math></b>	$8.0 \times 10^{-3}$
	$N_a = 8$	$3.5 \times 10^{-2}$	$3.4 \times 10^{-2}$	$5.0 \times 10^{-2}$
	$N_a = 10$	$2.6 \times 10^{-2}$	$1.3 \times 10^{-2}$	$3.6 \times 10^{-2}$
	$N_a = 12$	$2.7 \times 10^{-2}$	$1.6 \times 10^{-2}$	$2.3 \times 10^{-2}$
	$N_a = 14$	$2.9 \times 10^{-2}$	<b><math>9.3 \times 10^{-3}</math></b>	$2.1 \times 10^{-2}$
$ \hat{R}_1^* - R_1 $	No warping	$6.3 \times 10^{-3}$	$3.8 \times 10^{-3}$	<b><math>1.2 \times 10^{-3}</math></b>
	$N_a = 8$	$1.4 \times 10^{-2}$	$1.3 \times 10^{-2}$	$2.4 \times 10^{-2}$
	$N_a = 10$	<b><math>2.6 \times 10^{-4}</math></b>	$1.6 \times 10^{-2}$	$3.5 \times 10^{-2}$
	$N_a = 12$	$2.0 \times 10^{-3}$	$2.2 \times 10^{-2}$	$3.3 \times 10^{-2}$
	$N_a = 14$	$3.5 \times 10^{-3}$	$1.9 \times 10^{-2}$	$2.9 \times 10^{-2}$
$ \hat{R}_2^* - R_2 $	No warping	$1.8 \times 10^{-2}$	<b><math>4.6 \times 10^{-3}</math></b>	$5.1 \times 10^{-3}$
	$N_a = 8$	<b><math>3.7 \times 10^{-3}</math></b>	$7.9 \times 10^{-3}$	$1.8 \times 10^{-2}$
	$N_a = 10$	$1.0 \times 10^{-2}$	$1.4 \times 10^{-2}$	$2.7 \times 10^{-2}$
	$N_a = 12$	$8.6 \times 10^{-3}$	$1.8 \times 10^{-2}$	$2.5 \times 10^{-2}$
	$N_a = 14$	$6.8 \times 10^{-3}$	$1.6 \times 10^{-2}$	$2.1 \times 10^{-2}$

produce comparable results for these two quantities of interest, with  $N_a = 8$  being a bit worse than the others. However, the error in the estimates for  $R_{p_1}$  and  $R_{p_2}$  are at least an order of magnitude smaller for  $N_p = 8$  than for the other two orders, while the mean elevation and curvature errors are not considerably worse. In most cases, the estimates for the back surface quantities of interest obtained after dewarping are worse than when we did not consider refraction, although not dramatically so.

We also note that the best front surface model for the back surface quantities of interest seems to be  $N_a = 14$  (even though there are other models that do better for specific metrics), whereas the model that produced the best overall front surface results in Chapter 3 was  $N_a = 12$ . However,  $N_a = 14$  did in fact have a slightly lower mean

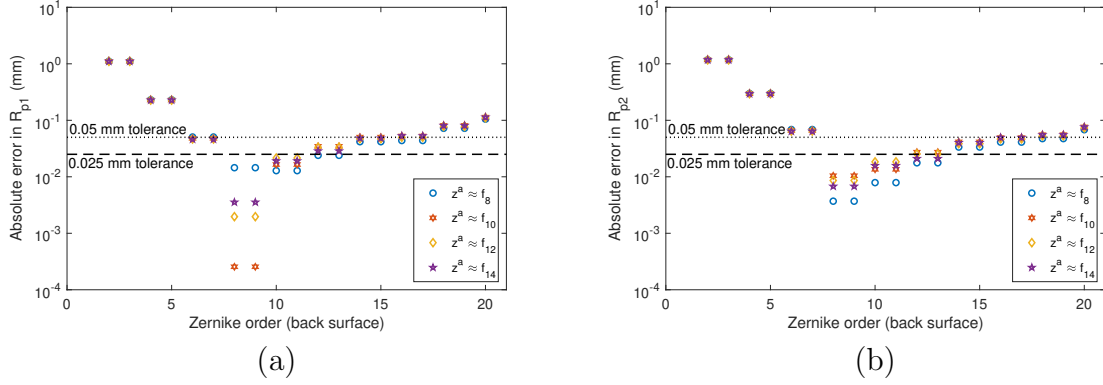


Figure 4.24: Absolute error in (a)  $\hat{R}_{p1}^*$  and (b)  $\hat{R}_{p2}^*$  for the toric lens after dewarping using Zernike fit to quantized front surface data.

radius of curvature error. As both the curvature calculation and the refraction correction algorithm rely on derivatives of the front surface, it is not surprising that the front surface model with the best curvature estimate would also be the most accurate for dewarping the back surface. (Note that in Chapter 6 we use  $N_a = 10$  for the toric lens, despite the slightly inferior results shown here. This choice is explained further in Section 6.3.1.)

As shown in Figure 4.24, most of the front and back surface model combinations in Table 4.5 meet the 0.025 mm tolerance on principal radius of curvature required for “Type A” ophthalmometers (as specified in [35]), with  $N_p = 14$  being right on the line but still below the 0.05 mm “Type B” threshold. In other words, we are still able to stay within the tolerance for both instruments given an intelligent selection of Zernike model orders for each surface.

The data used in this section is, of course, idealized. Real OCT data sets will have gaps where segmentation has failed and additional noise beyond quantization error. Furthermore, the algorithm we are using to construct the warped synthetic data for the posterior surface is based on the same set of equations we use to subsequently dewarp those points, so we are not truly validating the entire refraction correction algorithm. The next chapter will address how well this two-surface lens model fits our real OCT data and how accurately the model is able to predict surface curvature.

# Chapter 5

## Application to Imaging Data

### 5.1 Full Lens Model

#### 5.1.1 Realignment

In order for two topographic maps to be comparable to one another, the values they report must be calculated at the same surface locations. This is particularly true of parameters like meridional curvature that depend on the choice of reference axis [101]. For the analyses in Chapters 3 and 4, we constructed synthetic data that was already centered at the lens vertex and aligned with the design equation. However, perfect alignment is unlikely with real OCT data, even when imaging a stationary lens. In practice, the CT axis will not generally be centered with (or, in the case of a living eye, even parallel to) the chosen reference axis.<sup>i</sup> Since measurements made with respect to the wrong reference axis

---

<sup>i</sup>As discussed in Chapter 2, realignment for the human eye can be particularly challenging due to the lack of strict geometrical significance of the commonly used reference points, much less agreement as to the appropriate reference axis to use when diagnosing different eye conditions [7, 60, 62, 85, 101]. Some ophthalmological diseases can result in deformed or displaced reference points, and even in a healthy eye the relative position of certain reference points can change depending on the circumstances [60] (*e.g.*, the location of the pupil center varies as the pupil dilates or contracts to accommodate different amounts of ambient light). Therefore, realignment in the eye cannot be performed by simply translating the origin without accounting for the angle between the axes [78]. Although procedures do exist to approximately identify the various other reference axes once a data set has already been collected [101], these transformations rely on assumptions about the structure of the eye which may not be accurate for an individual subject—hence the need for technology that can obtain precise 3D measurements of the interior surfaces of a living eye [7, 62]. However, as the Envisu’s tip/tilt alignment protocol (described in [51]) is reasonably accurate for the stationary lens, the resulting error from misalignment is not likely to be nearly as significant for our lens analysis as it would be for the human eye.

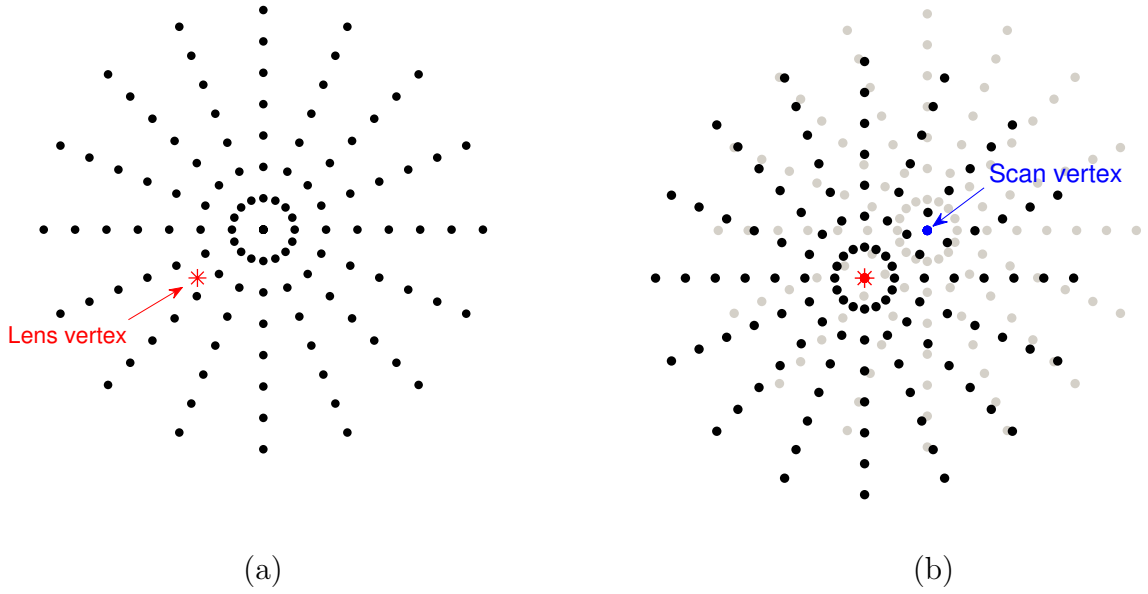


Figure 5.1: (a) Slight misalignment of radial scanning pattern relative to lens vertex. (b) Radial grid re-centered at the lens vertex for calculating final results.

can have a significant impact on the accuracy of the subsequent calculations, accurate realignment is critical.

Figure 5.1a illustrates the position of the lens vertex relative to the scan vertex in the case of off-axis imaging. The latter is taken to be the origin of the  $xy$ -plane during imaging; however, because the lens' refractive power is referenced to its optical axis, the grid must be re-centered at the lens vertex (as shown in Figure 5.1b) before the final measurements are computed. Since we are assuming that the CT axis is parallel to the optical axis (see footnote i), this re-centering can be accomplished by identifying the lateral “offset” between the scan vertex and the lens vertex, translating each grid point accordingly, and then interpolating the data set at the translated grid points *before* calculating any curvature results.

Recall that the  $z$ -axis of the point cloud data is defined by the CT axis. Given that the lens is rotational symmetric around the optical axis (and locally concave down in this coordinate system), it is trivial to see that the vertex of the lens must be a local maximum. We can approximate the location of this point by constructing a 3D representation of the front lens surface using Zernike polynomials and using an optimization routine to

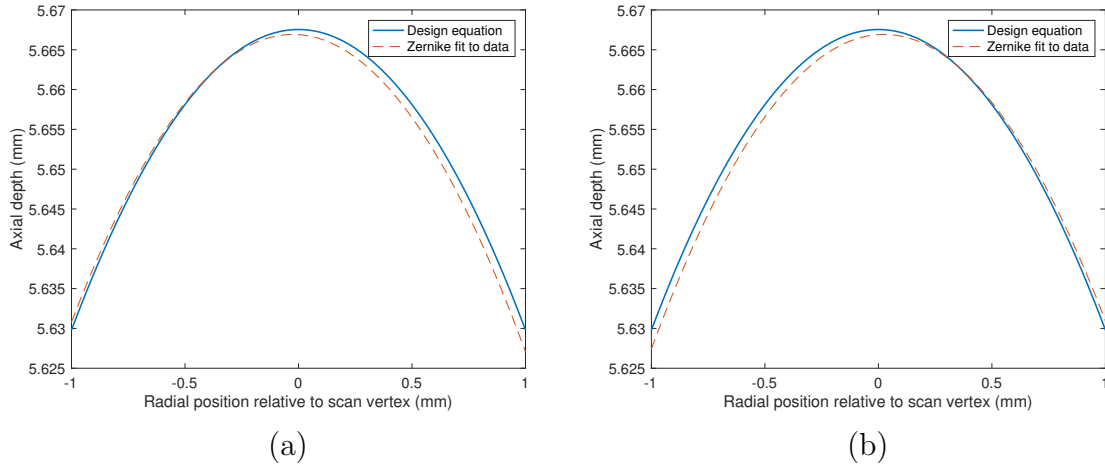


Figure 5.2: Meridians at (a)  $0^\circ$  and (b)  $90^\circ$  for the aspheric lens without realignment.

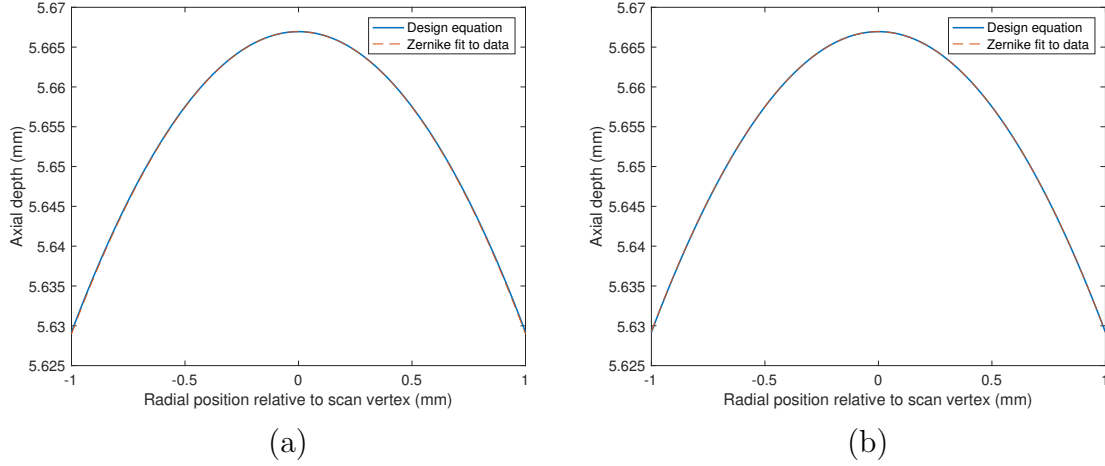


Figure 5.3: Meridians at (a)  $0^\circ$  and (b)  $90^\circ$  for the aspheric lens after realignment.

identify the local maximum closest to the scan vertex. This approach is detailed further in Section 5.1.2.

Figures 5.2–5.5 illustrate the meridians at  $0^\circ$  and  $90^\circ$  for the design equation and best-fitting Zernike polynomial for the front surfaces of both lenses (respectively  $N = 4$  and  $N = 8$  for the aspheric lens and toric lens), before and after re-centering. For simplicity, the  $y$ -axis in these figures is aligned with the optical axis of the design equation, so that  $x = 0$  denotes the location of the lens vertex. Note that because realignment of the

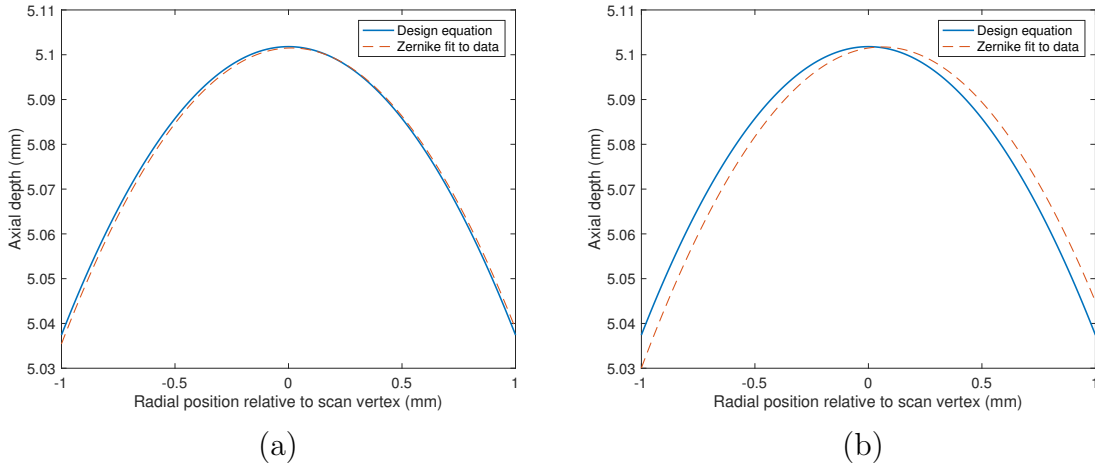


Figure 5.4: Meridians at (a)  $0^\circ$  and (b)  $90^\circ$  for the toric lens without realignment.

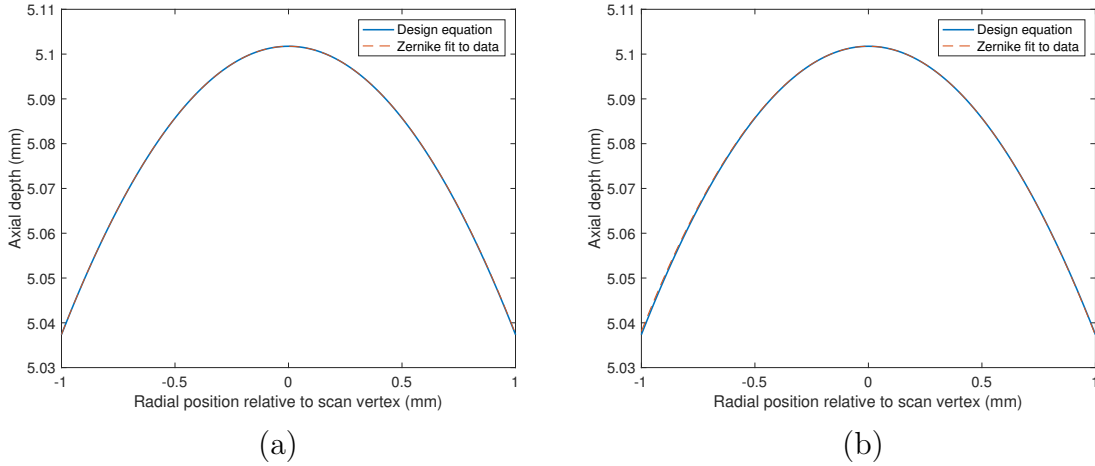


Figure 5.5: Meridians at (a)  $0^\circ$  and (b)  $90^\circ$  for the toric lens after realignment.

fitted data is done using the full three dimensional front surface model, the re-centered meridians in Figures 5.3 and 5.5 are *not* a simple translation of the meridians shown in Figures 5.2 and 5.4.

The ANSI standard on corneal topography details a different method of correcting de-centration between two data sets using a Zernike decomposition of the difference of the two sets of points [5, §D.1]. This method is based on the assumption that the two surfaces are nearly spherical, in which case the  $x$ - and  $y$ -coordinates of the offset would

be roughly proportional to the amount of horizontal and vertical tilt in the difference surface, or  $c_1^1$  and  $c_1^{-1}$  in the Zernike expansion (3.6). We compared this approach with the maximum point method described above, and found that the latter was *at least* as good (and in many cases significantly better) at reducing the error from misalignment in our data regardless of which quantity of interest we were measuring. The two main drawbacks to employing our method instead of the ANSI approach are the (small) additional computational cost of the optimization routine and the possible loss of accuracy due to the wrong choice of Zernike model to perform the fit—*i.e.*, choosing a Zernike order that gives a poor approximation of the surface shape near the lens vertex. However, in our case the computational cost was insignificant compared to the overall cost of the other algorithms used, and we considered multiple Zernike models to ensure the best fit to the data.

Regardless of the method used, a three dimensional data set is required for realignment. As the true vertex may be located between meridians, 2D interpolation within a cross-sectional frame is inadequate for identification of this point. In fact, the maximum point for each frame will not even necessarily correspond to the same position on the lens surface. Without a data set that includes the true lens vertex, interpolation of the data must be done in 3D in order to most accurately locate the lens vertex. However, if there are rapid changes in surface curvature near the vertex, even 3D interpolation may not be sufficient to describe the surface shape in this region. Therefore, realignment of the imaging axis should ideally be incorporated into the data collection process to mitigate the need for subsequent interpolation. Together with Leica Microsystems, we have filed a provisional patent application [28] for a method that would improve axial alignment of the CT scanner during imaging. This method has not yet been incorporated into their hardware, and therefore will not be discussed further in this thesis.

### 5.1.2 Model Overview

The entire process of fitting a two-surface lens and computing its curvature—including realignment with the design equation—can be broken down into the following steps:

1. **Anterior Surface Fit.**

Fit the front surface data to the  $N_a^{\text{th}}$  order Zernike polynomial  $f^a(\mathfrak{X}, c) \equiv f_{N_a}(\mathfrak{X})$ ,

where the values of  $\mathfrak{X}$  correspond to grid points in the sample grid  $S_A^{\text{ii}}$  whose origin is located at the scan vertex  $O = (0, 0)$  (defined in Section 2.2.3). That is, for anterior lens surface height data  $(\mathfrak{X}_i, w_i)$ —where  $\mathfrak{X}_i = (\rho_i, \theta_i)$ —compute the linear least squares estimates for the  $m_a = \frac{1}{2}(N_a + 1)(N_a + 2)$  Zernike coefficients  $c = [c_1, \dots, c_m]^T$  in the model

$$w_i = f^a(\mathfrak{X}_i, c). \quad (5.1)$$

## 2. Posterior Surface Fit.

Find the dewarped back surface coordinates  $(\tilde{\mathfrak{X}}_i, \tilde{w}_i)$  data corresponding to the geometric path length measurements  $(\mathfrak{X}_i, L_i)$ . Dewarping is performed using  $f^a(\mathfrak{X}, c)$  at the un-translated sample points  $\mathfrak{X}_i = (x_i, y_i) = (\rho_i \cos \theta_i, \rho_i \sin \theta_i)$  as described in Section 4.4:

$$\begin{aligned} \tilde{x}_i &= x_i + L_i \frac{\frac{\partial f^a}{\partial x} \left( \sqrt{1 + \left(1 - \frac{n_s^2}{n_\ell^2}\right) \left( \left(\frac{\partial f^a}{\partial x}\right)^2 + \left(\frac{\partial f^a}{\partial y}\right)^2 \right)} - \frac{n_s}{n_\ell} \right)}{1 + \left(\frac{\partial f^a}{\partial x}\right)^2 + \left(\frac{\partial f^a}{\partial y}\right)^2} \\ \tilde{y}_i &= y_i + L_i \frac{\frac{\partial f^a}{\partial y} \left( \sqrt{1 + \left(1 - \frac{n_s^2}{n_\ell^2}\right) \left( f_x^2 + f_y^2 \right)} - \frac{n_s}{n_\ell} \right)}{1 + \left(\frac{\partial f^a}{\partial x}\right)^2 + \left(\frac{\partial f^a}{\partial y}\right)^2} \\ \tilde{w}_i &= f^a(x_i, y_i) - L_i \frac{\sqrt{1 + \left(1 - \frac{n_s^2}{n_\ell^2}\right) \left( \left(\frac{\partial f^a}{\partial x}\right)^2 + \left(\frac{\partial f^a}{\partial y}\right)^2 \right)} + \frac{n_s}{n_\ell} \left( \left(\frac{\partial f^a}{\partial x}\right)^2 + \left(\frac{\partial f^a}{\partial y}\right)^2 \right)}{1 + \left(\frac{\partial f^a}{\partial x}\right)^2 + \left(\frac{\partial f^a}{\partial y}\right)^2}, \end{aligned} \quad (5.2a)$$

where the partial derivatives at each point are computed using central differences

$$\frac{\partial f^a}{\partial x}(x_i, y_i) \approx \frac{f^a(x_i + h, y_i) - f^a(x_i - h, y_i)}{2h} \quad \text{and} \quad \frac{\partial f^a}{\partial y}(x_i, y_i) \approx \frac{f^a(x_i, y_i + h) - f^a(x_i, y_i - h)}{2h}.$$

Fit the dewarped points to the  $N_p^{\text{th}}$  order Zernike polynomial<sup>iii</sup>  $f^p(\mathfrak{X}, c) \equiv f_{N_p}(\mathfrak{X})$ , to obtain the back surface model

$$\tilde{w}_i = f^p(\tilde{\mathfrak{X}}_i, c). \quad (5.2b)$$

---

<sup>ii</sup>Recall that the lens radius  $A$  is used to normalize the radial coordinate when fitting the data to the appropriate Zernike polynomial (see Section 3.1), and therefore  $f^a(\mathfrak{X}, c)$  is not defined for  $\|\mathfrak{X}\| > A$ .

<sup>iii</sup>The front and back model orders  $N_a$  and  $N_p$  do not need to be the same.

Note that due to the dewarping algorithm, the anterior surface model is inherently part of the posterior surface model.

### 3. Realignment.

Find a “reasonable” value of  $\mathfrak{X}_0$  that maximizes the objective function  $f^a(\mathfrak{X})$ ; *i.e.*,

$$\mathfrak{X}_0 = \max_{\|\mathfrak{X}\| \leq A} f^a(\mathfrak{X}).$$

If there is a unique solution, then  $\mathfrak{X}_0$  is the approximate lateral position of the lens vertex and the shifted sample grids are given by

$$\tilde{S} = \{\mathfrak{Z} = \mathfrak{X} + \mathfrak{X}_0 \mid \mathfrak{X} \in S\} \quad \text{and} \quad \tilde{S}_A = \{\mathfrak{Z} \in \tilde{S} \mid \|\mathfrak{Z}\| \leq A\}.$$

If  $\mathfrak{X}_0$  is not unique, or if there is no local maximum within a reasonably small neighborhood of the origin, do not shift the sample grid.<sup>iv</sup>

### 4. Surface Height and Curvature.

Calculate the surface fit at every point  $\mathfrak{Z} \in \tilde{S}_A$  using the anterior and posterior lens models

$$\hat{z}^a = f^a(\mathfrak{Z}) \quad \text{and} \quad \hat{z}^p = f^p(\mathfrak{Z}).$$

Calculating the meridional curvature on the shifted grid  $\tilde{S}_A$  (whose meridians now run through the lens vertex) requires a change of coordinates to compute the partial derivatives with respect to  $\rho_*$ , where  $\rho_* = 0$  at the lens vertex. A mild abuse of notation allows us to express the local anterior and posterior meridional curvature at a point  $\mathfrak{Z}$  on the shifted grid as

$$\hat{k}^a = -\frac{\partial^2 f^a(\mathfrak{Z})}{\partial \rho_*^2} \left( 1 + \left( \frac{\partial f^a(\mathfrak{Z})}{\partial \rho_*} \right)^2 \right)^{-3/2} \quad (5.3)$$

---

<sup>iv</sup>To obtain the results described in this chapter, we used the MATLAB algorithm `fminsearch` to calculate the local minimum of the objective function  $-f^a(\mathfrak{X})$  closest to the origin and subject to the constraint  $\|\mathfrak{X}\| \leq 1.5$  mm. The constraint was enforced by using an output function to abort the optimization protocol if the test point  $\mathfrak{X}$  ever fell outside the specified region. In such a case, the algorithm would not compute an offset.

and

$$\hat{k}^p = -\frac{\partial^2 f^p(\mathfrak{z})}{\partial \rho_*^2} \left( 1 + \left( \frac{\partial f^p(\mathfrak{z})}{\partial \tilde{\rho}_*} \right)^2 \right)^{-3/2}. \quad (5.4)$$

Principal curvatures of the front and back surfaces are obtained by evaluating the maximum and minimum values of (5.3) and (5.4) at the lens vertex,  $\mathfrak{X}_0$ .

### 5.1.3 Quantities of Interest

In Chapters 3 and 4 we used the mean absolute error in surface fit ( $\hat{z}^a, \hat{z}^p$ ) and curvature ( $\hat{k}^a, \hat{k}^p$ ) as a measure of model accuracy. In this chapter, we will be looking at slightly different quantities. In addition to the principal curvature value at the vertex, we will also consider the root mean square (RMS) error in the surface fit and twice the standard deviation of both the surface fit and curvature (*i.e.*, the interval  $[\mu - 2\sigma, \mu + 2\sigma]$ , where  $\mu$  and  $\sigma$  are respectively the mean and standard deviation of the signed error in the relevant metric). The RMS error allows us to compare our results to the asphere figure error tolerance provided by Edmund Optics [65], whereas the  $2\sigma$  interval is recommended by the ANSI corneal topography standard for specifying curvature tolerance [5, §5.4].

In each case described here, the “error” refers to the difference between the computed value of the given metric and the intended value based on the design specifications of the lens, as recommended by the ANSI standard. A detailed discussion of the *model error* (*i.e.*, the difference between the data and a particular model) can be found in Appendix B.

In addition to considering these “average error” measurements across the full diameter of each lens surface, we will further be breaking the lens surface into three zones based on the distance from the vertex in the radial plane. These three zones—which are detailed in Table 5.1 and come from the ANSI standard on corneal topography [5, §5.4]—represent the region of the lens closest to the optical axis (the “central diameter”), the periphery of the lens (the “outer diameter”), and the region in between the two (the “middle diameter”).

To accurately determine surface error, it is also necessary to align the test surface with the design equation in the  $z$ -direction. The offset  $\Delta z$  is the difference between the design equation  $z^a(\mathfrak{X})$  and the Zernike fit  $f^a(\mathfrak{z})$  at the lens vertex:

$$\Delta z = z^a(O) - f^a(\mathfrak{X}_0).$$

The surface error at each point is then given by

$$e_i = \left( f^a(\mathfrak{Z}_i) + \Delta z \right) - z^a(\mathfrak{X}_i),$$

where  $\mathfrak{Z}_i \in \tilde{S}_A$  and  $\mathfrak{X}_i \in S_A$  are corresponding points in the shifted and unshifted sample grids. The same principle can also be used to calculate the back surface error, with the caveat that using different offsets for the front and back surfaces suggests a discrepancy between the computed lens thickness and the design thickness. Such a discrepancy could be due to a number of factors unrelated to the accuracy of the dewarping algorithm, such as manufacturing tolerances on the thickness of the lens or an error in the calculated refractive index of the lens substrate. Note that it is not necessary to consider the vertical offset when analyzing the curvature errors for either surface.

We will also be discussing curvature in terms of keratometric diopters (D) rather than inverse millimeters, as the former are more readily understood in a clinical context (having arisen from an effort to relate the shape properties of the anterior corneal surface to the refractive power of the entire cornea [45]). Diopters are obtained by multiplying the curvature in inverse millimeters by the keratometric constant, 337.5 [5].

## 5.2 Results for OCT Data

In the following section, we will use the metrics discussed in Section 5.1 to evaluate the performance of our four models: 1) front surface fit ( $\hat{z}^a$ ), 2) front surface curvature ( $\hat{k}^a$ ), 3) back surface fit ( $\hat{z}^p$ ), and 4) back surface curvature ( $\hat{k}^p$ ). For each of these four models, we will consider both the results of the synthetic data with quantization error (as a benchmark for best-case performance) as well as the results obtained using the real

Table 5.1: Analysis zones from [5] for assessing accuracy of curvature estimates.

Zone name	Constraints on radial coordinate
Central diameter	$\rho \leq 1.5 \text{ mm}$
Middle diameter	$1.5 \text{ mm} < \rho \leq 3 \text{ mm}$
Outer diameter	$\rho > 3 \text{ mm}$

OCT data for each lens.

As explained in Section 5.1, surface fit accuracy will be evaluated using two quantities: the RMS error between the design equation and the interpolated values  $\hat{z}^a/\hat{z}^p$  from the Zernike model (5.1–5.2), and the  $2\sigma$  interval of the same error across each of the zones from Table 5.1. Curvature accuracy will be assessed using the principal curvature and the  $2\sigma$  interval of the error according to zone between the modeled curvature  $\hat{k}^a/\hat{k}^p$  from (5.3–5.4) and the corresponding curvature value computed analytically from the design equation.

### 5.2.1 Anterior Surface Fit

Based on the analyses from Ch. 3, we can narrow down the range of Zernike models that are worth considering for the front surface. We achieved the most accurate results for the synthetic asphere data with  $N_a \in \{4, 6, 8, 10, 12\}$ , whereas the synthetic data for the front surface of the toric lens performed best when  $N_a \in \{10, 12, 14, 16\}$ . Figures 5.6a and 5.7a show the RMS error in surface fit for the quantized synthetic data for these Zernike models—across the entire lens surface as well as within each zone. The corresponding  $2\sigma$  error intervals are illustrated in Figures 5.8a and 5.9a. We have also included  $N_a = 14$  for the aspheric lens and  $N_a = 8$  for the toric lens to see what happens to the results when the model doesn’t fit quite as well.

For the most part, the RMS error plots for the synthetic data (Figures 5.6a and 5.7a) reveal that the error for the best models tends to be lowest across the central diameter. This is what we would expect given that the goal of the hexapolar sampling pattern is to bias the least squares fit toward the center. This is even more pronounced for the real data—Figures 5.6–5.9 show that the RMS error and  $2\sigma$  intervals are smallest for the central diameter and get progressively worse as we move toward the outside of the fitting region. Note that we have excluded some of the higher order Zernike polynomials for the real data due to the rapid increase in overfitting error. We have also included some polynomials of lower order than were used for the synthetic data in order to see whether the underfitting error is as problematic as the overfitting error. Furthermore, while the rotational symmetry in the synthetic data ensures that odd Zernike polynomials are not needed for the fit, the odd polynomials do come into play for the real data due to the slight axial misalignments during imaging.

As we observed with the synthetic data in Ch. 3, the error from the real data is once

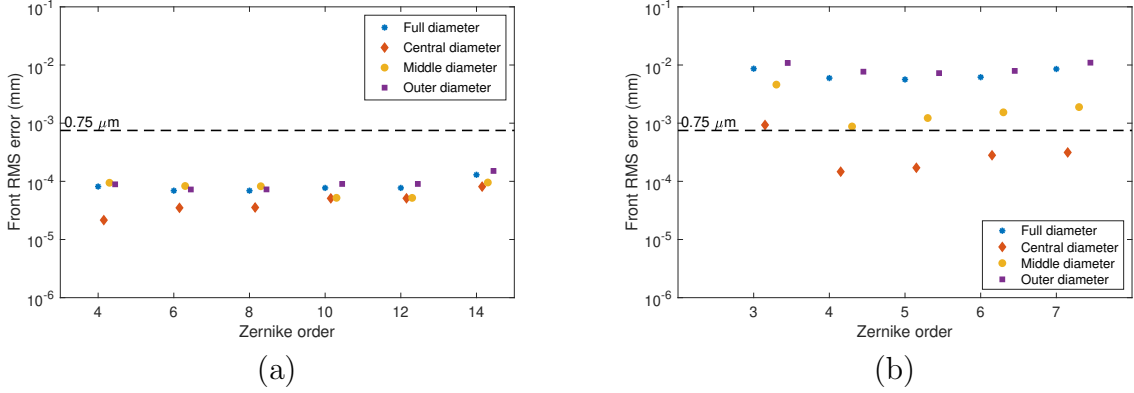


Figure 5.6: RMS surface error for the anterior aspheric lens from (a) synthetic data and (b) real lens data.

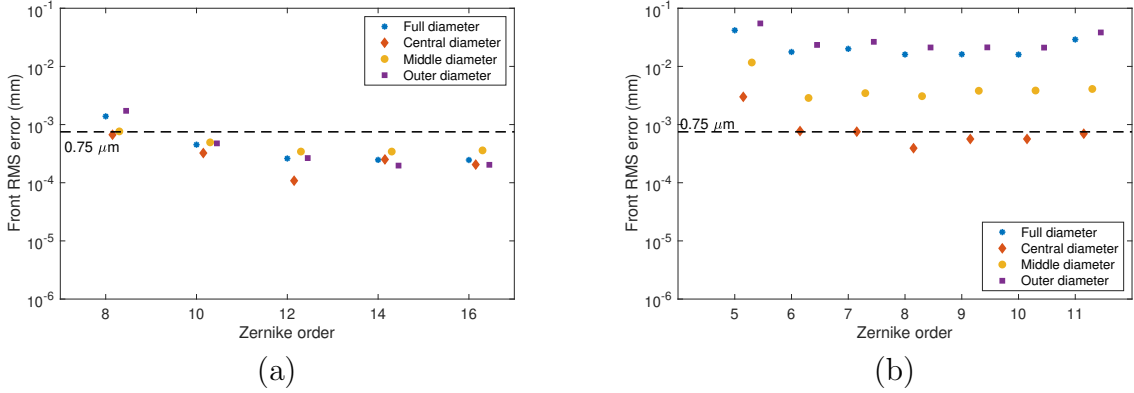


Figure 5.7: RMS surface error for the anterior toric lens from (a) synthetic data and (b) real lens data.

again higher overall for the spherical surface (*i.e.*, the front of the toric lens, shown in Figures 5.7b and 5.9b) than for the aspheric surface (Figures 5.6b and 5.8b). This is due to the fact that spheroids are rather difficult to model using Zernike polynomials and results in overfitting even without much noise present. This pattern is especially true of the  $2\sigma$  intervals for the outer diameter, which is an entire order of magnitude greater for the anterior toric lens. A method for addressing this issue is discussed further in Chapter 7.

In both cases, the results for the real data are several orders of magnitude greater

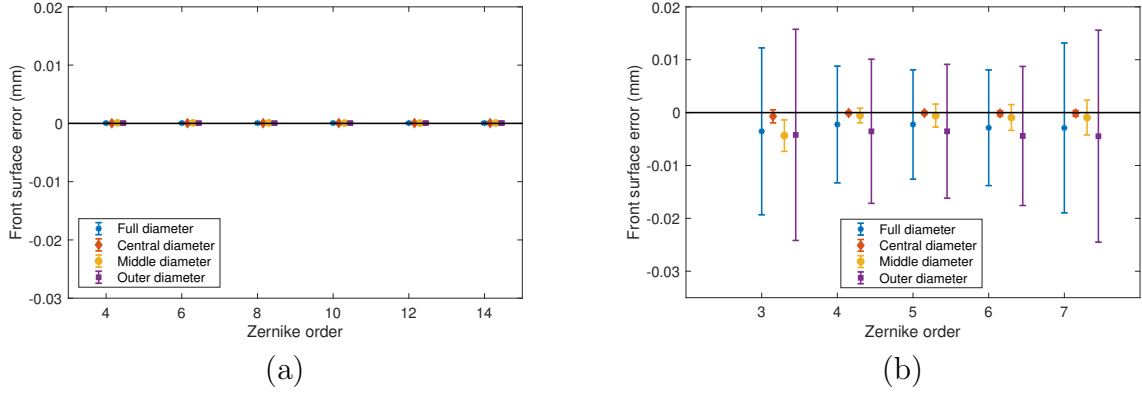


Figure 5.8: Mean surface error and  $2\sigma$  interval for the anterior aspheric lens from (a) synthetic data and (b) real lens data.

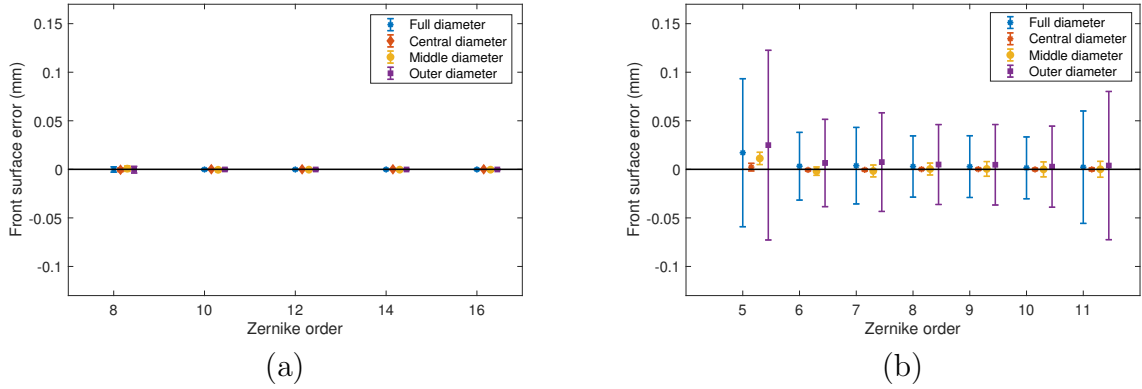


Figure 5.9: Mean surface error and  $2\sigma$  interval for the anterior toric lens from (a) synthetic data and (b) real lens data.

than the corresponding error for the synthetic data. This could be due in part to gaps and greater levels of noise in the real segmentation data. However, it could also be related to the manufacturing tolerances. While we were not provided with a tolerance for the toric lens surface accuracy, note that the RMS error in the asphere for both the central diameter is, for some model orders, even smaller than the  $0.75 \mu\text{m}$  RMS figure error indicated in the manufacturing specifications. The error in the middle and outer zones are each approximately one order of magnitude larger than the previous one, but even at its worst the error is only about 0.02 mm.

For the toric lens, the  $2\sigma$  intervals are smallest for the 6<sup>th</sup>–10<sup>th</sup> order fits, revealing that both underfitting and overfitting are potential concerns. Without knowing the manufacturer’s surface error tolerances, it is difficult to say how much of the error in the outer zone is due to the difficulties using Zernike polynomials to fit a spherical surface and how much is due to manufacturing error in the lens.

## 5.2.2 Anterior Surface Curvature

There are two values we care about in assessing the accuracy of the curvature model: principal curvature and mean curvature error. The front principal curvatures for both lenses—in keratometric diopters, as discussed in Section 5.1.3—are shown in Figures 5.10–5.11. Note that while there is a single principal curvature value for the synthetic data, the results from the real lens data may still be slightly off-center even after performing the axial realignment discussed in Section 5.1.1. Thus, the intervals depicted in Figures 5.10b and 5.11b represent the entire range of meridional curvatures measured at the *approximate* lens vertex after realignment. Figures 5.12–5.13 show the mean curvature error and  $2\sigma$  interval by zone, also in keratometric diopters.

All the principal curvature measurements from the synthetic asphere data (Figure 5.10a) are within  $\pm 0.25$  D of the design value. This is also true for the mean value of the principal curvature from the real aspheric lens data using the 4<sup>th</sup>–7<sup>th</sup> order Zernike fits (Figure 5.10b), although the error is larger for the two highest order models. In fact, for both the 4<sup>th</sup> and 5<sup>th</sup> order models, the entire range of principal curvature measurements falls within a quarter of a diopter of the design specification. However, Figure 5.12b reveals that the *mean* curvature error is worse for the 3<sup>rd</sup> and 5<sup>th</sup> order fits than for the 4<sup>th</sup> order fit, particular in the outer diameter zone. For the 4<sup>th</sup> order fit, the  $2\sigma$  error interval for the curvature is within  $\pm 0.25$  D over the central zone, and well within  $\pm 0.5$  D throughout the middle diameter zone. Note that the mean curvature for the real data is extremely sensitive to both underfitting and overfitting—particularly in the outer region.

The results for the toric lens tell a very different story. The principal curvature for the synthetic data (Figure 5.11a) is only within 0.25 D of the design value when  $N_a = 12$ . However, for the real toric lens data (Figure 5.11b), not only are the mean values of the principal curvature less than a quarter of a diopter off for the 8<sup>th</sup>–11<sup>th</sup> order fits, but the entire range of principal curvature measurements for the 8<sup>th</sup> order fit falls within 0.25 D of the specified design parameter. This is particularly interesting given that the principal

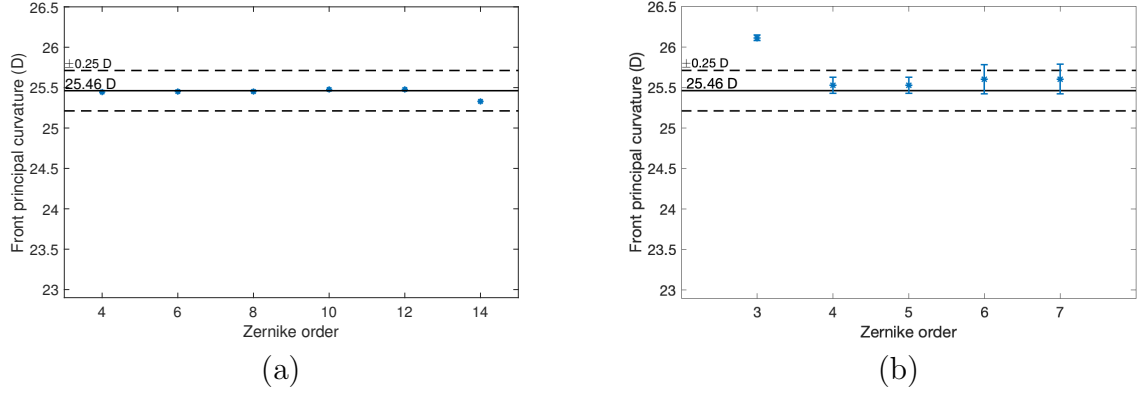


Figure 5.10:  $\hat{K}_a$  for the aspheric lens from (a) synthetic data and (b) real data.

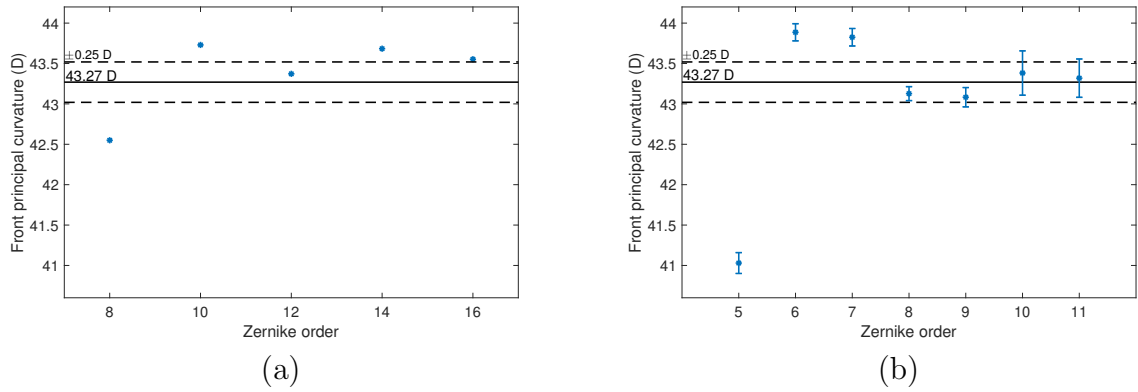


Figure 5.11:  $\hat{K}_a$  for the toric lens from (a) synthetic data and (b) real data.

curvature from the 8<sup>th</sup> order fit to the synthetic data is off by over half a diopter.

There are also some notable differences between the mean curvature error for the two lenses, shown in Figures 5.12–5.13. In particular, the synthetic toric lens data is much more sensitive to underfitting (Figure 5.13a) than the synthetic aspheric lens data. In fact, even without any added noise (Figure 5.13b), we need at least a 10<sup>th</sup> order fit before any of the  $2\sigma$  intervals comes close to being within  $\pm 0.5$  D, and half a diopter also appears to be the best we can do for any Zernike model using the quantized data. This suggests that it may be extremely difficult to accurately measure the curvature for this type of surface using our approach, as the noise present in the real data is likely to result in overfitting for the higher order Zernike models. Indeed, Figure 5.13c illustrates that the

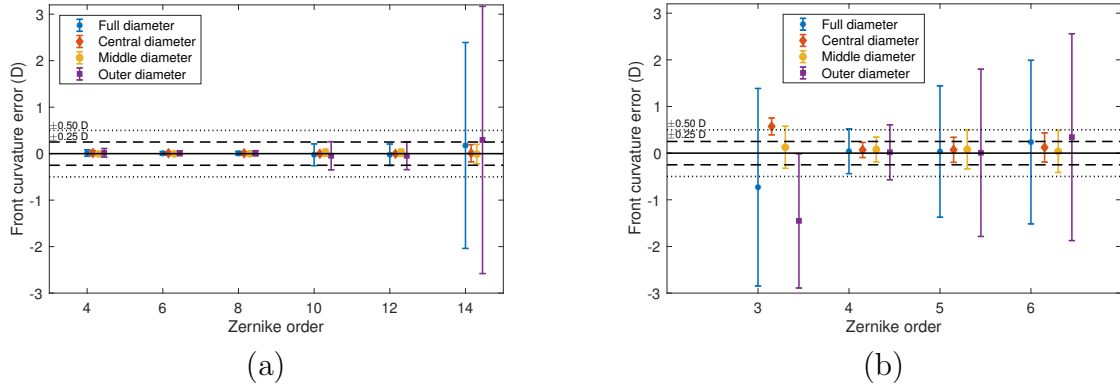


Figure 5.12: Mean curvature error and  $2\sigma$  interval for the anterior aspheric lens using (a) synthetic data and (b) real lens data.

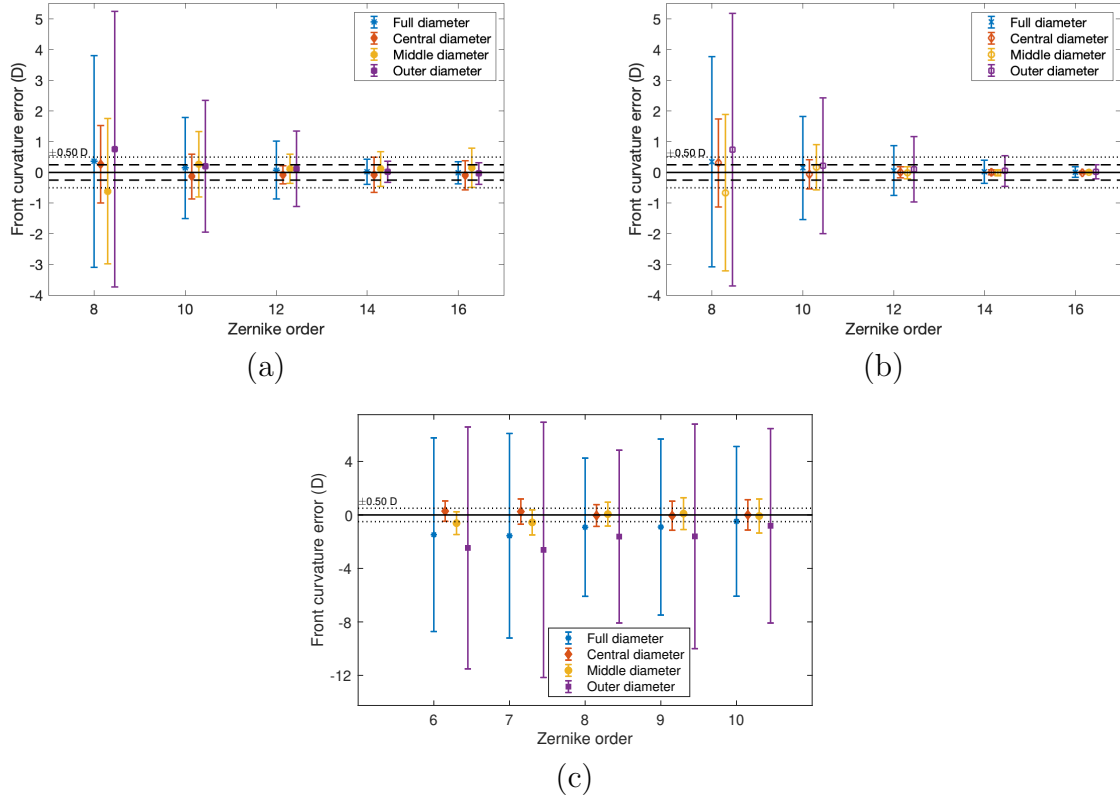


Figure 5.13: Mean curvature error and  $2\sigma$  interval for the anterior toric lens using (a) quantized synthetic data, (b) non-quantized synthetic data, and (c) real lens data. (Note different  $y$ -axis limits for synthetic and real data.)

$2\sigma$  interval for the curvature is, at best, still not quite within half a diopter when  $N_a = 8$ . However, note that for this particular model, the  $2\sigma$  intervals for the central and middle diameters are actually *larger* for the synthetic data, both quantized and non-quantized, than for the real data.

### 5.2.3 Posterior Surface Fit After Dewarping

Recall that the posterior surface model is more complicated than the anterior surface model, as the front surface model is necessary for performing dewarping. Figures 5.14 and 5.15 show the overall RMS surface error for each of the back surfaces after dewarping has been performed using the four best front surface models for the given data set based on the results in Sections 5.2.1–5.2.2. Note that the vertical alignment step for the real data (described in Section 5.1.3) means that the errors for the real and synthetic data sets are not obtained in a strictly identical manner (recall that realignment is *not* performed on the synthetic data).<sup>v</sup> This is why the RMS surface error for the back surface model  $z^p \approx f_0$  is exactly zero when we are using the real aspheric lens data as shown in Figure 5.14b, but  $\sim 10^{-6}$  mm when using the synthetic data as shown in Figure 5.14a. Since  $f_0$  is a flat plane (like the design equation for the back of the asphere), any error in this model would be uniform, and would also be eliminated by the vertical realignment.

For the higher model orders, the overall RMS error for the back surface of the aspheric lens is about  $10^{-4}$  mm from synthetic data and about  $10^{-3}$ – $10^{-2}$  mm from the real data. The RMS error for the back surface of the toric lens is also about  $10^{-4}$  from synthetic data (Figure 5.15a). In each case, the error is actually comparable to the overall RMS error we saw in Section 5.2.1 for the front surface of the same data set: Figure 5.6 shows that the error over the full diameter is around  $10^{-4}$  mm for the synthetic aspheric lens data and  $10^{-2}$  mm for the real aspheric lens data, while the overall RMS error for the synthetic toric lens data (in Figure 5.7a) is about  $10^{-4}$ – $10^{-3}$  mm. The error in the back surface fit is highest for the real toric lens data (Figure 5.15b); however, this value is also comparable to the front surface error of roughly  $10^{-2}$ – $10^{-1}$  mm for the real toric lens data shown in Figure 5.7b. This is likely due to the propagation of error from the front

---

<sup>v</sup>For this analysis, we chose to perform vertical realignment on the front and back lens surfaces independently so that any systematic error in the lens (*e.g.*, in the thickness or refractive index) would not have a disproportionate effect on our evaluation of the surface fit accuracy.

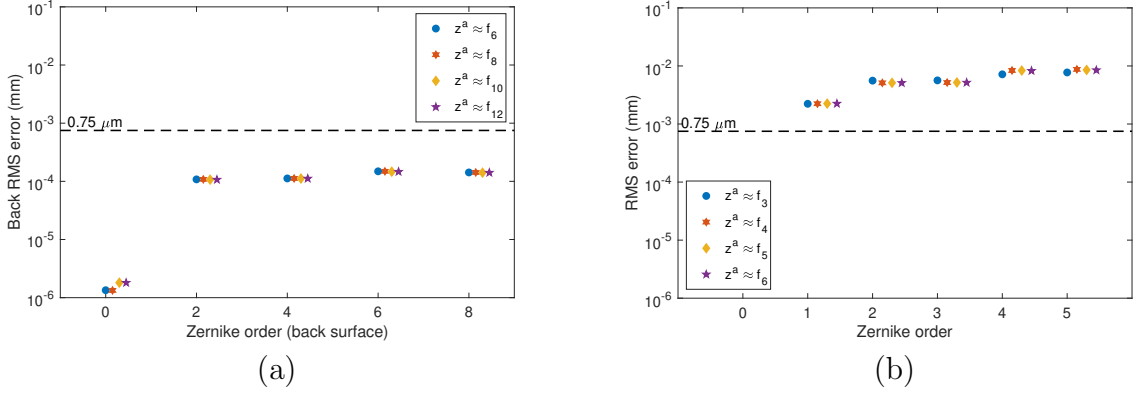


Figure 5.14: RMS surface error for the posterior aspheric lens after dewarping with anterior Zernike models  $z^a$ , using (a) quantized synthetic data and (b) real lens data.

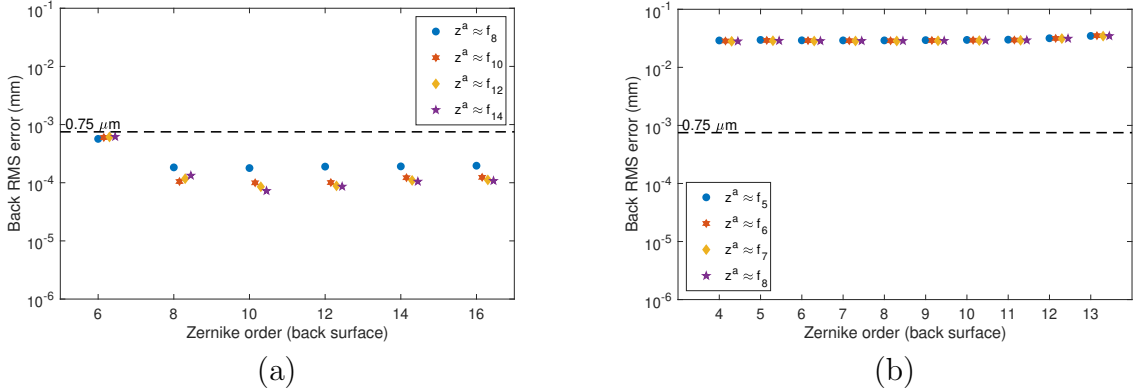


Figure 5.15: RMS surface error for the posterior toric lens after dewarping using (a) synthetic data and (b) real lens data.

surface through the dewarping algorithm.

In all but one or two cases, the RMS error in the back surface is comparable regardless of which of the four front surface models we choose. Figures 5.16 and 5.17 show the mean and  $2\sigma$  interval in the surface error (according to zone) for the back surface of each data set, after dewarping has been performed using the front surface model that appeared to yield the best results in Sections 5.2.1–5.2.2: *i.e.*,  $z^a \approx f_6$  for the synthetic aspheric lens data,  $z^a \approx f_4$  for the real aspheric lens data,  $z^a \approx f_{10}$  for the synthetic toric lens data, and  $z^a \approx f_8$  for the real toric lens data. As with the front surface, the outer zone is once

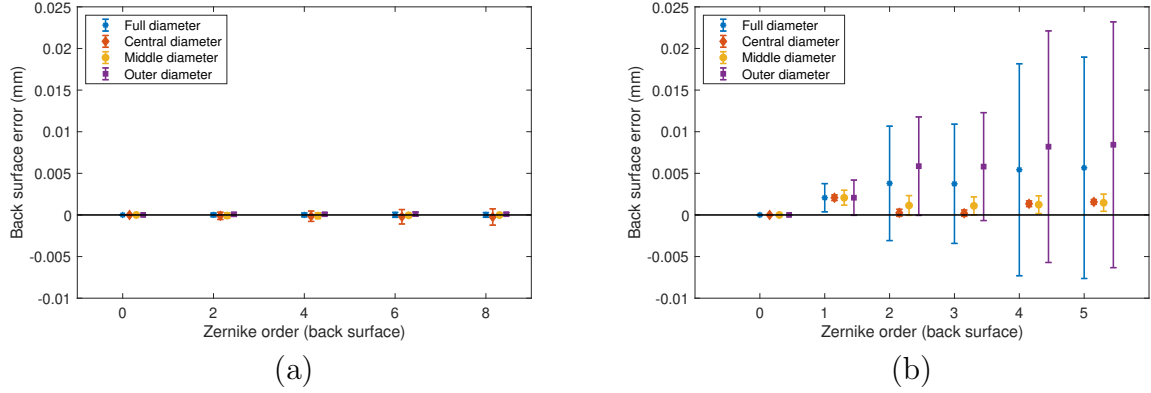


Figure 5.16: Mean surface error and  $2\sigma$  interval for the posterior aspheric lens after dewarping a) quantized synthetic data ( $z^a \approx f_6$ ), and b) real lens data ( $z^a \approx f_4$ ).

again the region with the greatest amount of error.

Unlike any of the other data sets, the error for the back surface of the asphere from the real data (Figure 5.16b) is heavily biased, suggesting that the vertical realignment may have shifted the entire surface too much in one direction. However, the  $2\sigma$  intervals for this surface are actually smaller than the corresponding front surface intervals we saw in Figure 5.8b. Because the back of the asphere is flat, overfitting causes the error to increase—particularly in the outer zone—as the Zernike order of  $z^p$  increases. Obviously the best model for this surface would be  $z^p \approx f_0$ , although  $z^p \approx f_1$  seems to produce acceptable results. This makes sense given that the odd Zernike polynomials included in  $f_1$  only serve to capture any uniform horizontal tilt present in the surface, whereas the Envisu’s sample alignment protocol ensures that the back of the aspheric lens is perpendicular to the CT axis during data collection. The higher model orders are also acceptable if the region of interest is restricted to the central and middle zones.

The front surfaces of both lenses are axisymmetric, so we only had to worry about axial realignment before computing the errors in Sections 5.2.1–5.2.2. This is also true for the back surface of the aspheric lens. However, the back surface of the toric lens has two distinct principal curvatures, so any discrepancy between the rotational orientation of the lens during imaging and that of the design equation will result in additional surface (and curvature) error. To account for this discrepancy, the results for the real toric lens data (Figure 5.17b) have been rotated about the optical axis—as approximated by the axial realignment step—so that the principal meridians are aligned with the design equation

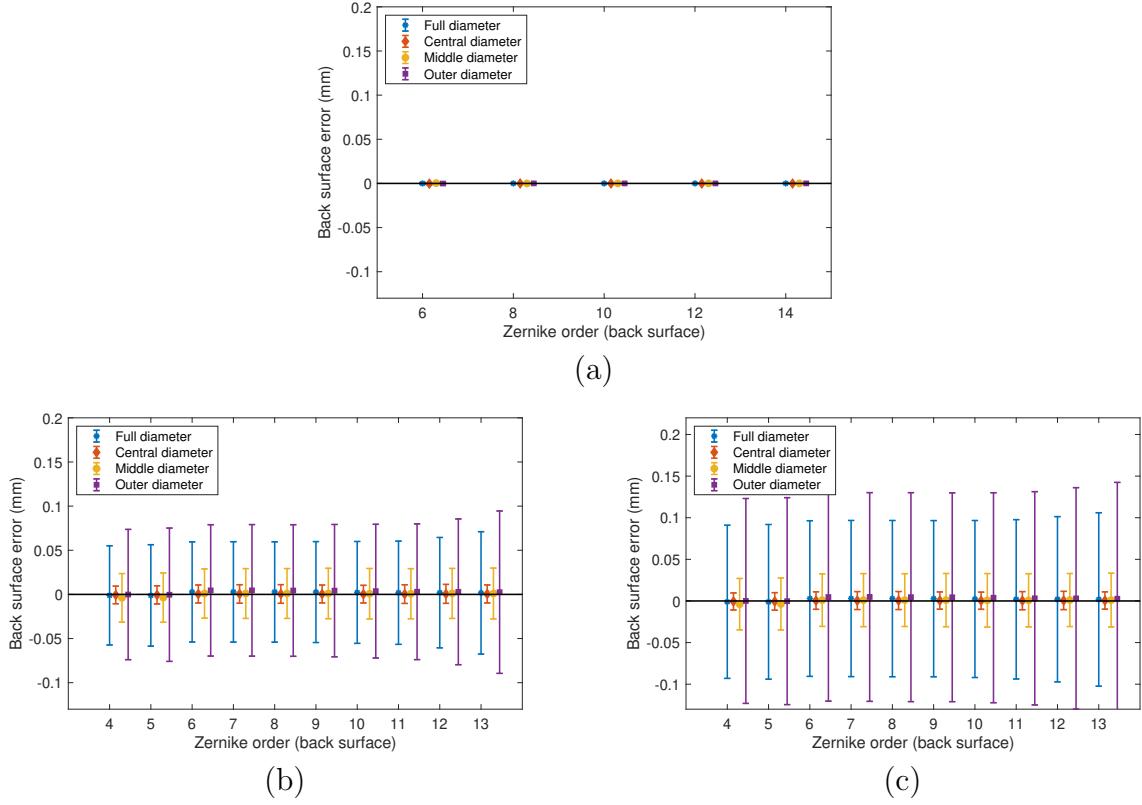


Figure 5.17: Mean surface error and  $2\sigma$  interval for the posterior toric lens after de-warping a) quantized synthetic data ( $z^a \approx f_{10}$ ), b) real lens data after reorientating the data to align the principal axes with the design equation ( $z^a \approx f_8$ ), and c) real lens data without principal axis reorientation ( $z^a \approx f_8$ ).

prior to error calculation.<sup>vi</sup> For comparison, Figure 5.17c shows the surface error for the back of the toric lens if we do not reorient the meridians to align the principal directions. Note that reorienting the meridians does not significantly impact the error in the central and middle zones, but the improvement in the outer zone is substantial.

To determine the principal directions for reorientation purposes, the principal curvatures were calculated along the translated meridians at angular increments of  $1.5^\circ$ . Depending on the order of the Zernike fit to the back surface ( $z^p$ ), we found that the minimum curvature was equally likely to be located at either  $19.5^\circ$  or  $21^\circ$  (respectively the 14<sup>th</sup> or 15<sup>th</sup> frame of imaging data). The direction of the principal meridians was

<sup>vi</sup>As with axial and vertical realignment, this correction is not necessary for the synthetic data.

not affected by our choice of front surface model  $z^a$ . For this type of lens (that is, one such that  $|R_{p1} - R_{p2}| > 0.3$  mm), the ISO standard on ophthalmology stipulates that compliant devices be able to measure the principal meridians to within  $\pm 2^\circ$  [35]. Since we have no way of knowing the precise original orientation of the lens during imaging, we cannot verify that our method satisfies this accuracy requirement, nor can we confirm the robustness without repeated measurements. Future validation of the principal meridians obtained in this manner will likely require a finer angular grid.

Overall, the  $2\sigma$  intervals for the surface error are slightly larger for the back of the toric lens than they were for the front (Figure 5.9b), which is likely due to the propagation of error from the front surface through the dewarping process. Furthermore, it is difficult to identify a best Zernike order for the back surface of the toric lens just from the surface fit alone, as all the models shown in Figure 5.17b seem to produce comparable results.

### 5.2.4 Posterior Surface Curvature After Dewarping

For both the synthetic and real aspheric lens data, the error in the back principal curvature (Figure 5.18) is well under 0.25 D no matter which combination of front and back surface models we use. The principal curvature error for the real data is slightly worse for  $z^a \approx f_3$  but comparable for the other front surface orders, once again confirming that  $z^a \approx f_4$  is a good choice for the front surface model.

Figure 5.20b shows the  $2\sigma$  error interval for the overall curvature by zone when  $z^a \approx f_4$ , and we can see that the error interval for each zone is within about a quarter diopter for up to a third order fit to the back surface. As with the surface error, the best results for the principal curvature and the overall curvature from the real asphere data occur with the models  $z^p \approx f_0$  and  $z^p \approx f_1$ . However, in the interest of allowing our model some leeway to account for manufacturing error (*i.e.*, deviations in the lens surface from a perfect plane) or residual optical error that might not have been fully corrected by dewarping, it is worth selecting the highest order model that still produces reasonable results. In this case, the best choice for the back surface model may actually be  $z^p \approx f_3$ —even for this model, the various measures of curvature for the back surface of the aspheric lens are still more accurate than the best front surface curvature results depicted in Figures 5.12–5.10.

Like the principal curvature results for the back surface of the aspheric lens, the principal curvatures for the back of the toric lens (shown in Figure 5.19) are fairly similar

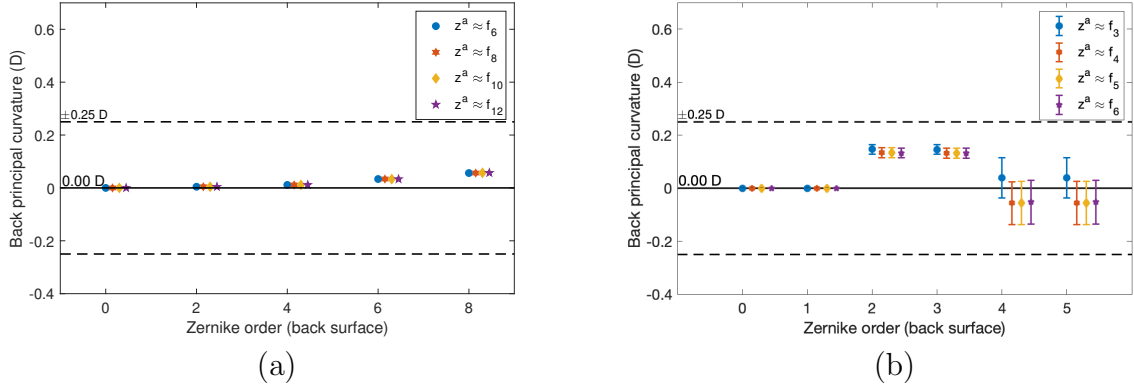


Figure 5.18: Back principal curvature for aspheric lens after dewarping, using (a) quantized synthetic data and (b) real lens data.

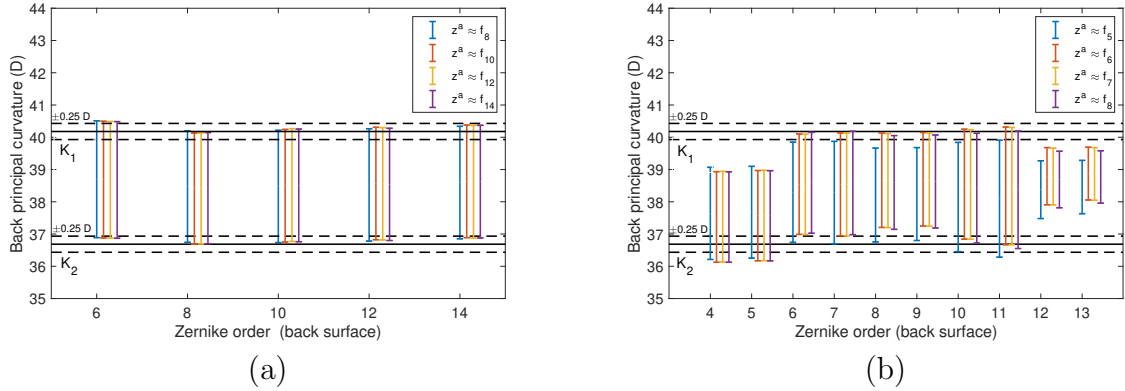


Figure 5.19: Back principal curvatures ( $K_{p_1} = 40.18$  D,  $K_{p_2} = 36.67$  D) for the toric lens after dewarping, using (a) synthetic data and (b) real lens data.

for most of the front surface models. Once again, the lowest order front surface model shown for the real lens data,  $z^a \approx f_5$ , produces slightly different results compared to the three higher order models, which appear to be comparable to one another. Since we obtained the best front surface curvature estimates with  $z^a \approx f_8$ , this seems like the best choice for the back surface model as well.

The only cases in which both the minimum and maximum curvature are within a quarter diopter of the design values for the real data is when we use a 6<sup>th</sup> order or higher front surface fit and either a 12<sup>th</sup> or 13<sup>th</sup> order back surface fit. However, while the error

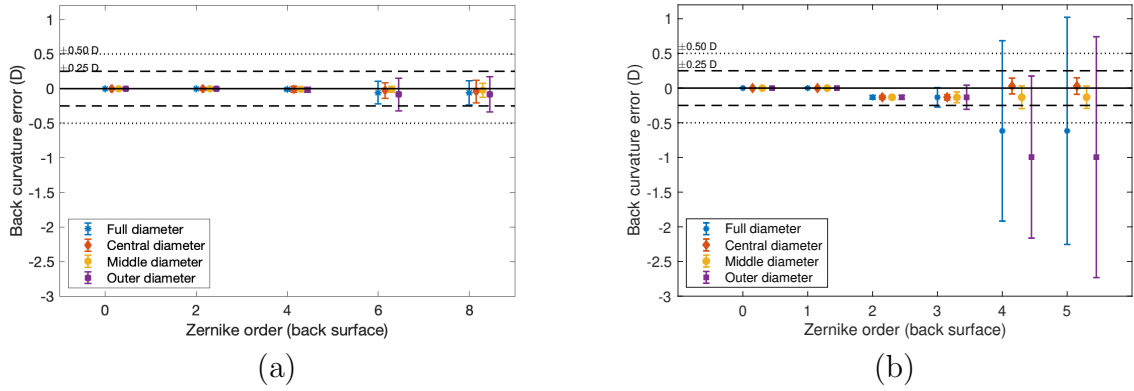


Figure 5.20: Mean curvature error and  $2\sigma$  interval for the posterior aspheric lens after dewarping a) synthetic data ( $z^a \approx f_6$ ), and b) real lens data ( $z^a \approx f_4$ ).

in the principal curvature and the surface fit does not seem to increase rapidly as the order of the back surface fit increases, overfitting *does* have a significant impact on the mean curvature error, shown in Figure 5.21—for back surface models of order  $N_p \geq 9$ , the overall curvature error becomes so large that we could not include it in the figures without obscuring the better results. Since the accuracy of the local surface curvature is important to us, this means that  $z^p \approx f_{12}$  and  $z^p \approx f_{13}$  are not viable models for this application. The next best back surface models for principal curvature are  $z^p \approx f_6$  and  $z^p \approx f_7$ , and it is clear from Figure 5.21 that  $z^p \approx f_6$  also provides the best local curvature estimates for the real data.

Note that while the principal axis reorientation did not have a major impact on the surface fit for the posterior toric lens in the central and middle zones, the curvature estimates in these zones are substantially better after reorientation. Without reorientation (Figure 5.21d), the  $2\sigma$  error intervals for  $z^p \approx f_6$  are close to 2 D; however, with reorientation (Figure 5.21c) these intervals drop to close to 0.5 D. Figures 5.21a and 5.21b show that for  $z^p \approx f_6$ , the error intervals are perhaps even slightly worse for the quantized synthetic data, even when warping (and subsequent dewarping) is not taken into account. However, if segmentation data can be cleaned up to the point that a higher order back surface fit (such as  $z^p \approx f_{10}$ ) could be used without overfitting, this could at least partially mitigate some of the mean curvature error. For the quantized synthetic data, the error intervals for the back surface model  $z^p \approx f_{10}$  are all around a quarter diopter. This also indicates that it may be very difficult to reduce the size of the  $2\sigma$  error

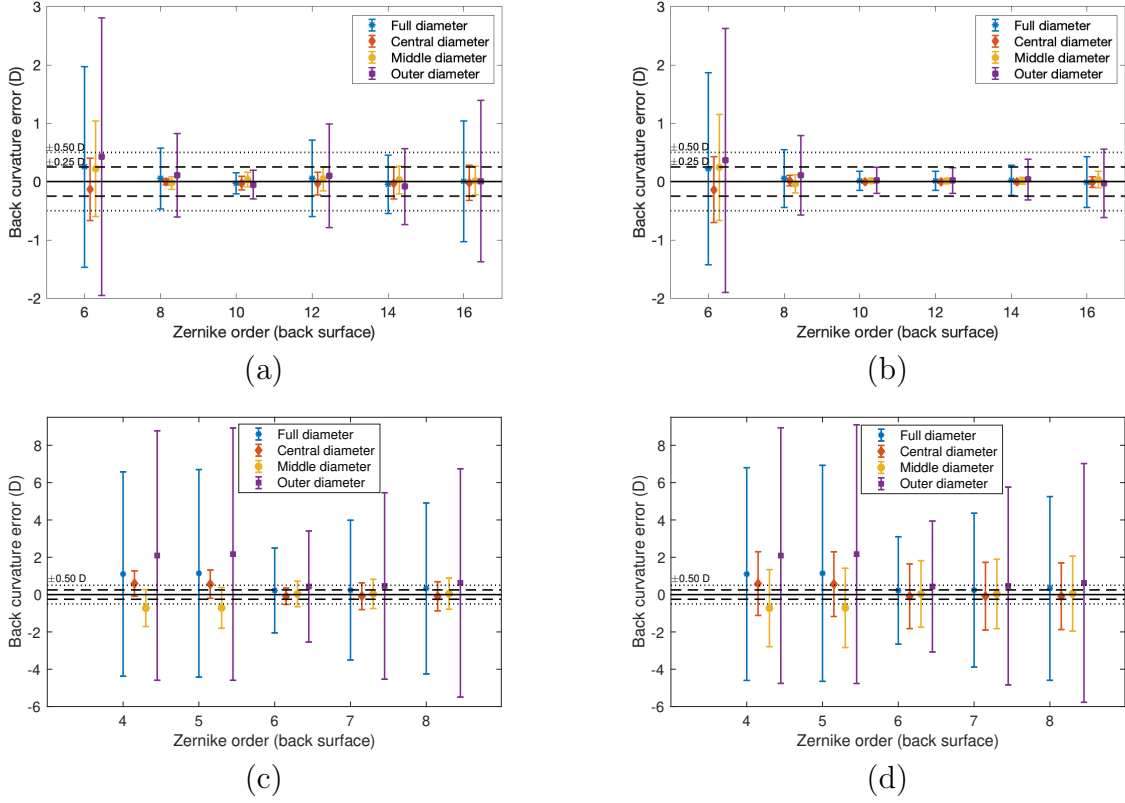


Figure 5.21: Mean curvature error and  $2\sigma$  interval for the posterior toric lens from a) quantized synthetic data dewarped using  $z^a \approx f_{10}$ , b) quantized synthetic data without warping/dewarping, and real lens data dewarped using  $z^a \approx f_8$  c) with axis reorientation and d) without axis reorientation.

intervals to less than a quarter of a diopter for real data obtained at this resolution.

For both the real and synthetic toric lens data, the best curvature results for the back surface are comparable in magnitude to (if not slightly better than) the best front surface results shown in Figure 5.13. For the quantized synthetic data, the smallest  $2\sigma$  error interval for the front surface ends up being plus or minus a quarter to half a diopter depending on the zone, whereas for the back surface the smallest error interval is about  $\pm 0.25$  D for each zone. For real data, the  $2\sigma$  interval for the central zone is around  $\pm 1$  D for the front surface and  $\pm 0.5$  D for the back surface. The middle zone interval is about  $\pm 1$  D for both surfaces, while the outer zone is largest at roughly  $-8$  to  $4$  D for the front and  $\pm 3$  D for the back.

## 5.3 Summary

In Section 5.2, we saw that the best Zernike models for the aspheric lens when using real data were  $z^a \approx f_4$  and  $z^p \approx f_3$ , while the toric lens was best modeled by  $z^a \approx f_8$  and  $z^p \approx f_6$ . The error—as compared to the design specifications—in our estimates of surface fit, curvature, and central lens thickness ( $t_C$ ) based on these models are summarized in Table 5.2. Most of these results have all been discussed in the previous section with the exception of  $t_C$ , which was within about 0.02 mm of its design value for the aspheric lens and 0.0002 mm for the toric lens. Note that the tolerance on the design thickness for the aspheric lens is several orders of magnitude larger than that of the toric lens, at 0.1 mm versus 0.002 mm.

We estimated the anterior and posterior principal curvatures of the aspheric lens as being within the ranges 25.43–25.63 D and 0.11–0.15 D, respectively—both of which are well within a quarter diopter of their design values of  $K_a = 25.46$  D and  $K_p = 0.0$  D. The anterior curvature of the toric lens was estimated to be 43.04–43.21 D, also within a quarter diopter of its design value of  $K_a = 43.27$  D. For the posterior toric lens, the estimates of the maximum and minimum curvatures were 40.15 D and 37.03 D. This is extremely close to the design value of  $K_{p_1} = 40.18$  D for the maximum curvature, but slightly over a quarter diopter from the minimum curvature’s design value of  $K_{p_2} = 36.67$  D.

To compare these results to those of the previous sections, we can also look at the corresponding principal radii of curvature. For the aspheric lens, the anterior radius of curvature estimates vary from 13.169 mm to 13.274 mm, which is at worst 0.086 mm from the design radius of  $R_a = 13.255$  mm. This is not quite within the 0.05 mm tolerance for “Type B” ophthalmometers; however, the mean value of 13.221 mm does meet this requirement.<sup>vii</sup> The estimates for the anterior radius of curvature of the toric lens range from 7.81 mm to 7.84 mm, deviating by at most 0.04 mm from the design value of  $R_a = 7.80$  mm—an order of magnitude *better* than the estimates obtained using the same model order with idealized synthetic data in Chapter 3. The maximum and minimum posterior radii were estimated to be 9.12 mm and 8.41 mm, which differ from their design values of  $R_{p_1} = 9.20$  mm and  $R_{p_2} = 8.40$  mm by 0.08 mm and 0.01 mm, respectively. Although we were able to obtain better estimates of these quantities with the idealized synthetic data in Chapter 4, this required using at least an 8<sup>th</sup> order Zernike fit for the

---

<sup>vii</sup>The tolerance on the design value of  $R_a$  for the aspheric lens was not provided by the manufacturer.

Table 5.2: Error in elevation and curvature estimates from real lens data.

Aspheric Lens		
	Front ( $z^a \approx f_4$ )	Back ( $z^p \approx f_3$ )
RMS error – overall	5.96 $\mu\text{m}$	5.18 $\mu\text{m}$
RMS error – central zone	0.15 $\mu\text{m}$	0.28 $\mu\text{m}$
RMS error – middle zone	0.88 $\mu\text{m}$	1.22 $\mu\text{m}$
RMS error – outer zone	7.68 $\mu\text{m}$	6.65 $\mu\text{m}$
Curvature error – overall	$0.04 \pm 0.24$ D	$-0.13 \pm 0.07$ D
Curvature error – central zone	$0.07 \pm 0.08$ D	$-0.13 \pm 0.02$ D
Curvature error – middle zone	$0.08 \pm 0.13$ D	$-0.13 \pm 0.04$ D
Curvature error – outer zone	$0.02 \pm 0.29$ D	$-0.13 \pm 0.09$ D
Absolute maximum error in $K$	0.17 D	0.15 D
Absolute error in $t_C$	0.019 mm	
Toric Lens		
	Front ( $z^a \approx f_8$ )	Back ( $z^p \approx f_6$ )
RMS error – overall	16.04 $\mu\text{m}$	28.49 $\mu\text{m}$
RMS error – central zone	0.39 $\mu\text{m}$	5.12 $\mu\text{m}$
RMS error – middle zone	3.08 $\mu\text{m}$	13.97 $\mu\text{m}$
RMS error – outer zone	21.16 $\mu\text{m}$	37.46 $\mu\text{m}$
Curvature error – overall	$-0.92 \pm 2.58$ D	$0.22 \pm 1.14$ D
Curvature error – central zone	$-0.04 \pm 0.41$ D	$-0.09 \pm 0.22$ D
Curvature error – middle zone	$0.06 \pm 0.45$ D	$0.04 \pm 0.34$ D
Curvature error – outer zone	$-1.62 \pm 3.23$ D	$0.43 \pm 1.49$ D
Absolute maximum error in $K$	0.23 D	0.03 D ( $K_{p_1}$ ) 0.34 D ( $K_{p_2}$ )
Absolute error in $t_C$	0.0002 mm	

back surface; for the 6<sup>th</sup> order fit used here, the estimates for both of the posterior radii fell at or slightly above the 0.05 mm threshold.<sup>viii</sup>

Figures 5.22–5.23 depict the meridional curvature maps of the three curved surfaces

<sup>viii</sup>Note that the tolerance on the design values of  $R_a$ ,  $R_{p_1}$ , and  $R_{p_2}$  for the toric lens is  $\pm 0.01$  mm.

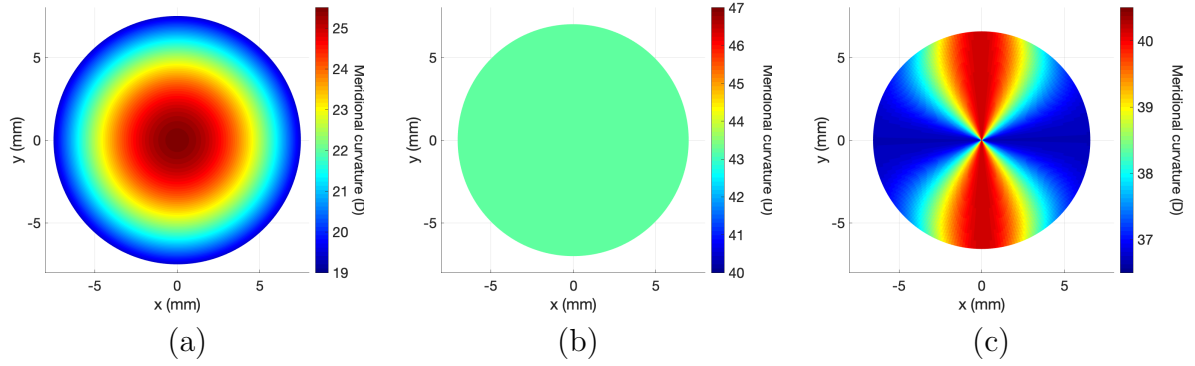


Figure 5.22: Meridional curvature maps based on the design equations for the (a) anterior aspheric lens, (b) anterior toric lens, and (c) posterior toric lens.

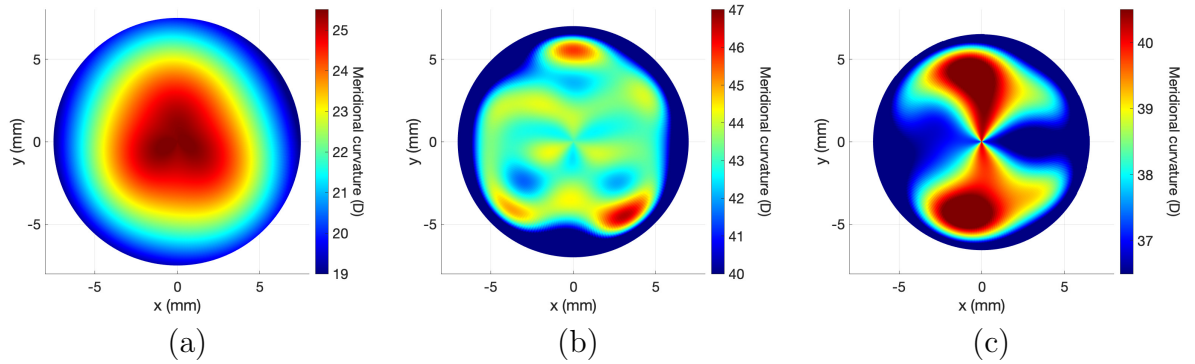


Figure 5.23: Meridional curvature maps from OCT data for the (a) anterior aspheric lens, (b) anterior toric lens, and (c) posterior toric lens.

generated from the OCT data using the Zernike models in Table 5.2, as well as maps of the design curvature for comparison. Recall that the anterior toric lens (Figures 5.22b) is spherical and therefore has a constant curvature. Error maps for all four lens surfaces are shown in Figure 5.24. The curvature of the posterior aspheric lens is 0, so its curvature map corresponds to its error map, Figure 5.24c.

The maps for the anterior and posterior aspheric lens appear reasonable, with the local curvature error never exceeding  $\pm 1$  D at any point for either lens surface. The curvature maps for the toric lens are less accurate, with especially large errors ( $\gg 5$  D) around the periphery. These edge errors are similar to what we saw in Chapter 3 when

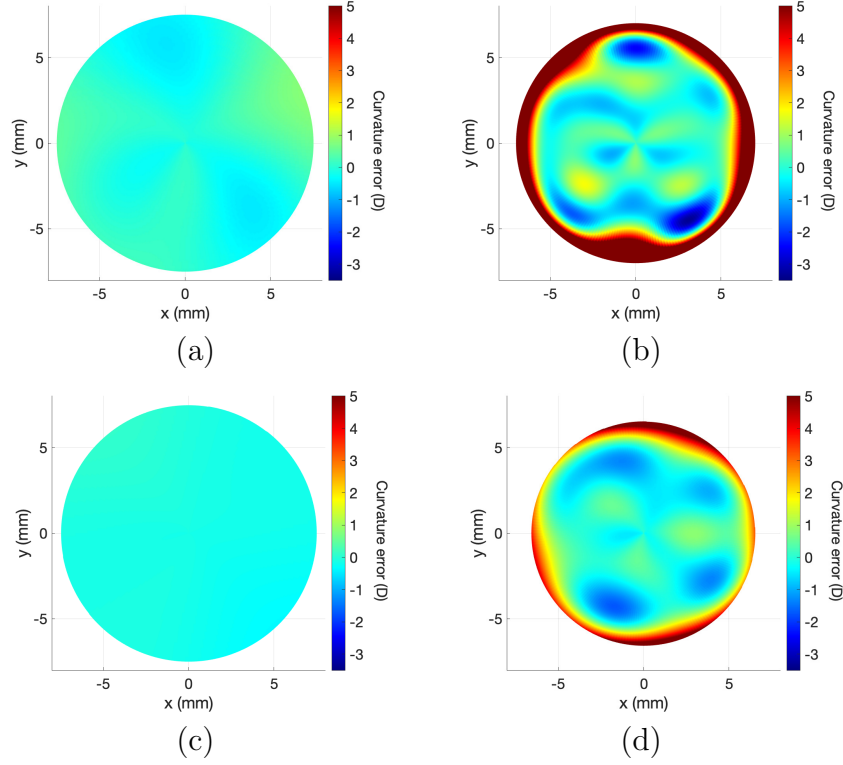


Figure 5.24: Local curvature error for the (a) anterior aspheric lens, (b) anterior toric lens, (c) posterior aspheric lens, and (d) posterior toric lens.

performing the same computations with synthetic data, so they may be unavoidable for some surfaces. Their influence can likely be at least partially mitigated by imaging a larger area and shrinking the diameter of the region of interest when reporting results. Another possible source of error for the toric lens is the difficulty determining the vertex due to the missing data in the very center of each lens, which would lead to the curvatures being computed along the incorrect meridians. Short of eliminating reflections and improving segmentation, an alternative solution might be using a 3D measure of local curvature such as Gaussian curvature, which completely avoids the issue of locating the lens vertex.

We will discuss the results of this chapter in greater detail in Chapter 7.

# Chapter 6

## Uncertainty Analysis

Research has been done involving uncertainty analysis in imaging data, including estimation of quantization error in image processing [42, 81, 106], uncertainty estimation in edge detection and segmentation algorithms [3, 12], uncertainty quantification in image reconstruction [10], and estimation and propagation of uncertainty through an entire imaging analysis pipeline [96]. Additionally, there has been work involving model calibration in the use of orthogonal polynomial moment descriptors of image intensity data [2, 46]. However, since we do not have access to the original imaging data or segmentation algorithms, we are not able to include any of these image processing steps in our uncertainty analysis. Instead, this chapter will address only the contributions associated with fitting the point cloud data to a three dimensional surface, as well as dewarping and curvature estimation based on the 3D surface model.

The first two sections of this chapter summarize the relevant mathematical and statistical models for the aspheric and toric lenses (Figure 6.1). Section 6.3 addresses model calibration, including identifiability and obtaining density estimates for the Zernike coefficients for the front and back surface. In Section 6.4 we will evaluate how the error in our coefficient estimates propagates through the models to impact the estimates of surface fit and curvature. In the final section, Section 6.5, we will employ several methods of global sensitivity analysis to evaluate how the different coefficients affect the estimates of the anterior and posterior principal curvatures based on the model response. All of the statistical methods and algorithms used for the analyses in Sections 6.3–6.5 are described in greater detail in *Uncertainty Quantification: Theory, Implementation, and Applications* and its upcoming second edition, both by Ralph C. Smith [89, 90].



Figure 6.1: Renderings of the aspheric lens (left) and the toric lens (right) from the design equations in Section 2.3.

Many of the methods used in this chapter are predicated on the assumption that the error in the data is (at a minimum) independent and identically distributed (iid) with a mean value of 0 [9, 89]. As the error in the real OCT data is clearly not iid (see Appendix B), we will conduct our statistical analyses using synthetic data per the method described in Section 4.3. However, instead of quantization error (which, as we pointed out in Section 2.4.2, is not iid), the noise added to the synthetic data used in this chapter is  $\overset{\text{iid}}{\sim} \mathcal{N}(0, \sigma_0^2)$ . Appendix B describes the synthetic data for this chapter in more detail, as well as an explanation of how we chose the error variance  $\sigma_0^2 = 0.0001$  mm.

It is worth commenting that the parameter estimation in Section 6.3.2 as well as the global sensitivity analyses in Section 6.5 were repeated for multiple choices of the finite difference step size used in the dewarping algorithm as well as the curvature estimation. We also compared the finite difference differentiation with the complex-step method discussed in [90, Ch. 8]. In every case, the results we obtained were identical to the ones presented in this chapter.

## 6.1 Mathematical Models

In Chapters 3–4 we developed mathematical models for the anterior lens surface, as well as the refraction-corrected posterior lens surface. In particular, we modeled both the anterior and posterior axial elevation at the radial coordinate  $\mathfrak{X} \in \mathbb{R}^2$  using a truncated

Table 6.1: Order of the Zernike expansion used to fit each lens surface ( $N$ ), as well as the total number of terms in the complete expansion ( $m$ ).

Surface	$N$	$m$
Aspheric lens front	4	15
Aspheric lens back	2	6
Toric lens front	10	66
Toric lens back	8	45

Zernike polynomial series of the form

$$f(\mathfrak{X}, c) = \sum_{j=1}^m c_j Z_j(\mathfrak{X}'), \quad (6.1)$$

where the normalized coordinate  $\mathfrak{X}' \in \mathbb{R}^2$  has been scaled to fit within the unit disk domain of the Zernike basis functions (see Section 3.1). As in previous chapters,  $c$  indicates the parameter vector containing all the Zernike coefficients.

We have selected the following orders for the finite polynomial expansion for each lens surface:  $N_a = 4$  and  $N_p = 2$  for the front and back of the aspheric lens (respectively), and  $N_a = 10$  and  $N_p = 8$  for the front and back of the toric lens. This information, along with the total number of terms  $m = \frac{(N+1)(N+2)}{2}$  in the corresponding expansion, is summarized in Table 6.1. Although these orders were not the optimal ones according to the analyses in Chapters 3 and 4, we will show in Section 6.3.1 that they are the highest order models for which the magnitude of the non-zero coefficients is greater than the numerical error in the coefficient estimates.

### 6.1.1 Anterior Lens Model

The anterior surface of each lens (which we will denote by  $f^a$ ) is modeled using the Zernike transform (6.1) with appropriate number of polynomials  $m_a$  indicated in Table 6.1

$$f^a(\mathfrak{X}, c) = \sum_{j=1}^{m_a} c_j Z_j(\mathfrak{X}'), \quad \mathfrak{X} \in \mathbb{R}^2, \quad (6.2)$$

where  $c = [c_1, \dots, c_{m_a}]^T$  is the vector of Zernike coefficients. The observed axial elevations are

$$z_i = f^a(\mathbf{x}_i, c) = \sum_{j=1}^{m_a} c_j Z_j(\mathbf{x}'_i).$$

For a set of  $s$  discrete axial elevation values  $z = [z_1, \dots, z_s]^T$ , the model can be written as the linear system

$$z = Xc, \tag{6.3a}$$

where the design matrix  $X$  consists of the Zernike polynomials  $Z_j$  evaluated at the normalized sample points  $\mathbf{x}'_i$ :

$$X = \begin{bmatrix} Z_1(\mathbf{x}'_1) & Z_2(\mathbf{x}'_1) & \cdots & Z_{m_a}(\mathbf{x}'_1) \\ \vdots & \vdots & & \vdots \\ Z_1(\mathbf{x}'_s) & Z_2(\mathbf{x}'_s) & \cdots & Z_{m_a}(\mathbf{x}'_s) \end{bmatrix}. \tag{6.3b}$$

### 6.1.2 Posterior Lens Model

We can formulate the back surface problem in two different ways. The first approach is the one used in Chapters 4–5, where we treat refraction correction as part of the data preprocessing step and simply model the posterior axial elevation the same way we modeled the anterior elevation. In the second approach, we will consider the dewarping step to be part of the model itself.

#### Posterior Model I

The first model is simply a Zernike expansion  $f^p$  of the dewarped back surface, analogous to the front surface model  $f^a$  in Section 6.1.1. That is, the axial elevation of the posterior surface at the dewarped point  $\tilde{\mathbf{x}}$  is given by

$$f^p(\tilde{\mathbf{x}}, c) = \sum_{j=1}^{m_p} c_j Z_j(\tilde{\mathbf{x}}'), \quad \tilde{\mathbf{x}} \in \mathbb{R}^2 \tag{6.4}$$

where the number of terms  $m_p$  in the back surface model may differ from  $m_a$  in the front surface model. The observations are the (non-distorted) points

$$\tilde{z}_i = f^p(\tilde{\mathbf{x}}_i, c) = \sum_{j=1}^{m_p} c_j Z_j(\tilde{\mathbf{x}}'_i).$$

As in Section 6.1.1, we can represent this model in terms of the linear system

$$z = Xc, \tag{6.5a}$$

except this time we let  $\tilde{z} = [\tilde{z}_1, \dots, \tilde{z}_s]^T$  be the vector of refraction-corrected posterior surface observations, and we evaluate the Zernike polynomials in the design matrix  $X$  at the dewarped coordinates  $\tilde{\mathbf{x}}_i$ :

$$X = \begin{bmatrix} Z_1(\tilde{\mathbf{x}}'_1) & Z_2(\tilde{\mathbf{x}}'_1) & \cdots & Z_{m_p}(\tilde{\mathbf{x}}'_1) \\ \vdots & \vdots & & \vdots \\ Z_1(\tilde{\mathbf{x}}'_s) & Z_2(\tilde{\mathbf{x}}'_s) & \cdots & Z_{m_p}(\tilde{\mathbf{x}}'_s) \end{bmatrix}. \tag{6.5b}$$

We will refer to this model as the “surface fit model” or the “linear model”.

## Posterior Model II

One issue with the surface fit model is that it assumes the dewarped points are the actual observations, and thereby fails to account for any error propagation due to refraction correction. Prior to dewarping, the actual back surface measurements consist of the optical path lengths (OPLs) between associated pairs of anterior and posterior data points—that is, the vertical distance (in the OCT image) between the front and back surfaces at the same radial coordinate. The OPLs are then converted to geometric path lengths (GPLs) by accounting for the refractive indices (see Section 4.1.4).<sup>i</sup>

In order to incorporate the effects of optical distortion into our statistical analysis, we can consider an alternative model that includes the 3D refraction correction algorithm described in Section 4.2.2 and returns the GPL based on the Zernike model (6.4) of

---

<sup>i</sup>Recall that at any given sample point  $\mathbf{x}$  for which there is a back surface segmentation result, there may not be a corresponding segmentation result for the front surface. To get around this, we computed the distance between surfaces using the Zernike model  $f^a$  rather than the point cloud data for the front surface.

the back surface elevation (denoted here by  $\tilde{z}$ ). Letting  $\mathbf{x} = (\mathfrak{X}, f^a) = (x, y, f^a)$  and  $\tilde{\mathbf{x}} = (\tilde{x}, \tilde{y}, \tilde{z}) = (\tilde{\mathfrak{X}}, \tilde{z})$  respectively denote the Cartesian representations of the anterior point of incidence and the refraction-corrected posterior point of incidence, the GPL model can be written as

$$g(\mathfrak{X}, c) = \sqrt{\left(x - \tilde{x}\right)^2 + \left(y - \tilde{y}\right)^2 + \left(f^a - \tilde{z}(\tilde{\mathfrak{X}}, c)\right)^2}. \quad (6.6a)$$

The GPL observations  $L_i$  corresponding to the points  $\mathbf{x}_i$  and  $\tilde{\mathbf{x}}_i$  are assumed to fit the dewarping model

$$\tilde{\mathbf{x}} = \mathbf{x} + L\mathbf{u}_{ref}, \quad \tilde{z}(\tilde{\mathfrak{X}}, c) = \sum_{j=1}^{m_p} c_j Z_j(\tilde{\mathfrak{X}}'), \quad (6.6b)$$

where the unit direction vector  $\mathbf{u}_{ref}$  for the refracted light ray at the anterior point of incidence  $\mathbf{x}$  is given by (4.18); that is,

$$\mathbf{u}_{ref} = \frac{\sqrt{1 + \left(1 - \frac{n_s^2}{n_\ell^2}\right) \left((f_x^a)^2 + (f_y^a)^2\right)}}{1 + (f_x^a)^2 + (f_y^a)^2} \begin{pmatrix} f_x^a \\ f_y^a \\ -1 \end{pmatrix} - \frac{\frac{n_s}{n_\ell}}{1 + (f_x^a)^2 + (f_y^a)^2} \begin{pmatrix} f_x^a \\ f_y^a \\ (f_x^a)^2 + (f_y^a)^2 \end{pmatrix}. \quad (6.6c)$$

Recall that  $f_x^a \equiv \frac{\partial f^a(\mathfrak{X})}{\partial x}$  and  $f_y^a \equiv \frac{\partial f^a(\mathfrak{X})}{\partial y}$  are the  $x$ - and  $y$ -partial derivatives of the front surface at the point of incidence, and  $n_\ell$  and  $n_s$  are the refractive indices of the lens and the saline imaging medium (which we treat as known and fixed). Finally, we assume the coefficients of  $f^a \equiv f^a(\mathfrak{X})$  have been determined and fixed, so they are not included in the parameter vector  $c$  for the posterior surface model.

Unlike the surface fit model (6.5), the GPL model (6.6) is not linear with respect to the parameters. The forward problem associated with this model is addressed in Section 4.3.

### 6.1.3 Normalized Model

As illustrated in Section 6.3, our estimates of the Zernike coefficients for a single surface can vary in order of magnitude from  $10^{-5}$  mm to  $10^0$  mm. This can pose problems for certain statistical methods, such as those involving numerical estimation of derivatives or Monte Carlo sampling of the parameters. It can be helpful in these situations to use an alternate model formulation for which the parameters have been normalized to have the same order of magnitude.

Consider the discrete Zernike transform based on (6.1):

$$\begin{bmatrix} z_1 \\ \vdots \\ z_s \end{bmatrix} = \begin{bmatrix} Z_1(\mathfrak{X}'_1) & \cdots & Z_m(\mathfrak{X}'_1) \\ \vdots & & \vdots \\ Z_1(\mathfrak{X}'_s) & \cdots & Z_m(\mathfrak{X}'_s) \end{bmatrix} \begin{bmatrix} c_1 \\ \vdots \\ c_m \end{bmatrix}. \quad (6.7)$$

For the parameter-normalized model, we want to find a way to rewrite this system in terms of the normalized parameter vector<sup>ii</sup>  $\theta = [\theta_1, \dots, \theta_m]^T$ , where the values of each  $\theta_j$  are the same order of magnitude. One way to accomplish this is by constructing an invertible linear function  $h(\theta_j; c_j^*) = c_j$  that always maps the same value to each of the nominal values  $c_j^*$  computed using the linear least squares fit for each surface (see Section 6.3). If we let the mean parameter values  $\theta_j^* = \frac{1}{2}$ , then

$$h(\theta_j; c_j^*) = 2c_j^*\theta_j \quad (6.8)$$

is one possible map.<sup>iii</sup>

We can now represent the parameter vector in terms of the normalized parameter vector using the linear system

$$\begin{bmatrix} c_1 \\ \vdots \\ c_m \end{bmatrix} = 2 \begin{bmatrix} c_1^* & & 0 \\ & \ddots & \\ 0 & & c_m^* \end{bmatrix} \begin{bmatrix} \theta_1 \\ \vdots \\ \theta_m \end{bmatrix}.$$

Plugging this into (6.7), we obtain the parameter-normalized model

$$\begin{bmatrix} z_1 \\ \vdots \\ z_s \end{bmatrix} = 2 \begin{bmatrix} Z_1(\mathfrak{X}'_1) & \cdots & Z_m(\mathfrak{X}'_1) \\ \vdots & & \vdots \\ Z_1(\mathfrak{X}'_s) & \cdots & Z_m(\mathfrak{X}'_s) \end{bmatrix} \begin{bmatrix} c_1^* & & 0 \\ & \ddots & \\ 0 & & c_m^* \end{bmatrix} \begin{bmatrix} \theta_1 \\ \vdots \\ \theta_m \end{bmatrix}.$$

If we let  $c^* = [c_1^*, \dots, c_m^*]^T$  and  $c_D^* = \text{diag}(c^*)$  (that is, the  $m \times m$  diagonal matrix for

---

<sup>ii</sup>Note that the Zernike coefficients  $c_j$  are already technically “normalized Zernike coefficients” because they correspond to normalized Zernike polynomials. To avoid confusion, we will refer to the values  $\theta_j$  as “normalized parameters”, rather than coefficients.

<sup>iii</sup>We also tried the parameter mapping  $h(\theta_j; c_j^*) = \frac{2}{5}c_j^*(\theta_j + 2)$ , which maps the interval  $[0, 1]$  to  $[0.8c_j^*, 1.2c_j^*]$ ; however, this did not change the results presented in this chapter.

which  $c^*$  comprises the diagonal entries), we can write this more compactly as

$$z = (2Xc_D^*)\theta = X_n\theta, \quad (6.9a)$$

where the normalized design matrix is now

$$X_n = 2 \begin{bmatrix} Z_1(\mathbf{x}'_1) & \cdots & Z_m(\mathbf{x}'_1) \\ \vdots & & \vdots \\ Z_1(\mathbf{x}'_s) & \cdots & Z_m(\mathbf{x}'_s) \end{bmatrix} \begin{bmatrix} c_1^* & & 0 \\ & \ddots & \\ 0 & & c_m^* \end{bmatrix} = \begin{bmatrix} 2c_1^*Z_1(\mathbf{x}'_1) & \cdots & 2c_m^*Z_m(\mathbf{x}'_1) \\ \vdots & & \vdots \\ 2c_1^*Z_1(\mathbf{x}'_s) & \cdots & 2c_m^*Z_m(\mathbf{x}'_s) \end{bmatrix}. \quad (6.9b)$$

Once the normalized parameter vector  $\theta$  has been computed, the corresponding unscaled coefficient vector  $c$  can be recovered using (6.8).

Note that the parameter-normalized model is a still linear; we have simply used the nominal values of the Zernike coefficients to scale the associated columns of the design matrix so that the dimensionless parameters  $\theta_i$  will all have roughly the same order of magnitude. Because the values of the Zernike coefficients are very different for each lens surface, each locally-normalized model will have a different design matrix.

The normalized model (6.9) can be used for both the linear surface models (6.3) and (6.5). The same principles involved here can also be applied to the GPL model (6.6).

## 6.2 Statistical Models

Since this chapter is concerned with quantifying model uncertainty through a statistical framework, we consider the following statistical formulations of the models (6.2), (6.4), and (6.6) presented in Section 6.1:

$$\gamma = f^a(\mathbf{x}, c_0) + \varepsilon \quad (6.10)$$

$$\tilde{\gamma} = f^p(\tilde{\mathbf{x}}, c_0) + \varepsilon \quad (6.11)$$

$$\zeta = g(\mathbf{x}, c_0) + \varepsilon \quad (6.12)$$

where  $\gamma$ ,  $\tilde{\gamma}$ , and  $\zeta$  respectively denote random vectors for the anterior surface elevation measurements at the points  $\mathbf{x} = [\mathbf{x}_1, \dots, \mathbf{x}_s]^T$ , the refraction-corrected posterior surface elevation measurements at the refraction-corrected points  $\tilde{\mathbf{x}} = [\tilde{\mathbf{x}}_1, \dots, \tilde{\mathbf{x}}_s]^T$ , and the GPL measurements at the points  $\mathbf{x}$ . The combined measurement and modeling error

for each model—represented by the random vector  $\varepsilon$ —is assumed to be iid with mean 0 and constant but unknown variance  $\sigma_0^2$  (see Appendix B). The random vectors and realizations for each of the aforementioned quantities are summarized below.

Quantity of interest	Random variable	Realization
Front surface elevation	$\gamma = [\gamma_1, \dots, \gamma_s]^T$	$w = [w_1, \dots, w_s]^T$
Back surface elevation (dewarped)	$\tilde{\gamma} = [\tilde{\gamma}_1, \dots, \tilde{\gamma}_s]^T$	$\tilde{w} = [\tilde{w}_1, \dots, \tilde{w}_s]^T$
Geometric path length (GPL)	$\zeta = [\zeta_1, \dots, \zeta_s]^T$	$L = [L_1, \dots, L_s]^T$
Measurement/modeling error	$\varepsilon = [\varepsilon_1, \dots, \varepsilon_s]^T$	$\epsilon = [\epsilon_1, \dots, \epsilon_s]^T$

As with their mathematical counterparts, the statistical models (6.10)–(6.12) can easily be formulated in terms of the normalized parameters  $\theta = [\theta_1, \dots, \theta_m]^T$  (see Section 6.1.3).

In this chapter, we are only interested in quantifying the uncertainty related to the Zernike coefficients. The remaining model inputs (the refractive indices of the lens and saline) will be treated as known and fixed. Because the Zernike polynomials represent types of spherical aberrations, the corresponding values of their coefficients have a real physical significance—particularly within the field of ophthalmology. The shape characteristics of the Zernike polynomials are discussed in greater depth in Chapter 3, and Appendix A contains a list of the first 66 polynomial functions (according to Noll’s indexing scheme) along with their visual representations. Interpretation of actual Zernike coefficient values is discussed in Chapter 7.

The vector  $c_0$  in (6.10)–(6.12) represents the “true” but unknown values of the Zernike coefficients for each model, which we are attempting to determine from our data. We do this using the ordinary least squares (OLS) estimator

$$c = \arg \min_{c \in \mathbb{R}^m} \sum_{i=1}^s \left( \gamma_i - f(\mathfrak{X}_i, c) \right)^2. \quad (6.13)$$

Note that the unbiased estimator for the error variance,

$$\sigma^2 = \frac{1}{s - m} [\gamma - f(\mathfrak{X}, c)]^T [\gamma - f(\mathfrak{X}, c)] = \frac{1}{s - m} R^T R, \quad (6.14)$$

is simply the cost functional  $J = \sum_{i=1}^s (\gamma_i - f(\mathfrak{X}_i, c))^2$  of (6.13) divided by the number of degrees of freedom, which is itself a scalar constant. Therefore, the least squares estimate

for the coefficient vector  $c_0$  can also be thought of as the set of coefficients  $\hat{c}$  that minimize the estimated error variance  $\hat{\sigma}^2$ . (The random vector  $R$  in (6.14) denotes the estimator for the model residual.)

As discussed in Section 3.5.2, the OLS problem for the linear surface models (6.3) and (6.5) can be solved using the Moore-Penrose pseudoinverse of the design matrix, denoted by  $X^+$ :

$$c = \arg \min_{c \in \mathbb{R}^m} \|\gamma - Xc\|^2 = (X^T X)^{-1} X^T \gamma = X^+ \gamma.$$

The magnitude of the OLS estimates  $\hat{c}_i$  based on the linear models for the front and back surfaces are shown in Figures 6.2, 6.4, 6.6, and 6.8, alongside the values obtained by solving for the coefficients directly using numerical integration (see Section 3.5.2). We will use these linear models for the parameter identification and model order reduction in Section 6.3.1, as well as for the anterior surface parameter densities in Section 6.3.2. However, in order to account for as much error as possible in the dewarping step, the posterior surface parameter densities in Section 6.3.2 are obtained using the nonlinear GPL model (6.6). The associated optimization problem

$$c = \arg \min_{c \in \mathbb{R}^m} \|\zeta - g(\mathfrak{X}, c)\|^2$$

is solved using the MATLAB function `lsqnonlin.m` with the solution to the linear problem (6.11) as an initial guess.<sup>iv</sup> Note that the theory behind some of the methods described in Sections 6.4 and 6.5 can be applied directly to the linearly parameterized anterior lens model, for which it is possible to compute the parameter means and variances explicitly. Due to the nonlinearity of the GPL model, however, sampling methods are required to study the uncertainty propagation and sensitivity associated with the posterior lens parameters. For consistency, we will apply the same methods to both models.

## 6.3 Model Calibration

### 6.3.1 Reduced Order Model

One of the first things that is apparent from the magnitude of the coefficient estimates shown in Figures 6.2, 6.4, 6.6, and 6.8 is that most of them seem to hover around

---

<sup>iv</sup>We solved the nonlinear problem for the normalized parameters  $\theta$  and then rescaled them.

Table 6.2: The  $\ell^2$  condition number of the Fisher information matrix  $X_n^T X_n$ .

Aspheric lens front	Toric lens front	Aspheric lens back	Toric lens back
$1.4952 \times 10^{13}$	$1.6308 \times 10^{15}$	$8.1287 \times 10^{10}$	$3.6867 \times 10^{13}$

$10^{-5}$  mm, while a select few are orders of magnitude greater. We hypothesize that the Zernike basis functions associated with the smallest coefficients provide negligible contributions to the overall shape of each lens surface. If this proves correct, we can construct *reduced order models* (ROMs) consisting of only the “significant” basis functions. One advantage to using ROMs is that they are much more computationally efficient, particularly for the Monte Carlo methods used to assess uncertainty.

Furthermore, for some coefficients—such as those that are very small relative to the other parameters—it may be difficult to uniquely estimate their magnitude if perturbations in these parameters have minimal effect on the model response. A parameter vector  $c$  is *identifiable* with respect to a subspace  $I(c)$  of the parameter space if the model response is one-to-one—that is, if  $f(c^1) = f(c^2)$  implies  $c^1 = c^2$  for all  $c^1, c^2 \in I(c)$  [89, Ch. 6]. For a linearly-parameterized problem like  $z = Xc$  (where  $z \in \mathbb{R}^s$  and  $c \in \mathbb{R}^m$ ), the identifiable subspace  $I(c)$  is defined by range of the transpose of the  $s \times m$  design matrix  $X$ , which is equivalent to the range of the  $m \times m$  Fisher information matrix  $X^T X$ :

$$I(c) = R(X^T) = R(X^T X).$$

The unidentifiable subspace  $NI(c)$  is simply the orthogonal complement of  $I(c)$ ; *i.e.*,  $NI(c) = N(X) = N(X^T X)$ .

Clearly, if the design matrix  $X$  (and hence  $X^T X$ ) is nonsingular, this means it is full rank and all the parameters are identifiable [86, Ch. 3]. However, although the sample grid  $S$  (described in Section 2.2.3) was deliberately selected in part to ensure that the design matrix  $X$  would be well-conditioned—and therefore nonsingular—this is no longer the case once the parameters have been normalized. In fact, the design matrix  $X_n$  for the normalized problem  $z = X_n \theta$  is very ill-conditioned, indicating that some of the normalized parameters are indeed unidentifiable. As illustrated by the  $\ell^2$  condition numbers in Table 6.2, this is the case for all four lens surfaces.

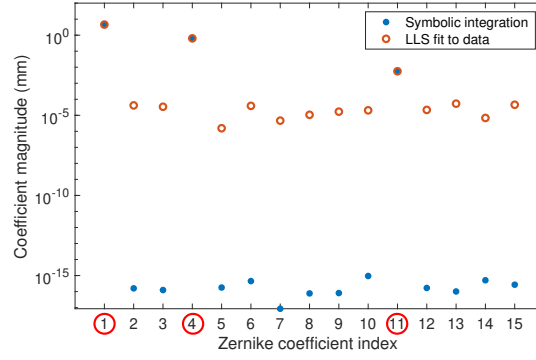


Figure 6.2: Zernike coefficients of the front surface of the aspheric lens, using numerical integration and linear least squares.

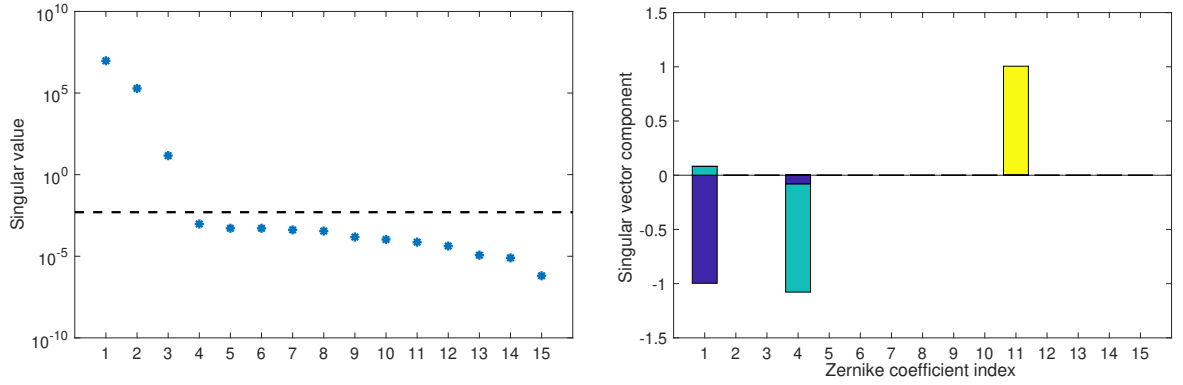


Figure 6.3: Singular values of  $X_n^T X_n$  (left) and components of the right singular vectors corresponding to the singular values above the dashed line (right) for the anterior surface of the aspheric lens.

For a general matrix  $A$ , the right singular vectors corresponding to the nonzero singular values of  $A$  comprise a basis for the range of  $A^T$ . Therefore, to construct a basis for the identifiable subspace  $I(\theta) = R(X_n^T X_n)^v$  we can use the MATLAB function `svd.m` to find the singular value decomposition

$$X_n^T X_n = U \Sigma V^T,$$

---

<sup>v</sup>The design matrix  $X$  (and therefore also  $X_n$ ) may be quite large if we have many observations, making direct computations on  $X$  very inefficient. We do not have this problem if we use the Fisher information matrix  $X^T X$ .

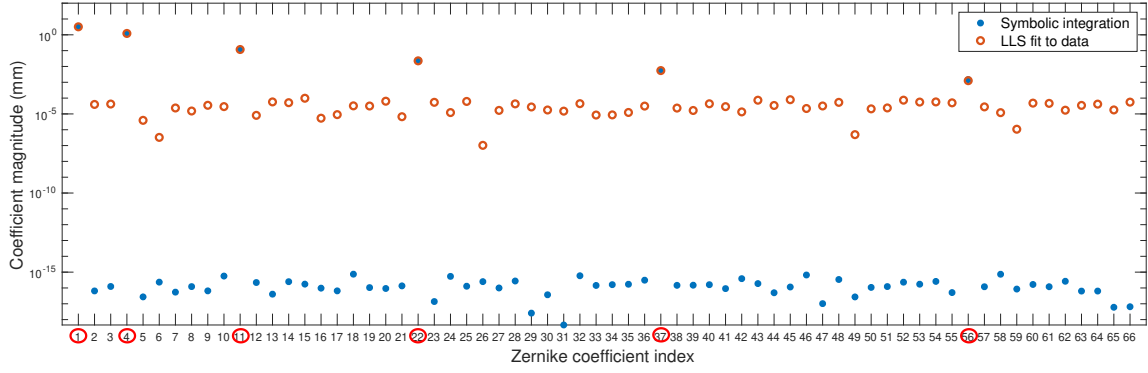


Figure 6.4: Zernike coefficients of the front surface of the toric lens.

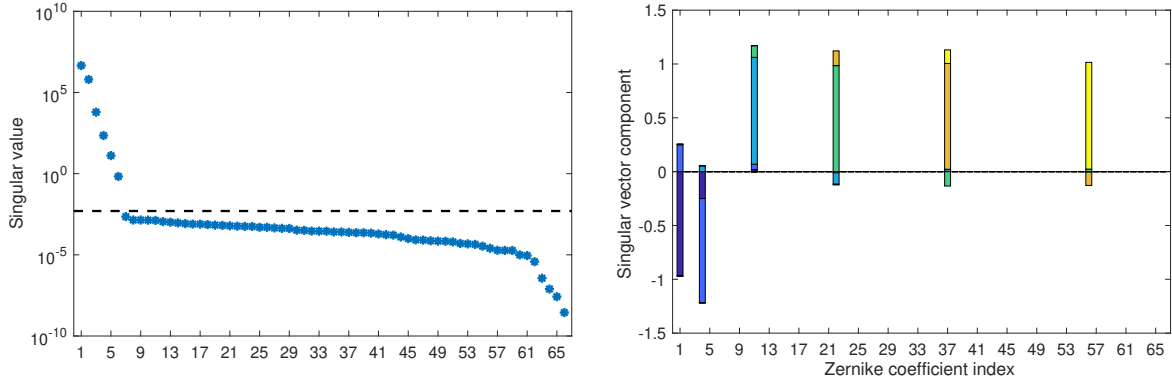


Figure 6.5: Singular values (left) and right singular vectors (right) for the anterior surface of the toric lens.

where  $U \in \mathbb{R}^{m \times m}$  and  $V \in \mathbb{R}^{m \times m}$  are orthogonal matrices whose columns represent the left- and right-singular vectors of  $X_n^T X_n$  (respectively), and

$$\Sigma = \begin{bmatrix} \sigma_{max} & & 0 \\ & \ddots & \\ 0 & & \sigma_{min} \end{bmatrix}$$

is the  $m \times m$  diagonal matrix of singular values arranged from largest to smallest.<sup>vi</sup>

<sup>vi</sup>We know that  $X_n^T X_n$  has no truly zero singular values because the normalized design matrix is constructed by scaling each of the linearly-independent columns of  $X$  by a nonzero scalar quantity, as shown in (6.9b).

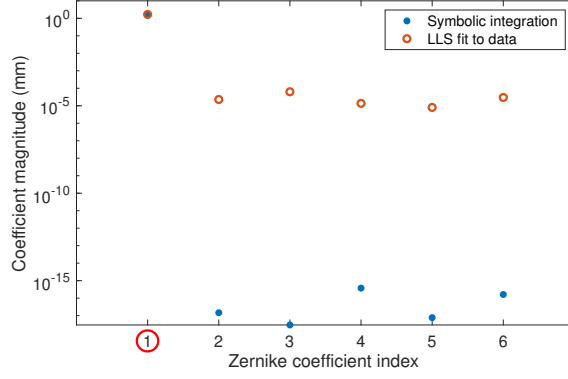


Figure 6.6: Zernike coefficients of the back surface of the aspheric lens.

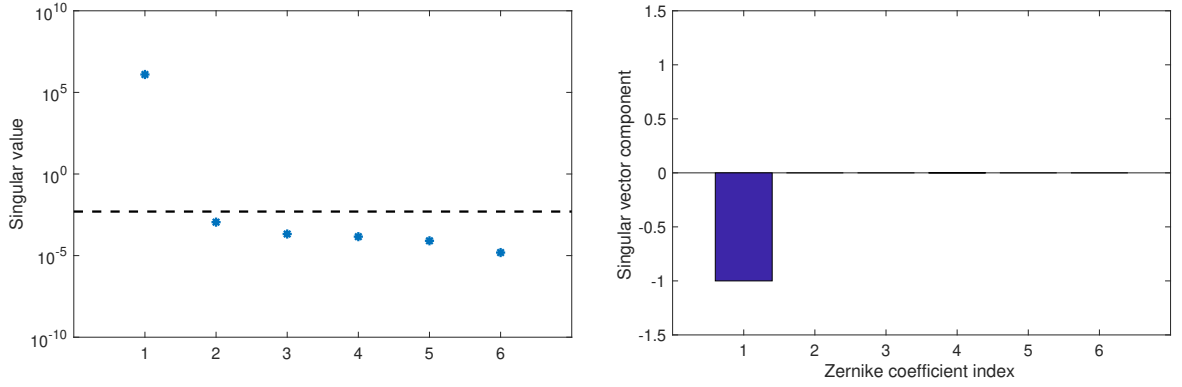


Figure 6.7: Singular values (left) and right singular vectors (right) for the posterior surface of the aspheric lens.

Note that the  $\ell^2$  condition number of a matrix is the ratio of its largest to smallest singular values—*i.e.*,  $\kappa(X_n^T X_n) = \frac{\sigma_{max}}{\sigma_{min}}$ . Therefore, a large condition number (such as those in Table 6.2) indicates that the smallest singular value  $\sigma_{min}$  is many orders of magnitude smaller than  $\sigma_{max}$ . By delineating between the singular values that exceed some reasonable tolerance  $\tau$  and those that are small enough to ignore, we can use the corresponding columns of  $V$  to form the bases for  $R(X_n^T X_n)$  and  $N(X_n^T X_n)$  [33, 89].

Once we have determined which parameters are unidentifiable for each surface, we can set those coefficients equal to zero to obtain the reduced order model (ROM). We can then compute the OLS estimates for the remaining coefficients using the ROM. Since each

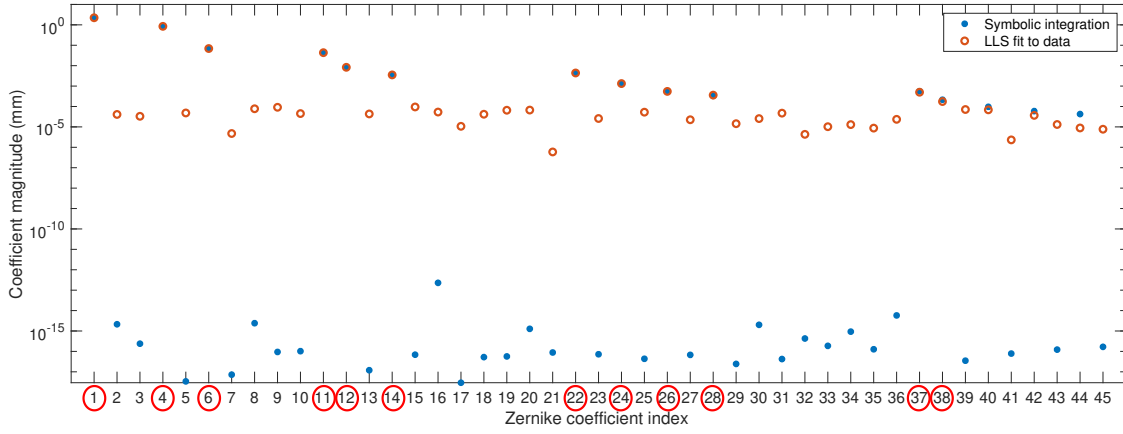


Figure 6.8: Zernike coefficients of the posterior surface of the toric lens.

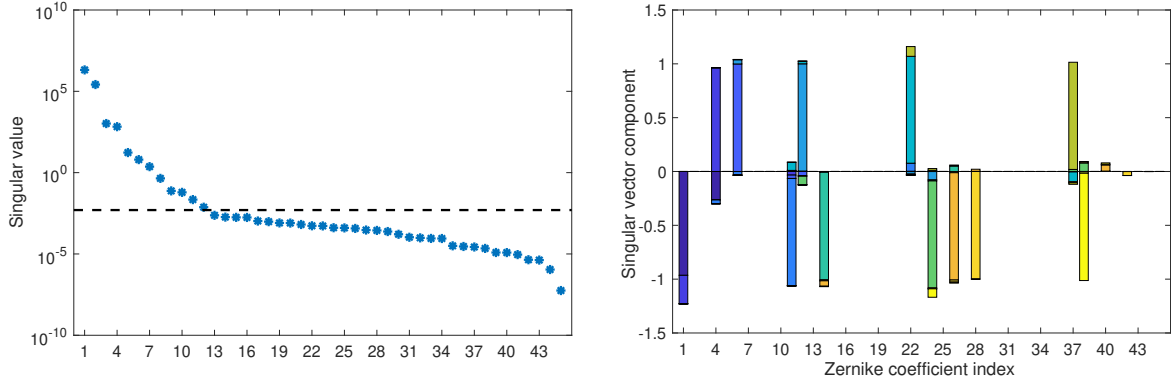


Figure 6.9: Singular values (left) and right singular vectors (right) for the posterior surface of the toric lens.

normalized parameter  $\theta_i$  is linearly mapped to a Zernike coefficient  $c_i$ , the unidentifiable parameters of the normalized model correspond to unidentifiable parameters in the non-normalized model.

The singular values of  $X_n^T X_n$  for each lens surface are shown in Figures 6.3, 6.5, 6.7, and 6.9, along with the components of the right singular vectors corresponding to  $\sigma_i > \tau$ . As hypothesized, the components of the right singular vectors do indeed correspond to the “significant” coefficients (circled in red) in Figures 6.2, 6.4, 6.6, and 6.8.

The tolerance  $\tau = 5 \times 10^{-3}$  (illustrated by the dashed line) was selected empirically by visual inspection of singular values. For both anterior surfaces as well as the posterior

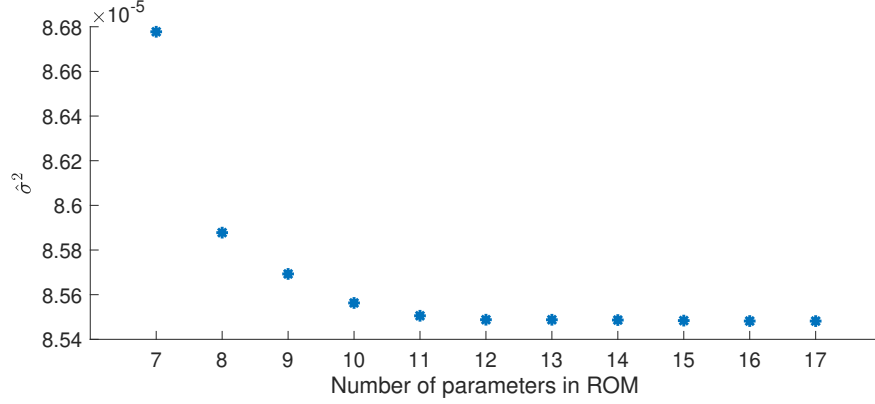


Figure 6.10: Error variance ( $\hat{\sigma}^2$ ) according to the number of Zernike polynomials included in the reduced order model (ROM) for the posterior toric lens.

surface of the aspheric lens, this tolerance coincides with a large gap in the singular values. Furthermore, most of the smallest singular values are clustered relatively close together below  $\tau$ , while the singular values that exceed the tolerance show a steep rate of change in magnitude.

No gap exists between the singular values on either side of  $\tau$  for the back of the toric lens (Figure 6.9). There is still a clear change in the slope that occurs between  $\sigma_{12}$  and  $\sigma_{13}$ , so it is tempting to infer that this means we only need the first 12 singular values. However, since the delineation between  $\sigma_{12}$  and  $\sigma_{13}$  is not definitive, we consider an alternative motivation for setting the tolerance at the proposed value.

Recall from (6.14) that the cost function for the OLS estimator is directly proportional to the error variance estimator

$$\sigma^2 = \frac{1}{s - m} R^T R,$$

where  $R$  is the estimator for the residual vector. To see if  $\tau = 5 \times 10^{-3}$  is indeed an appropriate value for the tolerance, we consider what happens to the error variance when the reduced order model is constructed using only the first 7 singular values, then the first 8 singular values, up through the first 17 singular values—that is, the 5 singular values on either side of  $\sigma_{12}$ . In each case, the specific parameters included in the model are determined by the space spanned by the right singular vectors. If we denote the set of Zernike coefficients in the 7-parameter model by  $C^7 = \{c_1, c_4, c_6, c_{11}, c_{12}, c_{14}, c_{22}\}$ , then

the coefficients in the higher-order models are the sets

$$\begin{aligned} C^8 &= C^7 \cup \{c_{24}\}, & C^9 &= C^8 \cup \{c_{37}\}, & C^{10} &= C^9 \cup \{c_{26}\}, & C^{11} &= C^{10} \cup \{c_{28}\}, \\ C^{12} &= C^{11} \cup \{c_{38}\}, & C^{13} &= C^{12} \cup \{c_8\}, & C^{14} &= C^{13} \cup \{c_9\}, & C^{15} &= C^{14} \cup \{c_{39}\}, \\ C^{16} &= C^{15} \cup \{c_{15}\}, & C^{17} &= C^{16} \cup \{c_{19}\}. \end{aligned}$$

Figure 6.10 shows the error variance estimates  $\hat{\sigma}^2$  for each of these 11 reduced order models. It is clear from this illustration that each new parameter included in the ROM helps improve the fit to the data—up to the 12<sup>th</sup> parameter. After that, the error variance remains the same no matter how many more parameters are included. This affirms our choice of  $\tau = 5 \times 10^{-3}$ , which also results in a 12-term ROM for the back of the toric lens. Another way of saying this is that  $X_n^T X_n$  for the back surface of the toric lens has rank 12. For the front of the aspheric and toric lenses, the rank is 3 and 6, respectively, while the back of the aspheric lens (a flat plane) is rank 1. The Zernike basis functions corresponding to the identifiable coefficients are summarized in Table 6.4 and Figure 6.11. (For comparison, recall that the true shape of both lenses is illustrated in Figure 6.1.)

The error variance estimates  $\hat{\sigma}^2$  for both the full and reduced order models for all for surfaces are shown in Table 6.3. In each case, the error variance  $\hat{\sigma}^2$  for the reduced order model (when the unidentifiable parameters are fixed at 0 before computing the OLS estimates) differs by well under 0.01% from the error variance estimate when all coefficients are included in the fit. In fact, for both front surface models the variance estimate is slightly *lower* when using the ROM.

The difference in axial elevation using the full model and the ROM for each surface is depicted in Figure 6.12.

Table 6.3: OLS error variance estimates ( $\hat{\sigma}^2$ ) in square millimeters for all lens surfaces, using the full model (all Zernike coefficients) versus the reduced order model.

	All coefficients	Reduced order
Aspheric lens front	$9.9631 \times 10^{-5}$	$9.9628 \times 10^{-5}$
Toric lens front	$9.9688 \times 10^{-5}$	$9.9683 \times 10^{-5}$
Aspheric lens back	$7.0113 \times 10^{-5}$	$7.0113 \times 10^{-5}$
Toric lens back	$8.5486 \times 10^{-5}$	$8.5488 \times 10^{-5}$

Table 6.4: Zernike polynomials included in reduced order models for each lens surface.

	Formula	Asphere Front	Asphere Back	Toric Front	Toric Back
$Z_1$	1	✓	✓	✓	✓
$Z_4$	$\sqrt{3}(2\rho^2 - 1)$	✓		✓	✓
$Z_6$	$\sqrt{6}\rho^2 \cos 2\theta$				✓
$Z_{11}$	$\sqrt{5}(6\rho^4 - 6\rho^2 + 1)$	✓		✓	✓
$Z_{12}$	$\sqrt{10}(4\rho^4 - 3\rho^2) \cos 2\theta$				✓
$Z_{14}$	$\sqrt{10}\rho^4 \cos 4\theta$				✓
$Z_{22}$	$\sqrt{7}(20\rho^6 - 30\rho^4 + 12\rho^2 - 1)$			✓	✓
$Z_{24}$	$\sqrt{14}(15\rho^6 - 20\rho^4 + 6\rho^2) \cos 2\theta$				✓
$Z_{26}$	$\sqrt{14}(6\rho^6 - 5\rho^4) \cos 4\theta$				✓
$Z_{28}$	$\sqrt{14}\rho^6 \cos 6\theta$				✓
$Z_{37}$	$3(70\rho^8 - 140\rho^6 + 90\rho^4 - 20\rho^2 + 1)$			✓	✓
$Z_{38}$	$\sqrt{18}(56\rho^8 - 105\rho^6 + 60\rho^4 - 10\rho^2) \cos 2\theta$				✓
$Z_{56}$	$\sqrt{11}(252\rho^{10} - 630\rho^8 + 560\rho^6 - 210\rho^4 + 30\rho^2 - 1)$			✓	

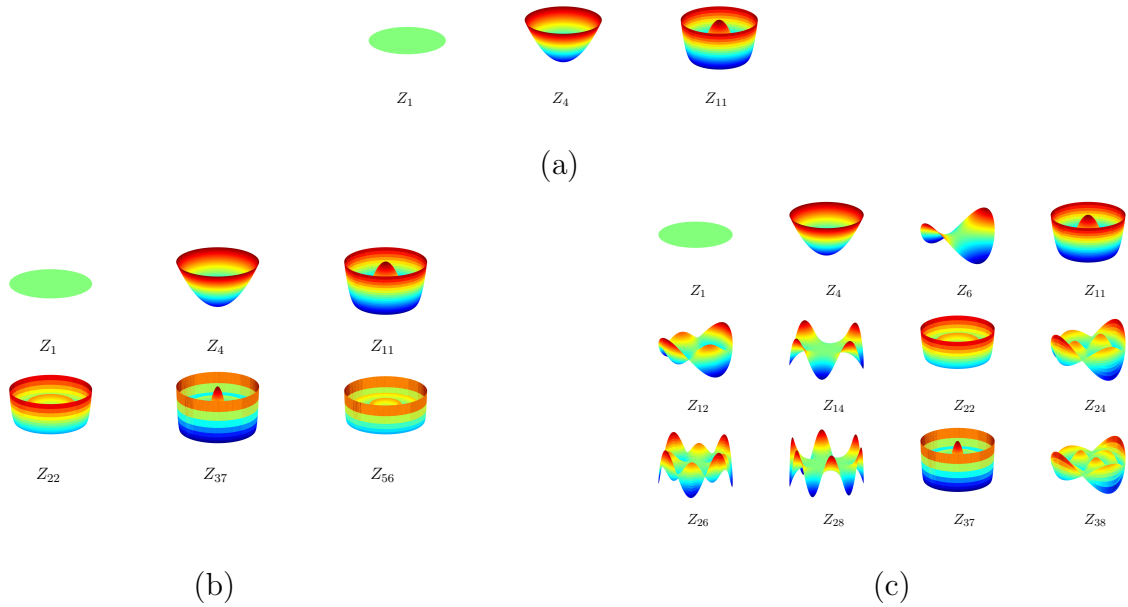


Figure 6.11: Significant Zernike polynomials for (a) the aspheric lens, (b) the front of the toric lens, and (c) the back of the toric lens.

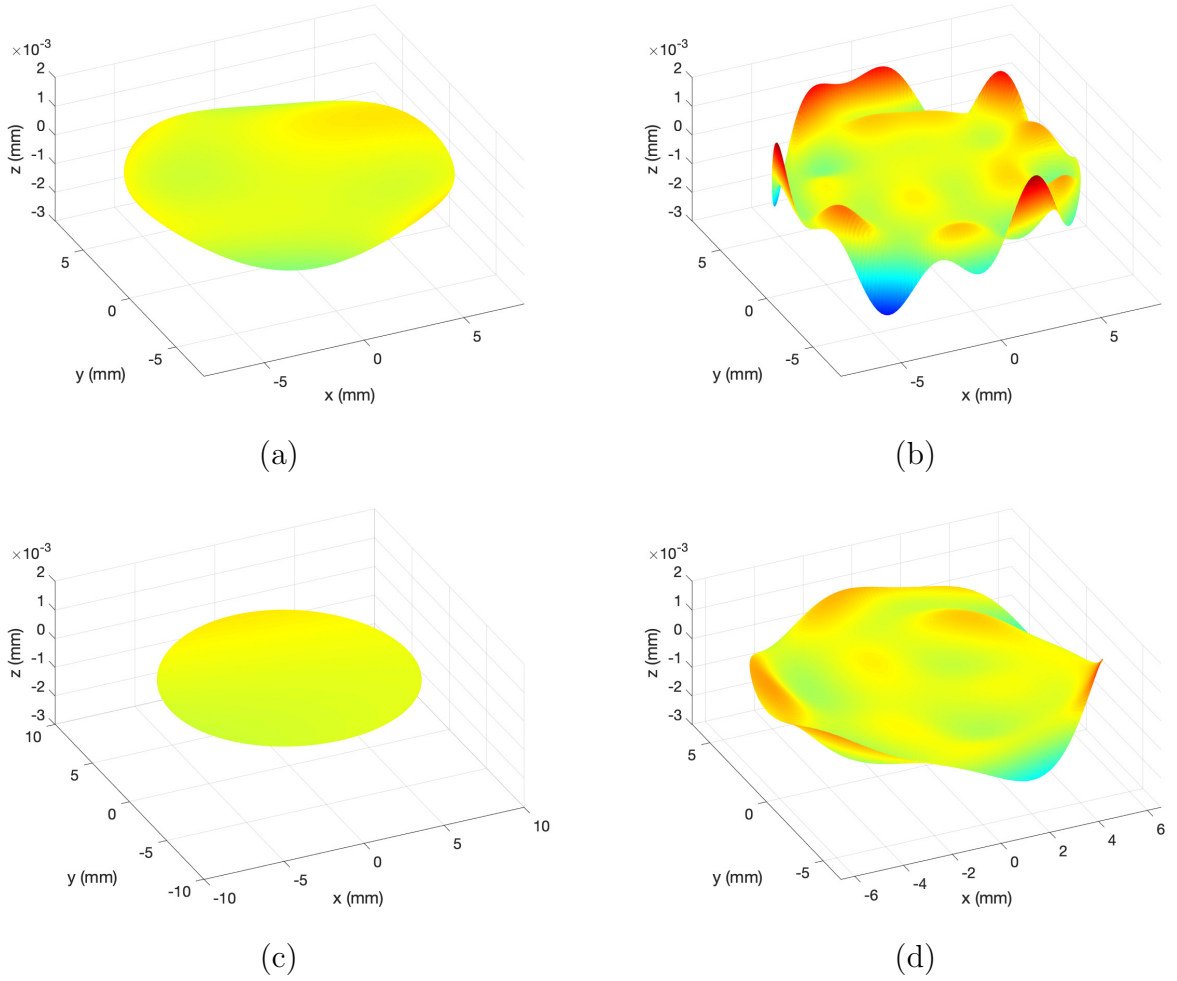


Figure 6.12: Difference between the full Zernike fit and the reduced order model for (a) the anterior aspheric lens, (b) the anterior toric lens, (c) the posterior aspheric lens, and (d) the posterior toric lens.

### 6.3.2 Model Calibration

Now that we have determined the identifiable coefficients and constructed reduced order models for each surface, our next goal is to obtain estimates for the parameters and quantify the associated uncertainty. In order to account for some of the error in the refraction correction step, we will use the nonlinear GPL model (6.6) for the posterior surface rather than the linear model. This is the model we will be using for the remainder of the chapter.

We will approach parameter estimation for the identifiable Zernike coefficients first from a frequentist perspective, in which we attempt to estimate the true but unknown parameter vector  $c_0$ , along with sampling distributions for the parameter estimate  $\hat{c}$ . We will then repeat the analysis from a Bayesian perspective, in which the parameters themselves are treated as random variables whose probability distributions are conditioned upon the observed data. The methods employed for both analyses are discussed in much greater detail in [89, Ch. 7–8].

## Frequentist Parameter Estimation

In Section 6.2, we explained how to find the OLS estimator  $c$  for the true model parameters  $c_0$ , using either the Moore-Penrose pseudoinverse (for the linear front surface model) or the MATLAB function `lsqnonlin.m` (for the nonlinear GPL model). These estimators required the assumption that the errors  $\varepsilon_i$  be iid with zero mean and constant variance  $\sigma_0$ , which is corroborated in Appendix B. The residuals shown in Appendix B further suggest that the errors are normally distributed.<sup>vii</sup> Therefore, we may assume that the sampling distributions for the parameter estimators are also normal [9, 86, 89]—specifically,  $c \sim \mathcal{N}\left(c_0, \sigma_0^2(\chi(c)^T \chi(c))^{-1}\right)$ .

The estimator for the parameter covariance  $\sigma_0^2(\chi(c)^T \chi(c))^{-1}$  is

$$V(c) = \sigma^2(\chi(c)^T \chi(c))^{-1}, \quad (6.15)$$

where  $\sigma^2$  is the error variance estimator from (6.14) and the sensitivity matrix  $\chi(c)$  is defined as

$$\chi(c) = \begin{bmatrix} \frac{\partial g_1(c)}{\partial c_1} & \dots & \frac{\partial g_1(c)}{\partial c_m} \\ \vdots & & \vdots \\ \frac{\partial g_s(c)}{\partial c_1} & \dots & \frac{\partial g_s(c)}{\partial c_m} \end{bmatrix}. \quad (6.16)$$

Note that for the linear model, the sensitivity matrix is equal to the design matrix  $X$ , so the covariance estimator is simply

$$V(c) = \sigma^2(X^T X)^{-1}. \quad (6.17)$$

---

<sup>vii</sup>We also know this to be true because the synthetic data were explicitly constructed using the addition of normally distributed noise.

To construct the sensitivity matrix (6.16) for the GPL model, recall that the GPL at a particular point is given by the function

$$g_i(c) = g(\mathfrak{X}_i, c) = \sqrt{\left(x_i - \tilde{x}_i\right)^2 + \left(y_i - \tilde{y}_i\right)^2 + \left(f_i^a - \tilde{z}_i(c)\right)^2}.$$

The dewarped axial coordinate  $\tilde{z}_i$  is also a linear function of the parameters

$$\tilde{z}_i(c) = \tilde{z}(\tilde{\mathfrak{X}}_i, c) = [X]_{i*} c,$$

where  $[X]_{i*}$  denotes the  $i^{\text{th}}$  row of the design matrix  $X$  defined in (6.5b). Taking the partial derivative with respect to the parameter  $c_j$  yields

$$[\chi(c)]_{ij} = \frac{\partial g_i(c)}{\partial c_j} = \frac{\tilde{z}_i - f_i^a}{g_i} [X]_{ij}.$$

The values of  $\tilde{z}_i$ ,  $g_i$ , and the front surface point  $f_i^a$  are the same regardless of whether we use the Zernike coefficients or the normalized parameters  $\theta$ . Given the definition (6.9a) of the normalized the design matrix  $X_n$ , the relationship between the  $ij^{\text{th}}$  entry of the normalized sensitivity matrix  $\chi_n(\theta)$  and that of the full sensitivity matrix can be expressed as

$$[\chi_n(\theta)]_{ij} = \frac{\partial g_i(\theta)}{\partial \theta_j} = \frac{\tilde{z}_i - f_i^a}{g_i} [X_n]_{ij} = \frac{\tilde{z}_i - f_i^a}{g_i} \cdot 2c_j^* [X]_{ij} = 2c_j^* [\chi(c)]_{ij}.$$

The transformation between the two sensitivity matrices is therefore given by

$$\chi_n(\theta) = 2\chi(c)c_D^* \quad \implies \quad \chi(c) = \frac{1}{2}\chi_n(\theta)c_D^{*-1}$$

where

$$c_D^* = \begin{bmatrix} c_1^* & & 0 \\ & \ddots & \\ 0 & & c_m^* \end{bmatrix}.$$

Note that this mirrors the relationship between the normalized and non-normalized design matrices for the linear model:

$$X_n = 2Xc_D^* \quad \implies \quad X = \frac{1}{2}X_nc_D^{*-1}.$$

If we let  $V_n(\theta) = \sigma^2(X_n^T X_n)^{-1}$  be the covariance of the normalized model, the covariance  $V(c)$  can be recovered from the normalized covariance according to the relationship

$$V(c) = \sigma^2(X^T X)^{-1} = \sigma^2 \left( \left( \frac{1}{2} X_n c_D^* \right)^T \left( \frac{1}{2} X_n c_D^* \right) \right)^{-1} = \sigma^2 \left( \frac{1}{4} c_D^{*-1} X_n^T X_n c_D^{*-1} \right)^{-1} \quad (6.18)$$

$$= 4c_D^* \left( \sigma^2(X_n^T X_n)^{-1} \right) c_D^* = 4c_D^* V_n(\theta) c_D^*. \quad (6.19)$$

The standard error  $SE_{c_k}$  associated with estimate of the  $k^{\text{th}}$  parameter  $\hat{c}_k$ —that is, the square root of the estimate’s covariance with itself—maps to the standard error of the normalized parameter  $SE_{\theta_k}$  according to

$$SE_{c_k} = \sqrt{[\hat{V}(c)]_{kk}} = \sqrt{4c_k^* [\hat{V}_n(\theta)]_{kk} c_k^*} = 2c_k^* \sqrt{[\hat{V}_n(\theta)]_{kk}} = 2c_k^* SE_{\theta_k}, \quad (6.20)$$

which is consistent with (6.8). It can easily be shown that the relationships (6.19) and (6.20) apply to the covariance and standard error of the nonlinear GPL model as well.

Tables 6.5–6.8 show the OLS estimates  $\hat{c}$  for the identifiable Zernike coefficients of each lens surface along with their 95% confidence intervals, constructed using a  $t$ -distribution with  $s - m$  degrees of freedom. We performed this analysis on both the reduced order models and the full version where all the Zernike polynomials were included in the fit. For comparison, Tables 6.5–6.8 also show the “true” coefficient values (which we’ll label  $c_j^{(i)}$ ), obtained by numerically integrating the design equations (as discussed in Section 6.3.1). The key observations from Tables 6.5–6.8 are summarized below.

For every coefficient in both aspheric lens surfaces,  $c_j^{(i)}$  lies well within the 95% confidence interval. The coefficient estimates  $\hat{c}_j$  for both the full model and the ROM are all well within 1% of  $c_j^{(i)}$ . Furthermore, both sets of coefficient estimates agree up to six significant figures for the front surface and are within 0.001% for the back surface, providing further evidence that the reduced order models are sufficient.

Both sets of estimates for the front of the toric lens also agree up to six significant figures, and the confidence intervals for all but two of the coefficients— $c_4$  and  $c_{56}$ —contain their respective “true” coefficient values. In the case of  $c_4$ , the “true” value falls just outside of the confidence interval, which is the same for both the full model and the ROM, but both estimates  $\hat{c}_4$  differ from  $c_4^{(i)}$  by  $< 0.01\%$ . The estimates for  $c_{56}$  are once again the same for both the full and reduced order models; however,  $c_{56}^{(i)}$  lies well outside

the 95% confidence interval for both models (which are nearly identical), and differs from both estimates  $\hat{c}_{56}$  by almost 15%. The remaining coefficient estimates for the front of the toric lens are well within 1% of  $c_j^{(i)}$  for both the full model and the ROM.

For the back of the toric lens, there are three parameters whose 95% confidence intervals do not contain  $c_j^{(i)}$ :  $c_6$ ,  $c_{14}$ , and  $c_{37}$ . The confidence interval for  $\hat{c}_6$  is slightly narrower for the ROM than the full model, despite the estimate also being slightly worse; however, both estimates are still only  $\sim 0.1\%$  away from  $c_6^{(i)}$ . The relative error in the ROM estimate for  $c_{14}$  is significantly worse at just under 3.5%, but the relative error in the estimate using the full model is nearly 4% (the two estimates differ from one another by roughly 0.5%). Both estimates for  $c_{37}$  are nearly 10.5% off from the “true” value, with the ROM estimate being slightly better than the estimate from the full model.

For the first three surfaces (the two front surfaces and the back surface of the aspheric lens), the relative error in the coefficient estimates increases as the coefficient index increases, regardless of whether we use the full model or the ROM. This is not strictly true for the back of the toric lens. In addition to the three coefficients for which the “true” value lies outside the 95% confidence interval, there are also several parameter estimates  $\hat{c}_j$  whose relative errors exceed 1% despite the fact that their confidence intervals do contain  $c_j^{(i)}$ . Both the ROM and full model estimates for  $c_{24}$  are off by a bit under 4%, while the estimates for  $c_{38}$  (which are within 0.6% of one another) both differ from the “true” value by nearly 20%. For  $c_{26}$  and  $c_{28}$ , the ROM estimates are significantly worse than the full model estimates, and differ from one another by roughly 6% and 3.5%, respectively. The relative error in  $c_{26}$  is 1% for the full model estimate, but increases to 5% for the ROM. Similarly, the relative error goes from 8% to 12% for the two estimates of  $c_{28}$ . The estimates for each of the remaining coefficients agree to within 0.1%.

## Bayesian Parameter Estimation

In the frequentist approach to parameter estimation, the parameter estimator  $c$  is a random variable that approximates the fixed but unknown true value of the parameter  $c_0$ . The estimator has an associated sampling distribution, which specifies the probability that a particular value is equal to  $c_0$ . The Bayesian approach to parameter estimation treats the parameters themselves as the random vector  $C$ —rather than fixed values—with realizations  $c$  and some prior probability density  $\pi_0(c)$ .

Table 6.5: Zernike coefficient estimates (in mm) and 95% confidence intervals using ordinary least squares (OLS) for full anterior aspheric lens model with all coefficients and reduced order lens model.

	Integration	OLS (All coefficients)		OLS (Reduced model)	
		OLS	95% confidence interval	OLS	95% confidence interval
$\hat{c}_1$	4.58226	4.58230	(4.58224, 4.58235)	4.58230	(4.58224, 4.58235)
$\hat{c}_4$	$-6.33748 \times 10^{-1}$	$-6.33710 \times 10^{-1}$	$(-6.33764 \times 10^{-1}, -6.33655 \times 10^{-1})$	$-6.33710 \times 10^{-1}$	$(-6.33764 \times 10^{-1}, -6.33655 \times 10^{-1})$
$\hat{c}_{11}$	$-5.60707 \times 10^{-3}$	$-5.59018 \times 10^{-3}$	$(-5.63818 \times 10^{-3}, -5.54217 \times 10^{-3})$	$-5.59018 \times 10^{-3}$	$(-5.63818 \times 10^{-3}, -5.54218 \times 10^{-3})$

Table 6.6: Coefficient estimates and 95% confidence intervals for full and reduced posterior aspheric lens models.

	Integration	OLS (All coefficients)		OLS (Reduced model)	
		OLS	95% confidence interval	OLS	95% confidence interval
$\hat{c}_1$	3.20400	3.20403	(3.20397, 3.20409)	3.20403	(3.20397, 3.20409)
$\hat{c}_4$	-1.22051	-1.22044	(-1.22050, -1.22039)	-1.22044	(-1.22050, -1.22039)
$\hat{c}_{11}$	$-1.17874 \times 10^{-1}$	$-1.17856 \times 10^{-1}$	$(-1.17913 \times 10^{-1}, -1.17799 \times 10^{-1})$	$-1.17856 \times 10^{-1}$	$(-1.17913 \times 10^{-1}, -1.17799 \times 10^{-1})$
$\hat{c}_{22}$	$-2.27060 \times 10^{-2}$	$-2.26500 \times 10^{-2}$	$(-2.27069 \times 10^{-2}, -2.25932 \times 10^{-2})$	$-2.26500 \times 10^{-2}$	$(-2.27069 \times 10^{-2}, -2.25932 \times 10^{-2})$
$\hat{c}_{37}$	$-5.47311 \times 10^{-3}$	$-5.49497 \times 10^{-3}$	$(-5.55149 \times 10^{-3}, -5.43845 \times 10^{-3})$	$-5.49497 \times 10^{-3}$	$(-5.55148 \times 10^{-3}, -5.43846 \times 10^{-3})$
$\hat{c}_{56}$	$-1.47927 \times 10^{-3}$	$-1.26240 \times 10^{-3}$	$(-1.31255 \times 10^{-3}, -1.21225 \times 10^{-3})$	$-1.26240 \times 10^{-3}$	$(-1.31255 \times 10^{-3}, -1.21226 \times 10^{-3})$

Table 6.7: Coefficient estimates and 95% confidence intervals for full and reduced anterior toric lens models.

	Integration	OLS (All coefficients)		OLS (Reduced model)	
		OLS	95% confidence interval	OLS	95% confidence interval
$\hat{c}_1$	1.66754	1.66755	(1.66750, 1.66760)	1.66754	(1.66750, 1.66758)

Table 6.8: Coefficient estimates and 95% confidence intervals for full and reduced posterior toric lens models.

Integration		OLS (All coefficients)		OLS (Reduced model)	
		OLS	95% confidence interval	OLS	95% confidence interval
$\hat{c}_1$	2.22439	2.22436	(2.22430, 2.22442)	2.22436	(2.22430, 2.22442)
$\hat{c}_4$	$-8.45313 \times 10^{-1}$	$-8.45317 \times 10^{-1}$	$(-8.45380 \times 10^{-1}, -8.45253 \times 10^{-1})$	$-8.45317 \times 10^{-1}$	$(-8.45380 \times 10^{-1}, -8.45253 \times 10^{-1})$
$\hat{c}_6$	$6.91482 \times 10^{-2}$	$6.90762 \times 10^{-2}$	$(6.90046 \times 10^{-2}, 6.91478 \times 10^{-2})$	$6.90741 \times 10^{-2}$	$(6.90026 \times 10^{-2}, 6.91457 \times 10^{-2})$
$\hat{c}_{11}$	$-4.33250 \times 10^{-2}$	$-4.32913 \times 10^{-2}$	$(-4.33573 \times 10^{-2}, -4.32253 \times 10^{-2})$	$-4.32914 \times 10^{-2}$	$(-4.33574 \times 10^{-2}, -4.32254 \times 10^{-2})$
$\hat{c}_{12}$	$8.35447 \times 10^{-3}$	$8.31336 \times 10^{-3}$	$(8.24284 \times 10^{-3}, 8.38388 \times 10^{-3})$	$8.31210 \times 10^{-3}$	$(8.24163 \times 10^{-3}, 8.38258 \times 10^{-3})$
$\hat{c}_{14}$	$-3.39284 \times 10^{-3}$	$-3.52714 \times 10^{-3}$	$(-3.60374 \times 10^{-3}, -3.45054 \times 10^{-3})$	$-3.50901 \times 10^{-3}$	$(-3.58306 \times 10^{-3}, -3.43495 \times 10^{-3})$
$\hat{c}_{22}$	$-4.38993 \times 10^{-3}$	$-4.38291 \times 10^{-3}$	$(-4.45209 \times 10^{-3}, -4.31374 \times 10^{-3})$	$-4.38314 \times 10^{-3}$	$(-4.45232 \times 10^{-3}, -4.31397 \times 10^{-3})$
$\hat{c}_{24}$	$1.27769 \times 10^{-3}$	$1.32561 \times 10^{-3}$	$(1.25446 \times 10^{-3}, 1.39676 \times 10^{-3})$	$1.32562 \times 10^{-3}$	$(1.25451 \times 10^{-3}, 1.39673 \times 10^{-3})$
$\hat{c}_{26}$	$-5.44659 \times 10^{-4}$	$-5.49006 \times 10^{-4}$	$(-6.23479 \times 10^{-4}, -4.74534 \times 10^{-4})$	$-5.18261 \times 10^{-4}$	$(-5.86114 \times 10^{-4}, -4.50407 \times 10^{-4})$
$\hat{c}_{28}$	$3.33321 \times 10^{-4}$	$3.59759 \times 10^{-4}$	$(2.80739 \times 10^{-4}, 4.38779 \times 10^{-4})$	$3.72016 \times 10^{-4}$	$(2.97455 \times 10^{-4}, 4.46577 \times 10^{-4})$
$\hat{c}_{37}$	$-5.57099 \times 10^{-4}$	$-4.99005 \times 10^{-4}$	$(-5.54369 \times 10^{-4}, -4.43642 \times 10^{-4})$	$-4.99141 \times 10^{-4}$	$(-5.54505 \times 10^{-4}, -4.43778 \times 10^{-4})$
$\hat{c}_{38}$	$2.14390 \times 10^{-4}$	$1.71763 \times 10^{-4}$	$(1.10177 \times 10^{-4}, 2.33349 \times 10^{-4})$	$1.72813 \times 10^{-4}$	$(1.11250 \times 10^{-4}, 2.34377 \times 10^{-4})$

The solution to the inverse problem is the posterior probability density of  $C$  given the observations  $(\chi_i, w_i)$ . As explained in [41, 89], the posterior density is given by Bayes' theorem:

$$\pi(c|w) = \frac{\pi(w|c)\pi_0(c)}{\pi(w)} = \frac{\pi(w|c)\pi_0(c)}{\int_{\mathbb{R}^m} \pi(w|c)\pi_0(c)dc}. \quad (6.21)$$

The likelihood function  $\pi(w|c) = L_w(c)$  in (6.21) is the probability of obtaining the vector of discrete observations  $w$  given a particular parameter realization  $c \in C$ . For errors  $\varepsilon_i \stackrel{\text{iid}}{\sim} \mathcal{N}(0, \sigma^2)$ , the likelihood function can be written

$$\pi(w|c) = L_w(c, \sigma^2) = \frac{1}{(2\pi\sigma^2)^{s/2}} e^{-SS_c/2\sigma^2}, \quad (6.22a)$$

where  $SS_c$  is the sum of squares error

$$SS_c = \sum_{i=1}^s [w_i - f_i(c)]^2 = R^T R. \quad (6.22b)$$

Rather than trying to use numerical integration to solve (6.21), we will estimate the posterior density stochastically using the delayed rejection adaptive Metropolis (DRAM) algorithm detailed in [25, 26]. The DRAM algorithm is a modified Metropolis Markov chain Monte Carlo (MCMC) method, whose stationary distribution (given a sufficiently long chain) estimates the posterior density (6.21). We provide a brief overview of the algorithm here; additional information about the use of DRAM specifically (as well as MCMC methods in general) can be found in [89, Ch. 8].

The idea behind the Metropolis algorithm is that a candidate parameter value  $c^*$  is drawn from a multivariate Gaussian proposal distribution and either accepted (*i.e.*,  $c^k = c^*$ ) with probability determined by the prior density and the likelihood function (6.22), or rejected in favor of the previous state ( $c^k = c^{k-1}$ ). During the adaptive Metropolis (AM) stage—which follows an initial nonadaptive period—the chain covariance matrix is then updated to account for this new parameter value. Note that the adaptive algorithm is not a true Markovian process, as the updated proposal distribution is determined by the entire sample path of the chain. The inclusion of the delayed rejection (DR) step means that instead of setting  $c^k = c^{k-1}$  if the candidate  $c^*$  is rejected, an alternative second stage candidate is constructed based on both  $c^{k-1}$  and the rejected candidate.

The results in this section were generated using a MATLAB implementation of DRAM

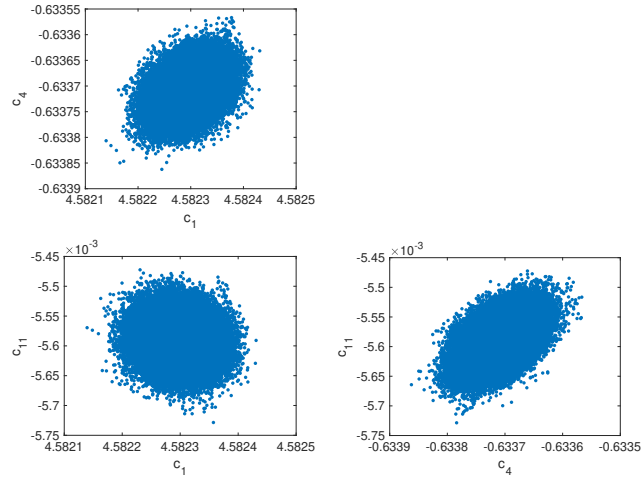


Figure 6.13: Joint sample points for the significant Zernike coefficients of the front surface of the aspheric lens.

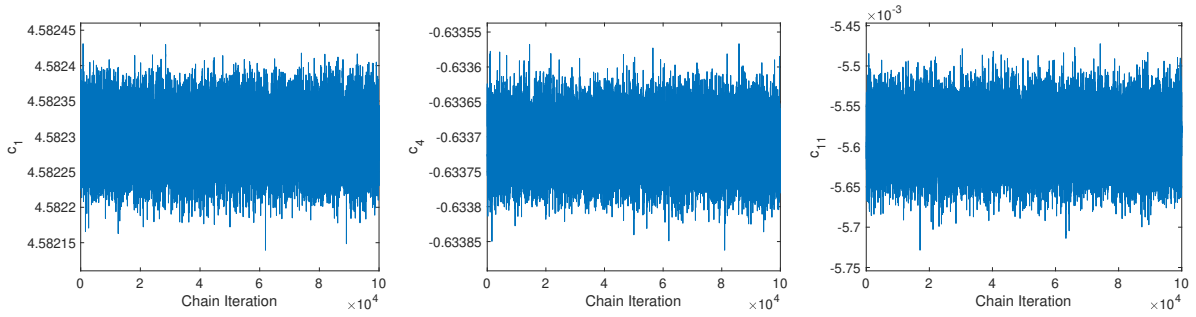


Figure 6.14: Sample paths for the front surface of the aspheric lens.

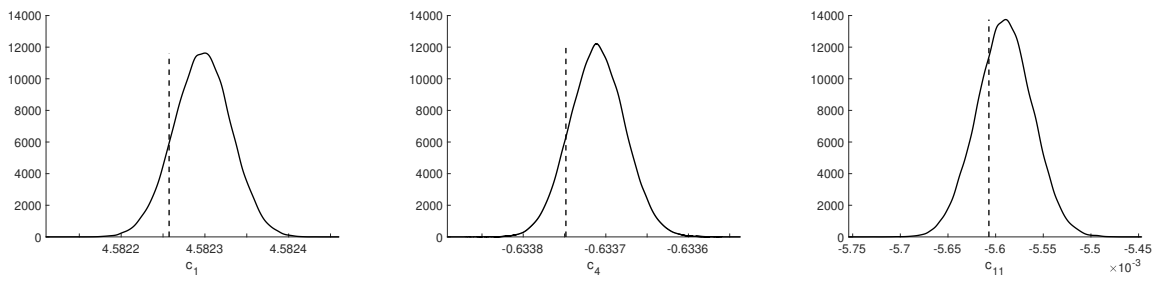


Figure 6.15: Parameter densities for the front surface of the aspheric lens.

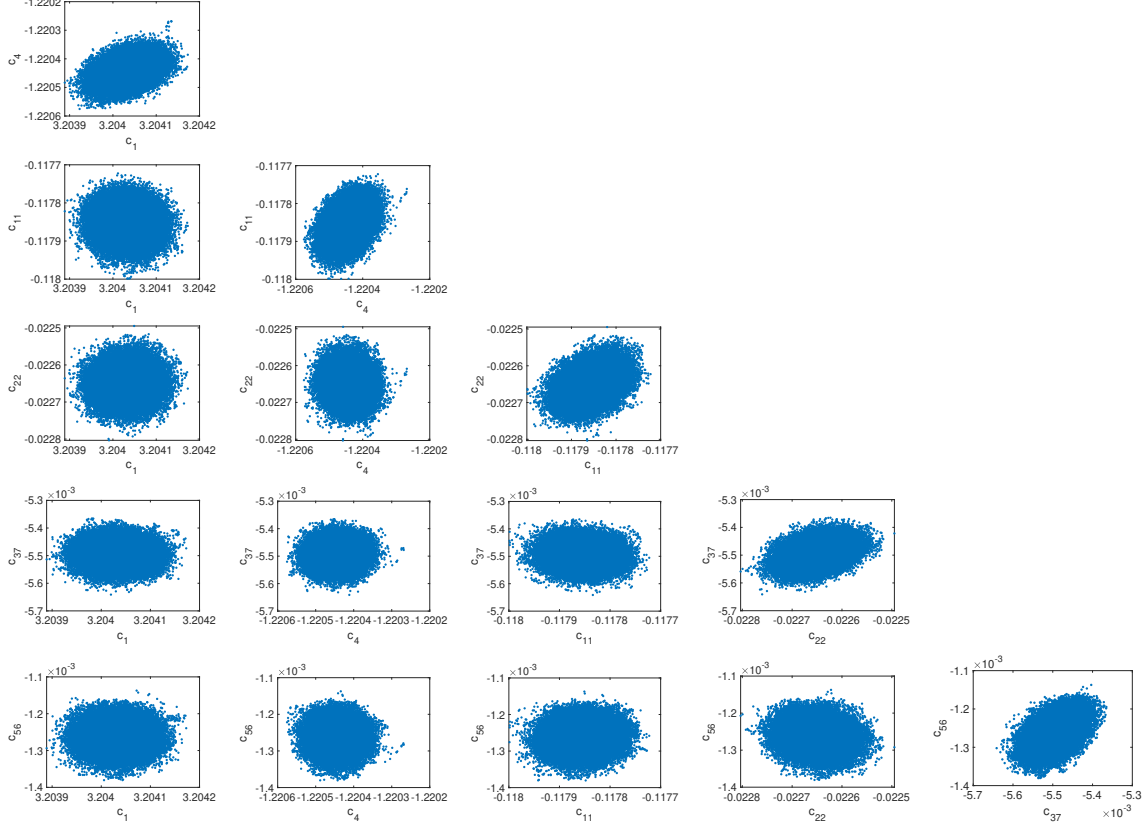


Figure 6.16: Joint sample points for the significant Zernike coefficients of the front surface of the toric lens.

(`mcmcrun.m`) that is available as part of the MCMC Toolbox [49] developed by Marko Laine, one of the co-authors of [25]. We ran the algorithm using the default noninformative Gaussian prior with infinite variance, which simulates a uniform distribution. The sum of squares error (6.22b) for the four lens surfaces was computed using the normalized ROMs discussed in Sections 6.1.3 and 6.3.1, and the initial parameter distributions correspond to the OLS sampling distributions in Tables 6.5–6.8. For each surface, we ran the algorithm for an initial shorter burn-in period to allow the chain to reach its stationary distribution, then re-ran the algorithm using the posterior densities from this first run as the initial distributions. Figures 6.13–6.22 show the joint sample points, paths, and marginal parameter density estimates from this second run.

We used 50000 iterations for the burn-in period for both front surfaces, as well as the back of the aspheric lens. The back of the toric lens required twice as many iterations to

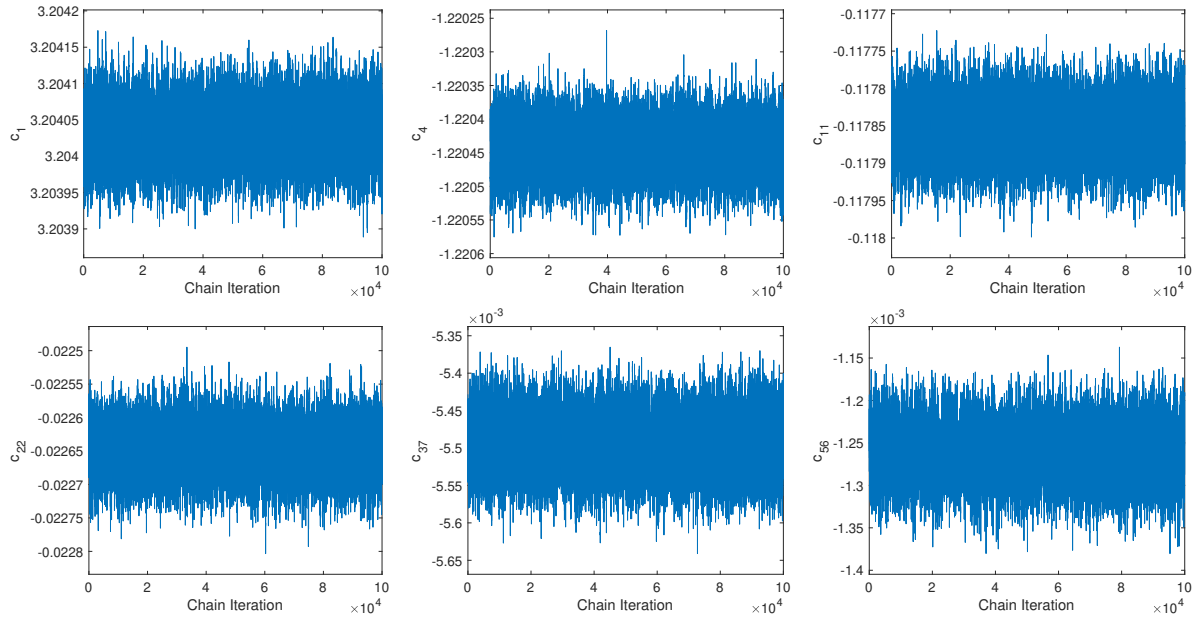


Figure 6.17: Sample paths for the front surface of the toric lens.

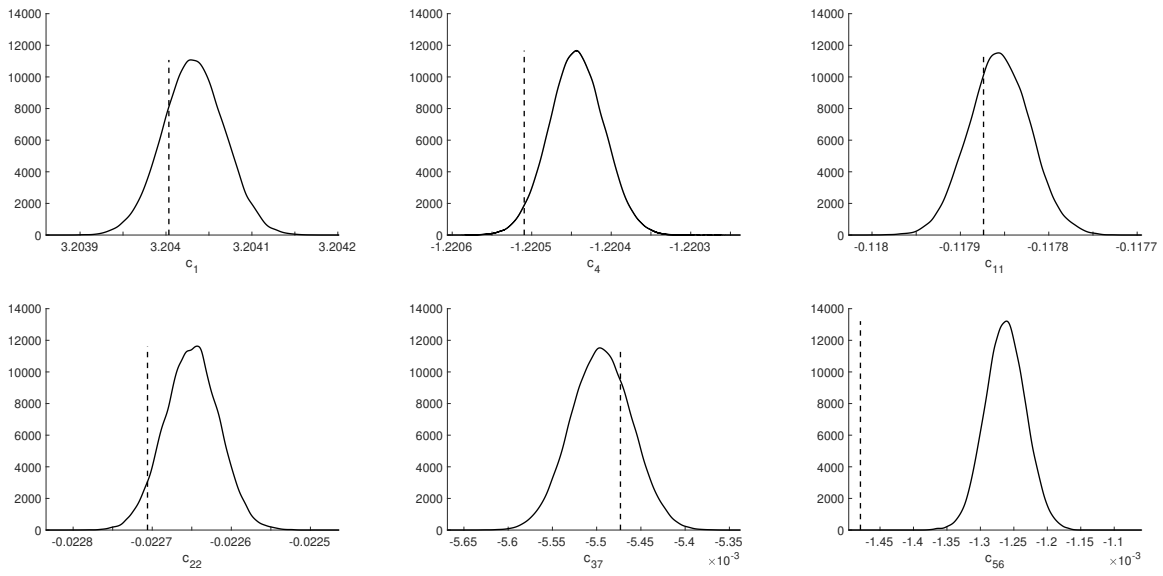


Figure 6.18: Parameter densities for the front surface of the toric lens.

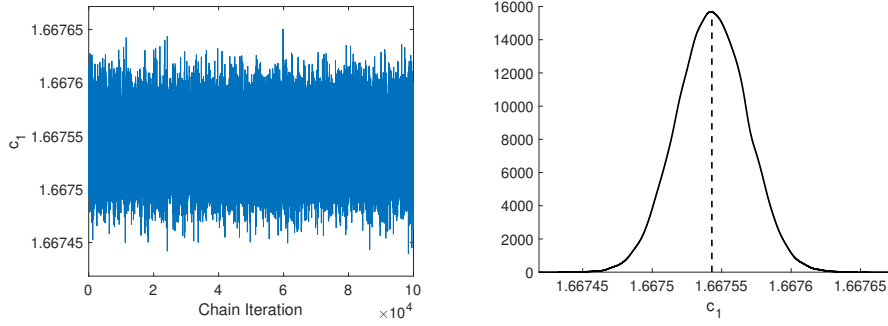


Figure 6.19: Sample path (left) and density (right) for  $c_1$  for the back surface of the aspheric lens.

stabilize. For the second run, we used 100000 iterations for the first three surfaces and 250000 for the back of the toric lens. These values were selected to ensure smoothness when constructing the kernel density estimates shown in Figures 6.15, 6.18, 6.19, and 6.22. The fact that the chains have burned-in is clear from the sample paths from the second run, which are depicted in Figures 6.14, 6.17, 6.19, and 6.21.

The dashed lines in the density estimates represent the “true” value  $c_j^{(i)}$  of the corresponding Zernike coefficient as computed directly from the design equation using numerical integration. These values are also listed in Tables 6.10–6.13 along with the mean ( $\hat{c}_j = \frac{1}{s} \sum_{i=1}^s c_j^{(i)}$ ) and standard error of the corresponding chain and the OLS results from the previous section. This “true” value falls within three standard deviations of the mean for every coefficient save  $c_{56}$  for the front surface of the toric lens. In fact, this is also true for the OLS results, even for the coefficients that were outside the 95% confidence interval. The estimate  $\hat{c}_{56}$  from DRAM is slightly worse than the OLS estimates, but like the OLS estimates it is still within 15% of  $c_{56}^{(i)}$ . In most other cases, the DRAM estimates are actually slightly closer than the OLS estimates to the “true” coefficient values, with the exception of  $c_{11}$ ,  $c_{12}$ ,  $c_{14}$ ,  $c_{22}$ ,  $c_{24}$ , and  $c_{28}$  for the back of the toric lens. However, none of the differences in either direction correspond to a particularly significant change in the relative error of the estimate when compared to  $c_j^{(i)}$ .

We also have the option to treat the error variance  $\sigma^2$  as another parameter with likelihood

$$\pi(w, c | \sigma^2) = L_{w,q}(\sigma^2) = \frac{1}{(2\pi\sigma^2)^{s/2}} e^{-SS_c/2\sigma^2}. \quad (6.23)$$

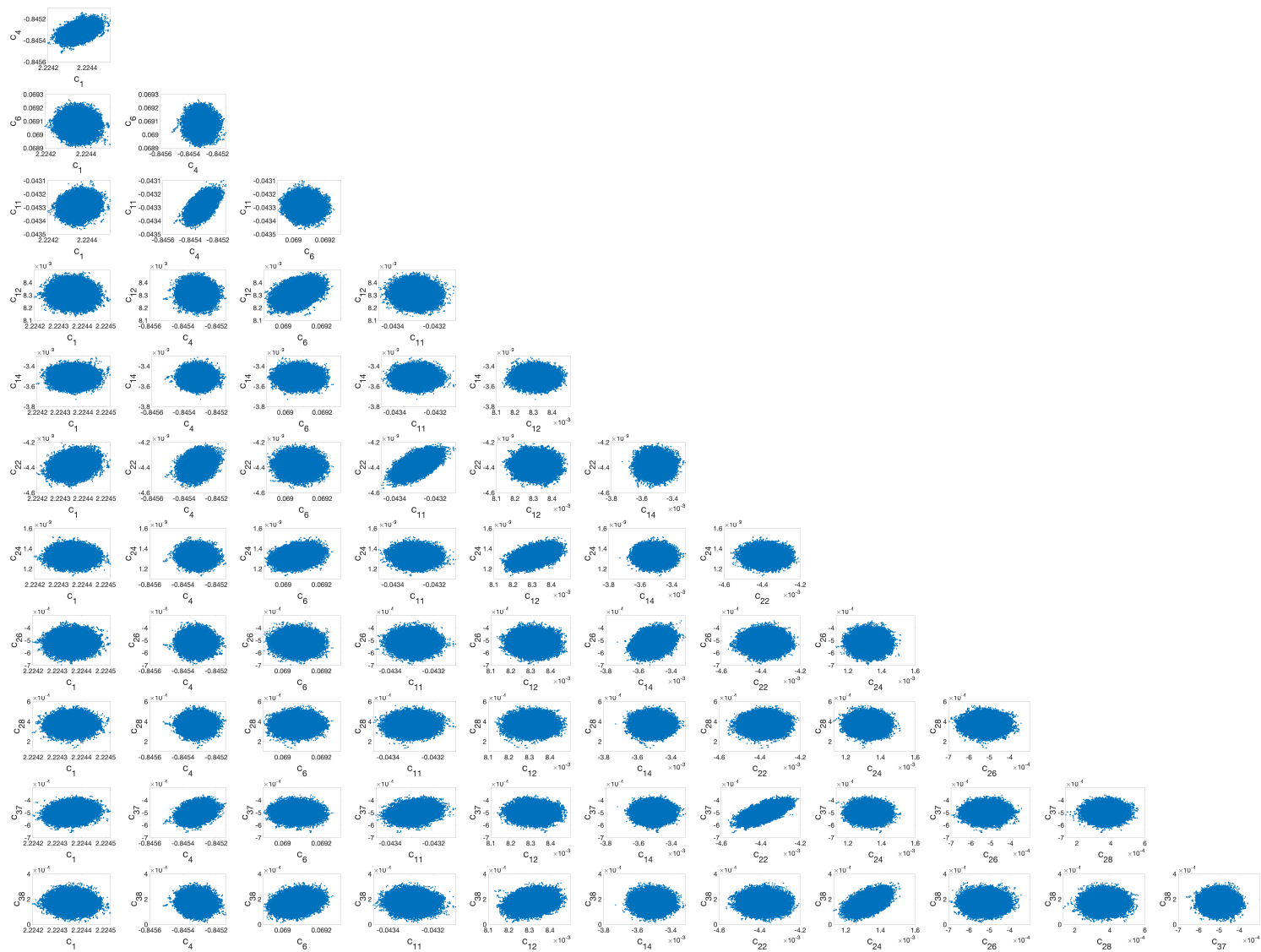


Figure 6.20: Joint sample points for the significant Zernike coefficients of the back surface of the toric lens.

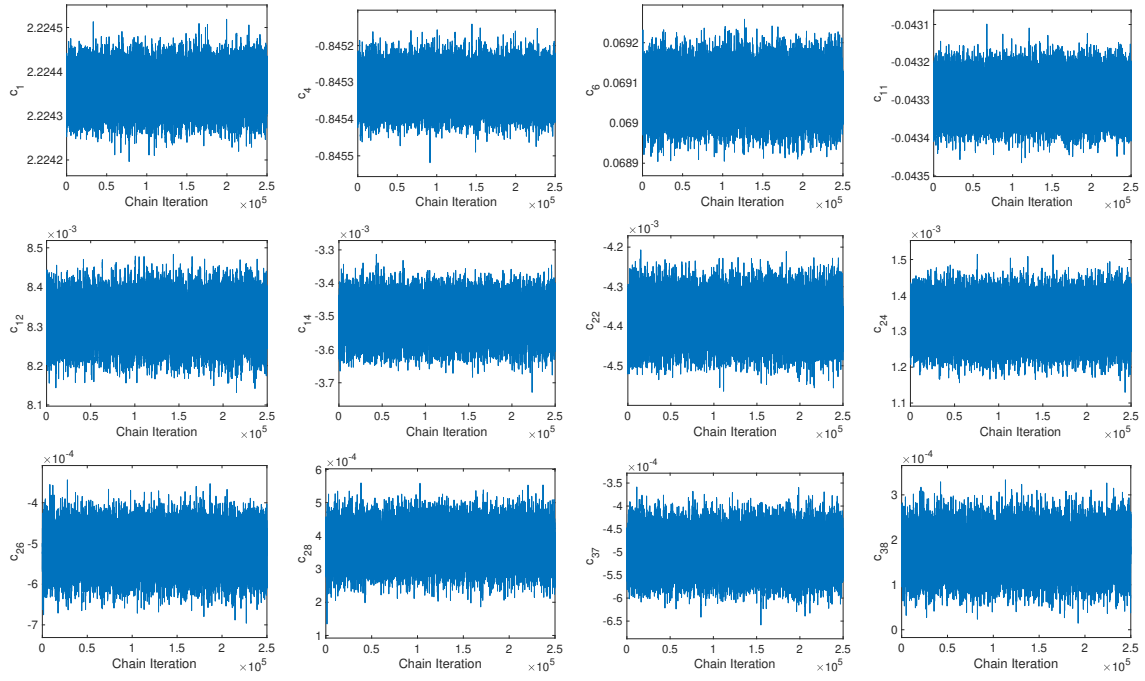


Figure 6.21: Sample paths for the back surface of the toric lens.

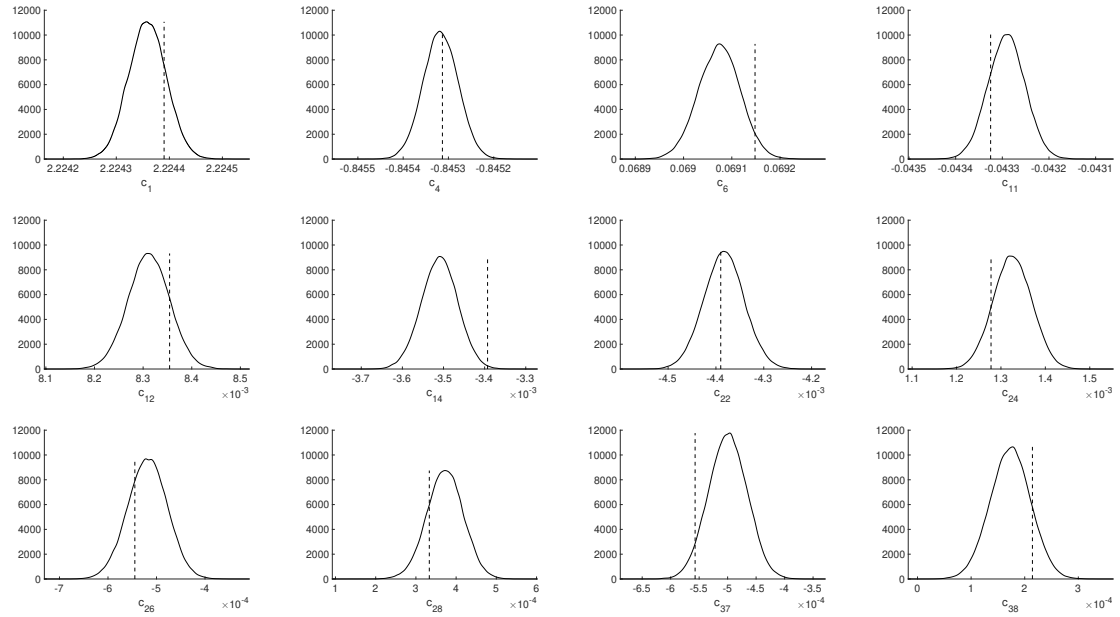


Figure 6.22: Parameter densities for the back surface of the toric lens.

Table 6.9: Error variance ( $\hat{\sigma}^2$ ) in square millimeters from OLS and DRAM.

	OLS	DRAM
Aspheric lens front	$9.9628 \times 10^{-5}$	$9.9629 \times 10^{-5}$
Toric lens front	$9.9683 \times 10^{-5}$	$9.9684 \times 10^{-5}$
Aspheric lens back	$7.0113 \times 10^{-5}$	$7.0114 \times 10^{-5}$
Toric lens back	$8.5488 \times 10^{-5}$	$8.5491 \times 10^{-5}$

The conjugate prior of (6.23) is an inverse gamma distribution that depends on the sum of squares error  $SS_{c^k}$  for the current iteration. During the AM step, the variance estimate is updated by sampling from this new distribution after the updated value  $c^k$  has been assigned but prior to the computation of the updated covariance matrix. The mean of the chain error variance for each surface is Table 6.9. In each case, we see that the chain variance is slightly greater than the initial OLS estimate; however, the OLS values of  $\hat{\sigma}^2$  are all well within 0.005% of their Bayesian estimates.

The joint sample points in Figures 6.13, 6.16, and 6.20 mostly indicate that most of the parameters appear to be independent or only very weakly correlated ( $\rho_{c_j c_k} < 0.4$ ). However, there are several cases where the correlation is more significant. For the front of the aspheric lens, the correlation between  $c_4$  and  $c_{11}$  is  $\rho_{c_4 c_{11}} \approx 0.5$ , and  $\rho_{c_{37} c_{56}} \approx 0.46$  for the front of the toric lens. The back of the toric lens has two groups of moderately correlated Zernike coefficients, with the strength of the correlation increasing within each group as the coefficient index increases. In the first group,  $c_1$  is correlated with  $c_4$  ( $\rho_{c_1 c_4} \approx 0.47$ ), which in turn is correlated with  $c_{11}$  ( $\rho_{c_4 c_{11}} \approx 0.55$ ), which is correlated with  $c_{22}$  ( $\rho_{c_{11} c_{22}} \approx 0.58$ ), which is then also correlated with  $c_{37}$  ( $\rho_{c_{22} c_{37}} \approx 0.65$ ). In the second group,  $c_{24}$  is correlated with both  $c_{12}$  and  $c_{38}$  ( $\rho_{c_{12} c_{24}} \approx 0.48$  and  $\rho_{c_{24} c_{38}} \approx 0.52$ ).

To better understand these correlations, we can look at the corresponding Zernike basis functions in Table 6.4 and Figure 6.11. Every pair of correlated coefficients are associated with polynomials of the same azimuthal degree.  $Z_1$ ,  $Z_4$ ,  $Z_{11}$ ,  $Z_{22}$ ,  $Z_{37}$ , and  $Z_{56}$  are all degree 0—that is, continuously rotationally symmetric—while  $Z_{12}$ ,  $Z_{24}$ , and  $Z_{38}$  are all degree 2 with an azimuthal component of  $\cos 2\theta$ . Furthermore, the correlations only occur between consecutive polynomials within each subgroup, which are also the surfaces with the most local similarity to one another. The correlations are positive because the central concavity of the basis functions alternates.

Table 6.10: Comparison of the mean and standard error (in mm) for Zernike coefficients of the anterior aspheric lens using OLS and DRAM.

	Integration	OLS (All coefficients)		OLS (Reduced model)		DRAM (Reduced model)	
		Mean	Std Error	Mean	Std Error	Mean	Std Error
$\hat{c}_1$	4.58226	4.58230	$3.43202 \times 10^{-5}$	4.58230	$3.43196 \times 10^{-5}$	4.58230	$3.39635 \times 10^{-5}$
$\hat{c}_4$	$-6.33748 \times 10^{-1}$	$-6.33710 \times 10^{-1}$	$3.31144 \times 10^{-5}$	$-6.33710 \times 10^{-1}$	$3.31138 \times 10^{-5}$	$-6.33719 \times 10^{-1}$	$3.33166 \times 10^{-5}$
$\hat{c}_{11}$	$-5.60707 \times 10^{-3}$	$-5.59018 \times 10^{-3}$	$2.91833 \times 10^{-5}$	$-5.59018 \times 10^{-3}$	$2.91828 \times 10^{-5}$	$-5.59184 \times 10^{-3}$	$2.91718 \times 10^{-5}$

Table 6.11: Comparison of the Zernike coefficients (in mm) of the anterior toric lens using OLS and DRAM.

	Integration	OLS (All coefficients)		OLS (Reduced model)		DRAM (Reduced model)	
		Mean	Std Error	Mean	Std Error	Mean	Std Error
$\hat{c}_1$	3.20400	3.20403	$3.55717 \times 10^{-5}$	3.20403	$3.55709 \times 10^{-5}$	3.20403	$3.56598 \times 10^{-5}$
$\hat{c}_4$	-1.22051	-1.22044	$3.45220 \times 10^{-5}$	-1.22044	$3.45213 \times 10^{-5}$	-1.22044	$3.43356 \times 10^{-5}$
$\hat{c}_{11}$	$-1.17874 \times 10^{-1}$	$-1.17856 \times 10^{-1}$	$3.45895 \times 10^{-5}$	$-1.17856 \times 10^{-1}$	$3.45887 \times 10^{-5}$	$-1.17881 \times 10^{-1}$	$3.45340 \times 10^{-5}$
$\hat{c}_{22}$	$-2.27060 \times 10^{-2}$	$-2.26500 \times 10^{-2}$	$3.45716 \times 10^{-5}$	$-2.26500 \times 10^{-2}$	$3.45708 \times 10^{-5}$	$-2.26785 \times 10^{-2}$	$3.42154 \times 10^{-5}$
$\hat{c}_{37}$	$-5.47311 \times 10^{-3}$	$-5.49497 \times 10^{-3}$	$3.43589 \times 10^{-5}$	$-5.49497 \times 10^{-3}$	$3.43582 \times 10^{-5}$	$-5.49221 \times 10^{-3}$	$3.41482 \times 10^{-5}$
$\hat{c}_{56}$	$-1.47927 \times 10^{-3}$	$-1.26240 \times 10^{-3}$	$3.04893 \times 10^{-5}$	$-1.26240 \times 10^{-3}$	$3.04886 \times 10^{-5}$	$-1.26030 \times 10^{-3}$	$3.00953 \times 10^{-5}$

Table 6.12: Comparison of the Zernike coefficients (in mm) of the posterior aspheric lens using OLS and DRAM.

	Integration	OLS (All coefficients)		OLS (Reduced model)		DRAM (Reduced model)	
		Mean	Std Error	Mean	Std Error	Mean	Std Error
$\hat{c}_1$	1.66754	1.66755	$3.01538 \times 10^{-5}$	1.66754	$2.50077 \times 10^{-5}$	1.66754	$2.50681 \times 10^{-5}$

Table 6.13: Comparison of the Zernike coefficients (in mm) of the posterior toric lens using OLS and DRAM.

	Integration	OLS (All coefficients)		OLS (Reduced model)		DRAM (Reduced model)	
		Mean	Std Error	Mean	Std Error	Mean	Std Error
$\hat{c}_1$	2.22439	2.22436	$3.58474 \times 10^{-5}$	2.22436	$3.58477 \times 10^{-5}$	2.22436	$3.56549 \times 10^{-5}$
$\hat{c}_4$	$-8.45313 \times 10^{-1}$	$-8.45317 \times 10^{-1}$	$3.86174 \times 10^{-5}$	$-8.45317 \times 10^{-1}$	$3.86176 \times 10^{-5}$	$-8.45317 \times 10^{-1}$	$3.86220 \times 10^{-5}$
$\hat{c}_6$	$6.91482 \times 10^{-2}$	$6.90762 \times 10^{-2}$	$4.35250 \times 10^{-5}$	$6.90741 \times 10^{-2}$	$4.35034 \times 10^{-5}$	$6.90741 \times 10^{-2}$	$4.32744 \times 10^{-5}$
$\hat{c}_{11}$	$-4.33250 \times 10^{-2}$	$-4.32913 \times 10^{-2}$	$4.00983 \times 10^{-5}$	$-4.32914 \times 10^{-2}$	$4.00985 \times 10^{-5}$	$-4.32910 \times 10^{-2}$	$3.96996 \times 10^{-5}$
$\hat{c}_{12}$	$8.35447 \times 10^{-3}$	$8.31336 \times 10^{-3}$	$4.28715 \times 10^{-5}$	$8.31210 \times 10^{-3}$	$4.28442 \times 10^{-5}$	$8.31186 \times 10^{-3}$	$4.28481 \times 10^{-5}$
$\hat{c}_{14}$	$-3.39284 \times 10^{-3}$	$-3.52714 \times 10^{-3}$	$4.65672 \times 10^{-5}$	$-3.50901 \times 10^{-3}$	$4.50231 \times 10^{-5}$	$-3.50962 \times 10^{-3}$	$4.40338 \times 10^{-5}$
$\hat{c}_{22}$	$-4.38993 \times 10^{-3}$	$-4.38291 \times 10^{-3}$	$4.20559 \times 10^{-5}$	$-4.38314 \times 10^{-3}$	$4.20562 \times 10^{-5}$	$-4.38310 \times 10^{-3}$	$4.23420 \times 10^{-5}$
$\hat{c}_{24}$	$1.27769 \times 10^{-3}$	$1.32561 \times 10^{-3}$	$4.32547 \times 10^{-5}$	$1.32562 \times 10^{-3}$	$4.32290 \times 10^{-5}$	$1.32598 \times 10^{-3}$	$4.32016 \times 10^{-5}$
$\hat{c}_{26}$	$-5.44659 \times 10^{-4}$	$-5.49006 \times 10^{-4}$	$4.52758 \times 10^{-5}$	$-5.18261 \times 10^{-4}$	$4.12519 \times 10^{-5}$	$-5.18611 \times 10^{-4}$	$4.06306 \times 10^{-5}$
$\hat{c}_{28}$	$3.33321 \times 10^{-4}$	$3.59759 \times 10^{-4}$	$4.80405 \times 10^{-5}$	$3.72016 \times 10^{-4}$	$4.53292 \times 10^{-5}$	$3.72485 \times 10^{-4}$	$4.51206 \times 10^{-5}$
$\hat{c}_{37}$	$-5.57099 \times 10^{-4}$	$-4.99005 \times 10^{-4}$	$3.36581 \times 10^{-5}$	$-4.99141 \times 10^{-4}$	$3.36584 \times 10^{-5}$	$-4.99689 \times 10^{-4}$	$3.38290 \times 10^{-5}$
$\hat{c}_{38}$	$2.14390 \times 10^{-4}$	$1.71763 \times 10^{-4}$	$3.74414 \times 10^{-5}$	$1.72813 \times 10^{-4}$	$3.74275 \times 10^{-5}$	$1.73317 \times 10^{-4}$	$3.76089 \times 10^{-5}$

## 6.4 Uncertainty Propagation

Once we have quantified the uncertainty in the parameter estimates  $\hat{c}_i$ , we want to see how the parameter means and covariances we computed in Section 6.3.2 will propagate through our models to impact the accuracy of the model fit to the data and the uncertainty associated with any model-based predictions. These are respectively quantified by the credible interval (determined by the mean and variance of the model response) and the prediction interval (which indicates where future observations are likely to fall given the measurement error).

So far in this chapter we have only been looking at the axial elevation models

$$f^a \equiv f^a(\mathfrak{X}, c) = \sum_{j=1}^{m_a} c_j Z_j(\mathfrak{X}'), \quad f^p \equiv f^p(\tilde{\mathfrak{X}}, c) = \sum_{j=1}^{m_p} c_j Z_j(\tilde{\mathfrak{X}}')$$

from Section 6.1. These both correspond to the statistical model

$$\gamma = f(c) + \varepsilon,$$

where  $f(c)$  is the relevant model response,  $\gamma$  is a random vector of observations, and  $\varepsilon$  is a vector of measurement errors with  $\varepsilon_i \stackrel{\text{iid}}{\sim} \mathcal{N}(0, \sigma_0^2)$ . For radial coordinates  $\mathfrak{X} = (\rho, \theta)$  within the calibration domain (which we have defined in previous chapters), we can construct a distribution for the model response by Monte Carlo sampling of the parameters from their respective distributions and evaluating the mean and variance of the responses  $f(c^i)$  at the point  $\mathfrak{X}$ . The mean response and variance are then used to construct the credible interval at  $\mathfrak{X}$ . The prediction interval is then constructed by adding the error variance estimate  $\hat{\sigma}^2$  to the estimated variance of the model response [89, Ch. 9].

In the previous chapters, we also considered the local meridional curvature, which we modeled as

$$k^a = -\frac{\partial^2 f^a}{\partial \rho^2} \left( 1 + \left( \frac{\partial f^a}{\partial \rho} \right)^2 \right)^{-3/2}, \quad k^p = -\frac{\partial^2 f^p}{\partial \rho^2} \left( 1 + \left( \frac{\partial f^p}{\partial \rho} \right)^2 \right)^{-3/2}, \quad (6.24)$$

and estimated using finite difference derivatives as described in Section 3.4.<sup>viii</sup> In both

---

<sup>viii</sup>Recall that the curvature must then be multiplied by the constant 337.5 to convert to units of diopters (D).

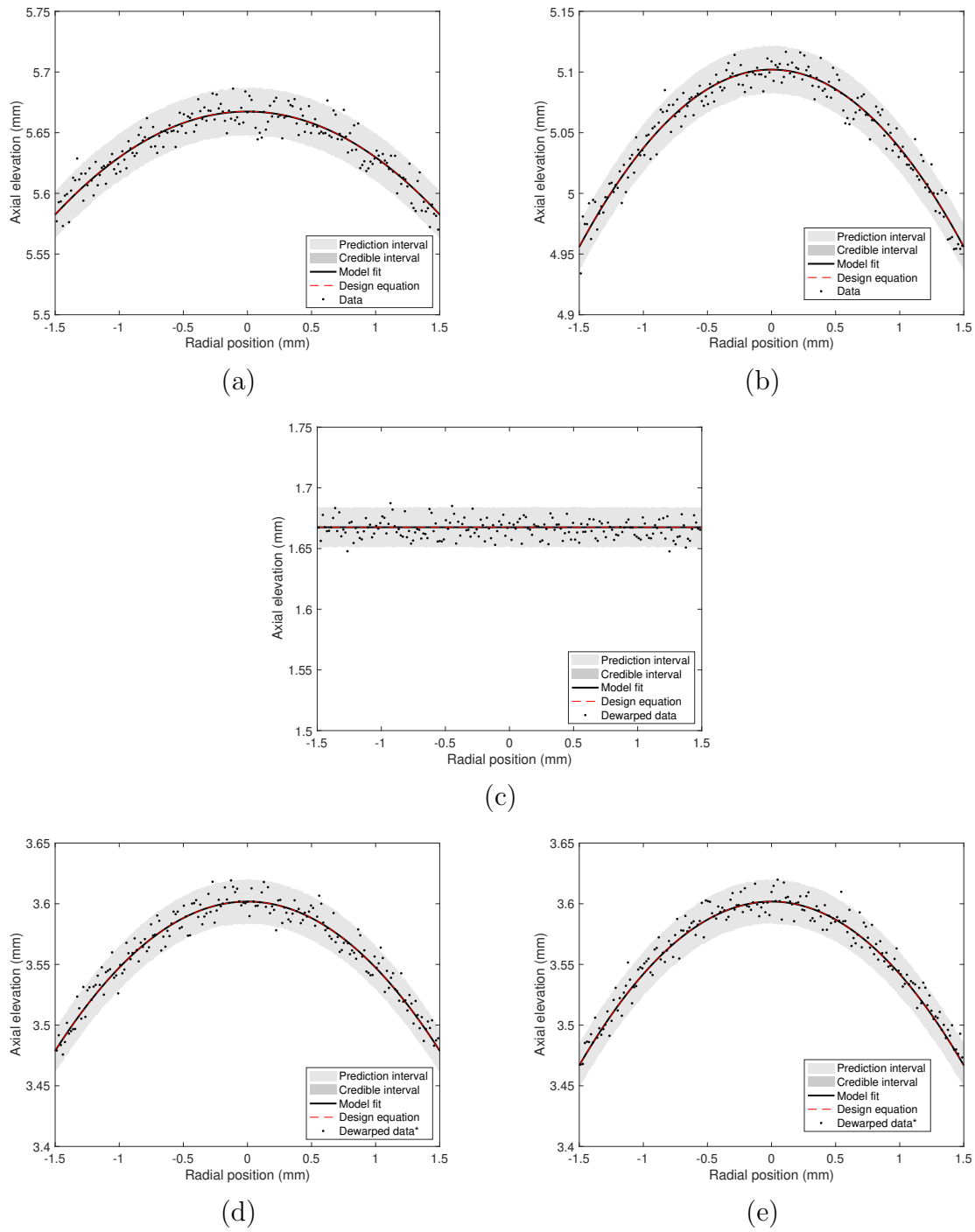


Figure 6.23: Prediction intervals for central elevation of the (a) anterior aspheric lens, (b) anterior toric lens, (c) posterior aspheric lens, and posterior toric lens (d) at  $0^\circ$ , and (e) at  $90^\circ$ . (Credible intervals are also depicted but are too narrow to be visible.)

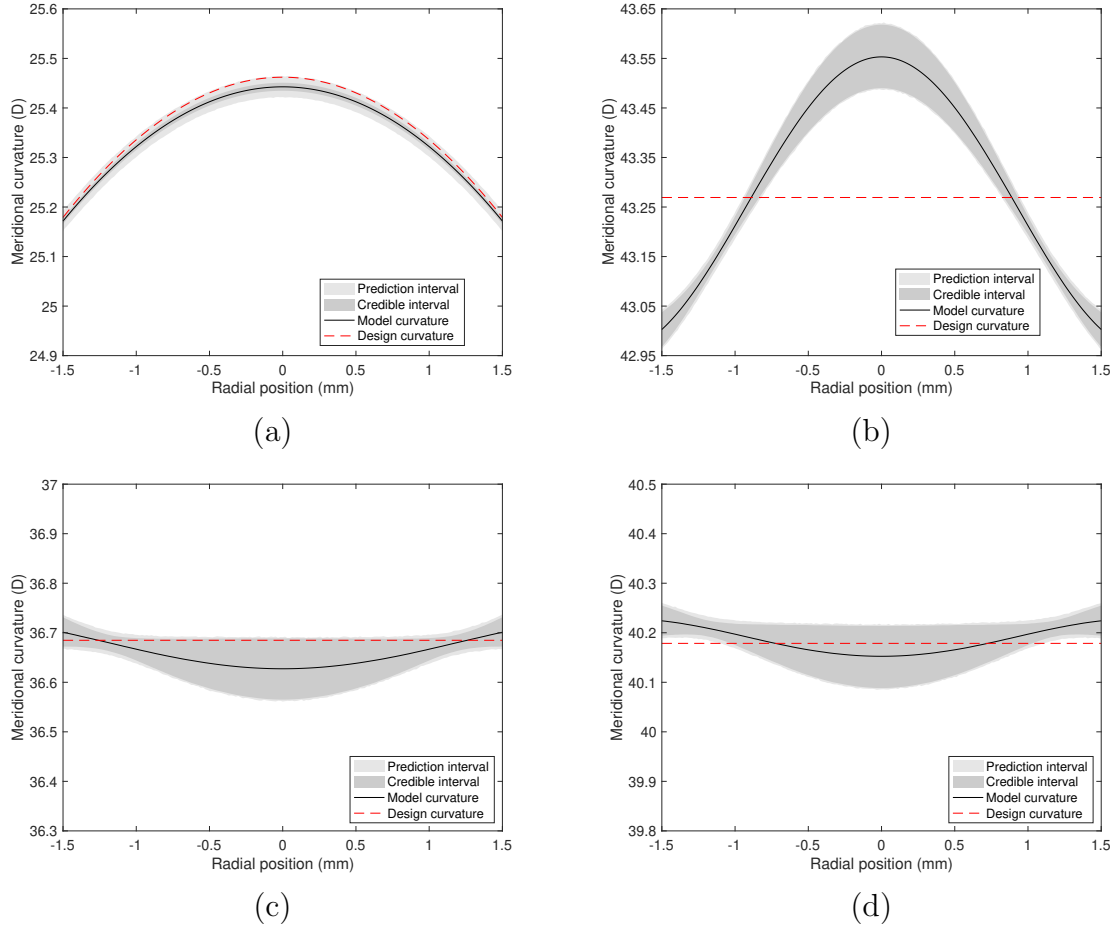


Figure 6.24: Prediction and credible intervals for meridional curvature of the (a) anterior aspheric lens, (b) anterior toric lens, and posterior toric lens (c) at 0°, and (d) at 90°.

Chapters 3 and 5, we saw that the Zernike polynomials provide a more accurate estimate of both the axial elevation and the meridional curvature closer to the center of the lens—particularly within the central 3 mm diameter region. Therefore, we will restrict our focus to this region.

Figures 6.23–6.24 show the 95% credible and prediction intervals for the axial elevation and meridional curvature of each lens surface—over the central 3 mm—for a single meridian. To obtain these interval estimates, we ran 5000 realizations of each model using parameter values sampled from the MCMC chains generated by DRAM. This was done using the function `mcmcpred.m`, which is included in the MCMC Toolbox [49]. Since

the back surface of the toric lens is not rotationally symmetric, we have included both principal meridians rather than just a single meridian. The back surface of the aspheric lens was not included for the curvature because the ROM is already a flat surface. In both figures, although the range of the  $y$ -axis is not the same for each subfigure, the scale is consistent.

Note that the 95% credible intervals for the axial elevation—shown in Figure 6.23—are too small to be seen in these illustrations, and that in every case the expected model fit is very close to the design equation. As expected, most of the data points lie within their 95% prediction intervals.

The credible intervals for the curvature (Figure 6.24) are much larger, illustrating that the uncertainty in the parameter estimates is amplified by the derivatives in the model. This effect is least significant for the front of the aspheric lens—shown in Figure 6.24a—however, even in this case the model predicts a curvature estimate that is consistently lower than the design curvature across the entire central diameter of the lens. The credible intervals are much larger for both of the toric lens surfaces, yet we still end up with too much oscillation in the predicted curvature (the design curvature is constant across the entire meridian). As we saw in Chapters 3 and 5, the estimated curvature of the front surface of the toric lens (Figure 6.24b) is by far the worst of all the curvature estimates. This is particularly true at the apex, where the true curvature from the design equation is nearly 0.25 D lower than the lower bound of the credible interval.

## 6.5 Global Sensitivity Analysis

In Section 6.4, we looked at the collective impact of the uncertainty in the parameter estimates on our local meridional curvature predictions. Next, we will use methods from global sensitivity analysis to understand how much the uncertainty in each parameter (or some combination of parameters) contributes to the uncertainty in the curvature as the parameters are varied across the entire range of allowed values. Specifically, we will consider the way in which the different parameters affect the model predictions related to the principal curvatures of the two lenses. Parameters that have a noticeable impact on the model response, whether on their own or in combination with other parameters, are termed *influential*.

Recall that the curvatures  $K_1$  and  $K_2$  are the maximum and minimum values of the

meridional curvature (6.24) at the vertex  $\rho = 0$ . If we denote the curvature at the vertex by  $k(0, \theta, c)$ , then the anterior principal curvature of both lenses is

$$K_a = \max_{\theta \in [0, \pi)} k^a(0, \theta, c), \quad (6.25)$$

and the posterior principal curvatures of the toric lens are

$$K_{p_1} = \max_{\theta \in [0, \pi)} k^p(0, \theta, c), \quad \text{and} \quad K_{p_2} = \min_{\theta \in [0, \pi)} k^p(0, \theta, c). \quad (6.26)$$

As mentioned in Section 6.4, the ROM for the back surface of the aspheric lens is already flat, so we will not discuss it here. The two front surfaces are rotationally symmetric, so their design equations will only produce one true principal curvature. We showed in Section 6.3.1 that the ROMs for the two front surfaces consist of a linear combination of rotationally symmetric polynomials—therefore, the front surface models  $f^a$  will also be associated with only one principal curvature value,  $K_a$ .<sup>ix</sup>

For the back of the toric lens, the choice of meridian does not affect the sensitivity measures—*i.e.*, the results for  $K_{p_1}$  are identical to those for  $K_{p_2}$ . However, the difference between the two principal curvatures is also clinically significant. Therefore, we will consider two quantities of interest for the back surface of the toric lens:  $K_{p_1}$  and  $K_{p_1} - K_{p_2}$ . Obviously both of these quantities will be affected by the values of the coefficients in the back surface model  $f^p$ , but since  $f^a$  is used to dewarp the data before fitting it to the model, the front surface coefficients will also influence the back surface curvature. In addition to looking at the sensitivities associated with the back surface coefficients, we will also consider the sensitivity of the posterior curvature to just the front surface coefficients, while the back surface coefficients are fixed at the mean values found in Section 6.3.2.

In this section, we compare three different methods of ranking the parameters' influence on the quantities of interest described above: parametric analysis (*i.e.*, centered parameter study), Morris screening, and Sobol' analysis. To ensure that the relative magnitudes of the Zernike coefficients do not affect the rankings, we use the normalized parameters discussed in Section 6.1.3. We also compare the ROMs to the full models to

---

<sup>ix</sup>It is less obvious that the full models using all the Zernike coefficients will also be rotationally symmetric given the noise in the data, however the contributions from the odd Zernike polynomials are so small that they have a negligible effect on the principal curvature. This was not the case for the real data in Chapter 5 due to off-axis imaging.

determine whether setting any of the parameters to zero has an effect on the ranking of the remaining parameters. All of the algorithms involved are described in detail in [90, Ch. 9].

The simplest of the three methods is the centered parameter study, in which we perturb each normalized parameter  $\theta_i$  about its mean value of  $\frac{1}{2}$  by  $\pm 20\%$  and measure the relative change in the given quantity of interest. The results (shown in Figures 6.25, 6.27, 6.29, 6.31, 6.33, and 6.35) provide a ranking of the parameters' influence over the specified model response, but they do not account for possible interactions between inputs nor do they quantify the relative amount of influence of each parameter.

Morris screening—proposed by Max Morris in [59]—is a derivative-based sensitivity method that based on estimating the distribution of the elementary effects

$$d_i = \frac{K(\theta + \Delta e_i) - K(\theta)}{\Delta} \approx \frac{\partial K(\theta)}{\partial \theta_i} \quad (6.27)$$

One of the main advantages to this method over parametric analysis is that, in addition to ranking influential parameters and identifying those with little influence, Morris screening also accounts for interactions between parameters. (It does not, however, quantify relative influence.)

The general idea described in [59] involves discretizing the parameter space into an  $m$ -dimensional  $\ell$ -level sample space  $\Gamma_\ell^x$ , and then computing elementary effects for  $r$  random samplings  $\theta^j \in \Gamma_\ell$  using the forward difference method in (6.27). The Morris sensitivity measures are the mean and standard deviation of the sampling distribution of the elementary effects:

$$\begin{aligned} \mu_i^* &= \frac{1}{r} \sum_{j=1}^r |d_i^j|, & \mu_i &= \frac{1}{r} \sum_{j=1}^r d_i^j, \\ \sigma_i^2 &= \frac{1}{r-1} \sum_{j=1}^r (d_i^j - \mu_i)^2, \end{aligned} \quad (6.28a)$$

where the elementary effect associated with  $\theta_i$  of the  $j^{\text{th}}$  sample is

$$d_i^j = \frac{K(\theta^j + \Delta e_i) - K(\theta^j)}{\Delta}, \quad (6.28b)$$

---

<sup>x</sup>For example, the  $\ell$ -level sample space corresponding to  $[0, 1]$  would be  $[0, \frac{1}{\ell-1}, \frac{2}{\ell-1}, \dots, 1 - \frac{1}{\ell-1}, 1]$ .

and the step size  $\Delta$  is chosen so that  $\Delta e_i \in \Gamma_\ell$ .

The mean  $\mu_i$  quantifies the individual effect of  $\theta_i$  on the model response; however, on its own it can fail to identify an influential parameter if there are a lot of sign changes in the derivatives across the sample space. We avoid this problem by using  $\mu_i^*$  in combination with the standard deviation  $\sigma_i$ , which quantifies any nonlinearity in the response as well as any interactions with other parameters.

To obtain the Morris measures in this section, we used  $r = 40$  parameter samplings, a discretization level of  $\ell = 41$ , and a step size of  $\Delta = \frac{1}{\ell-1} = \frac{1}{40}$ . (Other values were also tried without any effect on the results.) Although the strategy described in [59] assumes that the parameters are uniformly distributed across the  $m$ -dimensional unit hypercube, the choice of density did not appear to affect our results, which is consistent with observations in [90]. We obtained the exact same results up to at least six decimal places for both the uniform distribution on the unit hypercube and the normalized parameter distributions corresponding to the results from Section 6.3.2.

Variance-based sensitivity analysis (particularly the indices proposed by Ilya Sobol' in [94]) is not only able to account for higher order interactions, but unlike the first two methods it actually provides a qualitative measure of the relative influence of each parameter. The Sobol' indices  $S_i$  (with higher order indices denoted  $S_{ij}$ , etc.) quantify the influence of each parameter  $\theta_i$  or combination of parameters on the model response in terms of the corresponding partial variances. The total sensitivity indices  $S_{T_i}$  were introduced by Homma and Saltelli to combine all the effects of a parameter  $\theta_i$  on the model response, including higher order interactions [30]. The first order sensitivity indices and total sensitivity indices are given by

$$S_i = \frac{\text{var}(\mathbb{E}(K|\theta_i))}{\text{var}(K)} \quad \text{and} \quad S_{T_i} = 1 - \frac{\text{var}(\mathbb{E}(K|\theta_{\sim i}))}{\text{var}(K)} = \frac{\mathbb{E}(\text{var}(K|\theta_{\sim i}))}{\text{var}(K)}. \quad (6.29)$$

Because the Sobol' indices represent a fractional contribution from each parameter to the total variance, all of the main effects indices and higher order indices taken together will sum to 1. Also, note that the total effects index for a given parameter will always be greater than or equal to its main effects index.

The first order and total sensitivity indices are generally estimated using Monte Carlo or quasi-Monte Carlo methods, such as Andrea Saltelli's eponymous algorithm described in [79, 80]. Following the recommendations in [80, 90], we used the updated Saltelli

Table 6.14: First order Sobol’ indices ( $S_i$ ), total Sobol’ indices ( $S_{T_i}$ ), and Morris measures ( $\mu_i^*$ ,  $\sigma_i$ ) for the front of the aspheric lens.

	$S_i$	$S_{T_i}$	$\mu_i^*$	$\sigma_i$
$c_1$	< tol	< tol	< tol	< tol
$c_4$	0.9988	0.9988	52.6856	53.2901
$c_{11}$	0.0012	0.0012	1.8000	1.8229

Table 6.15: Sobol’ indices and Morris measures for the front of the toric lens.

	$S_i$	$S_{T_i}$	$\mu_i^*$	$\sigma_i$
$c_1$	< tol	< tol	< tol	< tol
$c_4$	0.8505	0.8505	116.4786	115.5792
$c_{11}$	0.1190	0.1190	43.5637	43.6195
$c_{22}$	0.0246	0.0246	19.8123	19.9642
$c_{37}$	0.0052	0.0052	9.0835	9.1877
$c_{56}$	0.0008	0.0008	3.4606	3.5003

estimators for the main effects  $S_i$  and the Jansen estimators [40] for the total effects  $S_{T_i}$ . Although this is the most efficient algorithm for computing the Sobol’ indices, it is important to note that these estimators assume independence among the parameters so the results may be misleading for correlated inputs.

The greatest drawback to variance-based sensitivity analysis is that it is extremely computationally intensive, as the estimation of each separate index requires sufficient model evaluations to ensure coverage of the entire sample space. To improve efficiency, [80] recommends using low-discrepancy Sobol’ sequences [92, 93] rather than true random sampling.<sup>xi</sup> However, even with the use of quasi-random sampling, some of the Sobol’ analyses for the full models took over a week to run on a dedicated multicore high performance computing cluster. The ROMs required 200000–400000 iterations to converge, while the full models took much longer to run but required only 20000–30000 iterations for convergence. Convergence of the Sobol’ indices is demonstrated in Appendix C.

The Sobol’ indices and Morris measures for each of the quantities of interest are

<sup>xi</sup>The Sobol’ sequences were generated using the MATLAB command `sobolset.m`.

Table 6.16: Sobol' indices and Morris measures for the back surface of the toric lens.

	$K_{p_1}$				$K_{p_1} - K_{p_2}$			
	$S_i$	$S_{T_i}$	$\mu_i^*$	$\sigma_i$	$S_i$	$S_{T_i}$	$\mu_i^*$	$\sigma_i$
$c_1$	< tol	< tol	< tol	< tol	< tol	< tol	< tol	< tol
$c_4$	0.9574	0.9574	91.5187	92.2200	< tol	< tol	< tol	< tol
$c_6$	0.0020	0.0023	5.2880	5.3486	0.7593	0.8648	10.5760	10.6973
$c_{11}$	0.0377	0.0377	18.1528	18.3611	< tol	< tol	< tol	< tol
$c_{12}$	0.0003	0.0006	2.4645	2.4928	0.1161	0.2135	4.9291	4.9856
$c_{14}$	< tol	< tol	< tol	< tol	< tol	< tol	< tol	< tol
$c_{22}$	0.0022	0.0022	4.3499	4.3554	< tol	< tol	< tol	< tol
$c_{24}$	< tol	< tol	0.9302	0.9122	0.0160	0.0347	1.8605	1.8243
$c_{26}$	< tol	< tol	< tol	< tol	< tol	< tol	< tol	< tol
$c_{28}$	< tol	< tol	< tol	< tol	< tol	< tol	< tol	< tol
$c_{37}$	0.0001	0.0001	0.9368	0.9440	< tol	< tol	< tol	< tol
$c_{38}$	< tol	< tol	0.2295	0.2312	0.0010	0.0022	0.4589	0.4624

shown in Figures 6.26, 6.28, 6.30, 6.32, 6.34, and 6.36, for both the ROMs and the full models. The numerical values of the Sobol' indices and Morris measures obtained using the ROMs are also listed in Tables 6.14–6.17.

Immediately clear from Figures 6.25–6.36 is that we consistently obtain nearly the same sensitivity measures for the identifiable parameters regardless of whether we use the full model or the ROM. Furthermore, both the centered parameter study and Morris screening produce the same parameter rankings for every quantity of interest. In each case, the Morris measure  $\sigma_i$  is very similar to  $\mu_i^*$ , which indicates that higher order interactions among parameters do not have a significant impact on the model response.

In Figures 6.25–6.30, we can see that all three methods of sensitivity analysis lead to the same conclusions for the anterior principal curvatures  $K_a$  of both lenses as well as the maximum posterior curvature  $K_{p_1}$  of the toric lens. The Sobol' indices  $S_i$  and  $S_{T_i}$  for each of these quantities are nearly equal and the first order indices appear to sum to 1, both of which are consistent with our previous observation that there are not many higher order effects. Note that the moderate parameter correlations we observed in Section 6.3.2 for the axial elevation model do not appear to cause problems for the curvature model.

From the magnitude of the Sobol' indices we can also infer that  $c_4$  is the most in-

Table 6.17: Sobol’ indices and Morris measures of the front surface Zernike coefficients for the posterior quantities of interest of the toric lens.

	$K_{p1}$				$K_{p1} - K_{p2}$			
	$S_i$	$S_{T_i}$	$\mu_i^*$	$\sigma_i$	$S_i$	$S_{T_i}$	$\mu_i^*$	$\sigma_i$
$c_1$	0.1115	0.5541	5.6922	5.5819	0.1286	0.8754	0.4496	0.4412
$c_4$	0.3583	0.7885	21.7062	21.5445	0.1222	0.8557	1.0421	1.0350
$c_{11}$	0.0568	0.1642	6.6185	6.6268	0.0007	0.0925	0.1229	0.1233
$c_{22}$	0.0078	0.0276	3.2474	3.2725	0.0005	0.0092	0.1082	0.1093
$c_{37}$	0.0023	0.0056	1.1631	1.1769	0.0002	0.0006	0.0790	0.0800
$c_{56}$	0.0001	0.0003	0.1044	0.1057	< tol	< tol	0.0117	0.0118

fluent parameter for all three principal curvatures—in fact, it is the sole influential parameter for the principal curvature of the aspheric lens. This makes sense given that  $Z_4$  (also referred to as the “defocus” term) is the first of the rotationally symmetric polynomials in each model that does not possess zero curvature, and in each case  $c_4$  is at least one order of magnitude larger than the next largest parameter. For both toric lens curvatures, the next most influential coefficient is  $c_{11}$ , and for  $K_a$  there also appears to be a small contribution from  $c_{22}$  as well.

When looking at the effect of the front surface parameters on the two back surface responses (Figures 6.33–6.36),  $c_4$  is once again the most influential coefficient. As was the case with the anterior curvature, the values of  $c_{11}$  and  $c_{22}$  used to construct the front surface also appear to influence the posterior curvature. However, this time  $c_1$  is almost as influential as  $c_{11}$ . This is likely because  $Z_1$  (the “piston” term) governs the axial distance between the two surfaces, and this in turn will influence the radial coordinates of the dewarped points.

For the difference in posterior principal curvatures, Figures 6.31–6.32 indicate that the most influential back surface parameters are the coefficients  $c_6$ ,  $c_{12}$ , and  $c_{24}$ , respectively. Once again, we recall that these all correspond to Zernike polynomials with azimuthal degree 2, as illustrated in Table 6.4. From Figure 6.11, we can see that  $Z_6$ ,  $Z_{12}$ , and  $Z_{24}$  all share the same general saddle shape characteristic. The front surface coefficients with the most influence on this quantity of interest (Figures 6.33–6.36) appear to be  $c_4$  followed by  $c_1$ .

As evidenced by the fact that  $\sum_i S_i < 1$  and  $S_{T_i} > S_i$ , there appears to be some statistical dependence among the parameters for the front and back Zernike coefficients with regard to the posterior principal curvatures (Figures 6.32 and 6.34). Furthermore, the fact that the Sobol' rankings for the front surface coefficients do not agree with the rankings produced by the two other methods suggests an algebraic dependence among the front surface parameters.

It is also worth noting that the relative error from the parametric analysis as well as the magnitude of the Morris measures are all quite small when compared to the effect from the back surface coefficients, although this is not necessarily proof that the front coefficients exert less influence as we did not consider both sets of coefficients in the same analysis.

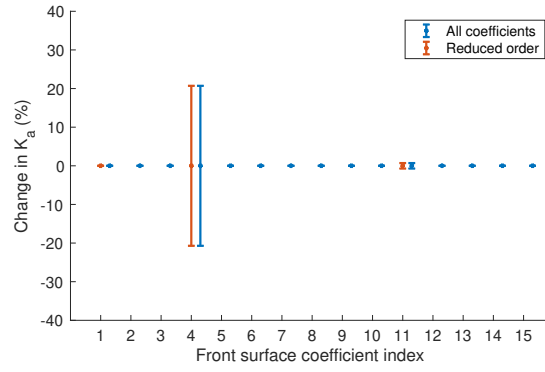


Figure 6.25: Centered parameter study for the anterior principal curvature ( $K_a$ ) of the aspheric lens.

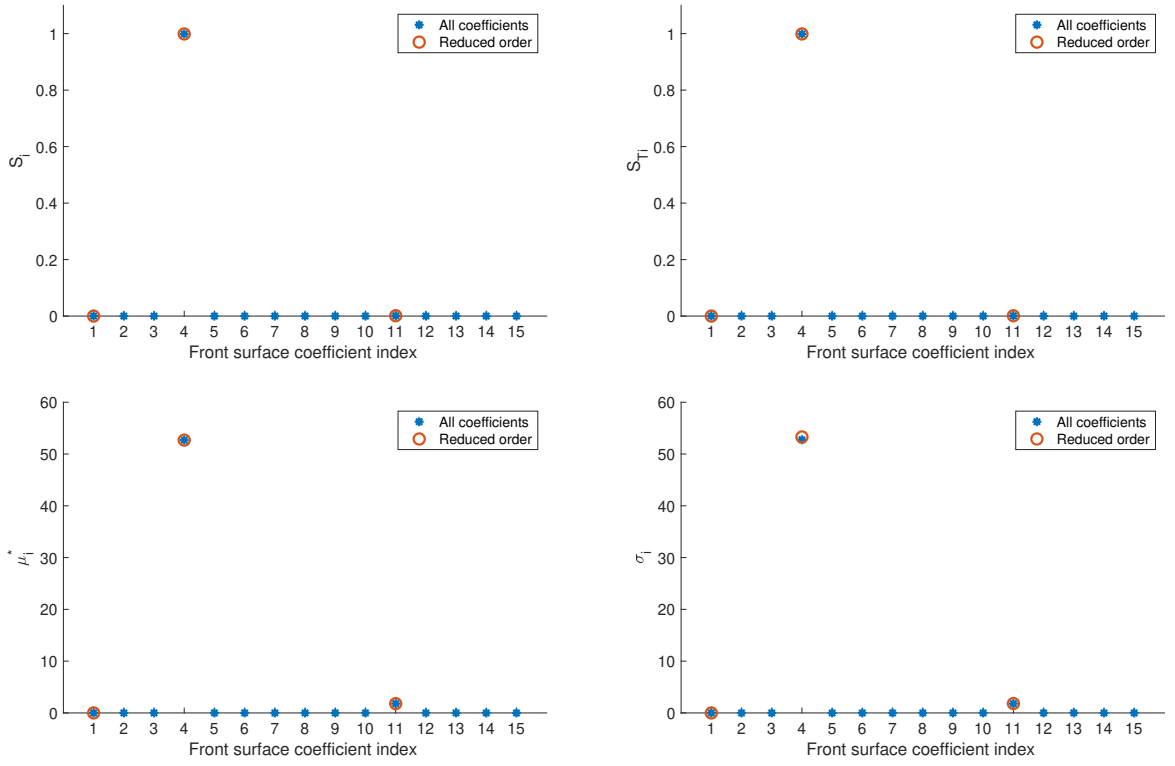


Figure 6.26: Sobol' indices ( $S_i$ ,  $S_{Ti}$ ) and Morris measures ( $\mu_i$ ,  $\sigma_i$ ) for the anterior principal curvature of the aspheric lens.

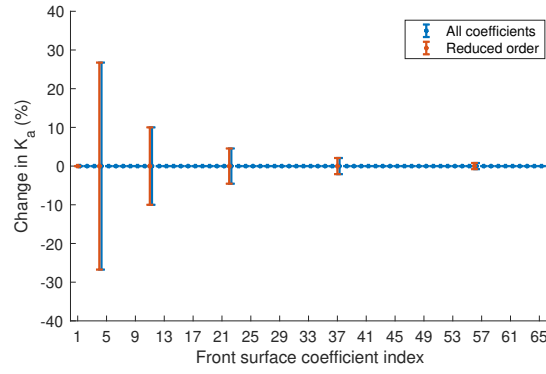


Figure 6.27: Centered parameter study for the anterior principal curvature of the toric lens.

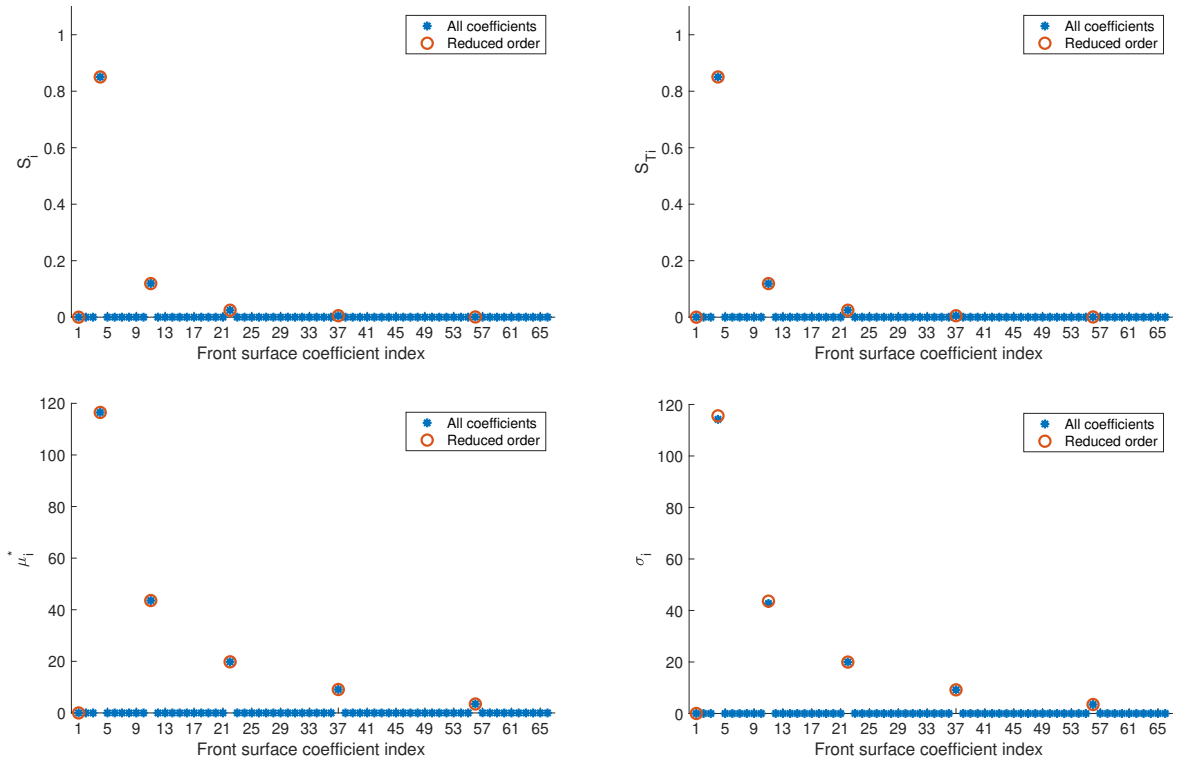


Figure 6.28: Sobol' indices and Morris measures for the anterior principal curvature of the toric lens.

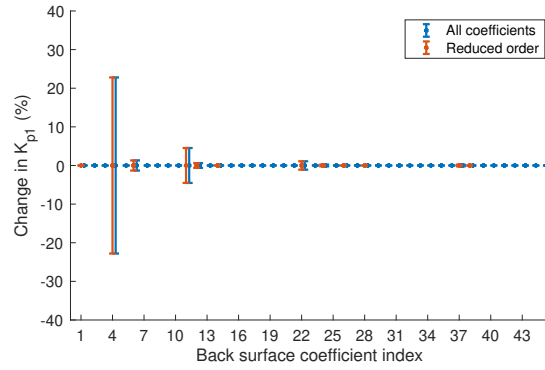


Figure 6.29: Centered parameter study of the back surface Zernike coefficients for the posterior maximum curvature ( $K_{p1}$ ) of the toric lens.

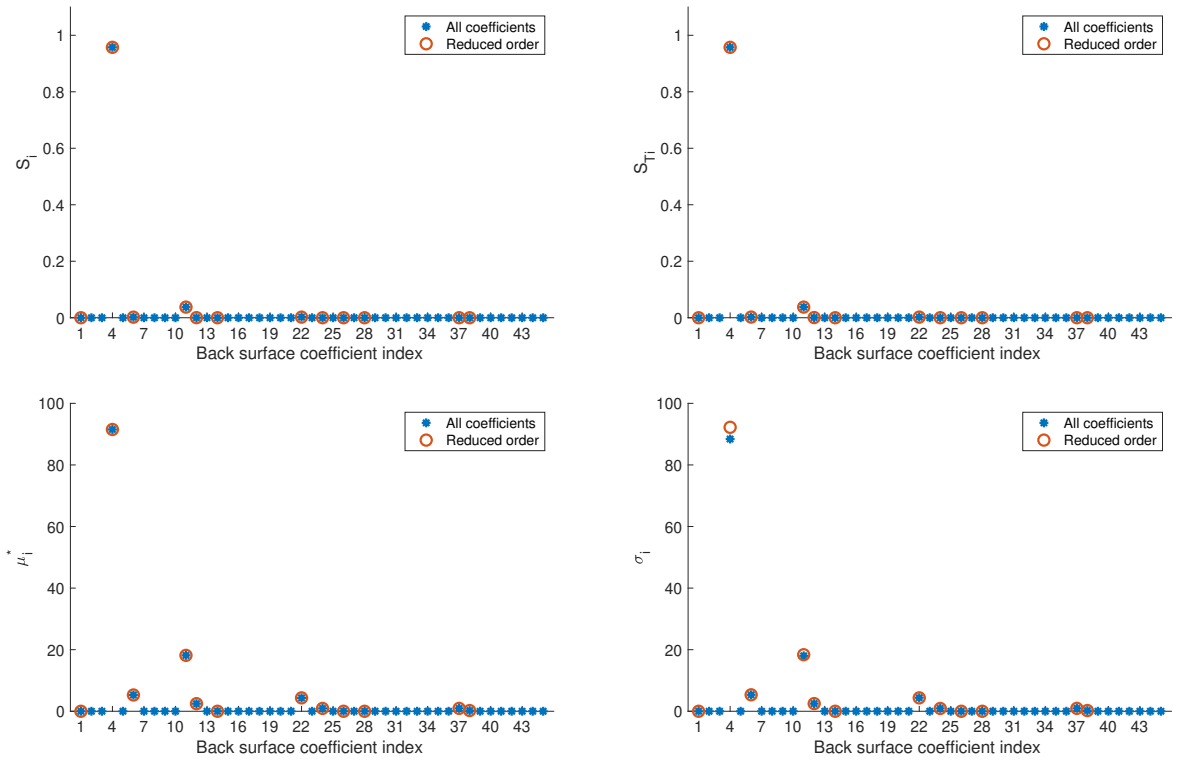


Figure 6.30: Sobol' indices and Morris measures of the back surface Zernike coefficients for the posterior maximum curvature of the toric lens.

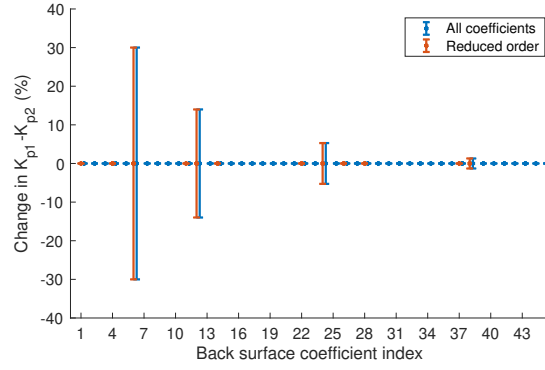


Figure 6.31: Centered parameter study of the back surface Zernike coefficients for the difference in the posterior principal curvatures ( $K_{p1} - K_{p2}$ ) of the toric lens.

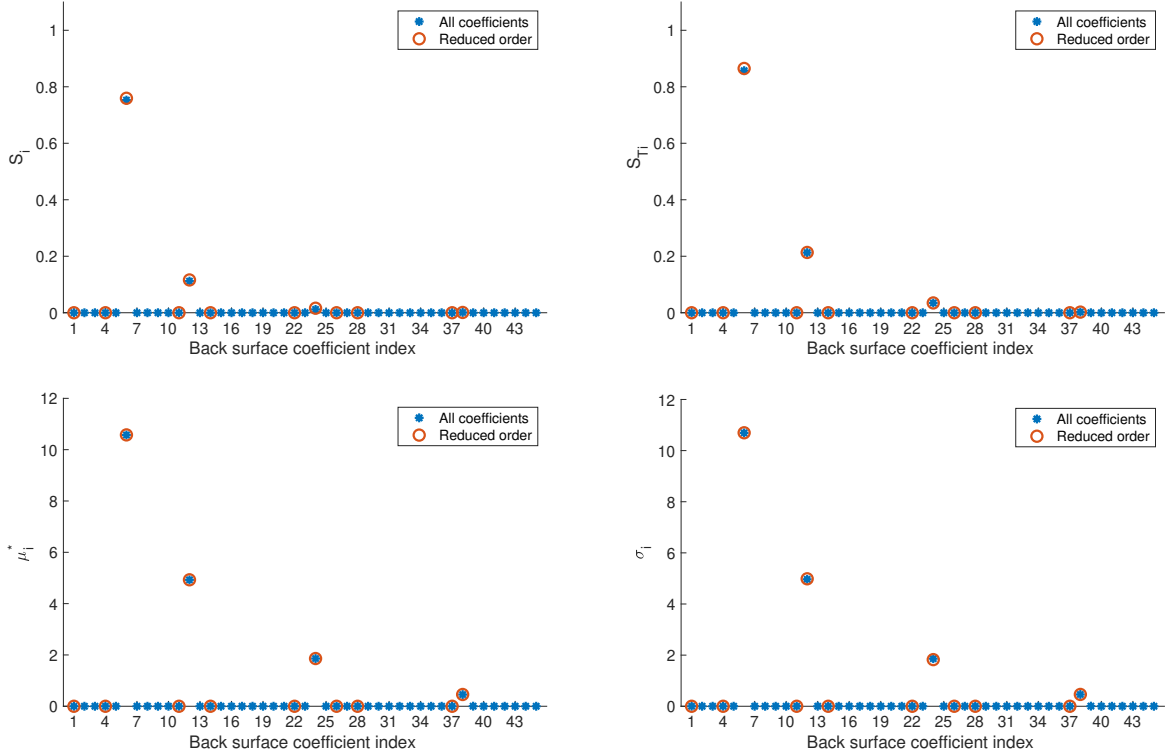


Figure 6.32: Sobol' indices and Morris measures of the back surface Zernike coefficients for the difference in the posterior principal curvatures of the toric lens.

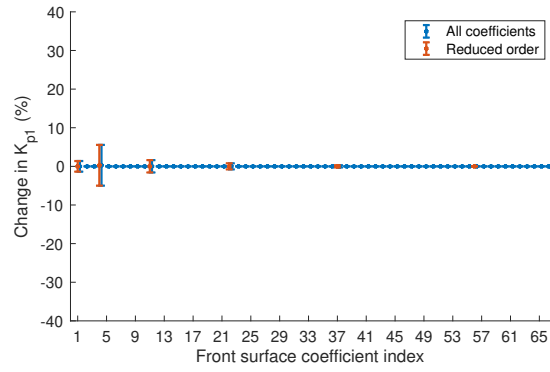


Figure 6.33: Centered parameter study of the front surface Zernike coefficients for the posterior maximum curvature of the toric lens.

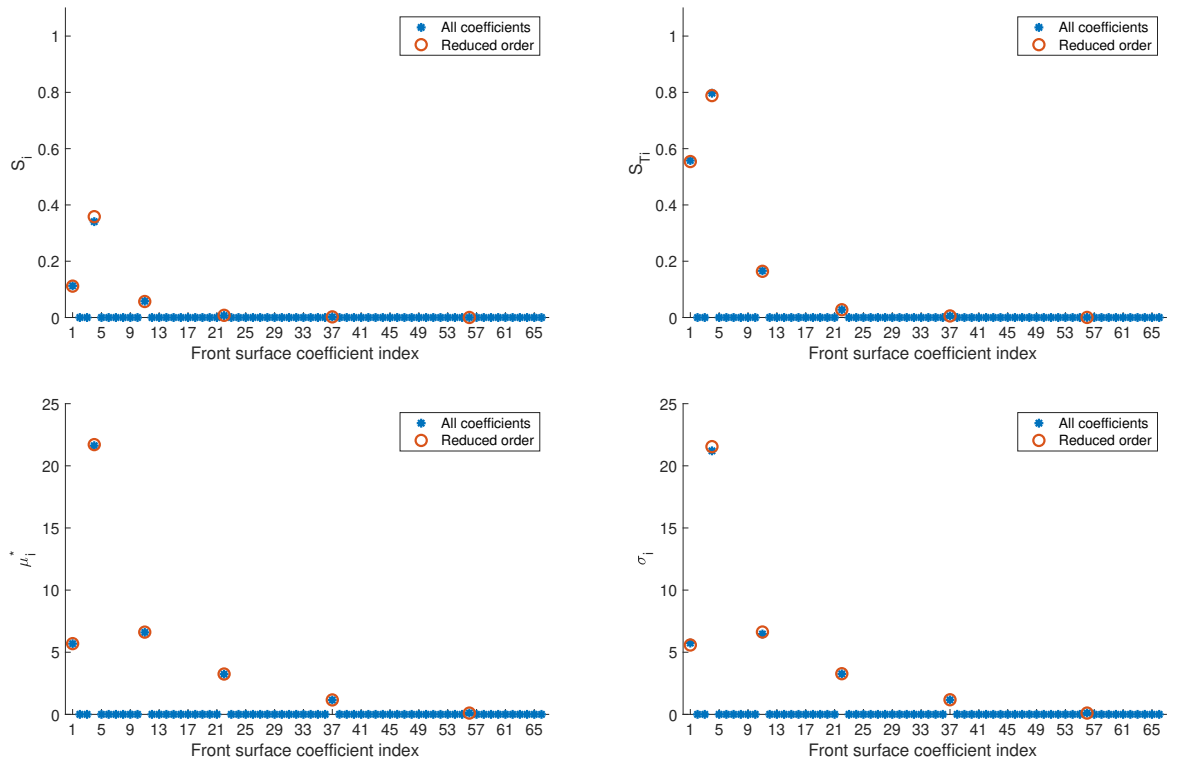


Figure 6.34: Sobol' indices and Morris measures of the front surface Zernike coefficients for the posterior maximum curvature of the toric lens.

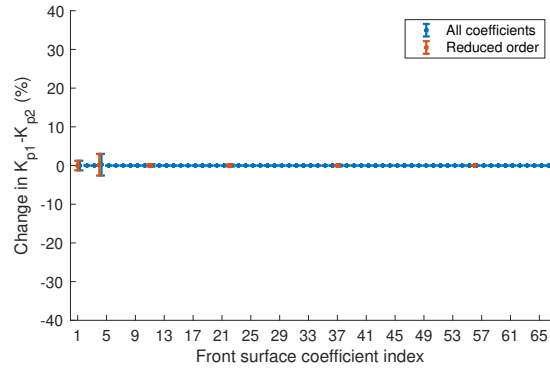


Figure 6.35: Centered parameter study of the front surface Zernike coefficients for the difference in the posterior principal curvatures of the toric lens.

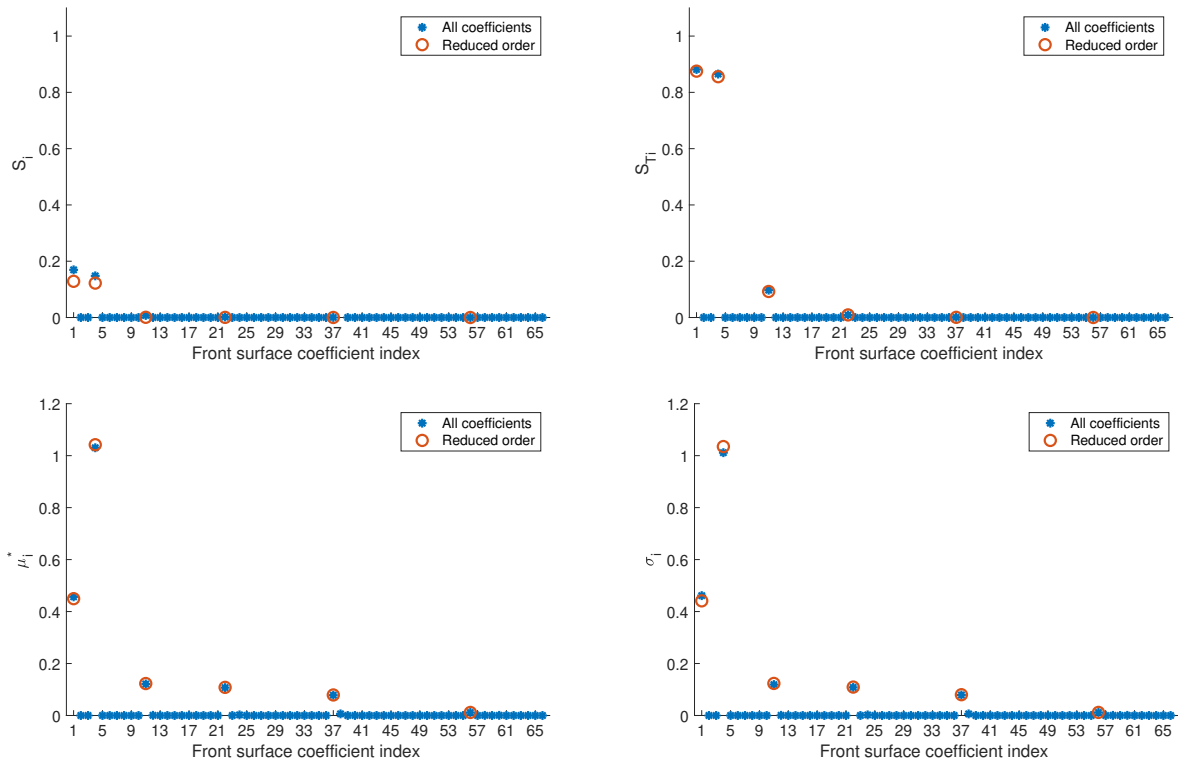


Figure 6.36: Sobol' indices and Morris measures of the front surface Zernike coefficients for the difference in the posterior principal curvatures of the toric lens.

# Chapter 7

## Discussion

In this thesis, we have investigated the propagation of error when using Zernike polynomial models for anterior and posterior corneal topography. Using synthetic point cloud data, we evaluated the suitability of each Zernike model order by considering the accuracy of not only the model fit but also the local curvature maps and principal curvatures computed from each model. We performed a similar analysis of model order in the context of a two-surface problem where the front surface model is used in correcting optical distortion in the back surface data prior to fitting those points. Although many papers have been written on Zernike model order selection for corneal surface fitting (discussed in depth in Section 3.5.1), few have rigorously focused on the accuracy of both elevation and curvature mapping. Furthermore, little previous work has been done to validate the use of Zernike elevation models for computing corneal curvature maps from OCT data, particularly for surfaces requiring refraction correction.

Table 7.2 contains a summary of the elevation and curvature errors obtained in Chapter 5 using the real OCT lens data, according to the zones described in Table 7.1. Recall that the anterior and posterior aspheric lens data were modeled using finite Zernike poly-

Table 7.1: Analysis zones used in Table 7.2.

Central zone	Middle zone	Outer zone
$\rho \leq 1.5 \text{ mm}$	$1.5 \text{ mm} < \rho \leq 3 \text{ mm}$	$\rho > 3 \text{ mm}$

Table 7.2: RMS elevation error and mean curvature error ( $\pm$  one standard deviation), and compared to quantized synthetic data using same model orders.

<b>Aspheric Lens</b>		
	Front ( $z^a \approx f_4$ )	Back ( $z^p \approx f_3$ )
RMS surface error		
Synthetic data		
Full 6 mm	0.07 $\mu\text{m}$	0.10 $\mu\text{m}$
OCT data		
Full 6 mm	0.63 $\mu\text{m}$	0.88 $\mu\text{m}$
Central zone	0.15 $\mu\text{m}$	0.28 $\mu\text{m}$
Middle zone	0.88 $\mu\text{m}$	1.22 $\mu\text{m}$
Outer zone	7.68 $\mu\text{m}$	6.65 $\mu\text{m}$
Mean curvature error		
Synthetic data		
Full 6 mm	0.00 $\pm$ 0.01 D	0.00 $\pm$ 0.01 D
OCT data		
Full 6 mm	0.07 $\pm$ 0.11 D	-0.13 $\pm$ 0.03 D
Central zone	0.07 $\pm$ 0.08 D	-0.13 $\pm$ 0.02 D
Middle zone	0.08 $\pm$ 0.13 D	-0.13 $\pm$ 0.04 D
Outer zone	0.02 $\pm$ 0.29 D	-0.13 $\pm$ 0.09 D
<b>Toric Lens</b>		
	Front ( $z^a \approx f_8$ )	Back ( $z^p \approx f_6$ )
RMS surface error		
Synthetic data		
Full 6 mm	0.72 $\mu\text{m}$	0.40 $\mu\text{m}$
OCT data		
Full 6 mm	2.20 $\mu\text{m}$	10.53 $\mu\text{m}$
Central zone	0.39 $\mu\text{m}$	5.12 $\mu\text{m}$
Middle zone	3.08 $\mu\text{m}$	13.97 $\mu\text{m}$
Outer zone	21.16 $\mu\text{m}$	37.46 $\mu\text{m}$
Mean curvature error		
Synthetic data		
Full 6 mm	0.17 $\pm$ 0.52 D	-0.04 $\pm$ 0.21 D <sup>1</sup>
OCT data		
Full 6 mm	0.01 $\pm$ 0.43 D	-0.03 $\pm$ 0.29 D
Central zone	-0.04 $\pm$ 0.41 D	-0.09 $\pm$ 0.22 D
Middle zone	0.06 $\pm$ 0.45 D	0.04 $\pm$ 0.34 D
Outer zone	-1.62 $\pm$ 3.23 D	0.43 $\pm$ 1.49 D

<sup>1</sup> The curvature error over the 6 mm using the quantized synthetic data for the posterior toric lens without warping was  $-0.05 \pm 0.22$  D.

nomial expansions of order  $N_a = 4$  and  $N_p = 3$ , while the Zernike orders for the toric lens were  $N_a = 8$  and  $N_p = 6$ . The diameter of the full circular region used in surface fitting was 15 mm for the anterior and posterior aspheric lens, 14 mm for the anterior toric lens, and 13.1 mm for the posterior toric lens.

As we observed in Section 5.3, the error in both the surface fit and curvature are substantially greater in the outer zone due to a combination of increased noise in the segmentation data and the edge effects noted in Section 3.5. Furthermore, it is not unusual for researchers to restrict the region of interest to the central 6 mm zone when evaluating the accuracy of corneal topography [70, 99, 110]. To facilitate comparisons, we have included in Table 7.2 the RMS elevation error and mean curvature error across this central 6 mm region. We have also included the elevation and curvature errors from the quantized synthetic data described in Chapters 3 and 4—using the same Zernike elevation models as the real data—to illustrate a possible bound on the accuracy of this computation.

For the anterior aspheric lens, the RMS error across the 6 mm region between the fitted Zernike model and the design surface was  $0.63\ \mu\text{m}$ , which is actually slightly *lower* than the manufacturer’s specified tolerance of  $0.75\ \mu\text{m}$  [65]. The error for the posterior aspheric lens was only slightly greater at  $0.88\ \mu\text{m}$ . The RMS elevation error for the toric lens was at least one order of magnitude higher, at  $2.20\ \mu\text{m}$  and  $10.53\ \mu\text{m}$  for the front<sup>i</sup> and back surfaces, respectively. These errors are considerably smaller than the difference between corneal elevation maps produced by OCT and Scheimpflug imaging—in one study, the RMS of this difference was measured at 0.04 mm for the anterior corneal surface and 0.06 mm for the posterior surface [99]. Our results are also in line with [70], in which OCT data from a reference sphere and an aspheric surface were each fit to a conic of revolution, resulting in RMS surface errors of  $0.8\ \mu\text{m}$  and  $2.6\ \mu\text{m}$ , respectively. In terms of relative errors,<sup>ii</sup> our results correspond to an error of about 0.005% for the anterior aspheric lens, 0.03% for the anterior toric lens, and 0.12% for the posterior toric lens, whereas the relative errors for the sphere and asphere in [70] were about 0.003% and 0.03%. Note that we expected the error in the posterior toric lens to be higher than the other surfaces due to the propagation of error from the front surface during dewarping.

---

<sup>i</sup>Recall that the anterior surface of the toric lens is spherical.

<sup>ii</sup>In the same manner described in [52], we determined the relative error by dividing the RMS error by the design value of the principal radius of curvature (or, in the case of the posterior toric lens, the average of the two principal radii).

Restricting the region of interest to the central 6 mm also results in considerable improvements to the meridional curvature maps. For both surfaces of the aspheric lens, the interval  $[\mu - \sigma, \mu + \sigma]$  is well within  $\pm 0.25$  D, and the  $3\sigma$  interval—which contains 99.7% of the measurements—is within half a diopter of the true curvature. The results for the toric lens are not quite as accurate, with only one standard deviation (about 68% of the measurements) falling within 0.5 D of the true curvature for the front surface, and roughly  $1.5\sigma$  ( $\sim 87\%$  of the measurements) doing the same for the back surface. However, these errors are comparable to—and, in some cases, better than—the errors for the quantized synthetic data over the same region.

The relatively high curvature error in both cases is caused by the unavoidable oscillations that arise when using Zernike polynomials to fit a spherical or spheroidal surface, as Zernike polynomials are only intended to model aberrations from a sphere rather than a sphere itself. Furthermore, as we saw in Section 6.4, the credible intervals for the curvature in the central zone are quite large for both toric lens surfaces, indicating that the error in the initial fit is amplified by the local curvature calculation. However, it is interesting to note that while error propagation from the anterior toric lens showed a pronounced effect on the posterior surface fit, the standard error in the posterior curvature map from the OCT data is only a bit worse than the error we obtained using synthetic data with no warping effects.

Corneal elevation maps from Zernike polynomials are typically displayed relative to a curved reference surface in order to equalize the dynamic range between largest height values near the apex of the eye and much smaller values near the periphery [84]. Due to the approximately spherical shape of the central cornea, a sphere is a popular choice of reference surface. Subtracting the best fit sphere from our point cloud data prior to Zernike polynomial fitting (and then adding it back for the final model) would likely mitigate some of the oscillation in the model. However, while this would help in the case of a surface that is close to spherical, it is not necessarily beneficial for other types of surfaces. For example, applying this to the anterior asphere data actually made our results substantially worse.

Our approach to mapping local curvature is similar to the one used in [52, 55], although neither paper addresses the local accuracy of their curvature maps. Both studies also used analytic differentiation of the Zernike polynomials to compute the curvatures. We do not believe that the numerical differentiation used in this thesis is a major contrib-

Table 7.3: Principal radii of curvature and central thickness ( $t_C$ ) in millimeters, from synthetic data with quantization error (QE) and from real data.

	Aspheric lens		Toric lens			
	$R_a$	$t_C$	$R_a$	$R_{p_1}$	$R_{p_2}$	$t_C$
Design value	13.255	4.0	7.800	9.200	8.400	1.500
Synthetic data (QE) <sup>1</sup>	13.264	—	7.932	9.154	8.337	—
Real data <sup>2</sup>	13.221	4.0	7.826	9.115	8.406	1.500
Real data (BFC to Zernike) <sup>3</sup>	13.221	—	7.814	9.115	8.416	—
Real data (BFC to data) <sup>4</sup>	13.135	—	7.795	9.015	8.573	—

<sup>1</sup> Note that the estimates for the non-quantized synthetic data were comparable.

<sup>2</sup>  $R_a$  is the mean value of the meridional radii of curvature at the lens vertex.

<sup>3</sup> Best fit conic (or biconic) from the central 6 mm of the Zernike elevation maps.

<sup>4</sup> Best fit conic (or biconic) from the central 6 mm of corrected point cloud data.

utor to our overall curvature error; however, using the pre-computed analytic derivatives for each Zernike mode would be more computationally efficient as it would reduce the number of required model evaluations.

The principal radii of curvature for the two lenses—from the real data as well as the quantized synthetic data—are depicted in Table 7.3. Both values for the anterior radius  $R_a$  from the real data have been approximated by the mean radius of curvature at the lens vertex after realignment. The posterior aspheric lens is flat—*i.e.*, its radius of curvature is infinite—so it was omitted from the table. We have also included the central thickness estimates ( $t_C$ ) from real data. Notably, both of our thickness measurements agreed with their design values to within the specified number of significant figures.

Before comparing our results to other published values, it is important to point out a difference in how they were computed. We are using the Zernike representation of the lens surface to estimate the location of the lens vertex and compute the maximum and minimum meridional radii of curvature at that point (this is also the method advocated in [55]). Currently, the standard practice for calculating the radius (or radii) of curvature for a corneal surface is using an ordinary least squares fit to a conic or biconic of rotation [62, 87]. The biconic model allows for a surface that is not axially symmetry, such as an

astigmatic cornea or the posterior surface of the toric lens, and has the form

$$z - z_0 = \frac{\frac{1}{R_x}(x - x_0)^2 + \frac{1}{R_y}(y - y_0)^2}{1 + \sqrt{1 - \frac{1+\kappa_x}{R_x^2}(x - x_0)^2 - \frac{1+\kappa_y}{R_y^2}(y - y_0)^2}}, \quad (7.1)$$

where  $R_x$ ,  $R_y$  are the principal radii of curvature, and  $\kappa_x$ ,  $\kappa_y$  are essentially conic constants. To obtain the conic model, simply set  $R_x = R_y$  and  $\kappa_x = \kappa_y$  in (7.1). Both the conic and biconic models rely on assumptions about the symmetry of the surface being measured—assumptions that may be reasonable for a healthy cornea, but are less accurate when modeling a surface with significant irregularity [34, 62]. However, for the sake of comparison, we have included in Table 7.3 the values for the principal radii of curvature obtained by fitting the central 6 mm of the sampled points from the Zernike elevation models to either a conic (for the two anterior surfaces) or a biconic (for the posterior toric lens). We have also included the results of fitting just the central 6 mm of point cloud data after refraction correction has been applied to the posterior toric lens surface. We performed these fits using the MATLAB function `lsqcurvefit.m`. All of the published results referenced below were obtained using a similar approach.

Using the methods described in Chapter 3, we computed the mean value of the anterior principal radii of the aspheric lens to be 13.221 mm (range: 13.168–13.274 mm), which differs from the design value of 13.255 mm by  $0.034 \pm 0.053$  mm. We obtained the same value using the best fit conic to the Zernike map. For the anterior toric lens, the mean value of meridional radius of curvature at the lens vertex was 7.826 mm (7.810–7.841 mm), for an error of  $0.026 \pm 0.015$  mm, while the best fit conic yielded a slightly better estimate of 7.815 mm. The synthetic aspheric lens data provided a better estimate of  $R_a$  than the OCT data using the same Zernike model order, with an error of only 0.009 mm. However, at 0.132 mm the error for the synthetic toric lens data was an entire order of magnitude worse than for either of the estimates from the real toric lens data. These estimates are comparable in accuracy to other anterior radius of curvature measurements from OCT of imaging phantoms. Reported errors in the measured value of  $R_a$  from OCT include: 0.02–0.04 mm for three calibration spheres [48], 0.03 mm for the PMMA cornea of a water cell model eye [68, 69],  $0.05 \pm 0.03$  mm for repeated measurements of a rigid gas permeable contact lens [110], and  $0.12 \pm 0.08$  mm for repeated measurements of the calibration sphere in [70].

For the toric lens, the maximum and minimum posterior radii ( $R_{p_1}$ ,  $R_{p_2}$ ) were 9.115 mm

and 8.406 mm when measured from OCT data using the method described in this thesis, versus 9.154 mm and 8.337 mm from the synthetic data using the same Zernike surface model. The error in  $R_{p_1}$  for the real data, 0.085 mm, is about twice that of the synthetic data, 0.046 mm. However, the estimate for  $R_{p_2}$  is actually an order of magnitude better when using the real data versus the synthetic data, with respective errors of 0.006 mm and 0.063 mm. Using the biconic fit to the Zernike maps, we obtained the same value for  $R_{p_1}$  and a slightly worse estimate of  $R_{p_2}$  (8.416 mm). In comparison, the PMMA cornea in [69] had a posterior radius of curvature error of 0.13 mm, while the error for the contact lens in [110] was  $0.03 \pm 0.02$  mm. Additionally, the base curvatures of six other contact lenses were measured to within 0.02 mm using OCT in [48].

Despite concerns regarding their suitability for modeling every possible type of eye condition [91], Zernike polynomials remain widely used within the field of ophthalmology [103]. While their primary application has been quantifying wavefront errors, they are gaining popularity as a basis for modeling corneal surfaces [91]. The Zernike coefficients from elevation mapping do not necessarily correspond to those of wavefront aberrometry, and have instead taken on their own significance: these coefficients have been used to evaluate the success of optical distortion correction [70] and determine correlations between the strength of certain aberrations in different surfaces of the same eye (including both the cornea and crystalline lens) [71], as well as simply reported along with other biometrics [99].

One of the drawbacks to using Zernike coefficients as a diagnostic tool, however, is that their magnitude—and even their relative importance—is entirely dependent on the value used to normalize the radial coordinate  $\rho$ . The coefficients also depend on the orientation of the surface [62]. Furthermore, the choice of normalization constant is not standardized. It is common in wavefront aberrometry to use the radial extent of the entrance pupil, but even this can vary from person to person, making it difficult to compare Zernike coefficients from different eyes [83]. For a surface such as a lens, it is even less clear what value to choose for this purpose. Although we did not find that the accuracy of our fit or curvature estimates was affected by the scaling parameter, the fact that we did not use the same value for all the lens surfaces means that we cannot compare the estimates of their Zernike coefficients. Nor can we conclude that the values obtained in Section 6.3.2 have any sort of absolute significance, even relative to other coefficients for the same surface. Because scaling does *not* affect the azimuthal component, Zernike polynomials

can be grouped into “families” of related aberrations that share the same frequency. For example,  $Z_5$ ,  $Z_6$ ,  $Z_{12}$ , and  $Z_{13}$ —whose azimuthal parts are either  $\sin 2\theta$  or  $\cos 2\theta$ —are all types of astigmatism. While the precise contribution of each term will depend on the scaling, there will still be a collective contribution of astigmatism to the overall surface shape. We saw this in Section 6.5, where our quantities of interest tended to be sensitive to Zernike coefficients belonging to the same family. However, a different scaling could change the relative rankings of the coefficients within each family. The adoption of a more rigorous criterion for selecting the radial scaling parameter would make this sort of sensitivity analysis more meaningful.

It is common for clinicians and researchers to consider only lower order corneal aberrations for diagnostic purposes. While the results of our sensitivity analysis suggest that this may be valid for certain quantities of interest like principal curvature, higher order Zernike aberrations that have no individual clinical significance may still impact vision in nontrivial ways [84, 91]. To evaluate this, the global sensitivity analysis techniques discussed in Section 6.5 could be applied to other shape descriptors such as the conic constants  $\kappa_x$ ,  $\kappa_y$  in the biconic fit (7.1), or to corneal biometrics like the combined refractive power of both surfaces. Another application of the model calibration techniques in Chapter 6 would be to treat the refractive indices of the lens and saline as parameters rather than fixed inputs in order to evaluate their contribution to model uncertainty. Ideally, we would also perform these analyses on real OCT data.

There are several areas to consider when trying to improve the accuracy of our elevation and curvature estimates from OCT imaging: the data collection stage, the image processing stage, and the modeling stage. Only the final stage has been discussed in this thesis. However, the accuracy of our models is limited by the quality of the data, so improvements in the first two stages would have a significant impact on our results. While the image resolution is fixed for a given SDOCT system, it is possible to reduce the vertical pixel spacing by padding the spectral range of scanner’s light source during data collection, thereby reducing the magnitude of the quantization error. The use of 3D algorithms for image segmentation and outlier removal, such as the methods described in [66], could possibly reduce the edge detection failure rate and eliminate the need for visual inspection to identify B-scans with problematic segmentation results (see Section 2.2.2). This sort of approach could also help remove some of the biased noise that prevented us from using the OCT data in our uncertainty analysis.

One mathematical technique that would likely improve the curvature estimates would be using a different cost function other than the sum of squares error when fitting the data. While ordinary least squares worked well for the aspheric lens, the OLS models for the toric lens were highly oscillatory and therefore far less accurate in their first and second derivative estimates across the entire surface. Adding penalty terms to the cost function that address sign changes in these derivatives would help reduce the overall error in the curvature. Weighting functions could also be considered to minimize oscillations in specific areas of concern. Such an approach would also improve the accuracy of the dewarping algorithm—which depends heavily on the anterior surface gradient—thereby leading to an improved posterior surface fit. Similar reasoning involving the importance of local curvature accuracy has so far motivated the development of at least one promising algorithm for fitting Zernike polynomials to point cloud data [32].

Other projects we are currently working on that are related to the material presented in this thesis include methods for correcting the misalignment in off-axis imaging (see [28]) and 3D pachymetry mapping.

## REFERENCES

- [1] W. Alkhalidi, D.R. Iskander, and A.M. Zoubir. Model-order selection in Zernike polynomial expansion of corneal surfaces using the efficient detection criterion. *IEEE Transactions on Biomedical Engineering*, 57:2429–2437, October 2010.
- [2] R. Allemang, M.M. Kolluri, M. Spottswood, and T. Eason. Decomposition-based calibration/validation metrics for use with full-field measurement situations. *The Journal of Strain Analysis for Engineering Design*, 51(1):14–31, September 2015.
- [3] R. Anchini, C. Liguori, and A. Paolillo. Evaluation of the uncertainty of edge-detector algorithms. *IEEE Transactions on Instrumentation & Measurement*, 56(3):681–688, 2007.
- [4] D. Anderson. Understanding corneal topography. *Paraoptometric Resource Center*.
- [5] *Corneal Topography Systems — Standard Terminology, Requirements*. ANSI Z80.23-2008.
- [6] *Methods for Reporting Optical Aberrations of Eyes*. ANSI Z80.28-2017.
- [7] M.C. Arbelaez, C. Vidal, and S. Arba-Mosquera. Clinical outcomes of corneal vertex versus central pupil references with aberration-free ablation strategies and LASIK. *Investigative Ophthalmology & Visual Science*, 49(12):5287–5294, 2008.
- [8] G.E.B. Archer, A. Saltelli, and I.M. Sobol. Sensitivity measures, ANOVA-like techniques and the use of bootstrap. *Journal of Statistical Computation & Simulation*, 58(2):99–120, 1997.
- [9] H.T. Banks, M. Davidian, J. Samuels, and K. Sutton. *An Inverse Problem Statistical Methodology Summary*, pages 249–302. Springer, June 2009.
- [10] J.M. Bardsley. MCMC-based image reconstruction with uncertainty quantification. *SIAM Journal on Scientific Computing*, 34(3):A1316–A1332, 2012.
- [11] M. Born and E. Wolf. *Principles of Optics*. Cambridge University Press, 7th edition, 1999.
- [12] J. Chang and J. Fisher. Efficient MCMC sampling with implicit shape representations. In *Proceedings. IEEE Computer Society Conference on Computer Vision & Pattern Recognition*, pages 2081–2088, June 2011.
- [13] A.E. Conrady and R. Kingslake. *Applied Optics & Optical Design*. Dover Books on Physics. Dover, New York, NY, 1957.

- [14] Ohara Corporation. [manufacturer specification sheet for L-BAL35]. <https://www.oharacorp.com/pdf/elbal35.pdf>. Accessed on 2018-08-14.
- [15] B. Davidson and J. Barton. Application of optical coherence tomography to automated contact lens metrology. *Journal of Biomedical Optics*, 15, January 2010.
- [16] X. Ding, Q. Wang, P. Chang, J. Li, G. Savini, J. Huang, S. Huang, Y. Zhao, N. Liao, L. Lin, X. Yu, and Y. Zhao. The repeatability assessment of three-dimensional capsule-intraocular lens complex measurements by means of high-speed swept-source optical coherence tomography. *PLOS ONE*, 10(11):1–14, November 2015.
- [17] C. Du, M. Shen, M. Li, D. Zhu, M.R. Wang, and J. Wang. Anterior segment biometry during accommodation imaged with ultralong scan depth optical coherence tomography. *Ophthalmology*, 119(12):2479–2485, 2012.
- [18] C. Du, J. Wang, L. Cui, M. Shen, and Y. Yuan. Vertical and horizontal corneal epithelial thickness profiles determined by ultrahigh resolution optical coherence tomography. *Cornea*, 31:1036–43, February 2012.
- [19] Edmund Optics. *All About Aspheric Lenses*. <https://www.edmundoptics.com/resources/application-notes/optics/all-about-aspheric-lenses>.
- [20] L. Euler. Recherches sur la courbure des surfaces. *Mémoires de l'Académie des Sciences de Berlin*, 16:119–143, 1760.
- [21] M.A. Fischler and R.C. Bolles. Random sample consensus: A paradigm for model fitting with applications to image analysis and automated cartography. *Communications of the ACM*, 24(6):381–395, June 1981.
- [22] P. Fricker. Analyzing LASIK optical data using Zernike functions. Webpage, MathWorks, 2008. <https://www.mathworks.com/company/newsletters/articles/analyzing-lasik-optical-data-using-zernike-functions.html>. Accessed: May 10, 2018.
- [23] M.W. Fung, D. Raja, P. Fedor, and S.C. Kaufman. Corneal topography and imaging. <http://emedicine.medscape.com/article/1196836>. Updated March 17, 2016.
- [24] G.J. Gbur. *Mathematical Methods for Optical Physics and Engineering*. Cambridge University Press, 2011.
- [25] H. Haario, M. Laine, and A. Mira. DRAM: Efficient adaptive MCMC. *Statistics & Computing*, 16(4):339–354, 2006.

- [26] H. Haario, E. Saksman, and J. Tamminen. An adaptive Metropolis algorithm. *Bernoulli*, 7:223–242, April 2001.
- [27] W. Harris. Optical axes of eyes and other optical systems. *Optometry & Vision Science*, 86:537–541, May 2009.
- [28] R.H. Hart, E.L. Buckland, M.R. Mendlow, M. Haider, D.M. Branco, and A. Pavaskar. Systems for off-axis imaging of a surface of a sample and related methods and computer program products. International patent application W02020191148. Filed March 19, 2020.
- [29] J.C. He and J. Wang. Measurement of wavefront aberrations and lens deformation in the accommodated eye with optical coherence tomography-equipped wavefront system. *Optics Express*, 22(8):9764–9773, April 2014.
- [30] T. Homma and A. Saltelli. Importance measures in global sensitivity analysis of nonlinear models. *Reliability Engineering & System Safety*, 52(1):1–17, 1996.
- [31] D. Huang, E.A. Swanson, C.P. Lin, J. Schuman, W.G. Stinson, W. Chang, M. Hee, T. Flotte, K. Gregory, C.A. Puliafito, and J.G. Fujimoto. Optical coherence tomography. *Science*, 254:1178–1181, January 1991.
- [32] D. Ibáñez, J. Gómez-Pedrero, J. Alonso, and J. Quiroga. Robust fitting of Zernike polynomials to noisy point clouds defined over connected domains of arbitrary shape. *Optics Express*, 24:5918–5933, 03 2016.
- [33] I.C.F. Ipsen. *Numerical Matrix Analysis: Linear Systems and Least Squares*. SIAM, 2009.
- [34] D.R. Iskander, M.J. Collins, and B.A. Davis. Optimal modeling of corneal surfaces with Zernike polynomials. *IEEE Transactions on Biomedical Engineering*, 48(1):87–95, 2001.
- [35] *Ophthalmic instruments — Ophthalmometers*. ISO 10343:2014.
- [36] *Ophthalmic optics — Contact lenses — Part 1: Vocabulary, classification system and recommendations for labelling specifications*. ISO 18369-1:2017.
- [37] *Ophthalmic instruments — Corneal topographers*. ISO 19980:2012.
- [38] *Optics and optical instruments — Ophthalmology — Graduated dial scale*. ISO 8429:1986.
- [39] J.A. Izatt, M. Zhao, and A.N. Kuo. Methods and computer program products for quantitative three-dimensional image correction and clinical parameter computation in optical coherence tomography. U.S. Patent 9,384,582. July 5, 2016.

- [40] M.J.W. Jansen. Analysis of variance designs for model output. *Computer Physics Communications*, 117(1):35–43, 1999.
- [41] J. Kaipio and E. Somersalo. *Statistical and Computational Inverse Problems*. Springer, 2005.
- [42] B. Kamgar-Parsi and B. Kamgar-Parsi. Evaluation of quantization error in computer vision. *IEEE Transactions on Pattern Analysis & Machine Intelligence*, 11(9):929–940, 1989.
- [43] C.T. Kelley. *Solving Nonlinear Equations with Newton’s Method*. Fundamentals of Algorithms. Society for Industrial and Applied Mathematics, 2003.
- [44] S.A. Klein. Corneal topography: A review, new ANSI standards and problems to solve. In *Vision Science and its Applications*, page NW8. Optical Society of America, 2000.
- [45] S.A. Klein and R.B. Mandell. Shape and refractive powers in corneal topography. *Investigative Ophthalmology & Visual Science*, 36(10):2096–2109, 1995.
- [46] M.M. Kolluri. Developing a validation metric using image classification techniques. Master’s thesis, University of Cincinnati, 2014.
- [47] A. Kuo, P. Verkicharla, R.P. McNabb, C. Cheung, S. Hilal, S. Farsiu, C. Chen, T.Y. Wong, K. Ikram, C. Cheng, T. Young, S.M. Saw, and J. Izatt. Posterior eye shape measurement with retinal OCT compared to MRI. *Investigative Ophthalmology & Visual Science*, 57:OCT196–OCT203, July 2016.
- [48] A.N. Kuo, R.P. McNabb, M. Zhao, F. LaRocca, S.S. Stinnett, S.Farsiu, and J.A. Izatt. Corneal biometry from volumetric SDOCT and comparison with existing clinical modalities. *Biomedical Optics Express*, 3(6):1279–1290, June 2012.
- [49] M. Laine. MCMC toolbox for matlab. Webpage, 2006. <https://mjlaine.github.io/mcmcstat/#orgb0c2686>. Accessed: May 5, 2020.
- [50] Leica Microsystems, Inc. [Sales sheet for Envisu S4410 SDOCT for Contact Lens Metrology]. <http://www.bioptigen.com/products/b-envisutm-s4410-for-contact-len-metrology/>. Accessed: August 8, 2018.
- [51] Leica Microsystems, Inc. *Vistakon R4410 OCT Metrology System with Temperature Chamber User Manual*, June 2016. Revision C-00.
- [52] A.S. Liu, D.M. Brown, R.E. Conn, R.P. McNabb, M.T. Pardue, and A.N. Kuo. Topography and pachymetry maps for mouse corneas using optical coherence tomography. *Experimental Eye Research*, 190, 2020.

- [53] D. Malacara. *Optical Shop Testing*. Wiley-Interscience, 3rd edition, 2007.
- [54] R.P. McNabb, S. Farsiu, S. Stinnett, J. Izatt, and A. Kuo. Optical coherence tomography accurately measures corneal power change from laser refractive surgery. *Ophthalmology*, 122, December 2014.
- [55] R.P. McNabb, A.N. Kuo, and J.A. Izatt. Quantitative single and multi-surface clinical corneal topography utilizing optical coherence tomography. *Optics Letters*, 38(8):1212–1214, April 2013.
- [56] R.P. McNabb, F. LaRocca, S. Farsiu, A.N. Kuo, and J.A. Izatt. Distributed scanning volumetric SDOCT for motion corrected corneal biometry. *Biomedical Optics Express*, 3(9):2050–2065, September 2012.
- [57] R.P. McNabb, J. Polans, B. Keller, M. Jackson-Atogi, C. James, R. Vann, J. Izatt, and A. Kuo. Wide-field whole eye OCT system with demonstration of quantitative retinal curvature estimation. *Biomedical Optics Express*, 10:338–355, January 2019.
- [58] C.D. Meyer. *Matrix Theory and Applied Linear Algebra*. SIAM, 2000.
- [59] M.D. Morris. Factorial sampling plans for preliminary computational experiments. *Technometrics*, 33(2):161–174, 1991.
- [60] S.A. Mosquera, S. Verma, and C. McAlinden. Centration axis in refractive surgery. *Eye & Vision*, 2, February 2015.
- [61] M. Muma and A. Zoubir. Robust model order selection for corneal height data based on  $\tau$  estimation. In *2011 IEEE International Conference on Acoustics, Speech & Signal Processing (ICASSP)*, pages 4096–4099, June 2011.
- [62] R. Navarro. The optical design of the human eye: a critical review. *Journal of Optometry*, 2(1):3–18, 2009.
- [63] R. Navarro, J. Arines, and R. Rivera. Direct and inverse discrete Zernike transform. *Optics Express*, 17(26):24269–24281, December 2009.
- [64] R.J. Noll. Zernike polynomials and atmospheric turbulence. *Journal of the Optical Society of America*, 66(3):207–211, March 1976.
- [65] Edmund Optics. [Technical specifications for aspheric lens #47-728]. <https://www.edmundoptics.com/optics/optical-lenses/aspheric-lenses/15mm-dia.-0.33-numerical-aperture-uncoated-aspheric-lens/>. Accessed: April 19, 2018.

- [66] S Ortiz, P. Pérez-Merino, N. Alejandre, E. Gamba, I. Jimenez-Alfaro, and S. Marcos. Quantitative OCT-based corneal topography in keratoconus with intracorneal ring segments. *Biomedical Optics Express*, 3:814–824, May 2012.
- [67] S. Ortiz, P. Pérez-Merino, S. Durán, M. Velasco-Ocana, J. Birkenfeld, A. de Castro, I. Jiménez-Alfaro, and S. Marcos. Full OCT anterior segment biometry: An application in cataract surgery. *Biomedical Optics Express*, 4:387–96, March 2013.
- [68] S. Ortiz, P. Pérez-Merino, E. Gamba, A. de Castro, and S. Marcos. In vivo human crystalline lens topography. *Biomedical Optics Express*, 3:2471–2488, October 2012.
- [69] S. Ortiz, D. Siedlecki, I. Grulkowski, L. Remon, D. Pascual, M. Wojtkowski, and S. Marcos. Optical distortion correction in optical coherence tomography for quantitative ocular anterior segment by three-dimensional imaging. *Optics Express*, 18(3):2782–2796, February 2010.
- [70] S. Ortiz, D. Siedlecki, P. Pérez-Merino, N. Chia, A. de Castro, M. Szkulmowski, M. Wojtkowski, and S. Marcos. Corneal topography from spectral optical coherence tomography (sOCT). *Biomedical Optics Express*, 2(12):3232–3247, December 2011.
- [71] P. Pérez-Merino, M. Velasco-Ocana, E. Martinez-Enriquez, and S. Marcos. OCT-based crystalline lens topography in accommodating eyes. *Biomedical Optics Express*, 6:5039–5054, December 2015.
- [72] P. Pérez-Merino, M. Velasco-Ocana, E. Martinez-Enriquez, L. Revuelta, S. McFadden, and S. Marcos. Three-dimensional OCT based guinea pig eye model: Relating morphology and optics. *Biomedical Optics Express*, 8:2173–2184, April 2017.
- [73] A. Podoleanu, I. Charalambous, L. Plesea, A. Dogariu, and R. Rosen. Correction of distortions in optical coherence tomography imaging of the eye. *Physics in Medicine & Biology*, 49(7):1277–1294, 2004.
- [74] M.N. Polyanskiy. Refractive index database. <https://refractiveindex.info>. Accessed on 2018-08-14.
- [75] D. Purves, G.J. Augustine, D. Fitzpatrick, L.C. Katz, A.-S. LaMantia, J.O. McNamara, and S.M. Williams. Types of eye movements and their functions. In *Neuroscience*. Sinauer Associates, 2nd edition, 2001. <https://www.ncbi.nlm.nih.gov/books/NBK10991/>. Accessed: August 30, 2018.
- [76] S.K. Radhakrishnan, A.M. Rollins, J.E. Roth, S. Yazdanfar, V. Westphal, D.S. Bardenstein, and J.A. Izatt. Real-time optical coherence tomography of the anterior segment at 1310 nm. *Archives of Ophthalmology*, 119:1179–1185, August 2001.

- [77] P. Rodríguez, R. Navarro, and J. Rozema. Eigencorneas: Application of principal component analysis to corneal topography. *Ophthalmic & Physiological Optics*, 34:667–677, September 2014.
- [78] T.O. Salmon and L.N. Thibos. Videokeratoscope–line-of-sight misalignment and its effect on measurements of corneal and internal ocular aberrations. *Journal of the Optical Society of America A*, 19(4):657–669, April 2002.
- [79] A. Saltelli. Making best use of model evaluations to compute sensitivity indices. *Computer Physics Communications*, 145(2):280–297, 2002.
- [80] A. Saltelli, P. Annoni, I. Azzini, F. Campolongo, M. Ratto, and S. Tarantola. Variance based sensitivity analysis of model output. design and estimator for the total sensitivity index. *Computer Physics Communications*, 181(2):259–270, 2010.
- [81] M. De Santo, C. Liguori, A. Paolillo, and A. Pietrosanto. Standard uncertainty evaluation in image-based measurements. *Measurement*, 36(3):347–358, 2004.
- [82] C. Saxer, R.H. Hart, and E.L. Buckland. Immersion lens assemblies for use in optical coherence tomography systems. U.S. Patent 9,733,152. August 15, 2017.
- [83] J. Schwiegerling. Scaling Zernike expansion coefficients to different pupil sizes. *Journal of the Optical Society of America A*, 19(10):1937–1945, October 2002.
- [84] J. Schwiegerling and J.E. Greivenkamp. Using corneal height maps and polynomial decomposition to determine corneal aberrations. *Optometry & Vision Science*, 74(11):906—916, November 1997.
- [85] J.T. Schwiegerling. Eye axes and their relevance to alignment of corneal refractive procedures. *Journal of Refractive Surgery*, 29(8):515–516, August 2013.
- [86] G.A.F. Seber and C.J. Wild. *Nonlinear Regression*. John Wiley & Sons, 2003.
- [87] V. Sicam, M. Dubbelman, and R. Heijde. Spherical aberration of the anterior and posterior surface of the human cornea. *Journal of the Optical Society of America A*, 23:544–549, April 2006.
- [88] V.A.D.P. Sicam, J. Coppens, T.J.T.P. van den Berg, and R.G.L. van der Heijde. Corneal surface reconstruction algorithm that uses Zernike polynomial representation. *Journal of the Optical Society of America A*, 21(7):1300–1306, July 2004.
- [89] R.C. Smith. *Uncertainty Quantification: Theory, Implementation, and Applications*. SIAM, 1 edition, 2013.
- [90] R.C. Smith. *Uncertainty Quantification: Theory, Implementation, and Applications*. SIAM, 2 edition, 2020. Unpublished draft.

- [91] M.K. Smolek and S.D. Klyce. Goodness-of-prediction of Zernike polynomial fitting to corneal surfaces. *Journal of Cataract & Refractive Surgery*, 31(12):2350–2355, 2005.
- [92] I.M Sobol’. On the distribution of points in a cube and the approximate evaluation of integrals. *USSR Computational Mathematics & Mathematical Physics*, 7(4):86–112, 1967.
- [93] I.M. Sobol’. Uniformly distributed sequences with an additional uniform property. *USSR Computational Mathematics & Mathematical Physics*, 16(5):236–242, 1976.
- [94] I.M. Sobol’. Sensitivity estimates for nonlinear mathematical models. *Mathematical Modeling & Computational Experiment*, 1(4):407–414, 1993.
- [95] A. Sommerfeld and J. Runge. Anwendung der Vektorrechnung auf die Grundlagen der geometrischen Optik. (German) [Application of vector calculus to the basis of geometric optics]. *Annalen der Physik*, 340(7):277–298, March 1911.
- [96] J. Stegmaier, A.M. Khan, M. Reischl, and R. Mikut. Challenges of uncertainty propagation in image analysis. In *Proceedings 22. Workshop Computational Intelligence, Dortmund, 6–7 December, 2012*, pages 55–69, 2012.
- [97] M. Sun, J. Birkenfeld, A. de Castro, S. Ortiz, and S. Marcos. OCT 3-D surface topography of isolated human crystalline lenses. *Biomedical Optics Express*, 5, October 2014.
- [98] M. Sun, A. de Castro, S. Ortiz, P. Perez-Merino, J. Birkenfeld, and S. Marcos. Intraocular lens alignment from an en face optical coherence tomography image Purkinje-like method. *Optical Engineering*, 53:53–59, 2014.
- [99] M. Sun, P. Pérez-Merino, E. Martinez-Enriquez, M. Velasco-Ocana, and S. Marcos. Full 3-D OCT-based pseudophakic custom computer eye model. *Biomedical Optics Express*, 7(3):1074–1088, March 2016.
- [100] M. Tang, A. Chen, Y. Li, and D. Huang. Corneal power measurement with Fourier-domain optical coherence tomography. *Journal of Cataract & Refractive Surgery*, 36:2115–2122, December 2010.
- [101] L.N. Thibos, R.A. Applegate, J.T. Schwiegerling, and R. Webb. Standards for reporting the optical aberrations of eyes. *Journal of Refractive Surgery*, 18(5):S652–S660, September 2002.
- [102] J. Turuwhenua. Corneal surface reconstruction algorithm using Zernike polynomial representation: improvements. *Journal of the Optical Society of America A*, 24(6):1551–1561, June 2007.




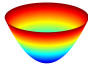
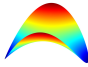
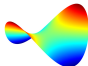
- [103] J. Wagner, D. Goldblum, and P. Cattin. Golden angle based scanning for robust corneal topography with OCT. *Biomedical Optics Express*, 8:475–483, February 2017.
- [104] J.Y. Wang and D.E. Silva. Wave-front interpretation with Zernike polynomials. *Applied Optics*, 19:1510–1518, May 1980.
- [105] V. Westphal, A.M. Rollins, S. Radhakrishnan, and J.A. Izatt. Correction of geometric and refractive image distortions in optical coherence tomography applying fermat’s principle. *Optics Express*, 10(9):397–404, May 2002.
- [106] J.J. Wu, R. Sharma, and T.S. Huang. Analysis of uncertainty bounds due to quantization for three-dimensional position estimation using multiple cameras. *Optical Engineering*, 37(1):280–292, 1998.
- [107] J. Wyant and K. Creath. Basic wavefront aberration theory for optical metrology. *Applied Optics & Optical Engineering*, 11, January 1992.
- [108] F. Zernike. Diffraction theory of the knife-edge test and its improved form, the phase-contrast method. *Monthly Notices of the Royal Astronomical Society*, 94(5):377–384, 1934.
- [109] L.C. Zhao, P.R. Krishnaiah, and Z.D. Bai. On detection of the number of signals in presence of white noise. *Journal of Multivariate Analysis*, 20(1):1–25, 1986.
- [110] M. Zhao, A.N. Kuo, and J.A. Izatt. 3D refraction correction and extraction of clinical parameters from spectral domain optical coherence tomography of the cornea. *Optics Express*, 18(9):8923–8936, April 2010.

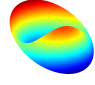

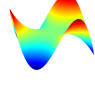
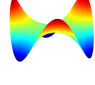
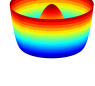
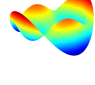
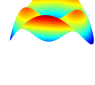
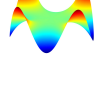
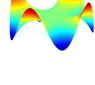
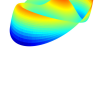
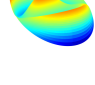
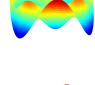
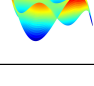
## APPENDICES

# Appendix A

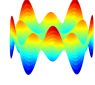
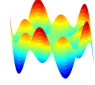
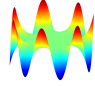
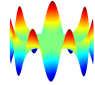
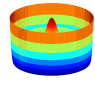
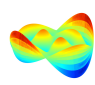
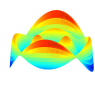
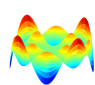
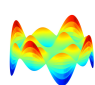
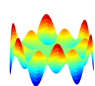
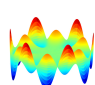
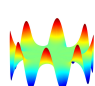
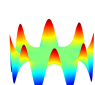
## Table of Zernike Polynomials

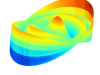
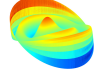
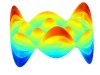
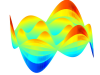
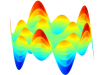
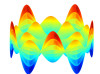
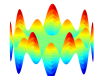
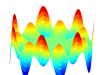
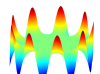
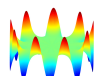
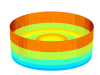
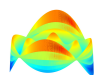
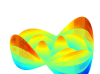
Table A.1: The first 66 Zernike basis functions (ordered according to Noll's index  $j$ ), corresponding to all polynomials up to and including radial order  $N = 10$ . The polynomials have been normalized to preserve the orthogonality relation in (3.3).

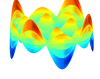
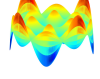
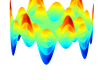
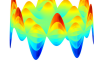
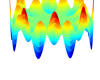
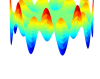
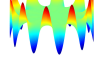
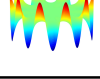
$j$	$n$	$m$	$Z_j(\rho, \theta)$	Graph
1	0	0	1	
2	1	1	$2\rho \cos \theta$	
3	1	-1	$2\rho \sin \theta$	
4	2	0	$\sqrt{3}(2\rho^2 - 1)$	
5	2	-2	$\sqrt{6}\rho^2 \sin 2\theta$	
6	2	2	$\sqrt{6}\rho^2 \cos 2\theta$	

$j$	$n$	$m$	$Z_j(\rho, \theta)$	Graph
7	3	-1	$\sqrt{8}(3\rho^3-2\rho)\sin\theta$	
8	3	1	$\sqrt{8}(3\rho^3-2\rho)\cos\theta$	
9	3	-3	$\sqrt{8}\rho^3\sin 3\theta$	
10	3	3	$\sqrt{8}\rho^3\cos 3\theta$	
11	4	0	$\sqrt{5}(6\rho^4-6\rho^2+1)$	
12	4	2	$\sqrt{10}(4\rho^4-3\rho^2)\cos 2\theta$	
13	4	-2	$\sqrt{10}(4\rho^4-3\rho^2)\sin 2\theta$	
14	4	4	$\sqrt{10}\rho^4\cos 4\theta$	
15	4	-4	$\sqrt{10}\rho^4\sin 4\theta$	
16	5	1	$\sqrt{12}(10\rho^5-12\rho^3+3\rho)\cos\theta$	
17	5	-1	$\sqrt{12}(10\rho^5-12\rho^3+3\rho)\sin\theta$	
18	5	3	$\sqrt{12}(5\rho^5-4\rho^3)\cos 3\theta$	
19	5	-3	$\sqrt{12}(5\rho^5-4\rho^3)\sin 3\theta$	

$j$	$n$	$m$	$Z_j(\rho, \theta)$	Graph
20	5	5	$\sqrt{12}\rho^5 \cos 5\theta$	
21	5	-5	$\sqrt{12}\rho^5 \sin 5\theta$	
22	6	0	$\sqrt{7}(20\rho^6 - 30\rho^4 + 12\rho^2 - 1)$	
23	6	-2	$\sqrt{14}(15\rho^6 - 20\rho^4 + 6\rho^2) \sin 2\theta$	
24	6	2	$\sqrt{14}(15\rho^6 - 20\rho^4 + 6\rho^2) \cos 2\theta$	
25	6	-4	$\sqrt{14}(6\rho^6 - 5\rho^4) \sin 4\theta$	
26	6	4	$\sqrt{14}(6\rho^6 - 5\rho^4) \cos 4\theta$	
27	6	-6	$\sqrt{14}\rho^6 \sin 6\theta$	
28	6	6	$\sqrt{14}\rho^6 \cos 6\theta$	
29	7	-1	$4(35\rho^7 - 60\rho^5 + 30\rho^3 - 4\rho) \sin \theta$	
30	7	1	$4(35\rho^7 - 60\rho^5 + 30\rho^3 - 4\rho) \cos \theta$	
31	7	-3	$4(21\rho^7 - 30\rho^5 + 10\rho^3) \sin 3\theta$	
32	7	3	$4(21\rho^7 - 30\rho^5 + 10\rho^3) \cos 3\theta$	

$j$	$n$	$m$	$Z_j(\rho, \theta)$	Graph
33	7	-5	$4(7\rho^7 - 6\rho^5) \sin 5\theta$	
34	7	5	$4(7\rho^7 - 6\rho^5) \cos 5\theta$	
35	7	-7	$4\rho^7 \sin 7\theta$	
36	7	7	$4\rho^7 \cos 7\theta$	
37	8	0	$3(70\rho^8 - 140\rho^6 + 90\rho^4 - 20\rho^2 + 1)$	
38	8	2	$\sqrt{18}(56\rho^8 - 105\rho^6 + 60\rho^4 - 10\rho^2) \cos 2\theta$	
39	8	-2	$\sqrt{18}(56\rho^8 - 105\rho^6 + 60\rho^4 - 10\rho^2) \sin 2\theta$	
40	8	4	$\sqrt{18}(28\rho^8 - 42\rho^6 + 15\rho^4) \cos 4\theta$	
41	8	-4	$\sqrt{18}(28\rho^8 - 42\rho^6 + 15\rho^4) \sin 4\theta$	
42	8	6	$\sqrt{18}(8\rho^8 - 7\rho^6) \cos 6\theta$	
43	8	-6	$\sqrt{18}(8\rho^8 - 7\rho^6) \sin 6\theta$	
44	8	8	$\sqrt{18}\rho^8 \cos 8\theta$	
45	8	-8	$\sqrt{18}\rho^8 \sin 8\theta$	

$j$	$n$	$m$	$Z_j(\rho, \theta)$	Graph
46	9	1	$\sqrt{20}(126\rho^9-280\rho^7+210\rho^5-60\rho^3+5\rho)\cos\theta$	
47	9	-1	$\sqrt{20}(126\rho^9-280\rho^7+210\rho^5-60\rho^3+5\rho)\sin\theta$	
48	9	3	$\sqrt{20}(84\rho^9-168\rho^7+105\rho^5-20\rho^3)\cos 3\theta$	
49	9	-3	$\sqrt{20}(84\rho^9-168\rho^7+105\rho^5-20\rho^3)\sin 3\theta$	
50	9	5	$\sqrt{20}(36\rho^9-56\rho^7+21\rho^5)\cos 5\theta$	
51	9	-5	$\sqrt{20}(36\rho^9-56\rho^7+21\rho^5)\sin 5\theta$	
52	9	7	$\sqrt{20}(9\rho^9-8\rho^7)\cos 7\theta$	
53	9	-7	$\sqrt{20}(9\rho^9-8\rho^7)\sin 7\theta$	
54	9	9	$\sqrt{20}\rho^9\cos 9\theta$	
55	9	-9	$\sqrt{20}\rho^9\sin 9\theta$	
56	10	0	$\sqrt{11}(252\rho^{10}-630\rho^8+560\rho^6-210\rho^4+30\rho^2-1)$	
57	10	-2	$\sqrt{22}(210\rho^{10}-504\rho^8+420\rho^6-140\rho^4+15\rho^2)\sin 2\theta$	
58	10	2	$\sqrt{22}(210\rho^{10}-504\rho^8+420\rho^6-140\rho^4+15\rho^2)\cos 2\theta$	

$j$	$n$	$m$	$Z_j(\rho, \theta)$	Graph
59	10	-4	$\sqrt{22}(120\rho^{10}-252\rho^8+168\rho^6-35\rho^4)\sin 4\theta$	
60	10	4	$\sqrt{22}(120\rho^{10}-252\rho^8+168\rho^6-35\rho^4)\cos 4\theta$	
61	10	-6	$\sqrt{22}(45\rho^{10}-72\rho^8+28\rho^6)\sin 6\theta$	
62	10	6	$\sqrt{22}(45\rho^{10}-72\rho^8+28\rho^6)\cos 6\theta$	
63	10	-8	$\sqrt{22}(10\rho^{10}-9\rho^8)\sin 8\theta$	
64	10	8	$\sqrt{22}(10\rho^{10}-9\rho^8)\cos 8\theta$	
65	10	-10	$\sqrt{22}\rho^{10}\sin 10\theta$	
66	10	10	$\sqrt{22}\rho^{10}\cos 10\theta$	

# Appendix B

## Error Distribution for OCT Data & Synthetic Data for UQ

All of the uncertainty quantification methods in Chapter 6 are predicated on the assumption that the noise in the data is independent and identically distributed (iid). We have already noted in Section 2.4 that the error in the quantized synthetic data is not iid, as there are patterns that appear when the residuals are plotted as a function of radial position. It turns out that similar patterns do in fact appear in the residuals for the real point cloud data used in Chapter 5, which are plotted in Figure B.1. In addition, there is also a significant amount of unaccommodated model error.

A third issue with using the real data for model calibration involves the off-axis imaging discussed in Section 5.1.1. Because the real data are not centered with respect to the Zernike basis, different Zernike functions are required to construct the model and therefore we would not be able to compare the estimated coefficient values to those obtained by integrating the design equations. Performing a second fit after realignment would double the computational cost, and many of the methods used in Chapter 6 are

Table B.1: Model error variance  $\sigma^2$  computed from real data, in square millimeters.

Aspheric lens front	Toric lens front	Aspheric lens back	Toric lens back
$2.1554 \times 10^{-5}$	$9.2203 \times 10^{-5}$	$4.8743 \times 10^{-5}$	$6.4319 \times 10^{-5}$

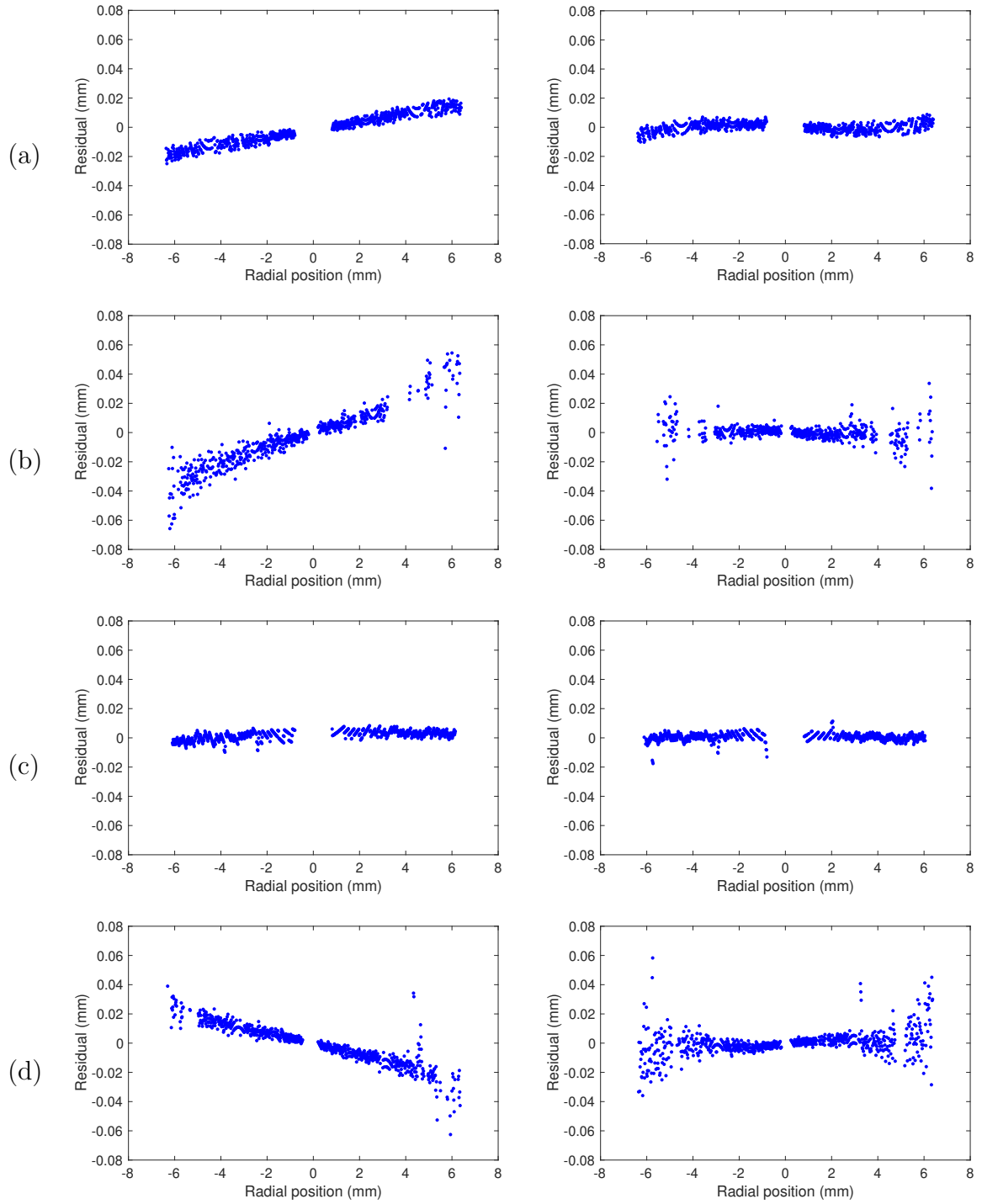


Figure B.1: Residuals for the 1<sup>st</sup> (left) and 60<sup>th</sup> (right) frames of real data for the (a) front of the asphere, (b) front of the toric lens, (c) back of the asphere, and (d) back of the toric lens.

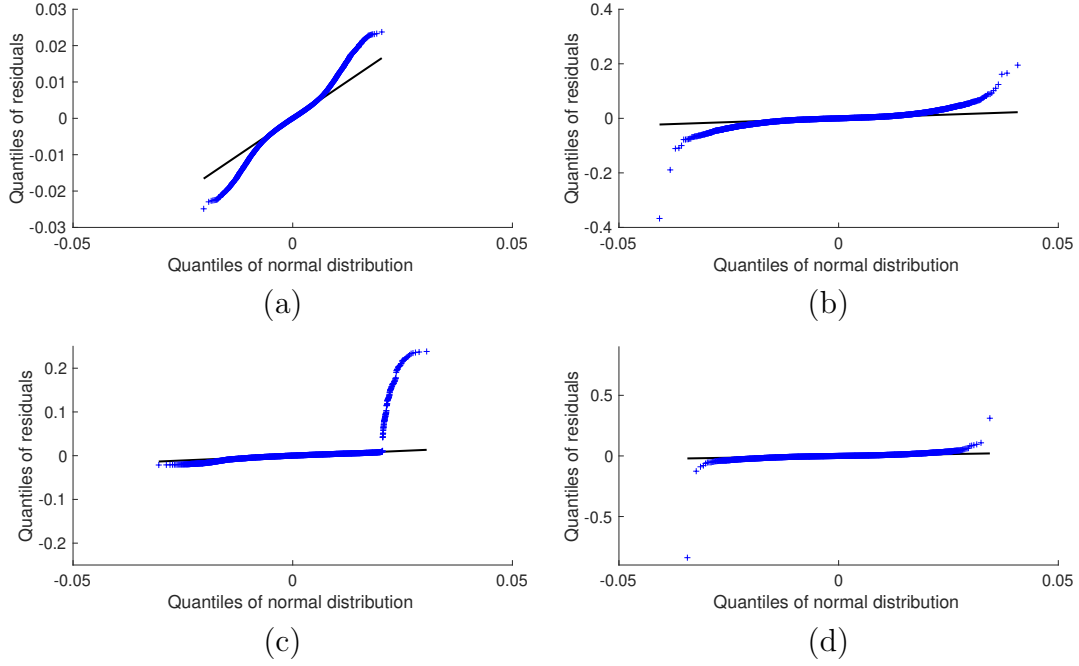


Figure B.2: Q-Q plots of real data residuals vs.  $\mathcal{N}(0, \sigma^2)$  for the (a) front of the asphere, (b) front of the toric lens, (c) back of the asphere, and (d) back of the toric lens.

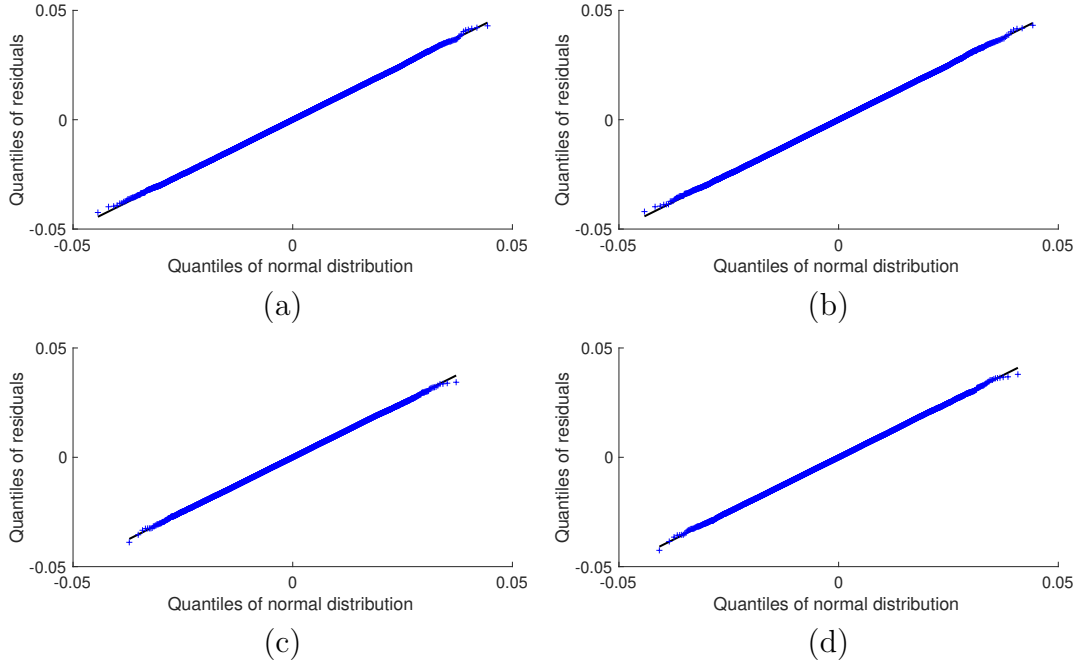


Figure B.3: Q-Q plots of synthetic data residuals vs.  $\mathcal{N}(0, \sigma^2)$  for the (a) front of the asphere, (b) front of the toric lens, (c) back of the asphere, and (d) back of the toric lens.

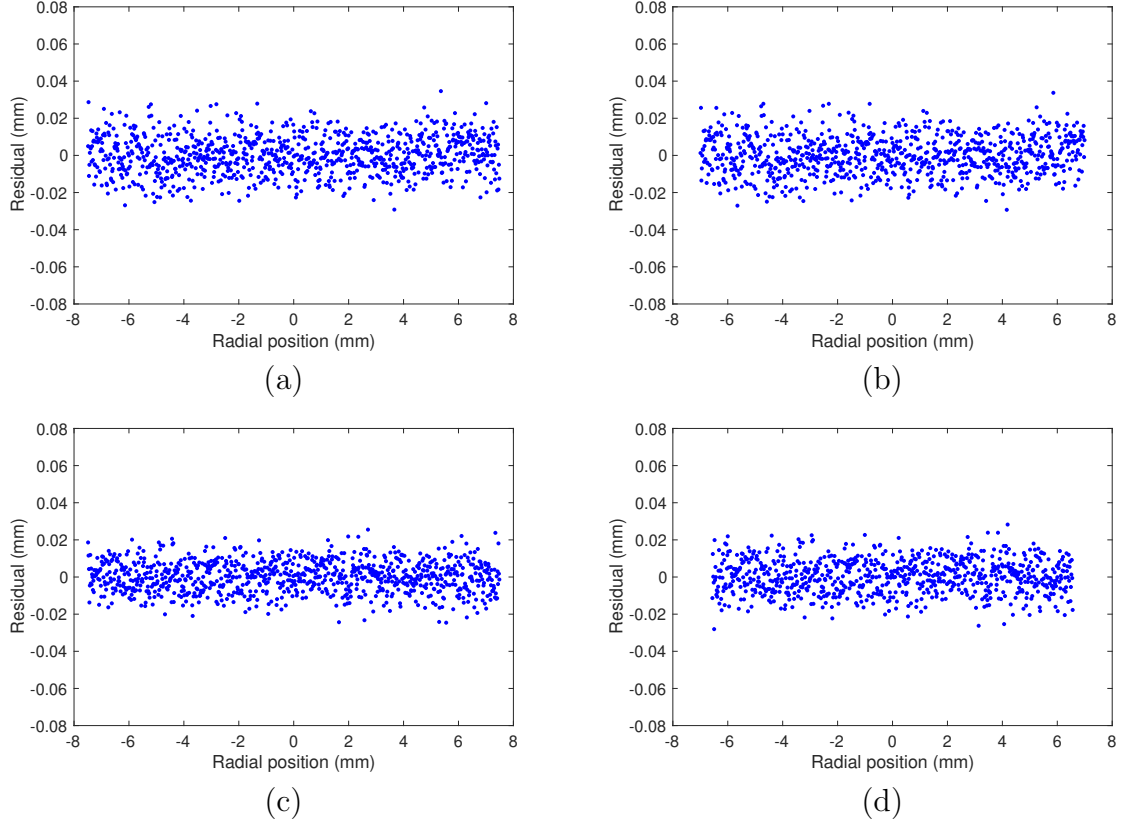


Figure B.4: Residuals for the 1<sup>st</sup> frame of synthetic data for the (a) front of the asphere, (b) front of the toric lens, (c) back of the asphere, and (d) back of the toric lens.

already extremely expensive.

For the reasons discussed above, we have chosen to conduct the uncertainty quantification in Chapter 6 on a new synthetic data set rather than on the real point cloud data or the quantized synthetic data. This new synthetic data set is constructed in the manner discussed in Section 4.3, except instead of adding quantization error we have added Gaussian error (which also has the benefit of allowing us to make certain assumptions about the distribution of error in the Zernike coefficients). Figures B.5–B.6 show examples of the synthetic data with normally distributed noise along with the corresponding frame of point cloud data for each lens surface.

Although the mean value of the error across all the point cloud data for each surface is fairly small ( $\sim 10^{-15}$  mm for both front surfaces and  $\sim 10^{-8}$ – $10^{-7}$  mm for the back surfaces), we see in Figure B.1 that this is due to a systematic, antisymmetric bias in

Table B.2: Zernike order  $N$  used to fit each lens surface.

Surface	Real data	Synthetic data
Aspheric lens front	4	4
Aspheric lens back	3	2
Toric lens front	8	10
Toric lens back	6	8

some of the frames. Furthermore, in addition to the non-iid nature of the quantization error, some of the frames also appear to exhibit error with non-constant variation. This is confirmed in the Q-Q plots in Figure B.2, which compare the residuals for the real data to a normal distribution with zero mean and constant variance  $\sigma^2$  computed from the data. The precise values of  $\sigma^2$  for each surface are shown in Table B.1. These are also the values used to construct the synthetic data in Figures B.5–B.6. The residuals for this new synthetic data shown in Figure B.4 and the Q-Q plots in Figure B.3 both confirm that the noise is indeed  $\stackrel{iid}{\sim} \mathcal{N}(0, \sigma^2)$ .

Table B.2 lists the Zernike order of the model used to fit each data set. These were selected based on the results of Chapters 3 and 5.

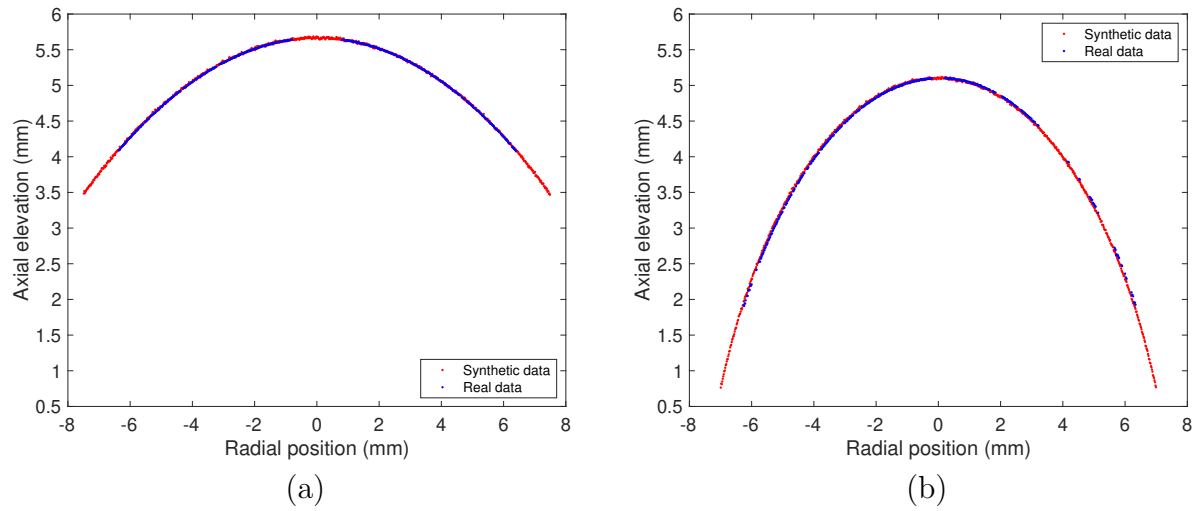


Figure B.5: Real axial elevation data and synthetic data with normally distributed noise for the front surface of the (a) aspheric lens and (b) toric lens.

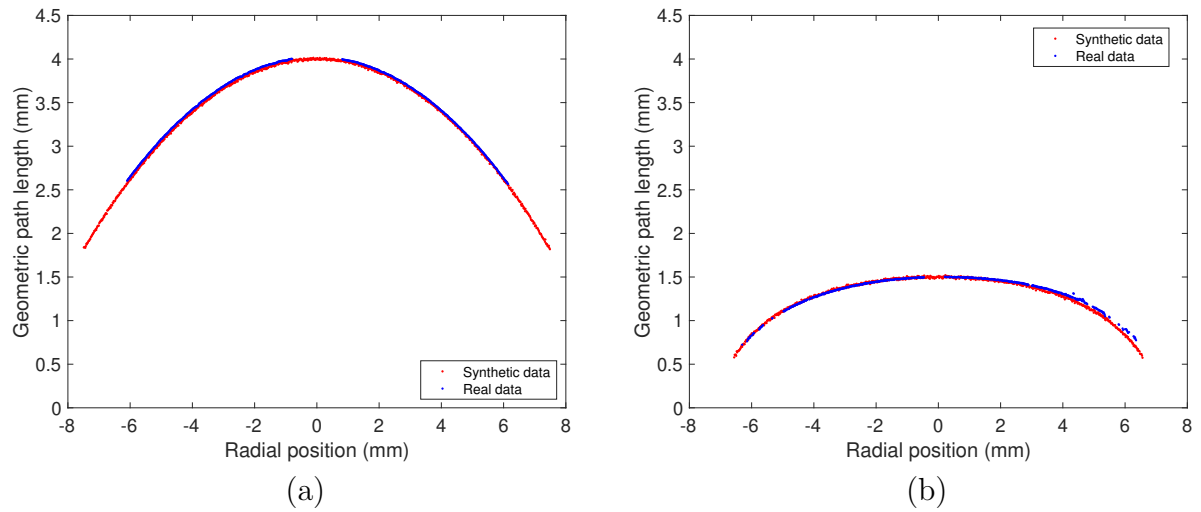


Figure B.6: Real geometric path length (GPL) data and synthetic GPL data with normally distributed noise for the back surface of the (a) aspheric lens and (b) toric lens.

# Appendix C

## Convergence of Sobol' Indices

Figures C.1–C.2 illustrate the convergence of the estimated Sobol' indices discussed Section 6.5 according to their 95% bootstrap confidence intervals, as recommended in [8, 80]. The confidence intervals were determined using the MATLAB function `bootci` with 10000 subsamples. For the reduced order models, 200000 model evaluations were required for convergence of both front surfaces as well as for the back of the toric lens; however, nearly twice as many evaluations were needed when considering the sensitivity of the posterior curvature to the anterior surface coefficients after dewarping.

For the results in Section 6.5 that were based on the full models, we used 20000 evaluations for both front surfaces as well as the back of the toric lens after dewarping. We needed 30000 evaluations for the back of the toric lens without dewarping. We have not included confidence intervals for the full models due to the computational cost of the bootstrap method.

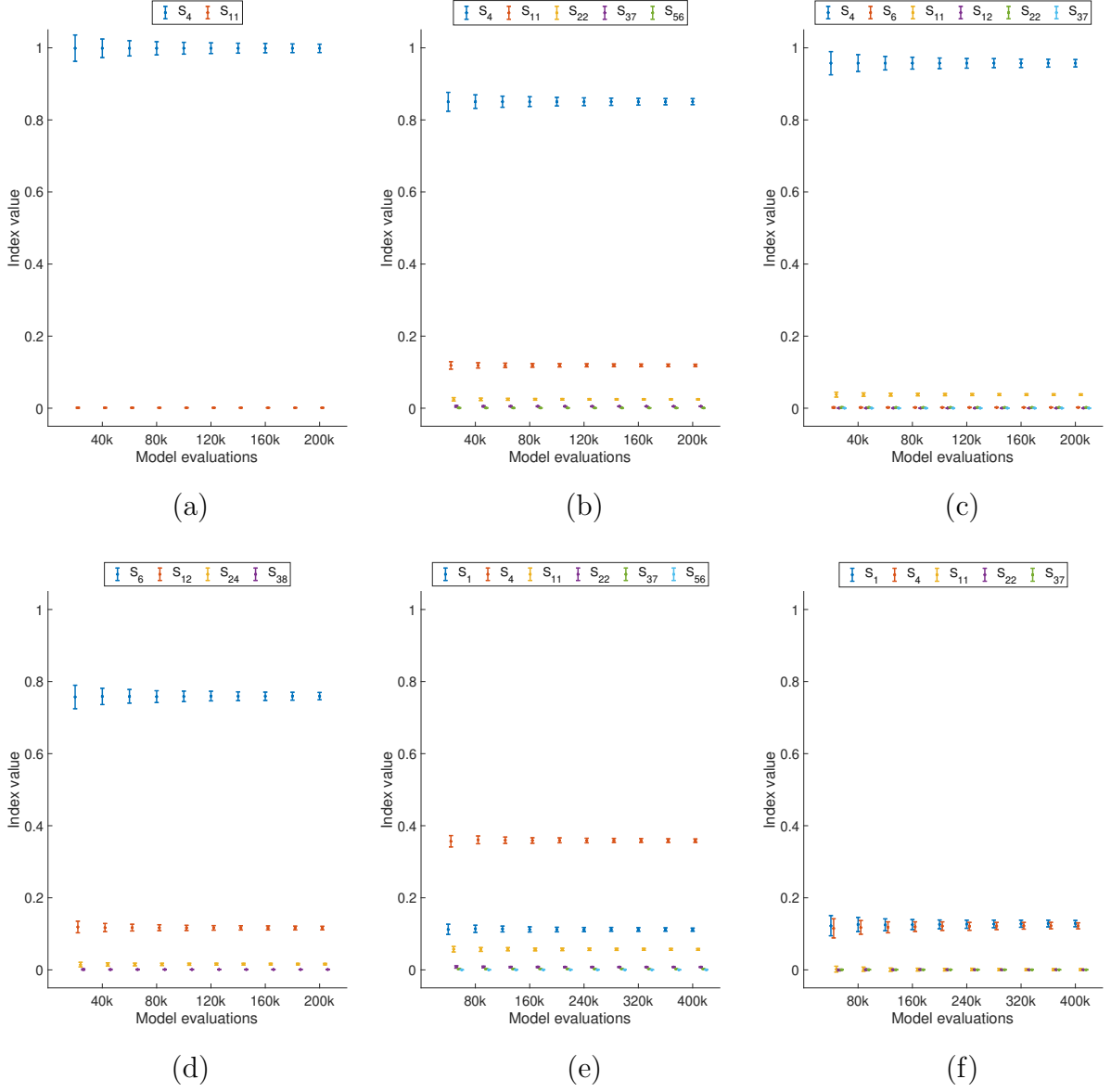


Figure C.1: Convergence of first order Sobol' indices ( $S_i$ ) for (a) the principal curvature of the anterior aspheric lens, (b) the principal curvature of the anterior toric lens, (c) the maximum principal curvature of the posterior toric lens with respect to the back surface coefficients, (d) the difference in principal curvatures of the posterior toric lens with respect to the back surface coefficients, (e) the maximum principal curvature of the posterior toric lens with respect to the front surface coefficients (after dewarping), and (f) the difference in principal curvatures of the posterior toric lens with respect to the front surface coefficients (after dewarping).

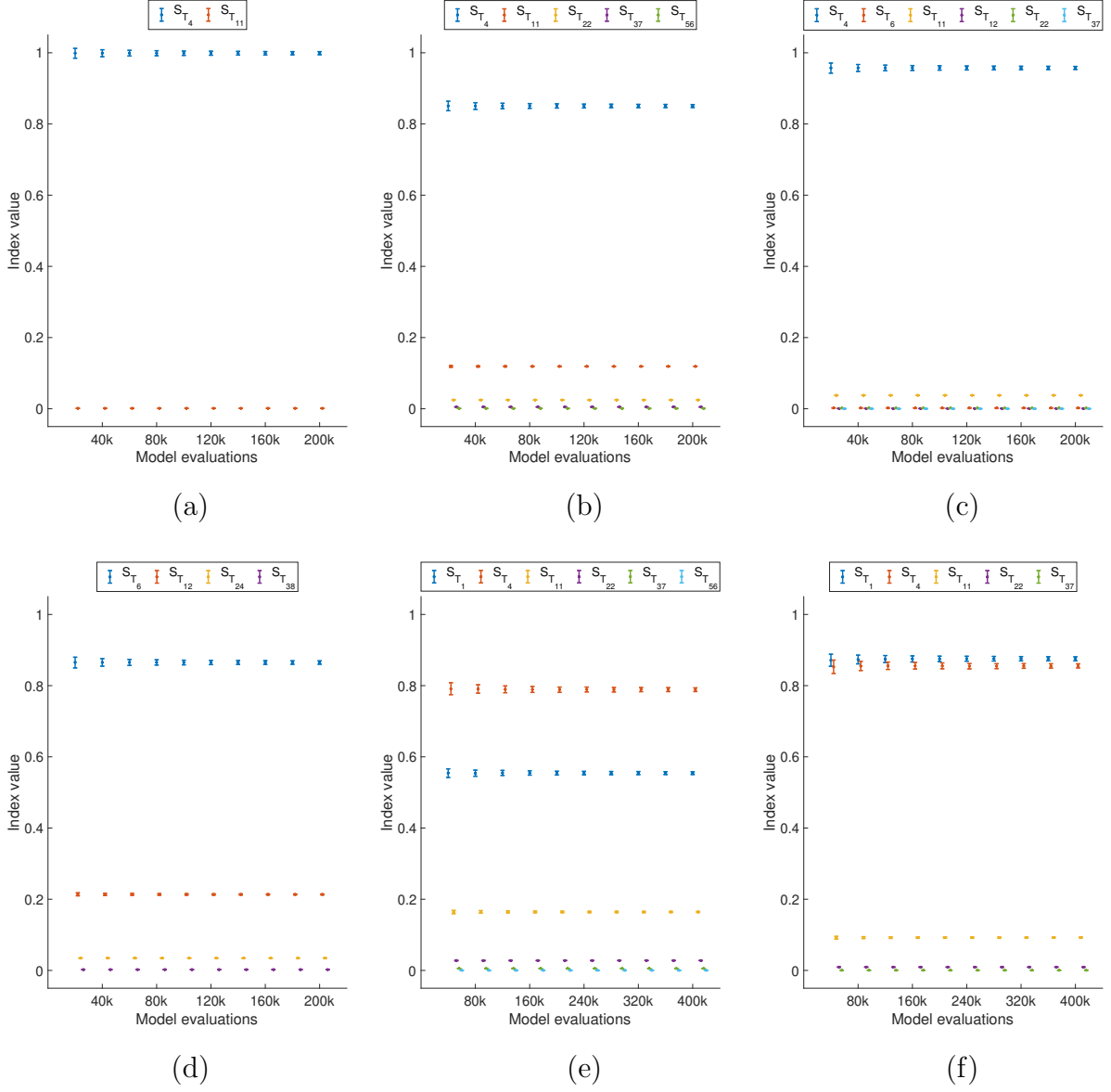


Figure C.2: Convergence of total Sobol' indices ( $S_{T_i}$ ) for (a) the principal curvature of the anterior aspheric lens, (b) the principal curvature of the anterior toric lens, (c) the maximum principal curvature of the posterior toric lens with respect to the back surface coefficients, (d) the difference in principal curvatures of the posterior toric lens with respect to the back surface coefficients, (e) the maximum principal curvature of the posterior toric lens with respect to the front surface coefficients (after dewarping), and (f) the difference in principal curvatures of the posterior toric lens with respect to the front surface coefficients (after dewarping).